UNIVERSITEIT VAN PRETORIA
UNIVERSITY OF PRETORIA
YUNIBESITHI YA PRETORIA

University of Pretoria

Sintering behaviour of model cobalt crystallites: Effect of support phase on the structure and size of crystallites.

By

Bongani Michael Xaba

Dissertation submitted in partial fulfilment for the degree
Master of Science (Applied Science) Metallurgy

In the Faculty of Engineering, the Built Environment and Information Technology
Department of Materials Science and Metallurgical Engineering

Supervisor: Prof. J.P.R. De Villiers

June 2016

ACKNOWLEDGEMENTS

I thank God, the Father, and Jesus Christ for the strength and perseverance to finish this work.

To Professor Johan de Villiers, thank you for the guidance, support and patience with me. Thank you for always pushing me to get things done and to work hard.

I would like to acknowledge the following people from Sasol Group Technology R&T Analytics for their contribution through advice and guidance:

- Petrie Steynberg – For believing in me and giving me the opportunity to study.
- Willem Erasmus – My manager
- Tracy Bromfield
- Esna du Plessis
- Alisa Govender

I dedicate this dissertation to my beautiful wife, Lehlogonolo Faith, my son, Thando and my daughter, Nandi.

“If something is important enough, even if the odds are against you, you should do it.”

- Elon Musk

Abstract

Cobalt-based catalysts are currently being used in the Fischer-Tropsch synthesis (FTS) process. These catalysts however deactivate with time on stream. Sintering has been identified as one of the most significant deactivation mechanisms for cobalt-based catalysts. Therefore understanding the sintering mechanism of cobalt crystallites is important since this can lead to the preparation of stable catalysts. The type of support has been shown to have an influence on the activity and stability of the FTS catalysts. Typical catalyst supports for FTS catalysts include Al_2O_3, SiO_2 and TiO_2. In this study, TiO_2 was used as support for model cobalt crystallites. This material occurs in different crystalline phases such as rutile, anatase and brookite. These phases have different bulk and surface properties.

Three titania supports were obtained. The supports were identified as anatase-, P25- and rutile-support. The anatase-support was shown to consist of 100% anatase phase by XRD. The support was shown to have the highest surface area and mesoporous pore structure. The P25-support was shown to consist of ~85% anatase and ~15% rutile phases. The support was shown to have a surface area lower than that of the anatase-support, but higher than that of the rutile-support. P25-support also has a mesoporous pore structure. The rutile-support was shown to consist of ~2% anatase and ~98% rutile phases. This support had the lowest surface area, although still had a mesoporous pore structure.

Cobalt catalysts were prepared by wet impregnation with constant cobalt loading of ~10 wt% onto the supports, followed by calcination at temperatures ranging from 200°C – 400°C. It was found that calcination temperature in this range did not affect the size of the Co_3O_4 crystallites for each support. The titania support influenced the phase composition of the calcined catalysts. In this case, the titanate phase $CoTiO_3$ was preferentially formed in rutile-supported catalysts and not in anatase- and P25-supported catalysts. Calcination in air at a temperature range from 200°C – 400°C did not significantly affect the pore structure of the calcined catalysts. The mesoporous nature of the catalysts was retained after calcination.

The calcined catalysts were reduced in H_2/Ar at 450°C to convert the cobalt oxide into metallic species. The starting metallic cobalt crystallite size was influenced by the type of titania support phase as evidenced by TEM analysis. Smaller crystallites were obtained in Anatase- and Rutile-supported catalysts. P25-support gave slightly larger cobalt crystallites. The smaller cobalt crystallites in the anatase-support were shown to undergo agglomeration in the reduction step. In a prior TPR experiment, the support itself was shown to interact with hydrogen, leading to a possible reduction of the surface. It is postulated that this interaction with hydrogen might have led to the formation of surface defects and/or oxygen vacancies which in turn may influence the anchoring of cobalt crystallites. The reduction behaviour of cobalt crystallites was shown to be influenced by the titania-support. TPR showed different reduction profiles in the different supports. The titania support also influenced the presence of fcc and hcp cobalt. Both fcc and hcp cobalt were obtained in Anatase- and Rutile-supported catalysts. Only fcc cobalt was obtained in P25-supported catalysts.

Sintering studies were conducted in a reducing environment and at higher temperature than usually used in Fischer-Tropsch synthesis. This was to accelerate the sintering process in order to observe changes that would otherwise occur over longer operating time.

The crystallite size data from the TEM were fitted well to a lognormal distribution function to obtain crystallite size distribution (PSD) plots. The PSD curves changed with sintering time, confirming the occurrence of sintering of the cobalt particles. The crystallite size data from XRD and TEM showed a power-law type of growth when plotted against time. The sintering kinetics was also studied. In this case, the data was fitted well to the simple power law expression (SPLE) and generalized power law expression (GPLE) models.

The sintering data in all three supports were fitted well to the first order GPLE model. The sintering was shown to be different in the three supports as shown by different sintering rate constants. The titania support phase influences the material science characteristics of model calcined, reduced and sintered crystallites. This effect may stem from the different metal-support interaction that occurs in the different titania phases. Sintering was seen to be more prevalent in anatase-supported catalyst compared to P25- and rutile-supported catalysts. The support porosity is also postulated to play a role in the sintering of cobalt crystallites. It was found that sintering tendency increases with decreasing pore size. From an industrial application point of view P25 is the most preferred support showing the least sintering probability.

Table of Contents

1. CHAPTER 1 – INTRODUCTION AND BACKGROUND 14

1.1. INTRODUCTION 14

1.1.1. Background 14

1.1.2. Deactivation of cobalt-based GTL catalysts 15

1.2. PROBLEM STATEMENT 15

1.3. RESEARCH QUESTIONS AND OBJECTIVES 16

1.4. RATIONALE OF THE RESEARCH 16

2. CHAPTER 2 – THEORY AND RESEARCH REVIEW 19

2.1. COBALT AND ITS OXIDES 19

2.1.1. Bulk Structure of Cobalt Oxides 19

2.2. TITANIA AND ITS POLYMORPHS 22

2.2.1. Bulk Structure of TiO_2 Polymorphs 22

2.2.2. Bonding and Defect Chemistry of TiO_2 23

2.3. FUNDAMENTAL THEORIES GOVERNING SINTERING 24

2.3.1. Ostwald Ripening (atomic migration) 25

2.3.2. Particle Migration and Coalescence (PMC) 27

2.3.3. Kinetics of Sintering – Simple Power Law Expression (SPLE) and Generalized Power Law Expression (GPLE) 28

2.4. REVIEW OF LITERATURE ON SINTERING STUDIES 29

2.4.1. Effect of support type and phase composition 30

2.4.2. Metal-support Interaction 30

2.4.3. Effect of metal particle size 31

2.5. MATERIALS CHARACTERIZATION TECHNIQUES 32

2.5.1. Powder X-ray Diffraction (XRD) 32

2.5.2. Transmission Electron Microscopy (TEM) 33

2.5.3. Raman Spectroscopy 36

2.5.4. Surface Area and Porosity 37

2.5.5. Temperature Programmed Reduction (TPR) 39

2.5.6. Hydrogen – Chemisorption 40

3. CHAPTER 3 – EXPERIMENTAL PROCEDURE 43

3.1. FURNACE PROFILING 43

3.2. CATALYST PREPARATION 44

3.2.1. Support Preparation 44

3.2.2. Catalyst Preparation 45

3.2.3. Calcination Study 45

3.2.4. Reduction Study 45

3.3. SINTERING STUDIES 47

3.4. CHARACTERIZATION TECHNIQUES 48

3.4.1. X-Ray Diffraction (XRD) 48

3.4.2. Transmission Electron Microscopy (TEM) 50

3.4.3. BET Surface Area and Pore Size Distribution 55

3.4.4. Raman Spectroscopy 55

3.4.5. Temperature Programmed Reduction (TPR) 55

3.4.6. Hydrogen Chemisorption 56

4. CHAPTER 4 – EXPERIMENTAL DESIGN 58

4.1. INTRODUCTION 58

4.2. RESPONSE SURFACE METHODOLOGY (RSM) AND FACTORIAL DESIGN 58

4.2.1. Experimental variables for the study 59

4.2.2. Statistical Variables 61

5. CHAPTER 5 – RESULTS AND DISCUSSION 65

5.1. STAGE 1 – TITANIA SUPPORT CHARACTERIZATION 65

5.1.1. XRD 65

5.1.2. Transmission Electron Microscopy (TEM) 68

5.1.3. BET Surface Area and Pore Size Distribution 71

5.1.4. Raman Spectroscopy 73

5.2. STAGE 2 – CATALYST CHARACTERIZATION (CALCINATION STUDY) 77

5.2.1 XRD 77

5.2.2. TEM 82

5.2.3. BET Surface Area and Pore Size Distribution 85

5.2.4. Raman Spectroscopy 88

5.3. STAGE 3 - CATALYST REDUCTION 95

5.3.1. XRD 95

5.3.2. High Temperature XRD 96

5.3.3. TEM 101

5.3.4. H_2-Chemisorption 105

5.3.5. Temperature Programmed Reduction (TPR) 107

5.3.6. BET Surface Area and Pore Size Distribution 112

5.4. STAGE 4 - SINTERING STUDIES 115

5.4.1. Crystallite Size Distributions (PSD) derived from TEM 115

5.4.2. Statistical Modelling – Regression Analysis (XRD and TEM) 119

5.4.3. Evaluation and Comparison of Crystallite Size Data (XRD and TEM) 135

5.4.4. Empirical Modelling of Sintering – SPLE and GPLE 136

5.4.5. Phenomenological Modelling of sintering – Ostwald Ripening or Particle Migration 142

6. CHAPTER 6 – SUMMARY AND CONCLUSIONS 148

6.1. SUMMARY 148

6.1.1. Stage 1 – Support Characterization 148

6.1.2. Stage 2 – Catalyst Characterization (Calcination study) 149

6.1.3. Stage 3 – Catalyst Reduction 149

6.1.4. Stage 4 – Sintering Studies 150

6.2. CONCLUSIONS 151

6.3. FUTURE WORK 152

7. REFERENCE 153

APPENDIX A 173

APPENDIX B 178

List of Figures

Figure 2. 1: Crystal structure of Co_3O_4 showing the spinel structure 19

Figure 2. 2: Crystal field splitting illustration showing paired and unpaired electrons in d^6 and d^7 configurations respectively. 20

Figure 2. 3: Crystal structure of CoO showing the rocksalt structure 21

Figure 2. 4: A schematic illustration of the crystal structures of TiO_2 phases showing Anatase and Rutile phases 23

Figure 2.5: A simplified schematic illustration of Ostwald ripening...................................... 26

Figure 2. 6: A simplified schematic illustration of coalescence. 27

Figure 2. 7: A schematic illustration of the Bragg-Brentano diffractometer showing the main components 33

Figure 2. 8: A schematic illustration of the electron beam – specimen interactions showing various signals emitted.. 34

Figure 2. 9: A simplified schematic illustration of a conventional TEM................................ 35

Figure 2. 10: A schematic illustration of Raman scattering process and various signals generated... 36

Figure 2. 11: A schematic illustration of the gas adsorption process. 38

Figure 3. 1: Schematic illustration of the furnace temperature profile 44

Figure 3. 2: Schematic illustration of the double-walled glass tube used in reduction and sintering studies. 46

Figure 3. 3: Schematic illustration of the experimental setup for reduction and sintering studies 47

Figure 3. 4: Schematic illustration showing the crystallite size measurement approach described as the Feret diameter of the particle.. 50

Figure 3. 5: Schematic illustration of lognormal distribution function (LNDF) curve showing the position of the mode, median and mean... 53

Figure 5. 1: Powder diffractograms of titania supports showing (a) Anatase support, (b) P25 support and (c) Rutile support. 66

Figure 5. 2: Bright Field TEM image of Anatase support 68

Figure 5. 3: Bright field TEM image of P25 support. 69

Figure 5. 4: Bright field TEM image of Rutile support. 70

Figure 5. 5: N_2-adsorption-desorption isotherms of titania supports showing the pore structure... 73

Figure 5.6: Raman spectra of titania supports showing characteristic bands....................... 74

Figure 5. 7: EDX mapping super-imposed onto a HAADF-STEM image of Cat_Anat_300.. 83

Figure 5. 8: EDX mapping super-imposed onto a HAADF-STEM image of Cat_P25_300... 84
Figure 5. 9: EDX mapping super-imposed onto a HAADF-STEM image of Cat_Rut_300.... 85
Figure 5. 10: Surface area results of titania supports and calcined catalysts plotted against calcination temperature. 86
Figure 5. 11: Pore size distribution results of titania supports and calcined catalysts showing pore size characteristics. 87
Figure 5. 12: Raman Spectra of Anatase-supported catalysts showing characteristic bands. 89
Figure 5. 13: Raman spectra of Anatase-supported catalysts showing the anatase E_g band 90
Figure 5. 14: Raman spectra of P25-supported catalysts 91
Figure 5. 15: Raman spectra of P25-supported catalysts showing the anatase E_g band 91
Figure 5. 16: Raman spectra of Rutile-supported catalysts showing characteristic bands. .. 92
Figure 5. 17: High temperature XRD diffractograms of Anatase-supported catalysts 97
Figure 5. 18: High temperature XRD relative phase abundances of Anatase-supported catalysts 97
Figure 5. 19: High temperature XRD diffractograms of Rutile-supported catalysts 99
Figure 5. 20: High temperature XRD relative phase abundances of Rutile-supported catalysts 99
Figure 5. 21: HAADF-STEM EDX mapping of RP_Cat_Anat_300 showing agglomeration of small crystallites into clusters 102
Figure 5. 22: HAADF-STEM EDX mapping of RP_Cat_P25_300.................................... 103
Figure 5. 23: HAADF-STEM EDX mapping of RP_Cat_Rut_300 104
Figure 5.24: Conceptual Model of Cobalt dispersion on TiO_2 (Adapted from Jongsomjit *et al*, 2005 p.575)... 106
Figure 5.25: Temperature Programmed Reduction (TPR) results of cobalt compounds 108
Figure 5.26: Temperature Programmed Reduction (TPR) results of titania-supported catalysts and supports showing the reduction profiles. 110
Figure 5. 27: Crystallite size distributions of Anatase-supported catalysts fitted onto lognormal distribution function, showing the effect of sintering time 117
Figure 5. 28: Crystallite size distributions of P25-supported catalysts fitted onto lognormal distribution function, showing the effect of sintering time.. 117
Figure 5. 29: Crystallite size distributions of Rutile-supported catalysts fitted onto lognormal distribution function, showing the effect of sintering time.. 119
Figure 5. 30: Plots of fcc cobalt crystallite size against sintering time for the titania-supported catalysts. (error ±1 nm).. 120

Figure 5. 31: Linearized log-log plots of fcc cobalt crystallite size against sintering time for the titania-supported catalysts........120
Figure 5. 32: Normal probability plot of residuals of the *2FI* model of fcc cobalt crystallites. 123
Figure 5. 33: A plot of externally studentized residuals of the *2FI* model of fcc cobalt crystallites........123
Figure 5. 34: An updated plot of log CS_fcc Co against log Sintering Time showing 95% CI bands and interaction between variables........124
Figure 5. 35: Plots of hcp cobalt crystallite size against sintering time for the titania-supported catalysts. (error ±1 nm)........125
Figure 5. 36: Linearized plots of log hcp cobalt crystallite size against log sintering time for the titania-supported catalysts........125
Figure 5. 37: A plot of Normal probability of residuals for response log CS_hcp Co........127
Figure 5. 38: A plot of externally studentized residuals for response log CS_hcp Co........128
Figure 5. 39: Plots of response log CS_hcp Co against log Sintering Time (factor A) and Support (factor B) showing the 95% CI bands........129
Figure 5. 40: Plots of TEM-based cobalt crystallite size against sintering time for Anatase, P25 and Rutile (error ±1 nm)........130
Figure 5. 41: Linearized plots of log cobalt crystallite size (TEM) against log sintering time for the titania-supported catalysts........130
Figure 5. 42: A plot of Normal probability of residuals for response CS_Co (TEM)........133
Figure 5. 43: A plot of externally studentized residuals for response CS_Co (TEM)........133
Figure 5. 44: Illustration of the crystallite size measured by XRD and TEM........51
Figure 5. 44: Plots of log (D/D_0) against log time for anatase-, P25- and rutile-supported catalysts showing the sintering order as slope........136
Figure 5. 45: Plots of normalized dispersion against time for anatase-, P25- and rutile-supported catalysts fitted to the GPLE (m=1)........138
Figure 5. 46: Plots of normalized dispersion against time for anatase-, P25- and rutile-supported catalysts fitted to the GPLE (m=2)........138
Figure 5. 47: A HAADF-STEM image superimposed with EDX mapping of Rutile-supported catalyst showing wetting of the support by cobalt species........140
Figure 5. 48: HAADF-STEM – EDX map images of anatase – supported catalyst showing cobalt crystallites sintered for (a) 4 hours and (b) 48 hours........143
Figure 5. 49: HAADF-STEM – EDX map images of P25 – supported catalyst showing cobalt crystallites sintered for (a) 4 hours and (b) 48 hours........144
Figure 5. 50: HAADF-STEM – EDX map image of Rutile – supported catalyst showing cobalt crystallites sintered for (a) 4 hours and (b) 48 hours........145

Figure 5. 51: Correlation of GPLE first-order sintering rate constant with support pore size. 146

List of Tables

Table 3. 1: Instrument settings for ambient XRD analysis at Sasol Technology and University of Pretoria 48
Table 3. 2: Instrument settings for high temperature XRD analysis 49
Table 4. 1: Parameters for calcination study 60
Table 4. 2: Parameters for variable time sintering study 60
Table 5. 1: Quantitative phase analysis results of titania supports 67
Table 5. 2: Textural properties of titania supports showing BET surface area and pore sizes. 71
Table 5. 3: Quantitative PXRD results of Anatase-supported catalysts 77
Table 5. 4: Quantitative PXRD results of P25-supported catalysts 78
Table 5. 5: Quantitative PXRD results of Rutile-supported catalysts 79
Table 5. 6:Co_3O_4 crystallite size of titania supported catalysts at different calcination temperatures 80
Table 5. 7: Co_3O_4 crystallite sizes across the different titania supports 80
Table 5. 8: Crystallite Sizes of Co_3O_4 and Co^0 in the titania-supported catalysts 95
Table 5. 9: H_2-Chemisorption results showing reduction properties of titania-supported cobalt species 106
Table 5. 10: BET surface area and Pore size results of calcined and reduced catalysts ... 113
Table 5. 11: Fit summary for fcc cobalt crystallite size data 121
Table 5. 12: Model summary statistics for fcc cobalt crystallite size 122
Table 5. 13: ANOVA Statistics for the 2FI model for fcc cobalt crystallite size 122
Table 5. 14: Fit summary for hcp cobalt crystallite size data 126
Table 5. 15: Model summary statistics for hcp cobalt crystallite size 126
Table 5. 16: ANOVA Statistics for the 2FI model for hcp cobalt crystallite size 127
Table 5. 17: Fit summary for TEM derived cobalt crystallite size data 131
Table 5. 18: Model summary statistics for TEM derived cobalt crystallite size 131
Table 5. 19: ANOVA Statistics for the 2FI model for TEM derived cobalt crystallite size ... 132
Table 5. 20: Sintering results from the SPLE and GPLE kinetic models 137

CHAPTER 1

INTRODUCTION AND BACKGROUND

1. CHAPTER 1 – INTRODUCTION AND BACKGROUND

1.1. INTRODUCTION

1.1.1. Background

Gas-to-liquid (GTL) technology has been shown to provide clean fuels compared to the crude-oil derived counterparts (Sadeqzadeh *et al,* 2012 p.11955, Sadeqzadeh *et al*, 2014 p.6913). GTL technology is primarily concerned with the conversion of natural gas into liquid hydrocarbon fuels, through the Fischer-Tropsch synthesis (FTS) process (Shimura *et al*, 2013 p.8). The former have lower sulphur and aromatics content than the latter. These sulphur and aromatics are usually detrimental to the environment (Khodakov *et al*, 2007 p.1694).

Major industrial players in GTL and hydrocarbon synthesis technology include Sasol, and Shell (Claeys *et al*, 2015 p.841). Sasol is currently operating a GTL plant in RasLafan, Qatar. The plant is a joint venture between Sasol and Qatar Petroleum. The plant named Oryx has a capacity of 34 000 barrels per day and uses Sasol's proprietary Slurry Phase Distillate (Sasol SPD™) technology (Leckel 2009 p.2343, Sasol 2014). Shell is operating the largest GTL plant also situated in Qatar. The plant named Shell Pearl is designed to produce 140 000 bpd (Leckel 2009 p.2343, Sills 2013 p.5). Shell has gained experience in GTL operation by operating the first commercial GTL plant in Bintulu, Malaysia since 1996. The plant uses Shell's Middle Distillate Synthesis (SMDS) technology. (Shell 2014).

It has been stated that all metals of group VIII are active in hydrogenation of CO to liquid hydrocarbon (Khodakov *et al*, 2007 p.1694). Atashi *et al*, (2010 p.952) have stated that although Ni, Fe, Co, Ru and Rh have significant activity for commercial FTS application, only Co- and Fe-based catalysts have been developed for commercial use. Co-based catalysts are the most preferred for GTL processes, over Fe-based catalysts. This is due to the high per pass FT activity, low oxygenate and CO_2 selectivity of Co-based catalysts (Moodley *et al*, 2009 p.102).

The activity of the catalyst depends on the final state of the metal precursor after reduction, and the morphology and size of the metal crystallites (Rytter 2010 p.4140). The choice of support is also of importance as the type and structure of the support influences the dispersion and therefore the activity of the catalyst.

1.1.2. Deactivation of cobalt-based GTL catalysts

Deactivation of cobalt-based catalysts is a major challenge facing the commercial users of GTL technology. In addition, the cobalt metal and noble metal usually used as promoter are expensive (Tsakoumis *et al*, 2010 p.162). Deactivation is expressed as loss of catalytic activity with time on stream. In a review by Saib *et al*, (2010 pp.271-282), it was postulated that deactivation mechanisms for cobalt-based catalysts include (i) poisoning by sulphur and nitrogen compounds, (ii) cobalt oxidation, (iii) cobalt-support compound formation, (iv) sintering of cobalt crystallites, (v) surface reconstruction and (vi) carbon formation. Of all the deactivation mechanisms stated, sintering, carbon formation and surface reconstruction are said to be intrinsic to cobalt and therefore will be present in most cobalt-catalyst systems (Sadeqzadeh *et al*, 2014, Saib, *et al*, 2006, Xiong, *et al*, 2012, Wynblatt & Gjostein, 1975, Tsakoumis, *et al*, 2010). Sintering is the main focus of study, and therefore is discussed in detail in the sections below.

1.2. PROBLEM STATEMENT

Cobalt-based catalysts for GTL technology are prone to deactivation by various mechanisms including sintering. The cobalt metal is significantly expensive. Therefore methods to reduce or reverse deactivation are urgently required. In addition, there are not many studies reported in literature detailing deactivation of cobalt crystallites supported on titania support. There is a gap in the materials science research into the deactivation of cobalt on titania. A fundamental study into the process of sintering, in terms of material science is therefore of utmost importance.

1.3. RESEARCH QUESTIONS AND OBJECTIVES

The following research questions arise when considering the problem statement:

- How does the titania support phase composition affect sintering behaviour of model cobalt crystallites?
- What is the nature of metal-support interaction?
- Does sintering depend on the initial crystallite size?
- Is sintering time-dependent?
- What is the mechanism of sintering of cobalt crystallites?

By answering the above research questions, the main objective of this study was to understand the process of sintering of model cobalt crystallites on different titania supports in terms of changes in crystallite size. The relationship of selected parameters such as calcination temperature, sintering time, phase composition and crystallite size were explored.

The objectives of the study were thus:

- To prepare and characterize cobalt catalysts supported on different titania phases
- To study the metal-support interaction
- To study the effect of the titania support phase on the cobalt crystallite size during sintering
- To study the effect of time on the sintering behaviour of cobalt crystallites
- To study the mechanism of sintering of model cobalt crystallites

1.4. RATIONALE OF THE RESEARCH

Fundamental material science research is essential in technology development. In this field, material properties are studied on an atomic and molecular scale. These properties are then linked to the performance and behaviour of systems such as catalyst systems. Such research is essential in cobalt-based catalysts in order to establish reaction mechanisms; understand catalyst-support inter-relationships and surface science.

It has been stated that sintering can have a significant effect as a deactivation mechanism. Therefore focusing on fundamentally understanding the process of sintering is of importance. This would lead to the future design of stable cobalt-based catalysts for GTL technology.

CHAPTER 2

THEORY AND RESEARCH REVIEW

2. CHAPTER 2 – THEORY AND RESEARCH REVIEW

2.1. COBALT AND ITS OXIDES

Cobalt metal is one of transition metals which is being extensively studied due to its properties, which makes it useful as a catalytic material. (Wang *et al*, 2012 p.23310; Petito *et al*, 2008 p.281; de la Peña O'Shea *et al,* 2009 p.5637) Most of the applications stem from the crystal structure and phase composition of cobalt compounds. These compounds are briefly discussed.

2.1.1. Bulk Structure of Cobalt Oxides

2.1.1.1. Co_3O_4

The most studied compound of cobalt is Co_3O_4 which has the spinel structure. This oxide is mostly used as catalyst in Fischer-Tropsch synthesis, water-oxidation, methane combustion and CO oxidation (Chen & Selloni 2012 p.085306). Co_3O_4 is the most stable oxide of cobalt hence the vast applicability (Petito *et al*, 2008).

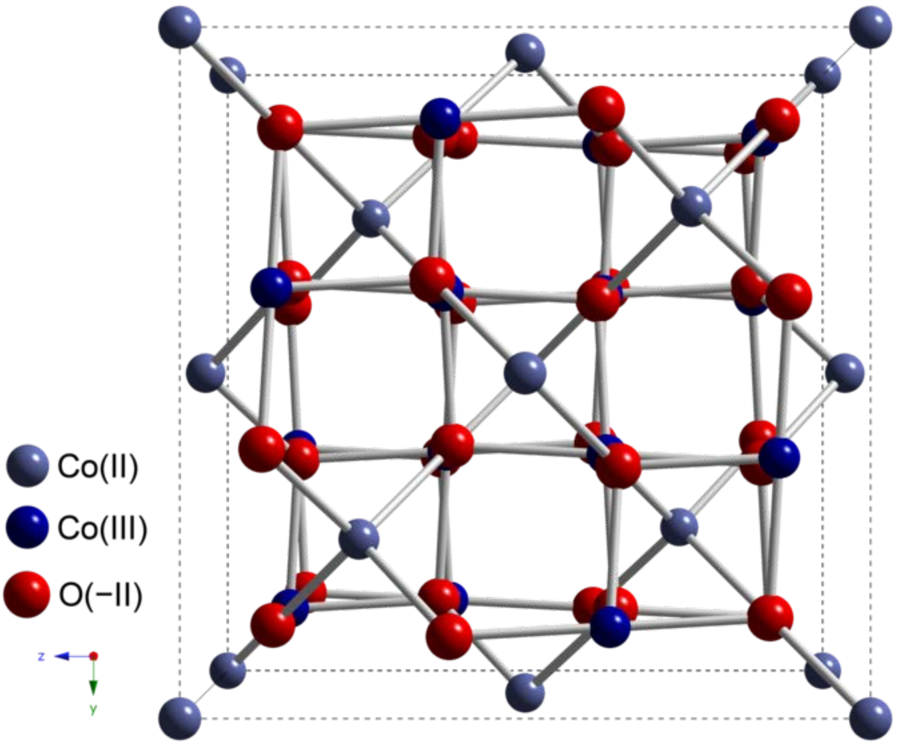

Figure 2. 1: Crystal structure of Co_3O_4 showing the spinel structure (Adapted from http://en.wikipedia.org/wiki/Cobalt(II,III)_oxide)

Co_3O_4 has a cubic structure as shown in Figure 2.1. It falls in the Fd-3m space group (Chen *et al*, 2011; Chen & Selloni 2012). An interesting structural phenomenon is the presence of cobalt ions with different oxidation states in Co_3O_4. These are Co^{2+} and Co^{3+} (Wang *et al,* 2012 p.23311; Petito *et al*, 2008 p.49). The Co^{2+} are tetrahedrally coordinated and are situated *8a* sites. The Co^{3+} ions are octahedrally coordinated and are situated at *16d* sites. The oxygen anions complete the lattice by face-centered cubic packing. The Co_3O_4 unit cell therefore consist of 56 ions, which comprise of 16 Co^{3+} ions, 8 Co^{2+} ions and 32 O^{2-}. The spinel oxide has a Pearson symbol of *cF56* (Okamoto 2008 p.548).

One of the most interesting properties of Co_3O_4 is the paramagnetic behaviour at room temperature. This property stems from the partially filled t_{2g} orbitals in the tetrahedral crystal field splitting of Co^{2+}. In this d^7 system, there are three unpaired electrons which result in the presence of a magnetic moment. In the case of $Co^{3+,}$ all electrons are paired in the octahedral crystal field which has a d^6 configuration (Petito *et al*, 2008 p.49). The crystal field splitting is illustrated in Figure 2.2

.

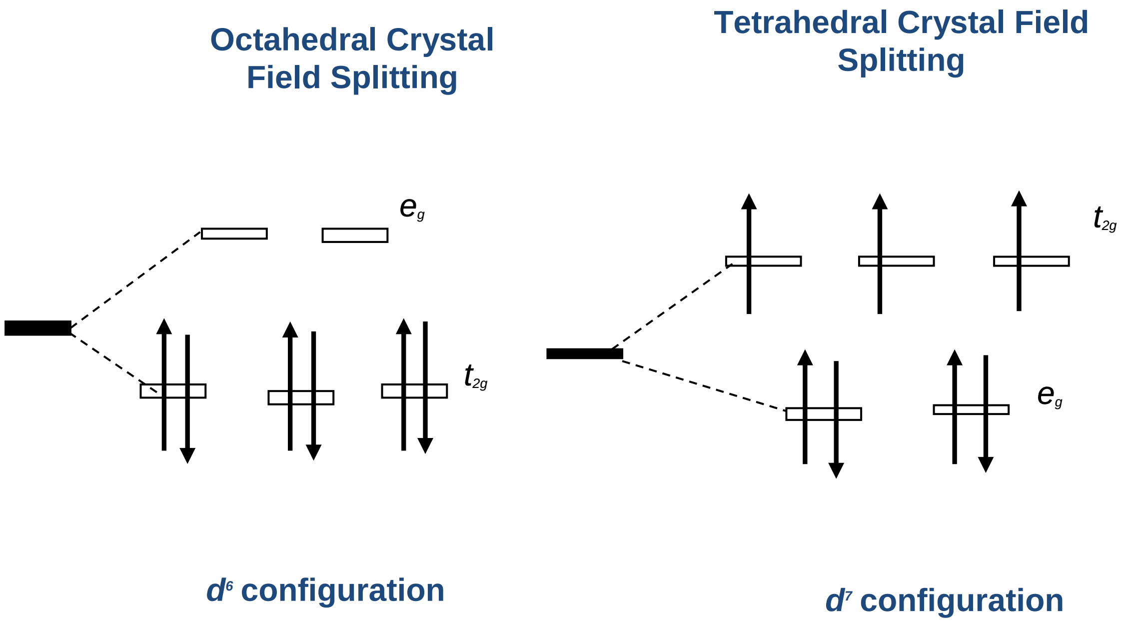

Figure 2. 2: Crystal field splitting illustration showing paired and unpaired electrons in d^6 and d^7 configurations respectively.

2.1.1.2. CoO

The monoxide form of cobalt has a rocksalt structure and falls in the Fm-3m space group (Okamoto 2008 p.548; Petito *et al,* 2008 p.49). Each Co^{2+} ion is octahedrally coordinated to O^{2-} anions to form a cubic structure. The unit cell of CoO is smaller than that of Co_3O_4 since only 4 Co^{2+} ions and 4 O^{2-} anions make up the unit cell. The Pearson symbol for CoO is *cF8* (Okamoto 2008 p.548).

An interesting phenomenon of the Co^{2+} ions is the change in behaviour as a result of either high spin or low spin configuration in an octahedral field. In a high spin state, the Co^{2+} ion which has a d^7 configuration has 3 unpaired electrons. In the low spin state, the Co^{2+} ion has 1 unpaired electron. The number of unpaired electrons has a direct influence on the magnetic properties of cobalt compounds (Gerloch and Constable 1994 pp.79-89).

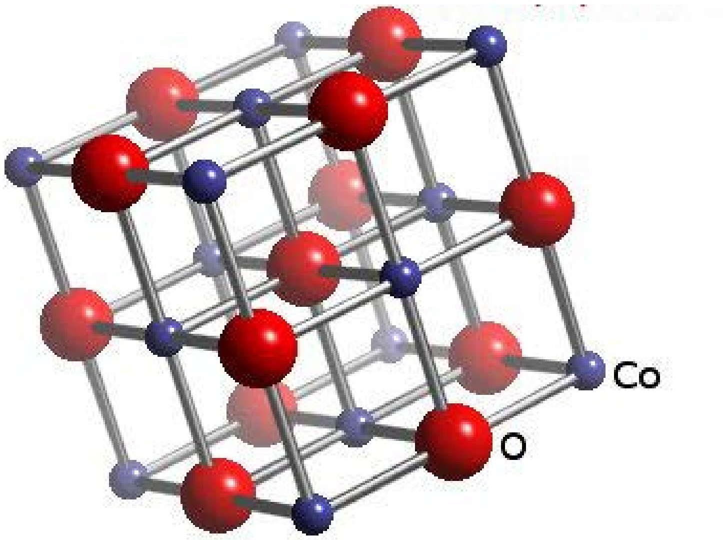

Figure 2. 3: Crystal structure of CoO showing the rocksalt structure (Adapted from https://www.webelements.com/compounds/cobalt/cobalt_oxide.html)

2.1.1.3. Metallic Cobalt

Metallic cobalt has three crystal phases. These are hexagonal-close packed (hcp), face-centered cubic (fcc) and primitive cubic phase. The hcp, fcc and primitive cubic phases are also known as α-, β-, and ε-phases respectively (de la Peña Ŏ Shea *et al,* 2009 p.5637).

The α-phase (hcp) falls in the P6/mmc space group. This phase is stable at lower temperature and transforms to the β-phase at around 420°C-450°C. The β-phase is stable at higher temperatures, and falls in the Fm-3m space group (de la Peña Ŏ Shea *et al*, 2009 p.5637). It has been shown that the α- and β-phase are structurally similar. The main difference arises in the stacking sequence, where the α-phase has stacking sequence of *ABABAB*, and the β-phase shows a sequence *ABCABC*. These differences are usually observed as stacking faults in supported cobalt catalysts (Ducreax *et al,* 2009 p.60; Cherepanova *et al,* 2008 p.514)

2.2. TITANIA AND ITS POLYMORPHS

Titania occurs in different crystalline phases such as rutile, anatase and brookite. Rutile is the most stable phase at high temperatures; however anatase and brookite do occur in fine grained natural or synthetic forms. Phase transformations occur on heating. These are anatase going to brookite to rutile, brookite to anatase to rutile, anatase to rutile, brookite to rutile (Chen & Mao 2007 p.2911).

2.2.1. Bulk Structure of TiO_2 Polymorphs

The crystal structures of anatase and rutile TiO_2 consists of similar building blocks. Each building unit is composed of Ti^{4+} ion surrounded by six O^{2-} anions to form an octahedron. It has been said that this octahedron is somewhat distorted (Diebold 2003 p.66; Li *et al,* 2011 p.878). The Ti ions located at the interstitial sites have longer bond lengths, due to the distortion of the octahedron. The arrangement of the building blocks and degree of distortion is different in anatase and rutile phases (Hanaor and Sorrell 2011p.859).

Anatase has a body-centered tetragonal structure, and falls in the $I4_1/amd$ space group. The bond angles in the TiO_2 octahedra are slightly larger than 90^o owing to the distortion of the octahedron. The octahedra in anatase share four edges. Rutile also has a tetragonal crystal structure and falls in the $P4_2/mnm$ space group. The octahedra in rutile share two edges, as opposed to four in anatase. This shows a major difference in the physical structure of the two phases as illustrated in Figure (Diebold 2003 p.66; Li *et al,* 2011 p.878).

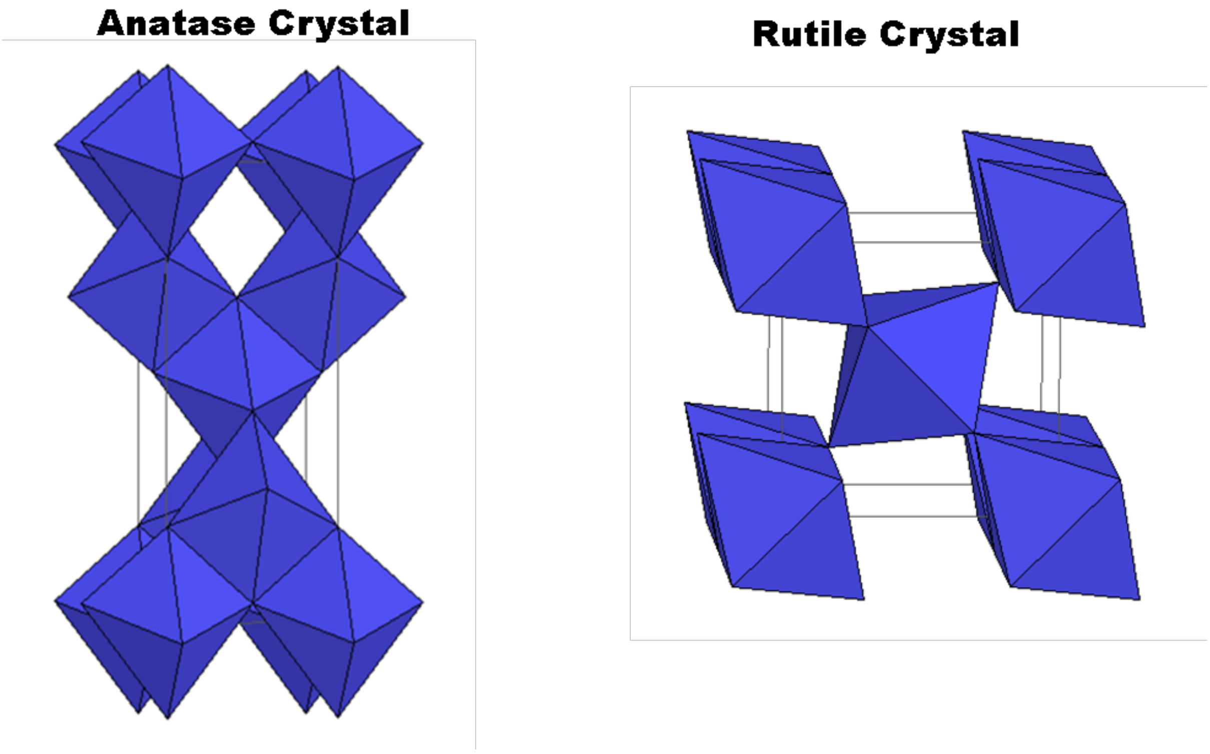
Anatase Crystal
Rutile Crystal

Figure 2. 4: A schematic illustration of the crystal structures of TiO_2 phases showing Anatase and Rutile phases

2.2.2. Bonding and Defect Chemistry of TiO_2

The bonding properties of TiO_2 are heavily influenced by defect sites located both in the surface and bulk (Shiraishi *et al,* 2013 p.2323; Yan *et al,* 2013 p.10983). According to Li *et al,*(2011 p.881), there are four types of defects found in TiO_2. These include oxygen vacancies (V_O), oxygen interstitial (O_i), titanium vacancy (V_{Ti}) and titanium interstitial (Ti_i). Diebold (2003 p.68) also added crystallographic shear planes (CSP) as another type of defect.

These defect sites can be induced in TiO_2 by methods such as vacuum annealing, reduction by H_2 gas or through ion sputtering thereby creating impurity sites in the TiO_2 lattice (Li *et al,* 2011 p881; Diebold 2003 p.68).

Oxygen vacancies are the most influential defects among the known defects sites. This is because, as an oxygen vacancy is created, two electrons are transferred into the nearest Ti atoms. This becomes possible since the Ti ions consist of empty 3d orbitals in their most stable oxidation state. The excess electrons therefore lead to the formation of two Ti^{3+} ions (Shiraishi *et al,* 2013 p.2318; Strunk *et al,* 2010 pp.16937-16938) The presence of the Ti^{3+} sites greatly influences the interaction of metals supported on TiO_2. The process of oxygen vacancy creation can be expressed as:

$$Ti^{4+}\text{-}O\text{-}Ti^{4+} \rightarrow Ti^{3+}\text{-} \square \text{-}Ti^{3+} + {}^{1}/_{2}O_2$$

2.3. FUNDAMENTAL THEORIES GOVERNING SINTERING

Sintering can be defined as the change in dispersion of the active metal during use or during treatment at high temperatures (Flynn & Wanke 1975 p.432). Bartholomew (2001 p.35) further states that sintering results in loss of catalytic surface area due to crystal growth or loss of support area due to collapse of support

There are two generally accepted mechanisms of sintering (Simonsen *et al,* 2012 p.5646):

- Ostwald ripening (Atomic migration) – migration of atomic species or molecular species in the gaseous state to form large entities The large particle grow at the expense of smaller ones as depicted in Figure 2.5.

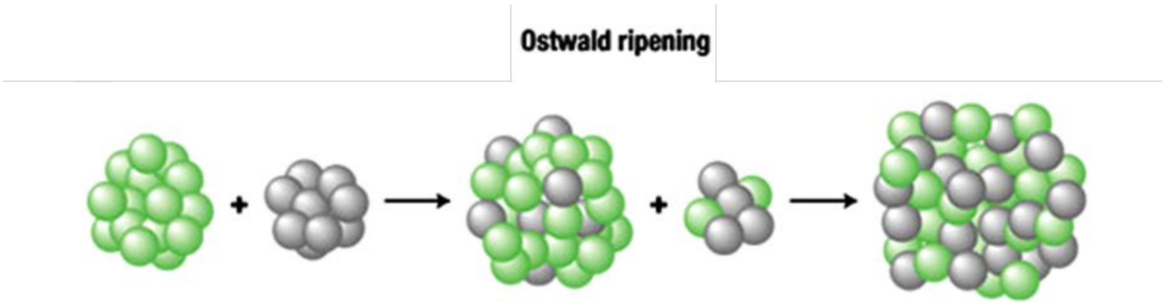

Figure 2.5: A simplified schematic illustration of Ostwald ripening.

- Particle migration and coalescence (PMC) – migration of whole particles or crystallites until collision with other particles. The particles grow as a result of collision as depicted in Figure 2. 6

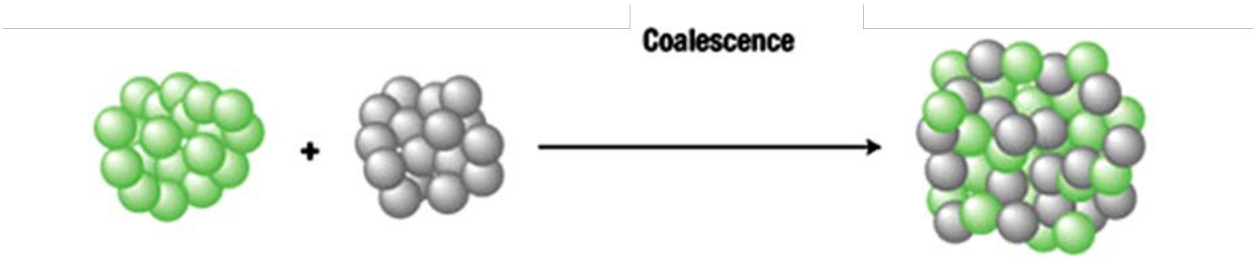

Figure 2. 6: A simplified schematic illustration of Particle migration and coalescence.

2.3.1. Ostwald Ripening (atomic migration)

Ostwald ripening (OR) has been described based on the pioneering theories of Lipshiftz, Slyozov and Wagner (Zhdanov *et al,* 2012 p.1). The LSW theory is used to study kinetics and particle size distributions (PSDs) resulting from sintering where OR is the main mechanism. The growth process and kinetics of the OR mechanism are usually explained by the mean-field approach (Simonsen *et al,* 2011 p.147). In this approach, the concentration of atomic species on the support is assumed to be constant from the edge of the specified particle up to a given distance, *L*. This mean-field approach forms the basis of atomic migration process. Growth during the OR can be described by the Gibbs-Thompson equation which relates the surface concentration of atomic species to the particle radius (Houk *et al,* 2009 p.11225, Simonsen *et al,* 2011 p.147,Gentry *et al,* 2011 p.12736):

$$\boldsymbol{C_{(r)} = C_{\infty} \exp\left(\frac{2\gamma\Omega}{kTr}\right)}$$ **(Equation 2.1)**

Where $C_{(r)}$is the concentration of atomic species near the particle, $C_{\infty}$is the surface concentration of atomic species in equilibrium with an infinitely large particle, γ is the surface free energy, Ω is the atomic volume, k is the Boltzman constant T is the temperature and r is the particle radius. Equation 2.1 clearly shows that smaller particle will have a higher concentration of atomic species in equilibrium with the particle than their larger counterparts. This is in line with the phenomenon of a larger chemical potential for small particles that for larger particles (Alloyeau *et al,* 2010 p.255901).

Since the growth mode of OR involves the growth of larger particles at the expense of smaller particles, the conservation of mass has been highlighted as very important (Houk *et al,* 2009: 11226). In this regard, a parameter known as the critical radius r^{*}has been described (Behafarid & Roldan Cuenya 2012 p.910). The critical radius is the radius of the particle which remains stationary in terms of mass gain. This is due to the equal number of incoming and emitted atomic species. Therefore the total mass gain remains zero for a specified set of particles (Houk *et al,* 2009 p.11225, Behafarid & Roldan Cuenya 2012 p.910).

The mechanism can be classified further into two growth schemes which characterize kinetics and mode of growth (Houk *et al* 2009 p.11226). These are:

- Interface-transfer-limited growth
- Diffusion-limited growth

The expression of ripening for the two schemes is given as:

$$\boldsymbol{\frac{dr}{dt}\Big|_{int} = K_{int}\frac{1}{r}\left(\left[\frac{2\gamma\Omega}{kTr^{*}}\right] - \left[\frac{2\gamma\Omega}{kTr}\right]\right)}$$ **Equation 2.2**

$$\boldsymbol{\frac{dr}{dt}\Big|_{diff} = K_{diff}\frac{1}{r^{2}}\left(\left[\frac{2\gamma\Omega}{kTr^{*}}\right] - \left[\frac{2\gamma\Omega}{kTr}\right]\right)}$$ **Equation 2.3**

Where $r^*|_{int}$and $r^*|_{diff}$ are the critical radii for interface-transfer-limited and diffusion-limited growths respectively. K_{int} and K_{diff} are constants describing activation-energy dependent parameters for interface-transfer-limited and diffusion-limited growth schemes respectively (Houk *et al,* 2009 p.11226).

2.3.2. Particle Migration and Coalescence (PMC)

Particle migration and coalescence (PMC) is the growth mechanism that occurs due to weak contact between the particle and the support. This results in the diffusion or migration of the entire particle. Kinetics and PSDs of coalescence have been described using early scholarly work of Smoluchowski (Harris 1995 p.98, Thiel *et al,* 2009 p.5047). In this early work, the growth and kinetics were explained based on the need for reduced surface free energy for particles in interfacial systems (Thiel *et al,* 2009 p.5047).

The concept of diffusion and diffusion coefficient are important when describing coalescence. Harris (1995 p.98) showed the derivation of the expression for particle diffusion coefficient, D_P. Assuming a spherical particle, the expression is given as:

$$\boldsymbol{D_P = \frac{3\Omega^2 \rho D_S}{\pi r^4}}$$ **Equation 2.4**

Where ρ is the density of atomic species on the surface of the particle cluster, Ω is the atomic volume, r is the particle radius and D_S is the surface self-diffusion coefficient. The concept of diffusion takes into account the movement of a particle over a given distance in a given time. ρ in equation (4) is given by equation (5):

$$\boldsymbol{\rho = \rho_\infty exp\left(\frac{2\gamma\Omega}{kTr}\right)}$$ **Equation 2.5**

Equation 2.4 shows an inverse relationship of particle diffusion and particle size. This indicates that a smaller particle will migrate faster and cover a larger distance than a larger particle (Behafarid & Roldan Cuenya 2012 p.911). The observation is in line with thermodynamic principles which dictate that smaller particles will have a larger surface free energy than larger particles. Therefore in order to reduce the surface free energy, smaller particles will migrate readily and coalesce into larger entities. This reduction in free energy is the driving force behind coalescence (Sehested *et al,* 2006 p.238, Alloyeau *et al,* 2010 p.255901). The expression for growth where coalescence is the main mechanism is given in equation (6):

$$\frac{\partial f(v,t)}{\partial t} = \int_0^v D_P(v')f(v',t)f(v-v',t)dv - \int_0^\infty [D_P(v)+D_P(v')]f(v,t)f(v',t)dv'$$

Equation 2.6

v is the particle volume and $f(v)$ is the density of particles with volume v. The above expression is based on the mean-field approach as discussed in earlier sections (Behafarid & Roldan Cuenya 2012 p.911).

2.3.3. Kinetics of Sintering – Simple Power Law Expression (SPLE) and Generalized Power Law Expression (GPLE)

The kinetics of sintering has been studied extensively. Empirical models which describe the sintering behaviour have been developed. These empirical models also give kinetic parameters such as sintering kinetic constant and activation energy (Flynn & Wanke 1974 pp.390 – 399; Flynn & Wanke 1975 pp.423 – 448; Ruckenstein & Pulvermacher 1973 pp. 224 – 245; Fiedorow & Wanke 1976 pp. 34 – 42; Wynblat & Gjostein 1975 pp. 21 – 58)

In our study, empirical models developed by Ruckenstein & Pulvermacher (1973, p.224) and Fuentes (1985, p.36), have been studied. The Simple Power Law Expression (SPLE) which describes the sintering rate in terms of normalized dispersion and sintering kinetic constant, is expressed as:

$$-d\left(\frac{D}{D_0}\right)dt = k_s\left(\frac{D}{D_0}\right)^n$$

Equation 2.7

In the expression above, D is the dispersion at time t, D_0 is the initial dispersion, k_s is the sintering constant and n is the sintering order (Bartholomew 1993 p.6). The sintering order n can vary between 2 – 15 for a specific catalyst system at specific temperature.

The SPLE model has been criticized, however, for this exact reason. This varying of *n* even for a specific catalyst, makes it difficult to calculate the sintering kinetic constant which is representative of the catalyst system. The SPLE model was later refined by Fuentes *et al*, (1991 p.637) to include a term that accounts for the dispersion at infinite time. This term, describes the limiting dispersion. The modified model is known as the Generalized Power Law Expression (GPLE). The GPLE is expressed as:

$$-d\left(\frac{D}{D_0}\right)dt = k_s\left[\left(\frac{D}{D_0}-\frac{D_{eq}}{D_0}\right)\right]^m \qquad \textbf{Equation 2.8}$$

In the GPLE equation, D_{eq} is the limiting dispersion and m is the sintering order. m can vary between 1 and 2 (Bartholomew 1993 p.7).

2.4. REVIEW OF LITERATURE ON SINTERING STUDIES

Major parameters affecting sintering rates are temperature and atmosphere (Bartholomew 2001 p.35). It is clear from the definitions above, that the sintering process also depends on the physical properties of the metal and support such as surface area, porosity, metal type, metal dispersion and promoters. Various authors have observed the effect of temperature on sintering.

Datye *et al,* (2006 p.59) observed the effect of temperature in the sintering behaviour of platinum crystallites supported on alumina. They observed an increase in crystallite size from 14.6 nm to 31.1 nm upon heating from 600^{o}C to 700^{o}C in air. The same phenomenon was observed when the catalyst was heated in H_2 atmosphere from 600^{o}C to 700^{o}C, with crystallite size increasing from 15.5 nm to 34.4 nm. This observation reiterates Bartholomew's (2001 p.35) statement, that sintering increases exponentially with increasing temperature. Other parameters which affect sintering in supported metal catalysts are highlighted below.

2.4.1. Effect of support type and phase composition

Lif *et al,*(2007 p.62) have studied sintering of alumina-supported nickel catalysts after heat treatment in ammonia + hydrogen. They used different kinds of alumina supports which included γ-alumina, α-alumina and trans-alumina. It was observed that nickel supported on γ-alumina is more stable against sintering than nickel supported on other types of alumina. They also correlated the sintering to the bond strength between the metal and support. The stronger the metal-support interaction due to the large numbers of low coordinated surface aluminium sites, the lesser the extent of sintering.

Goeke & Datye (2007 p.9) studied the effect of the support on sintering of palladium particles. Model supports in the form of disks of quartz (silica) and sapphire (alumina) were used in the study. They observed that for the same palladium loading, the mean particle size was smaller in quartz support compared to that in sapphire. The difference in size was observed even after sintering, where palladium crystallites were larger in sapphire than in quartz. They concluded that quartz stabilises palladium crystallites against sintering, better than sapphire. This effect can be related to the metal-support interaction phenomenon. This phenomenon is discussed in detail in the subsequent section. It is clear from the studies discussed above, that the type and phase of the support influences the sintering behaviour of supported metal catalysts.

2.4.2. Metal-support Interaction

Riva *et al,* (2000 p.121) observed the strong metal-support interaction (SMSI) in cobalt catalysts supported on titania. In their study, they looked at metal-support interaction in silica- and titania-supported cobalt catalyst. The formation of surface compounds between cobalt and titania support was observed indicating strong metal-support interaction. The same SMSI effect has been reported for other metals other than Co and Ni. Li *et al,* (2004 p.107) observed the strong SMSI effect in titania-supported palladium hydrogenation catalysts. Linsmeler & Taglauer (2011 p.175) observed the effect on rhodium model catalysts supported on titania. It is interesting to note that the surface compounds formed by titania support and noble metals behave similarly.

In another study, de la Peña O'Shea *et al,*(2011 p.7133) have shown the SMSI effect of titania on Co by using electron microscopy. They showed that cobalt nanoparticles were encapsulated with a layer of titania species after reduction. An interesting observation from the study was that of Moiré fringes formed by the encapsulated Co crystallites. The phenomenon was explained as resulting from the increase in the number of Ti^{3+} species giving rise to the rupture of the Ti – O bond. This leads to the rearrangement in the crystal lattice and support surface, resulting in the formation of an amorphous phase of $TiO_{x.}$ It has been shown conclusively, that titania as a support alters the behaviour of the active metal. It is expected that the sintering behaviour of such metals supported on titania will be different when compared to that supported on other supports such as silica and alumina.

2.4.3. Effect of metal particle size

Metal particle size is one of important parameters which affect the deactivation behaviour of supported metal catalysts. Studies have been reported in literature where particle size had an influence. Saib *et al* (2006 p.338) studied the oxidation stability of cobalt crystallites with different sizes in silica-supported catalysts. They observed that the catalyst with the largest crystallite size (Co-28 nm) was difficult to oxidise. The catalyst with medium-sized crystallites (Co-13 nm) did oxidise substantially while the smallest crystallite sized catalyst (Co-4 nm) did not oxidise.
They explained the deviation from bulk thermodynamics as caused by the encapsulation of the small cobalt crystallites with silica thereby preventing them from being oxidised.

Park *et al,* (2012 p.12) have recently studied the behaviour of cobalt nano-crystallites with different sizes in alumina-supported catalysts. The catalyst with the smallest crystallite size (4.8 nm) showed lower CO conversions and rapid deactivation. An increase in particle size from 4.8 to 17.5 nm resulted in a decrease in the deactivation rate of the catalysts, and the catalysts showed consistent performance even after 54 hours. They explained the rapid deactivation of the smaller-sized crystallite catalyst as resulting from the susceptibility to sintering. They concluded that most stable particles were those with an average size of ~9 nm.

2.5. MATERIALS CHARACTERIZATION TECHNIQUES

2.5.1. Powder X-ray Diffraction (XRD)

X-ray diffraction is another characterization technique that offers a wealth of information. This technique can be used to determine crystallographic information of materials which are very important in the research fields of catalysis and solid-state physics (Azároff & Buerger 1958 p.1, David *et al,*(2002 p.1). The use of X-rays was discovered by von Laue in 1912 while working on diffraction of radiation by matter. This paved the way for the development of the X-ray diffraction (XRD) technique for the analysis of crystalline materials (Eckert 2012 p.A83). The powder method was developed by Debye, Scherrer and Hull after the First World War (Azároff & Buerger 1958 p.1; Paszkowicz 2006 p.116)

The main principle behind the X-ray diffraction technique stems from the Bragg and Laue principles (Eckert 2012 p.A84). In a similar phenomenon as seen in electron beam – specimen interaction, X-rays are also scattered upon interacting with matter. This interaction can lead to reinforcement or cancellation of the scattered X-ray waves depending on their phase in relation to the incident wave. For Bragg diffraction to take place, the scattered X-ray wave should be in-phase with the incident wave. In this instance, constructive interference takes place (Azároff & Buerger 1958 p.6; Levi 2006 p.58)

The powder diffractometer consists of the following main components; the X-ray tube, focusing slits, sample holder, anti-scatter slits and detector (Connolly 2007 p.2). The arrangement of the components inside the diffractometer differs for different manufacturers. In one system, the sample is fixed and aligned horizontally. The X-ray tube and detector rotate about an axis with the angle between the incident beam and the diffracted beam increasing by steps or continually. This type of setup is called the Bragg-Brentano diffractometer as illustrated in Figure 2.7. (Connolly 2007 p.3; Roussou 1998 p.195)

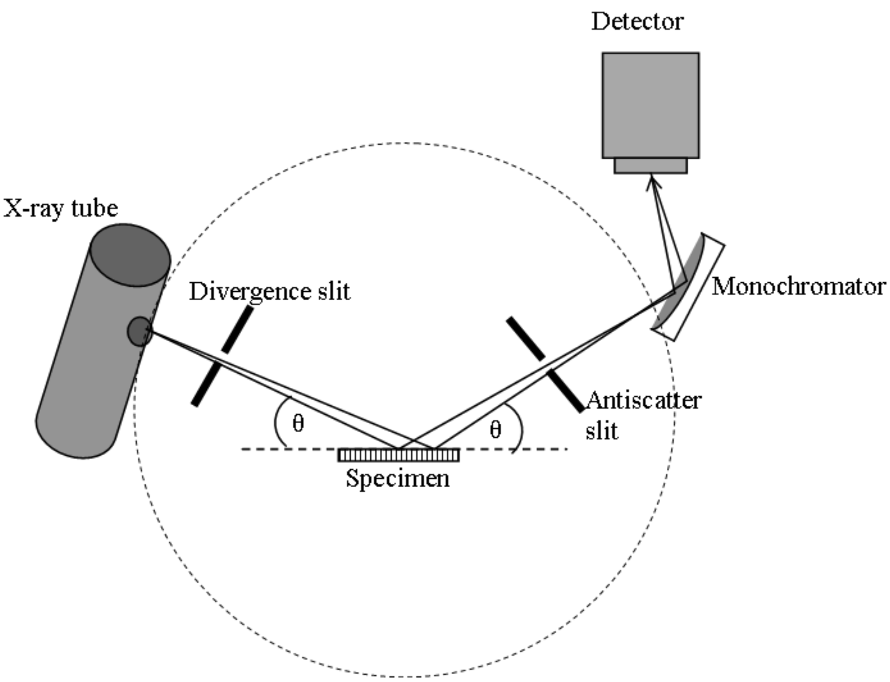

Figure 2. 7: A schematic illustration of the Bragg-Brentano diffractometer showing the main components (Adopted from Connolly 2007 p.2)

2.5.2. Transmission Electron Microscopy (TEM)

Transmission electron microscopy (TEM) is one of the most important characterization techniques in the research of heterogeneous catalysts (Gai 2001 p.371). This technique allows one to obtain information on the chemical and physico-chemical properties of a material down to the atomic scale. The TEM can give information such as internal structure, crystallography, chemical composition, phase composition and bonding states (Thomas & Midgely 2011 p.1).

The science of the TEM instrument can be explained by looking closely at the interaction between the electron beam and specimen. When the beam of electrons interacts with the specimen, various reactions occur. These reactions lead to the emission of various signals which form the basis of electron microscopy techniques. The various signals as illustrated in Figure 2.8 can be collected by using suitable detectors inside the microscope. The most important signals in TEM are those transmitted through the specimen and collected below the specimen. This configuration forms the basis of transmission electron microscopy (Thomas & Gai 2004 p.178)

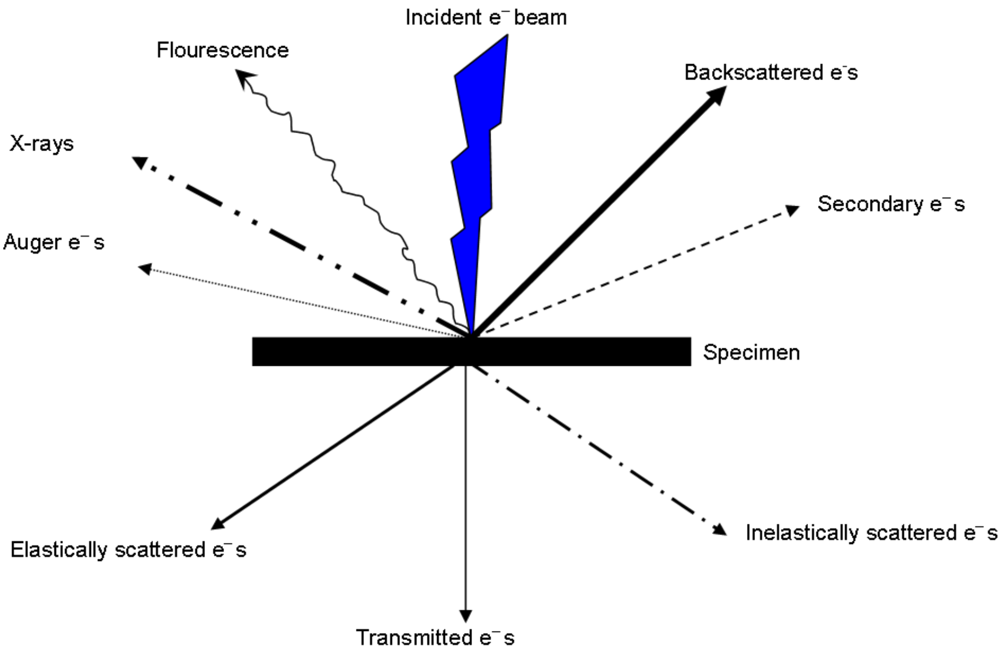

Figure 2. 8: A schematic illustration of the electron beam – specimen interactions showing various signals emitted (Adopted from Thomas & Gai 2004 p.179)

A TEM consists of an electron source, lenses, apertures, specimen holder, pumps, detectors and a viewing screen as illustrated in Figure 2.9 (Williams & Carter 2009 p.91). The electron source or electron gun serves to illuminate the specimen with electrons. The electrons can either be obtained by heating the filament or by applying an electric field around the tip of the electron source (Voutou & Stefanaki 2008 p.2).

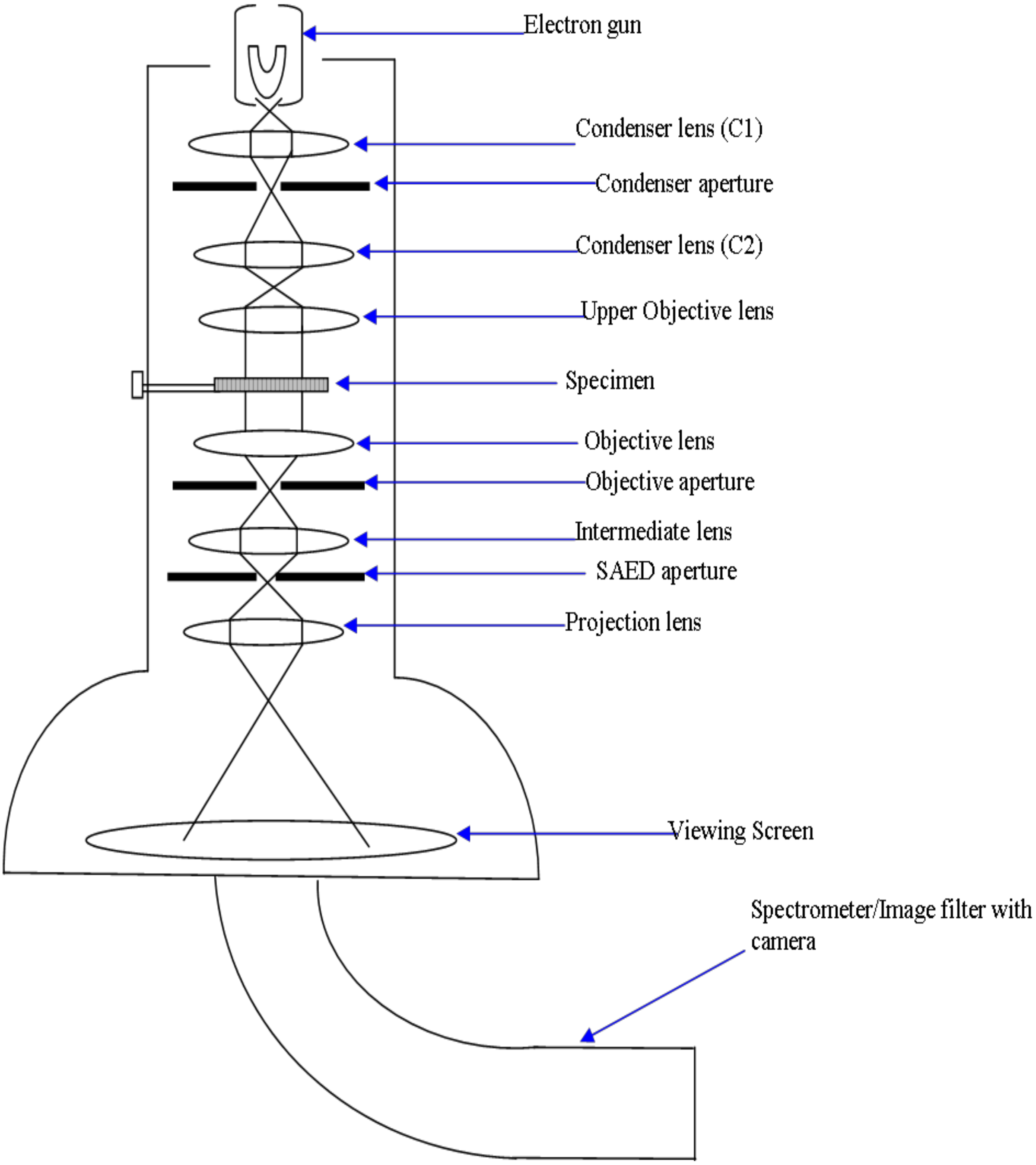

Figure 2. 9: A simplified schematic illustration of a conventional TEM (Adopted from Williams & Carter 2009 p.142)

2.5.3. Raman Spectroscopy

Raman spectroscopy is a spectroscopic technique based on the interaction of a molecule with an electric field generated by a monochromatic beam of radiation (Long 1977 p.1; Fadini & Schnepel 1986 p.16). The molecule will vibrate and scatter the radiation and in the process change its polarizability (McCreery 2000 p.15; Willard *et al,* 1988 p.321). The interaction is illustrated in Figure 2.10. Raman spectroscopy can give information such as phase composition, bonding or oxidation states, chemical structure and composition.

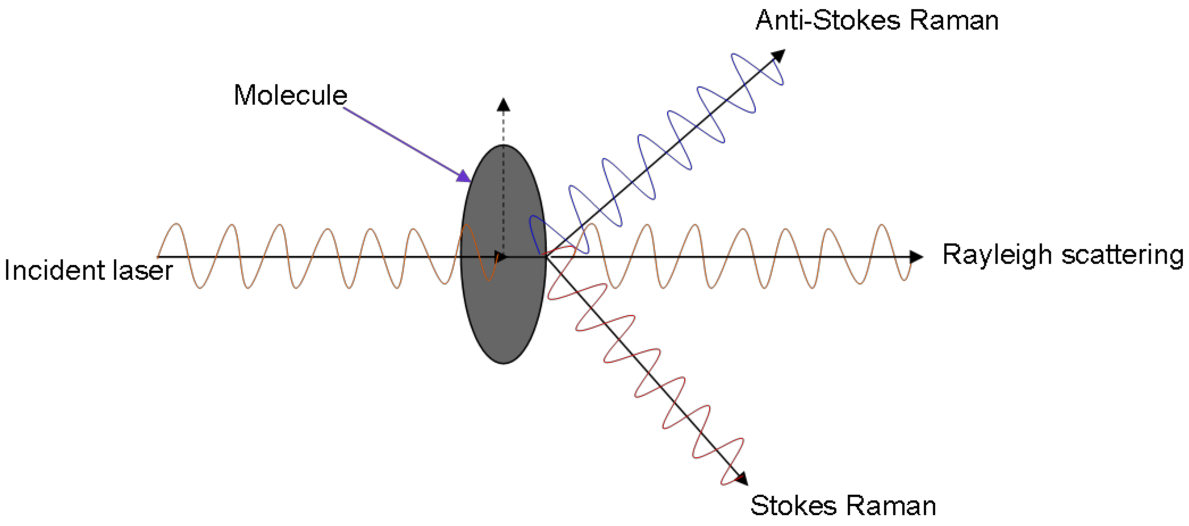

Figure 2. 10: A schematic illustration of Raman scattering process and various signals generated

During the Raman scattering process, radiation with various frequencies is generated. These include the Rayleigh frequency which has energy equal to the incident frequency. The Rayleigh frequency results from the interaction whereby no energy loss occurred. In the case where energy was lost from the molecule and transferred to the radiation, a frequency called the Anti-Stokes frequency is obtained. In the case where energy is transferred from the incident radiation into the molecule, a frequency called the Stokes frequency results. The Stokes frequency has a lower energy than the incident while the Anti-Stokes frequency has higher energy than the incident radiation.

2.5.4. Surface Area and Porosity

The determination of structural properties is one of the most important aspects in materials characterization. This is because most catalytic materials have some porosity or texture. The texture and porosity results from the process of preparation of these catalysts and supports (Leofanti *et al,* 1998 p.207). It is therefore important to determine the porosity of the catalysts since the reaction process where these catalysts are employed are also influenced by the porosity. In this case, mass transfer processes of reactants and products inside the catalyst particles are determined by the pore size (Leofanti *et al,* 1997 p.308).

The gas adsorption method in which nitrogen is used as an adsorbate molecule is based on the physical adsorption phenomenon. In this process, the gas interacts weakly with support due to weak Van der Waals forces between the adsorbate and the support (Condon 2006 p.1). The basis of nitrogen adsorption is the measurement of the volume of gas adsorbed at a certain relative pressure range. The result is expressed as an adsorption isotherm where the quantity adsorbed is plotted versus the relative pressure (Condon 2006 p.4).

During the measurement of the adsorption isotherm, the total surface area and pore size distribution can be determined using BET and BJH models respectively. The BET model was developed by Brunauer, Emmet and Teller in 1938 (Ladavos *et al,* 2012 p.126). The BJH model was developed by Barret, Joyner and Halenda in 1951 (Sing 1998 p.5). The BET model expresses the surface area based on the monolayer coverage, relative pressure and heat of adsorption of the adsorbate molecule as shown in Stage 1 and 2 of Figure 2.11.

$$\boldsymbol{V_{ads} = V_m \frac{C(P/P_0)}{\left[1-(P/P_0)\right]\left[1+(C-1)(P/P_0)\right]}} \qquad \textbf{Equation 2.9}$$

Where V_{ads} is the volume of gas adsorbed, V_m is the volume of the monolayer covering gas, C is the heat of adsorption or liquefaction also known as the BET constant and (P/P_0) is the relative pressure.

The BJH model is based on the Kelvin equation which expresses the relative pressure at which capillary condensation begins as shown in Stage 3 and 4 of Figure 2.11. The BJH model therefore expresses the pore size taking into account the thickness of the multilayer film.

$$\boldsymbol{d_{BJH} = \frac{2\gamma V_m}{RT\ln(P/P_0)} + 2t}$$

Equation 2.10

Where d_{BJH} is the BJH pore size, γ is the surface tension and t is the thickness of the multilayer film.

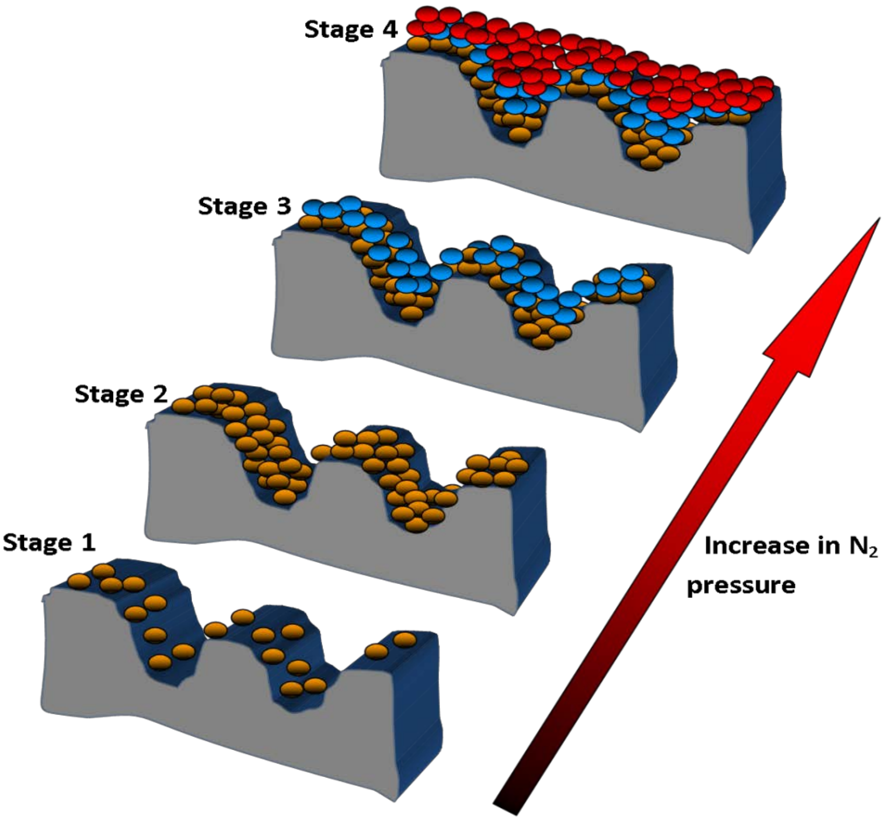

Figure 2. 11: A schematic illustration of the gas adsorption process. (Adopted from http://www.micromeritics.com/Repository/Files/Gas_Adsorption_Theory_poster.pdf)

2.5.5. Temperature Programmed Reduction (TPR)

Temperature programmed reduction (TPR) is a characterization in which the reducible species in a metal oxide are determined. The temperature of reduction is also determined (Webb & Orr 1997 p.13). The reduction characteristics are important since hydrocarbon synthesis via Fischer – Tropsch (FT) is performed on reduced catalyst surfaces. It is known that the activity of FT catalysts is determined by the number of active metallic species obtained by reduction of the metal oxide (Gnanamani *et al,* 2013 p.1).

In the TPR analysis, a gas mixture composed of 10% hydrogen and inert gas is passed over a sample at ambient temperatures. The hydrogen molecules start to interact with the surface of the catalyst and become consumed in the process. The interaction of hydrogen and metal oxide surface leads to the formation of water. As the temperature is increased linearly, the activation energy associated with the reduction of certain oxide species is overcome, and these species become reduced (Webb & Orr 1997 p.13). A general scheme that explains the reduction process is given in as:

$$MO_{2(s)} + nH_{2(g)} = M_{(s)} + nH_2O_{(g)}$$

In the above scheme, M is a transition metal cation. The hydrogen consumed during the reduction is monitored as a function of temperature increase. The hydrogen consumption is then plotted as a function of temperature to yield a temperature reduction profile of the catalyst (Subramanian 1992 p.98).

2.5.6. Hydrogen – Chemisorption

Hydrogen chemisorption is similar to TPR, in that hydrogen molecules interact with the catalyst surface. In this case, the gas adsorbs on the surface forming a monolayer. Thereafter, dissociation of hydrogen molecules into atoms occurs. Each atom then adsorbs onto a single active site on a reduced metal (Bartholomew & Farrauto 2006 p.145). The adsorption of hydrogen onto the surface of the metal can be described by classical adsorption isotherms such as Langmuir, Freundlich and Temkin isotherms (Webb & Orr 1997 pp.222 – 224).

The Langmuir isotherm expresses the chemisorption in terms of the surface coverage and partial pressure of the reducing gas. The Langmuir isotherm is expressed as:

$$\boldsymbol{\theta = \frac{KP}{1+KP}} \qquad \textbf{Equation 2.11}$$

In equation 2.9, θ is the surface coverage, P is the partial pressure and K is the constant expressing the rate constants for adsorption and desorption as expressed in equation 2.10 (Webb 2003 p.4).

$$\boldsymbol{K = \frac{k_{ads}}{k_{des}}} \qquad \textbf{Equation 2.12}$$

The surface coverage is determined by measuring the volume of gas (V_m) required to form monolayer coverage. This volume is obtained by measuring the volume of gas (V) at a specified pressure. Therefore the surface coverage can be expressed as:

$$\boldsymbol{\theta = \frac{V}{V_m}} \qquad \textbf{Equation 2.13}$$

Equation 2.9 and equation 2.11 can be combined to give an expression that explains the analysis principle of hydrogen chemisorption. This expression is given as equation 2.12.

$$\frac{1}{V} = \frac{1}{KV_m} \cdot \frac{1}{P} + \frac{1}{V_m}$$ **Equation 2.14**

A plot of $\frac{1}{V}$ against $\frac{1}{P}$ will yield a straight line with slope $\frac{1}{KV_m}$ and intercept $\frac{1}{V_m}$ (Russa 2012 p.15).

The dispersion of active metal species is of importance in heterogeneous catalysis (Sewell *et al,* 1996 p.255). This is because heterogeneous catalysis is a surface phenomenon. The dispersion ($D\%$) is expressed as the fraction (N_s) of total active metal surface (N_T) which the reactant molecules can access. The dispersion is given as:

$$D\% = \frac{N_s}{N_T}$$ **Equation 2.15**

where $$N_s = \frac{V_m \times N_A \times F_s}{V_{mol}}$$ **Equation 2.16**

Equation 2.14 also consists of the stoichiometric factor (F_s), Avogadro's number (N_A) and the molar mass (M_{mol}). The active metal surface area (A_m) can be calculated in terms of the number of moles of gas adsorbed (n_a) and the cross-sectional area of the adsorptive atom (A_g), in addition to the factors given above (Webb & Orr 1997 p.229).

$$A_m = \frac{A_g \times V_m \times N_A \times F_s}{V_{mol}}$$ **Equation 2.17**

CHAPTER 3

EXPERIMENTAL PROCEDURE

3. CHAPTER 3 – EXPERIMENTAL PROCEDURE

3.1. FURNACE PROFILING

The temperature profile of the furnace used in reduction and sintering studies, was determined. The profiling was done in order to locate the hot zones inside the cylindrical furnace. The temperature profile was done at 250°C and 500°C. Two thermocouples were used in the profiling. One thermocouple was fixed on the outside shell of the furnace, measuring the temperature at the perimeter of the cylindrical furnace. This was set as the control temperature. Another thermocouple was place inside the furnace measuring the actual temperature inside the furnace.

The thermocouple inside the furnace was moved from the bottom to the top of the furnace, at intervals of 2 cm. An equilibration time of 15 minutes was allowed before each temperature measurement was recorded. At the end, a temperature profile was obtained showing the hot zone inside the furnace. The study also served to determine the temperature offset between the outside shell and the inside of the furnace. During reduction and sintering studies, the thermocouple located inside the glass tube, which measured the temperature inside the furnace, was used as the control thermocouple. In this case, the outside temperature (shell temperature) was slightly higher than the inside temperature (glass tube temperature).

The profile experiment showed that the hot zone was located at the first 10 cm length of the furnace. Thereafter the furnace becomes cooler than the set temperature. This hot zone was located in the right area for the glass tube to be used for reduction and sintering studies. Follow up profile experiments with the glass tube inside the furnace, showed that the area in which the catalyst bed would be placed was hot enough and the heat was sufficient to reach the required temperatures in the catalyst bed.

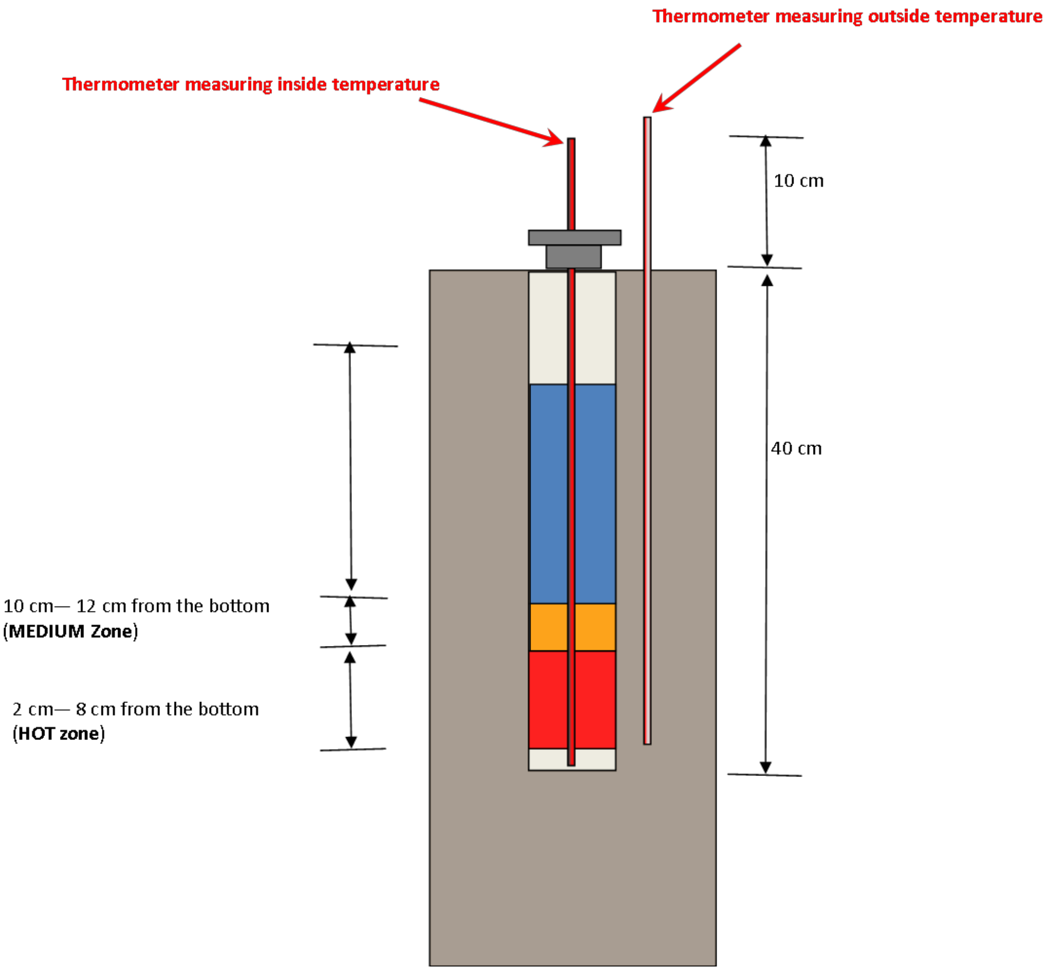

Figure 3. 1: Schematic illustration of the furnace temperature profile

3.2. CATALYST PREPARATION

3.2.1. Support Preparation

Three TiO_2 supports with different phase composition were used for the study. The supports consisted of different percentages of the TiO_2 phases. An Engelhard TiO_2 which consisted of 100% anatase phase was used as the pure anatase support. This material was labelled ‘’Anat’’ support. The Evonik P25 TiO_2 which consisted of 85% anatase and 15% rutile phases was used as the mixed-phase support. This material was labelled ‘’P25’’ support. A rutile support was derived from the P25 TiO_2. In this case, the P25 TiO_2 was calcined in a muffle furnace at 700^{o}C for 8 hours to convert most of the anatase phase into rutile. The resulting material consisted of 98% rutile and 2% anatase phases. This material was labelled ‘’Rut” support. The supports were characterized by XRD, TEM, BET and Raman spectroscopy.

3.2.2. Catalyst Preparation

Prior to catalyst preparation, the TiO_2 supports were calcined in air at 500^{o}C in a muffle furnace to clear the pores. A Thermo Power muffle furnace was used for calcination.

The catalysts were prepared using the slurry phase impregenation method described by van Berge *et al,* (2008). In the procedure, 42.3g of cobalt acetate tetrahydrate was weighed and dissolved in ~50 ml water in a round bottom flask. 100g of TiO_2 support was weighed and added into the round bottom flask to form a slurry. The round bottom flask was connected to a Rotavap. The temperature was kept between 60^{o}C – 80^{o}C by using a silicone oil bath. The slurry was stirred continuously. Vacuum was applied gradually to dry the slurry into a dry catalyst powder. The dry catalyst powder was transferred to a glass tube for calcination.

3.2.3. Calcination Study

The calcination was performed at high air flows and at temperatures ranging from 200^{o}C – 400^{o}C. The calcination was performed in a bench top cylindrical furnace that was constructed in-house. In the setup, the catalyst powder is fluidized by air at high velocity. Calcination was conducted for 6 hours. The catalysts were labelled according to the type of support and calcination temperature i.e. Cat_Anat_300 indicates a cobalt catalyst on anatase support calcined at 300^{o}C. The calcined catalysts were characterized by XRD, TEM, BET and Raman spectroscopy.

3.2.4. Reduction Study

The catalysts calcined at different temperatures (200°C - 400°C) were reduced in a mixture of 4% H_2 in argon at a fixed temperature of 450^{o}C. The reduction was conducted in a cylindrical furnace that was controlled by a temperature controller. A Carbolite cylindrical furnace which was controlled by a Rex P300 temperature controlled was used. The catalyst powder was placed in a double-walled glass tube which had a porous bottom in the inside. The glass tube allowed gases to flow through the catalyst bed resulting in a fluidized catalyst bed. A schematic illustration of the glass tube is given in Figure 3.1. The experimental setup is illustrated in Figure 3.2.

After the glass tube was inserted inside the furnace, the furnace was heated to 450°C at a rate of 10°C/min. The temperature was held for 6 hours. The gas flow was changed to CO_2 with 99.0% purity, after 6 hours, and the glass tube was removed from the furnace and allowed to cool to ambient temperature. The CO_2 served to passivate the reduced catalyst to prevent excessive re-oxidation of metallic cobalt. The reduced catalysts were labelled “RP_Cat_***_***” to indicate “reduced & passivated” catalyst. The reduced and passivated catalysts were characterized by XRD, TEM, BET and Raman Spectroscopy.

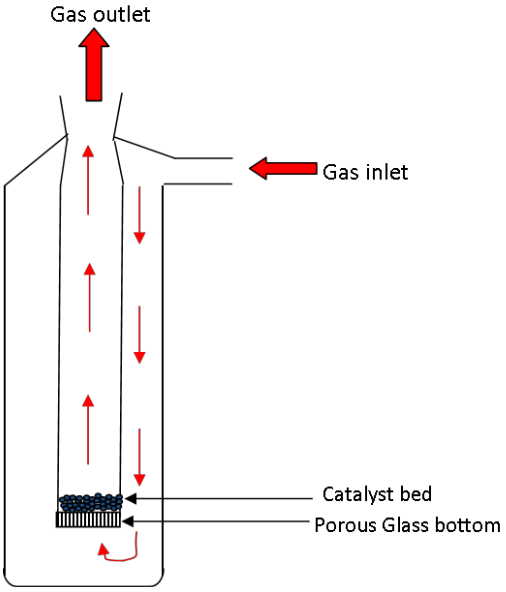

Figure 3. 2: Schematic illustration of the double-walled glass tube used in reduction and sintering studies.

In-situ reduction of the calcined catalysts was also conducted in a reduction cell coupled to an XRD diffractometer. In this procedure, the calcined catalyst was reduced in pure H_2 gas while the temperature was increased from 40°C to 380°C at 10°C/min. XRD scans were recorded at intervals to study the reduction of Co_3O_4 to CoO and subsequently to metallic cobalt.

Temperature programmed reduction (TPR) was used to study the reduction behaviour of the catalysts. H_2-Chemisorption was also used to compliment the in-situ XRD and TPR results.

3.3. SINTERING STUDIES

Catalysts calcined at 300°C and reduced at 450°C were subjected to sintering studies. The studies were performed on the same set-up used for reduction studies as illustrated in Figure 3.3. A gas mixture of 4% H_2 in argon was used for sintering studies. In a typical sintering run, a certain mass of the reduced & passivated catalyst was weighed and transferred into the glass tube. The glass tube was placed into the furnace and the gas mixture was allowed to flow through the bed. The furnace was heated to the sintering temperature i.e. 365°C, at 10°C/min. The sintering time was started once the furnace temperature reached the set sintering temperature. After the sintering hold time was completed, the glass tube was removed from the furnace and the gas flow was switched to CO_2. The CO_2 was allowed to flow through the catalyst bed for 1 hour to passivate the sintered catalyst from reoxidation. The sintered catalysts were characterized by TEM and XRD. Experimental design was used to structure the sintering studies.

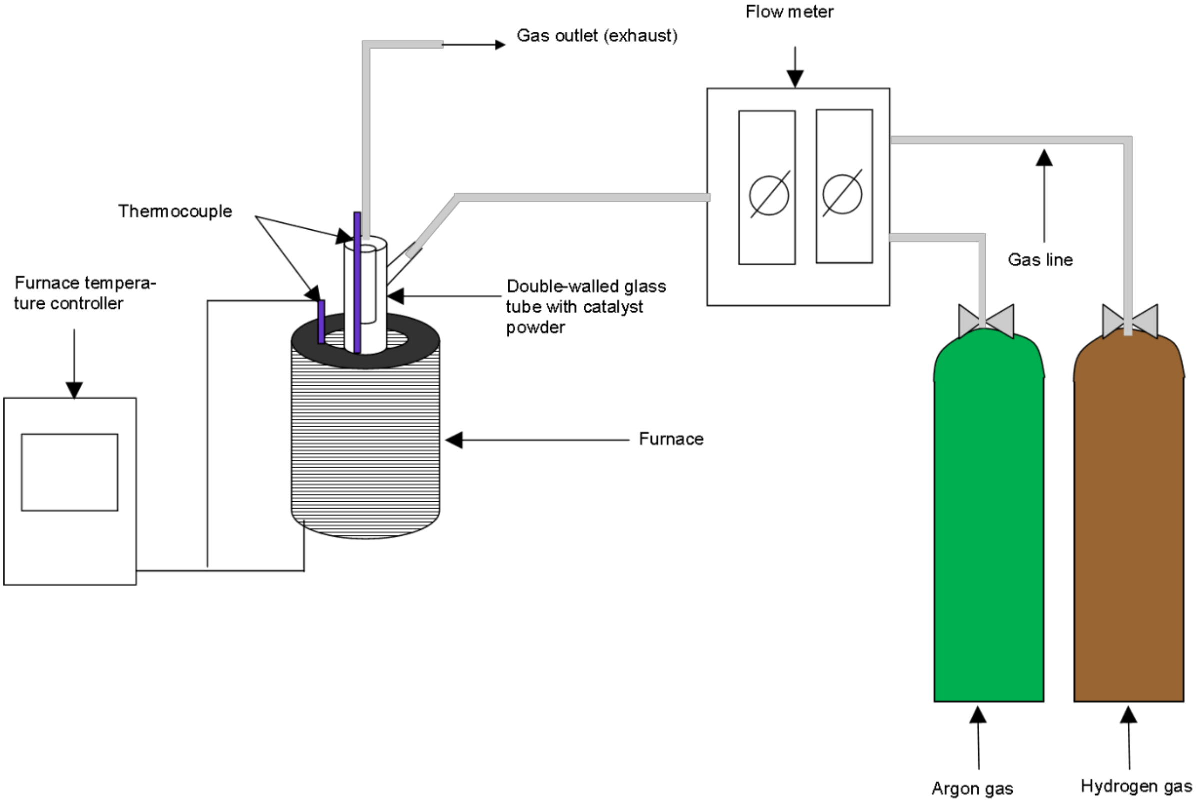

Figure 3. 3: Schematic illustration of the experimental setup for reduction and sintering studies

3.4. CHARACTERIZATION TECHNIQUES

3.4.1. X-Ray Diffraction (XRD)

(Ambient XRD)

XRD was used to determine the phase abundance and crystallite size of cobalt catalysts. The samples were tightly packed in XRD sample holders and transferred into the instrument for analysis. Two instruments were used for ambient XRD measurements. One instrument was housed in Sasol Technology, and another was housed at the University of Pretoria. The instruments were both Panalytical X'Pert Pro multipurpose diffractometers each fitted with the X'Celerator detector. The settings for the instruments are given in Table 3.1. Phase identification was performed by X'Pert HighScore Plus software V2.2.1. The relative abundances and crystallite sizes were calculated by the Rietveld refinement method using Topas software V4.2. The fundamental parameter approach was used for profile fitting. Full pattern refinement was performed for crystallite size determination.

Table 3. 1: Instrument settings for ambient XRD analysis at Sasol Technology and University of Pretoria

Instrument setting	Sasol XRD	UP XRD
Tube Voltage	40 kV	35 kV
Tube current	40 mA	50 mA
Source	Cobalt (1.7889 Å)	Cobalt (1.7889 Å)
Divergance Slit	Fixed	Fixed
Detector	X'Celerator	X'Celerator
Scan from	5°2θ	5°2θ
Scan to	105°2θ	90°2θ
Step size	0.0167°2θ	0.017°2θ

(High Temperature XRD)

In situ reduction and XRD was done in an Anton Paar XRK600 cell coupled to a Panalytical X'Pert Pro multipurpose diffractometer. The reduction was done in pure H_2 gas flow. The cell was heated to 380^oC at 10^oC/min. Scans were collected at intervals of 2 minutes. Phase identification was performed by X'Pert HighScore Plus software V2.2.1. The relative abundances and crystallite sizes were calculated by the Rietveld refinement method using Topas software V4.2. The fundamental parameter approach was used for profile fitting. Full pattern refinement was performed for crystallite size determination. The instrument settings for high temperature XRD are given in Table 3.2.

Table 3. 2: Instrument settings for high temperature XRD analysis

Instrument setting	Sasol XRD
Tube Voltage	40 kV
Tube current	50 mA
Source	Cobalt (1.7889 Å)
Soller Slit	0.04 rad
Automatic divergance Slit	2°
Anti-scatter slit	2°
Detector	X'Celerator
Scan from	5° 2θ
Scan to	105° 2θ
Step size	0.0167°
Time step	25 seconds
Scan duration	20 minutes

3.4.2. Transmission Electron Microscopy (TEM)

TEM was used to determine the crystallite size and elemental composition through imaging and X-ray mapping techniques respectively. An FEI Technai Osiris TEM was used for analysis. The instrument has a field emission gun as an electron source. Bright field (BF) images were captured on a Gatan CCD camera that was controlled by Gatan Digital Micrograph software. Scanning transmission electron microscopy (STEM) images were captured by a HAADF-STEM detector that was controlled by FEI TIA software. EDS elemental mapping was performed using ChemiStem EDS detector system controlled by Bruker Espirit software. The system consists of 4 EDS detectors that are aligned around the specimen. This setup allows for collection of more X-rays than in conventional TEM instruments.

The sample was prepared by crushing and mixing with ethanol to form a suspension. The suspension was placed in an ultrasonic bath for 5 minutes to disperse the particles into fine particulates. Immediately after ultrasonication, a small amount of sample was transferred into a holey carbon-copper TEM grid using a pipette. The copper grid was placed in a single-tilt TEM specimen holder and transferred into the TEM for analysis. Image J software V1.47u was used for image processing. Crystallite sizes were measured on HAADF-STEM images after scale calibration. The diameter of the particle was measured as shown in Figure 3.4. In this case, the diameter of the particle was measured as the length perpendicular to the breadth of the particle. This length is known as the Feret diameter and can be explained as the caliper length of the particle (Merkus, 2009 p.38).

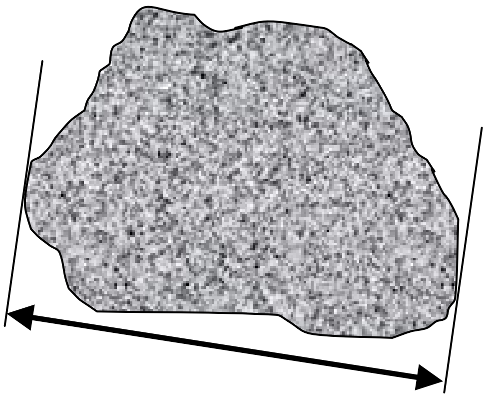

Figure 3. 4: Schematic illustration showing the crystallite size measurement approach described as the Feret diameter of the particle.

In order to understand the differences between XRD and TEM data, it is important to revisit the principles of measurement for each technique. XRD crystallite size measures the smallest coherent scattering domain or smallest unfaulted region as depicted in Figure 3.5 (Akbari *et al*, 2011 p.52). In a multigrained polycrystalline material, there can be more than one of these domains. These can be separated by grain boundaries, or can be closely to form polycrystalline aggregates (Linsinger *et al*, 2012 p.36). In addition, XRD measurements express crystallite size as a volume-weighted average diameter or so-called de Brouckere mean diameter. This is expressed as a volume moment diameter $d[4{,}3]$ as shown in Equation 3.1 (Mingard *et al,* 2009 p.12).

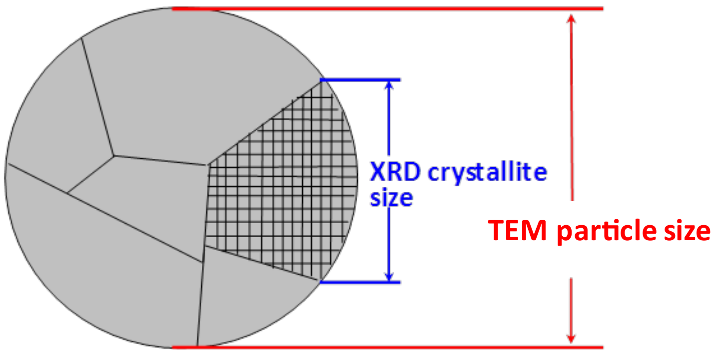

Figure 3. 5: Illustration of the crystallite size measured by XRD and TEM.

$$\boldsymbol{d[4,3] = \frac{\sum d^4}{d^3}}$$ **Equation 3. 1**

XRD can distinguish between phases and is sensitive to the crystallinity and orientation of scattering domains in the specimen (Akbari 2011 p.53).

TEM is a counting method and measures the size of particles on a number-basis (Ozkaya 2008 p.61). The diameter is expressed a number-length moment diameter $d[1,0]$ given by Equation 3.2.

$$\boldsymbol{d[1,0]=\frac{\sum d}{n}}$$ **Equation 3. 2**

The particle size measured by TEM is observed as a projection on 2-D surface. The contrast seen in HAADF-STEM images results from chemical differences (z-contrast) rather than diffraction or phase composition seen in XRD (Willams & Carter 2009 p.161). As a result, a difference in the atomic number is required between the particle and background to obtain clear contrast differences in an image. It can be expected that the size measured by TEM will be larger than that measured by XRD since TEM measures the whole particle and not specific coherent scattering domains as depicted in Figure 5.44 (Akbari 2011 p.53). For the convention of this thesis, the “crystallite” size refers to the XRD-measured entity and “particle” size refers to the TEM-measured entity.

The TEM-measured particle size data was expressed as a distribution showing the particle size range. The size distributions usually referred to as the particle size distribution (PSD) were plotted as histogram which shows the frequency of particle size classes (Akbari *et al*, 2011 p.50).

The PSD was then modelled by fitting into a mathematical model from which appropriate data such as mean and standard deviation can be extracted. In our case, the data was fitted to the lognormal distribution function (LNDF), since it is known that particle size data of supported catalysts follows a LNDF-type of function. The LNDF is a function in which the logarithm of the variable is normally distributed (Granqvist & Burman 197 p.477). A LNDF curve is illustrated in Figure 3.5. The LNDF is expressed as:

$$\boldsymbol{F(x,\mu,\sigma)=\frac{1}{x\sigma\sqrt{2\pi}}\cdot e^{-\left[\frac{(\ln(x)-\mu)^2}{2\sigma^2}\right]} \qquad x>0}$$ **Equation 3. 3**

In the above equation, x is the particle diameter, μ is the geometric mean and σ is the geometric standard deviation (Granqvist & Burman 197 p.477). It should be noted that the geometric mean and standard deviation are different from the arithmetic mean and standard deviation in that they have no direct physical meaning, therefore should not be treated the same. The geometric mean μ and standard deviation σ are used to calculate the mode, median, the actual mean and the full-width-at-half-maximum (FWHM) statistic variables as shown in Equation 3.4, 3.5, 3.6 and 3.7. These are the appropriate values to be reported for particle sizes. These statistical variables are described as:

Median: $$\widehat{x_a} = e^{\mu-\sigma^2}$$ **Equation 3. 4**

Mode: $$\widehat{x_b} = e^{\mu}$$ **Equation 3. 5**

Mean: $$\widehat{x_c} = e^{\mu+\sigma^2}$$ **Equation 3. 6**

FWHM: $$\Delta x_{FWHM} = 2e^{\mu-\sigma^2} sinh\left(\sqrt{(\ln(4)\ln(\sigma^2))}\right)$$ **Equation 3. 7**

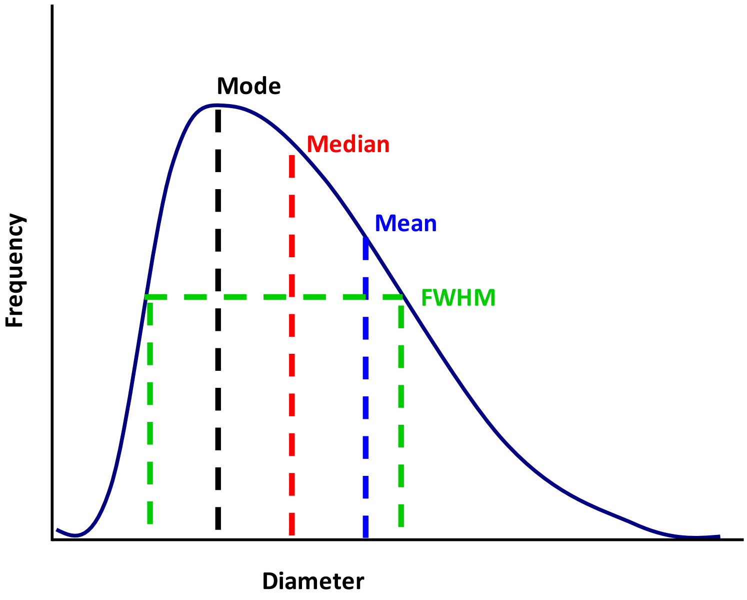

Figure 3. 6: Schematic illustration of lognormal distribution function (LNDF) curve showing the position of the mode, median and mean.

To assess whether there are significant differences in the size distributions, the Kolmogorov-Smirnov test was used (Helsel, 1987 p.179, Massey, 1951 p.68). The t-test which is usually used for comparison purposes is a parametric test which uses the mean and standard deviation of a normally distributed data set (Helsel, 1987 p.179). The Kolmogorov-Smirnov test is a nonparametric test in that it does not matter what type of distribution is the data (Young, 1977 p.935). This test is thus suitable for lognormally distributed data. The test compares the whole distribution in the form of a cumulative distribution function with another distribution. The result is scalar statistic D which gives the maximum difference between the two cumulative distribution functions. The statistic is computed by Equation 3.8. The D statistic is then compared to a value of D_{crit} through hypothesis testing in a similar manner to the t-test (Young, 1977 p.938). D_{crit} is computed by multiplication of a tabled α value and $s(n)$ which is computed using Equation 3.9, where n_1 and n_2 are number of observations in each data set.

$$D = \max_x \left| F_{n_1}(x) - F_{n_2}(x) \right|$$ **Equation 3. 8**

$$s(n) = \sqrt{\frac{(n_1+n_2)}{(n_1 n_2)}}$$ **Equation 3. 9**

The Kolmogorov-Smirnov test can also be used to assess whether a data set is lognormally distributed or not (Massey, 1951 p.68). This is done by comparing the cumulative distribution function with an empirical model in order to assess the fit. The error in the fit is expressed as root mean square error (RMSE). This was calculated by methods such as least squares fitting and maximum likelihood (Evans *et al*, 2008 p.1396).

3.4.3. BET Surface Area and Pore Size Distribution

BET surface area and pore size distribution were determined by the nitrogen physisorption method. A Micromeritics ASAP 2420 Surface Area and Porosity analyser was used. A sample mass of approximately 0.25 g was weighed into a glass tube. The tube was connected to the degassing port in the instrument. The sample was degassed by heating to 250^{o}C under nitrogen flow for 6 hours. After degassing, the sample tube was weighed after cooling to room temperature. The sample tube was then connected to the analysis port in the instrument. BET surface area and pore sizes were measured at nitrogen relative pressures ranging from 0.08 to 0.98 (p/p_o). The temperature during analysis was kept at ~77 K (-195^{o}C) by submerging the sample glass tube in liquid nitrogen. Micromeritics ASAP 2420 software V2.04 was used to calculate BET surface area and pore size distribution using the BET and BJH theories.

3.4.4. Raman Spectroscopy

A Horiba Jobin Yvon TX64000 Raman spectrometer was used for analysis. A green laser with a wavelength of 514 nm was used for excitation. The laser power was kept at 10 mV at the sample. An aperture size of 150 µm was used. An exposure time of between 10 – 30 s with up to 5 times accumulation was used. A small amount of the sample was scooped and gently sprinkled onto a microscope glass slide. The slide was transferred directly to the spectrometer for analysis.

3.4.5. Temperature Programmed Reduction (TPR)

A Micromeritics Autochem 2920 TPR instrument was used for TPR analysis. A sample mass of approximately 50 mg was weighed into a U-shaped quartz tube, which was then plugged with quartz wool. The sample was dried by heating to 120^{o}C at a rate of 5^{o}C/min under helium gas flow of 50 ml/min. The drying was performed for 10 minutes. The sample was cooled to room temperature.

The cooled sample tube was connected to the instrument and the sample was heated to 900^{o}C at a rate of 10^{o}C/min under a 10% hydrogen/argon mixture flow. The temperature was kept at 900^{o}C for 10 minutes. Since the reduction reaction forms water as a by-product, a water trap composed of dry ice and isopropanol was used. The hydrogen consumed during the reduction reaction was measured by a Thermal Conductivity Detector (TCD)..

3.4.6. Hydrogen Chemisorption

A Micromeritics ASAP 2020 Chemisorption instrument was used for hydrogen-chemisorption analysis. A sample mass of approximately 0.25 g was weighed into a U-shaped quartz tube which contained a layer of quartz wool. The sample was dried by heating to 80^{o}C in vacuum in the degassing unit. The degassing process was kept for 8 hours. The sample tube was allowed to cool to room temperature. After cooling, the sample tube was transferred to the analysis port of the instrument. Reduction was performed at 450^{o}C under a flow of pure hydrogen gas at a flow of 100 ml/min. After the reduction was completed, static chemisorption was performed with pure hydrogen as an adsorbate molecule. Active metal surface area, degree of reduction and cobalt metal dispersion were calculated using Micromeritics software.

CHAPTER 4
EXPERIMENTAL DESIGN

4. CHAPTER 4 – EXPERIMENTAL DESIGN

4.1. INTRODUCTION

A successful experimental part of any scientific and engineering project relies on a clear and statistically sound experimental design. The experimental design must address the objectives of the study, in addition to determining the interaction between the response and control variables. At the same time, the objectives must be addressed within constraints of time, materials and costs (Alsan 2008 p.80). Response surface methodology (RSM) is the most appropriate experimental design method that covers the criteria discussed above (Chen *et al,* 2012 p.3068, Makokha *et al*, 2012 p.150).

4.2. RESPONSE SURFACE METHODOLOGY (RSM) AND FACTORIAL DESIGN

Response surface methodology (RSM) is a method comprising of mathematical and statistical techniques which are used model and analyse scientific and engineering problems (Aslan 2008 p.81, Chen *et al*, 2012 p.3068). RSM is commonly used as an optimization tool to determine optimum operating conditions. In this case, the optimum can either be a minimum or a maximum of a certain relationship between response factor y, and control factor x_i (Makokha *et al*, 2012 p.150).

RSM allows for accurate determination of the relationship between the response and control factors. This relationship can either be first-order or second-order (Oraon *et al*, 2006 p.1037). The significance of the control variables can also be determined by hypothesis testing in RSM.

In the case of a first-order interaction between the response variable y and control variables x_1 and x_2, the relationship is expressed as:

$$\boldsymbol{y = \beta_0 + \beta_1 x_1 + \beta_2 x_2 + \epsilon}$$

The Linear model is usually expressed in the above form where β_1 and β_2 are the coefficients of x_1 and x_2 respectively.

In the case of second-order interactions, as is the case with most scientific and engineering problems, the relationship between response variable y and control variables x_1 and x_2 is expressed as:

$$\boldsymbol{y = \beta_0 + \beta_1 x_1 + \beta_2 x_2 + \beta_1 x_1^2 + \beta_2 x_2^2 + \beta_{12} x_1 x_2 + \epsilon}$$

The output from RSM includes a model which shows the interaction of the response and control variables, and graphical illustrations called response surfaces. In the case of factorial designs, the interaction of main variables is explored, and a model describing the relationship is given.

Possible models such as the *2Factor Interaction*, *Quadratic* and *Cubic* are usually explored and fitted to data.

The *2Factor Interaction* model for variables A and B can be expressed as:

$$\boldsymbol{y = \beta_0 + \beta_1 A + \beta_2 B + \beta_{12} AB}$$

The *Quadratic* model for variables A and B can be expressed as:

$$y = \beta_0 + \beta_1 A + \beta_2 B + \beta_{12} AB + \beta_1 A^2 + \beta_2 B^2$$

4.2.1. Experimental variables for the study

The calcination temperatures range was from 200°C - 400°C. This was chosen in order to cover the range of calcination temperatures used in patents of titania-supported cobalt catalysts (Mauldin *et al*, 1991, p.6, Lok 2011, p.0028). The range is also sufficient to evaluate the effect of calcinations temperature on the initial cobalt crystallite size.

Table 4. 1: Parameters for calcination study

Independent variables					
Calcination Temperature (°C)	200	230	300	370	400
TiO_2 support	Anatase	P25	Rutile		

The sintering studies were performed as constant-temperature variable time studies. In this case, the time was varied to study the kinetics of sintering and to obtain the sintering kinetic constant term. The experimental design was designed as one-factor RSM. This is because only sintering time was the numerical variable. The other variable, the titania support, was treated as a categorical variable. Therefore the experiments were structured as 3 x one-factor RSM design.

Table 4. 2: Parameters for variable time sintering study

Independent variables						
Sintering Time (Hour)	**(Variable A)**	4	8	16	32	48
TiO_2 support	**(Variable B)**	Anatase		P25		Rutile

4.2.2. Statistical Variables

The data was evaluated using statistical regression analysis. The following statistical parameters were of importance when analysing the data:

- *Sum of Squares (SS)* – Defined as the sum of the squared deviation from the observed value and the mean of *y,*

$$SS = \sum_{i=1}^{n}(y_i - \bar{y})^2$$

- *Error Mean Square (MS)* – Defined as the sum of square deviations from the actual values divided by the degrees of freedom.

$$MS = \frac{SS}{df}$$

- *Degrees of Freedom (df)* – Defined the number of model parameters minus one.

$$df = n - 1$$

- *F-value* – Defined as the ratio of the error mean squares and the residual mean squares.

- *p-value* - Defined as the probability of observing the *F-value* when the null hypothesis is true. A small value of less than 0.05 indicates rejection of the null hypothesis.

- *Predicted Residual Error Sum of Squares (PRESS)* – Defined as the parameter that measures how well the model fits each point in the design.

- *R-squared (R^2)* – Defined as the regression correlation coefficient. The term gives an idea of the goodness of fit of the model.

$$R^2 = 1 - \left[\frac{SS_{resdiual}}{(SS_{model} + SS_{residual})}\right]$$

- *Predicted R-squared* – Defined as the correlation coefficient which measures the goodness of the model prediction for a response value.

$$Pred\ R^2 = 1 - \left[\frac{PRESS}{(SS_{model} + SS_{residual})}\right]$$

CHAPTER 5

RESULTS AND DISCUSSION

Stage 1 – Titania support characterization

5. CHAPTER 5 – RESULTS AND DISCUSSION

5.1. STAGE 1 – TITANIA SUPPORT CHARACTERIZATION

5.1.1. XRD

The powder diffractograms of the supports are given in Figure 5.1. The diffractogram of Anatase support shows characteristic reflections of the anatase phase (JCPDS card: 01-075-2547), and no other phase was detected. The most intense peak which is at 29.5° 2θ can be indexed to the (101) plane of anatase. The second most prominent peak at 56.5° 2θ can be indexed to the anatase (200) plane. Other prominent peaks at 44°, 65°, and 74° 2θ correspond to the anatase (004), (211) and (118) planes respectively (Teoh *et al,* 2010 p.2; Orendorz *et al,* 2007 p.4391). Quantitative phase analysis showed that the sample was composed of 100% anatase phase.

The powder diffractogram of P25 support shows the presence of both anatase and rutile titania phases. The most prominent peak which is at 29.5° 2θ corresponds to the anatase (101) phase. Other anatase peaks can be seen at 44°, 56.5°, 64° and 74° 2θ. These peaks correspond to anatase (004), (200), (105), (211) and (118) respectively (JCPDS card: 01-075-2547) (Orendorz *et al,* 2007 p.4391). Peaks indicating the presence of rutile phase can also be seen. These are present at 32°, 42°, 48°, 64° and 67° 2θ. These peaks can be indexed to rutile (110), (101), (111), (211) and (220) planes respectively (JCPDS card: 04-008-4342). Quantitative phase analysis showed that anatase phase was the most abundant phase with concentration of 84.06 %. Rutile phase was shown to have a concentration of 15.94 %. The quantitative results are in agreement with the manufacturer's specifications for the AEROXIDE P25 TiO_2 material.

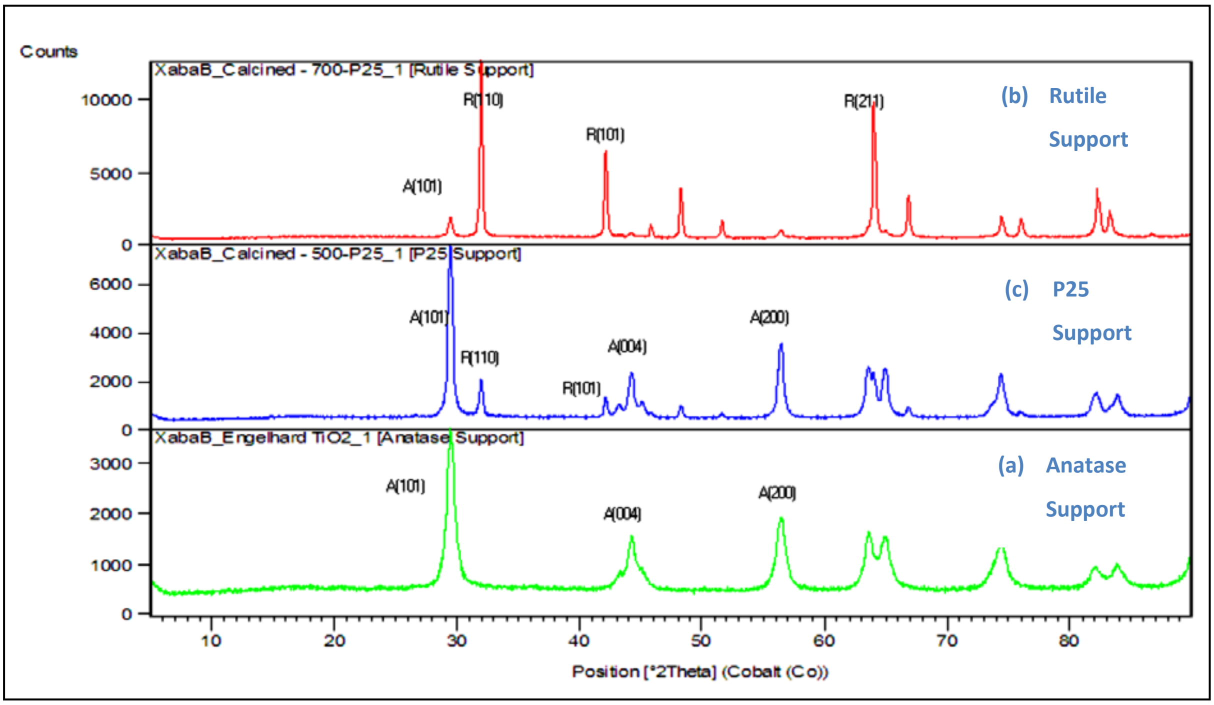

Figure 5. 1: Powder diffractograms of titania supports showing (a) Anatase support, (b) P25 support and (c) Rutile support.

The powder diffractogram of the Rutile support showed the presence of both anatase and rutile phases. Rutile was identified as the major phase. The most prominent peak at 32° 2θ corresponds to the rutile (110) plane. Other intense peaks were also identified. These peaks are at 42°, 48° and 64° 2θ and correspond to rutile (101), (111) and (211) planes respectively (JCPDS card: 04-008-4342). Peaks indicating the presence of anatase phase can be seen at 29.5°, 44° and 56.5° 2θ. These correspond to anatase (101), (004) and (200) planes as already seen in the other supports (JCPDS card: 01-075-2547). Quantitative phase analysis showed that rutile and anatase phases had concentrations of 97.5% and 2.5% respectively. The quantitative results of the supports are given in Table 5.1.

Table 5. 1: Quantitative phase analysis results of titania supports

Quantitative Analysis	Anatase	3σ error	P25	3σ error	Rutile*	3σ error
Anatase %	100	0.27	84.06	0.57	2.48	0.27
Rutile %	0	0.27	15.94	0.57	97.52	0.27
R_{wp}	3.98		3.79		4.72	
GOF	1.00		1.08		1.68	
Crystallite size						
LVol_IB (anatase) nm	13		19		22	
LVol_IB (rutile) nm	0		32		64	

The volume-based crystallite size was obtained from crystallite size broadening contributions. The anatase crystallites are shown to be smaller than rutile crystallites in all the titania supports. The crystallite size of anatase in Anatase- , P25- , and Rutile-support was shown to be 13 nm, 19 nm and 22 nm respectively. The rutile crystallite size in P25- and Rutile-support was shown to be 32 nm and 64 nm respectively. The results indicate a slight increase in the anatase crystallite size due to heat treatment upon preparing the Rutile support. The rutile crystallites also increase in size with heat treatment. This is evident in the rutile crystallite size in P25-support being twice that in Rutile-support.

Mathpal *et al,* (2013 p.183) reported an increase in TiO_2 crystallite size upon heating from 400°C up to 700°C. The crystallite size increased from 19 nm at 400°C up to 68 nm at 700°C. Luis *et al,* (2011 p.22) also reported a crystallite size increase from 9.3 nm to 68.7 nm after heat treatment from 350°C to 850°C. These observations point to a size increase accompanying the anatase-to-rutile transformation.

5.1.2. Transmission Electron Microscopy (TEM)

The BF-TEM image of the Anatase-support given in Figure 5.2 shows a typical structure of crystalline particles with a size ranging from 6 nm – 35 nm. The mean particle size and FWHM were found to be 11.7 nm and 8.1 nm respectively. The histogram of the size distribution is given in Figure B.1 in the Appendix B. The particles have a different morphology. Others have a somewhat spherical shape while others have an “oval” –shape. The particle size from TEM is in agreement with that calculated from XRD. In this case, the crystallite size of anatase particles was shown to be 13 nm.

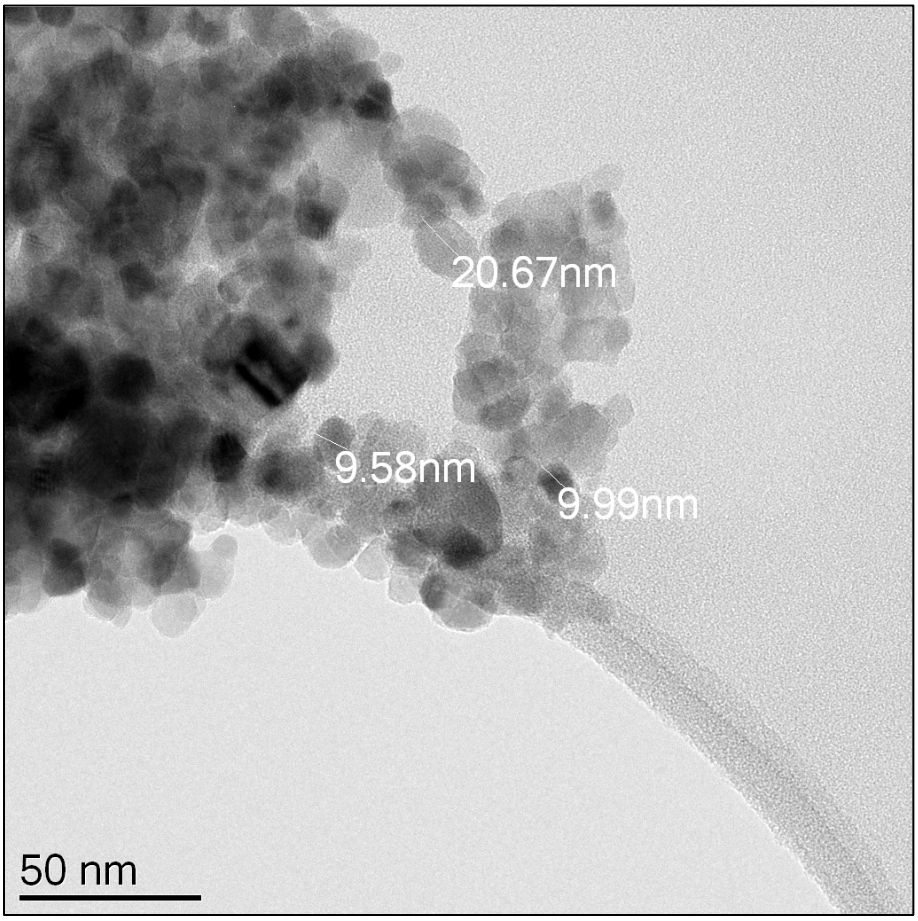

Figure 5. 2: Bright Field TEM image of Anatase support

The BF-TEM image of P25 support given in Figure 5.3 shows the presence of two classes of particles. The first class is that of particles with a size ranging between 6 nm – 20 nm. This class of particles is the major fraction in P25 support. Selected area electron diffraction (SAED) showed that these particles are most likely to be anatase particles. The second class of particles is that with a size ranging between 20 nm – 50 nm. These particles are likely to be rutile particles, the presence of which was confirmed by XRD. The overall mean particle size and FWHM were found to be 22.8 nm and 16.1 nm respectively. The observed particle size from TEM is in agreement with XRD results which showed crystallite sizes of 18 nm and 32 nm for anatase and rutile phases respectively.

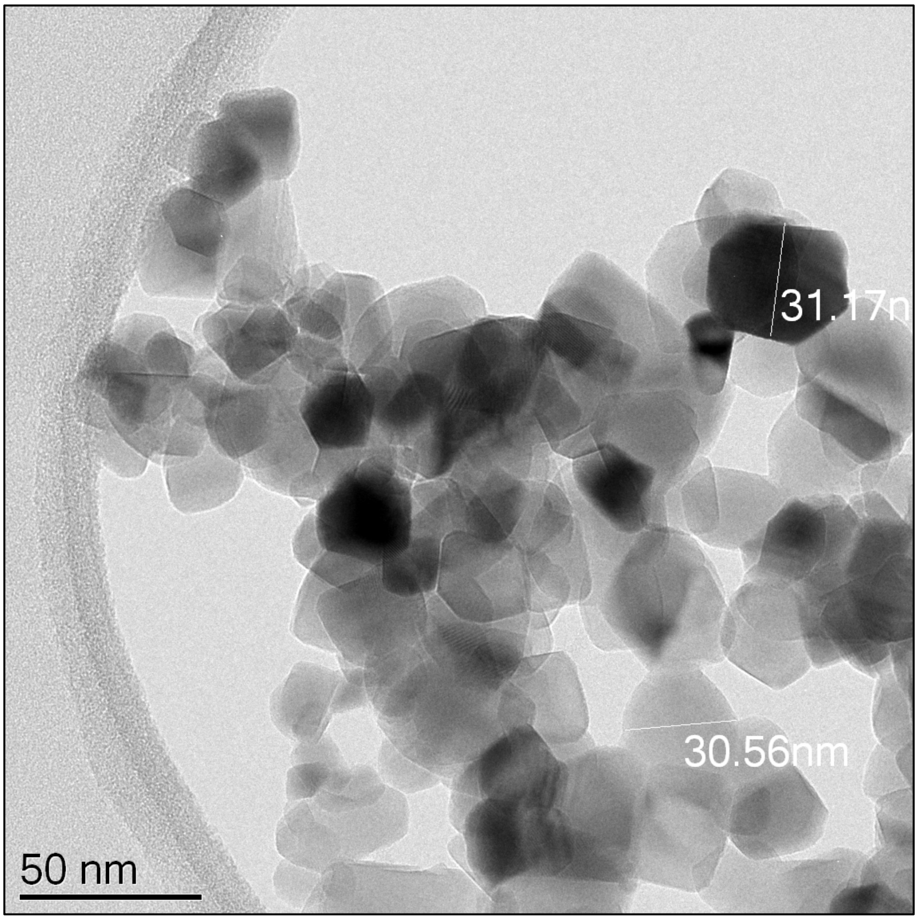

Figure 5. 3: Bright field TEM image of P25 support.

The BF-TEM image of Rutile-support given in Figure 5.3 shows the presence of large particles. These particles are in the size range between 60 nm – 120 nm. The mean particle size and FWHM were found to be 79.7 nm and 71.1 nm respectively. The particles were showed to be rutile phase through SAED. The particles have a solid dense appearance which further confirms the rutile nature. It is known that rutile phase is denser than anatase and brookite phases (Hanaor & Sorrell 2011 p.856). The observed particle size from TEM images is in agreement with XRD results which showed crystallite size of 64 nm for rutile phase.

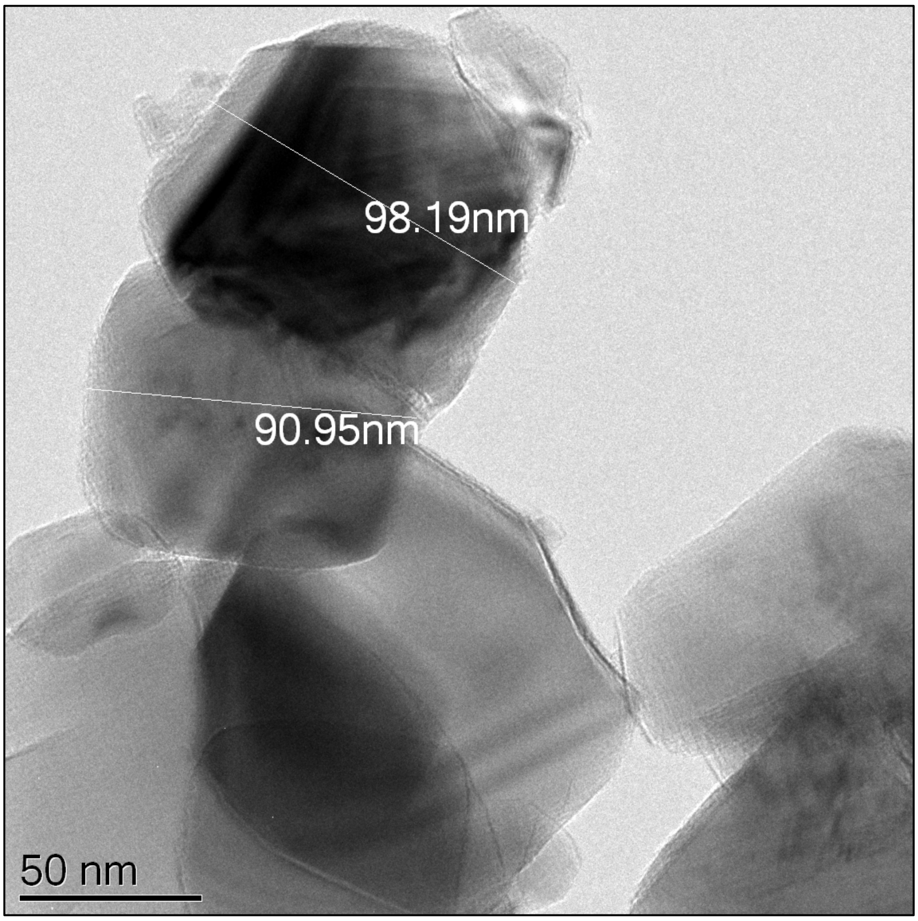

Figure 5. 4: Bright field TEM image of Rutile support.

The TEM results of the bare supports are in agreement with values reported in literature. Ohno *et al*, (2001 p.83) reported particle sizes of 25 nm and 85 nm for anatase and rutile phases respectively, measured by TEM. Porter *et al*, (1999 p.1525) reported slightly different results from Ohno *et al,* (2001) and our study. They reported particle sizes of 20.6 nm and 14.4 nm for anatase and rutile phases respectively. These values were measured by XRD in fresh P25. They also reported crystallite sizes ranging from 15 nm – 25 nm measured from TEM images.

5.1.3. BET Surface Area and Pore Size Distribution

The textural properties of the supports were determined. In this case, BET surface area and pore size distribution were determined. The surface area of the supports shows a decreasing trend with increasing rutile content. The support consisting of 100% anatase phase (Anatase support) has the highest surface area of 109 m^2/g. The mixed phase support consisting of ~16% rutile (P25 support) follows with a surface area of 52 m^2/g. The Rutile support, which consists of 98% rutile phase, has the lowest surface area of 8 m^2/g.

Table 5. 2: Textural properties of titania supports showing BET surface area and pore sizes.

Support	Rutile phase (%)	BET Surface Area (± 6 m^2/g)	Pore Size (nm)
Anatase	0	109	9.8
P25	16	52	26.9
Rutile*	98	8	22.8

The decrease in surface area with increasing rutile content can be attributed to the higher density of rutile compared to anatase (Hanaor & Sorrell 2011 p.856). It can be expected that as the rutile content increases, the material gets denser and the pore structure is lost due to the presence of large crystallites. The loss of pore structure leads to the loss of surface area. This observation is in agreement with XRD and TEM results which showed larger crystallites of rutile compared to anatase particles. The observation has been reported in literature by other authors (Zhang *et al,* 2002 p.377; Weibel *et al,* 2005 p.2381; Raj & Viswanathan 2009 p.1381).

Raj & Viswanathan (2009 p.1381) observed a decrease in surface area with increasing calcination temperature of P25 titania. The increase in calcination temperature led to the increase in the rutile content, which subsequently led to the loss of surface area. Zhang *et al,* (2002 p.377) and Weibel *et al,* (2005 p.2381) also reported a decrease in surface area with increasing calcination temperature. This observation indicates a change in the pore structure with rutilation.

The pore structure of the titania supports was further explored by looking at the N_2-adsorption–desorption isotherms. The isotherm of Anatase support shown in Figure 5.5 is a type IV isotherm with a H2 hysteresis loop between 0.75 and 0.90 P/P_0 (Condon 2006 p.9). The type IV isotherm indicates the presence of mesoporous structure (Zhang *et al,* 2002 p.378). This is in line with the narrow pore size and high surface area of the support. The hysteresis loop also highlights the type of pores found in a porous material. The type IV isotherm indicates narrow pore structure or interconnected pore structure. The Anatase support has an average pore size of 9.8 nm. This support has the smallest pore sizes among the three supports

The N_2-adsorption-desorption isotherm of the P25-support is also given in Figure 5.5. The isotherm shows behaviour between type II and type IV isotherm. This indicates the presence of both mesopores and macropores in the titania support. The type II isotherm does not have a hysteresis loop similar to that seen in the type IV isotherm. This can also highlight the type of pore structure. The type II isotherm usually indicates the presence of wide non-connecting pores. This observation can be confirmed by looking at the pore size distribution of the support. It could be seen that the support had pores with sizes ranging from ~10 nm – 100 nm with an average of 26.9 nm.

The Rutile support also has an isotherm with characteristics of type II and type IV isotherms. This again shows the presence of mesopores and macropores.

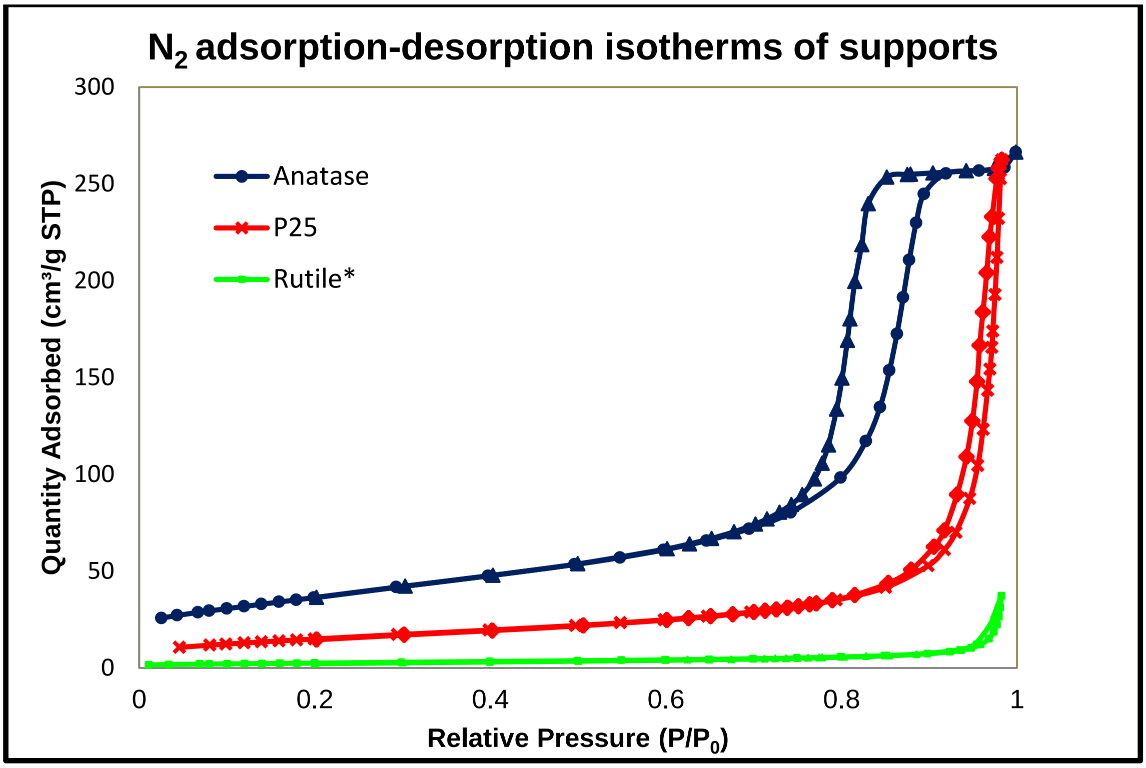

Figure 5. 5: N_2-adsorption-desorption isotherms of titania supports showing the pore structure.

5.1.4. Raman Spectroscopy

Anatase TiO_2 has six Raman active modes. These are A_{1g} + $2B_{1g}$ + $3E_g$ (Orendorz *et al,* 2007 p.4392). The characteristic vibrations for Anatase occur at 141 cm^{-1} (E_g), 194 cm^{-1} (E_g), 396 cm^{-1} (B_{1g}), 513 cm^{-1} (A_{1g}), 519 cm^{-1} (B_{1g}) and 637 cm^{-1} (E_g). Rutile TiO_2 has four Raman active modes. These are A_{1g} + B_{1g} + B_{2g} + E_g (Yoshitake & Abe 2009 p.273). The bands for Rutile occur at 143 cm^{-1} (B_{1g}), 243 cm^{-1} (B_{2g}), 447 cm^{-1} (E_g) and 612 cm^{-1} (A_{1g}).

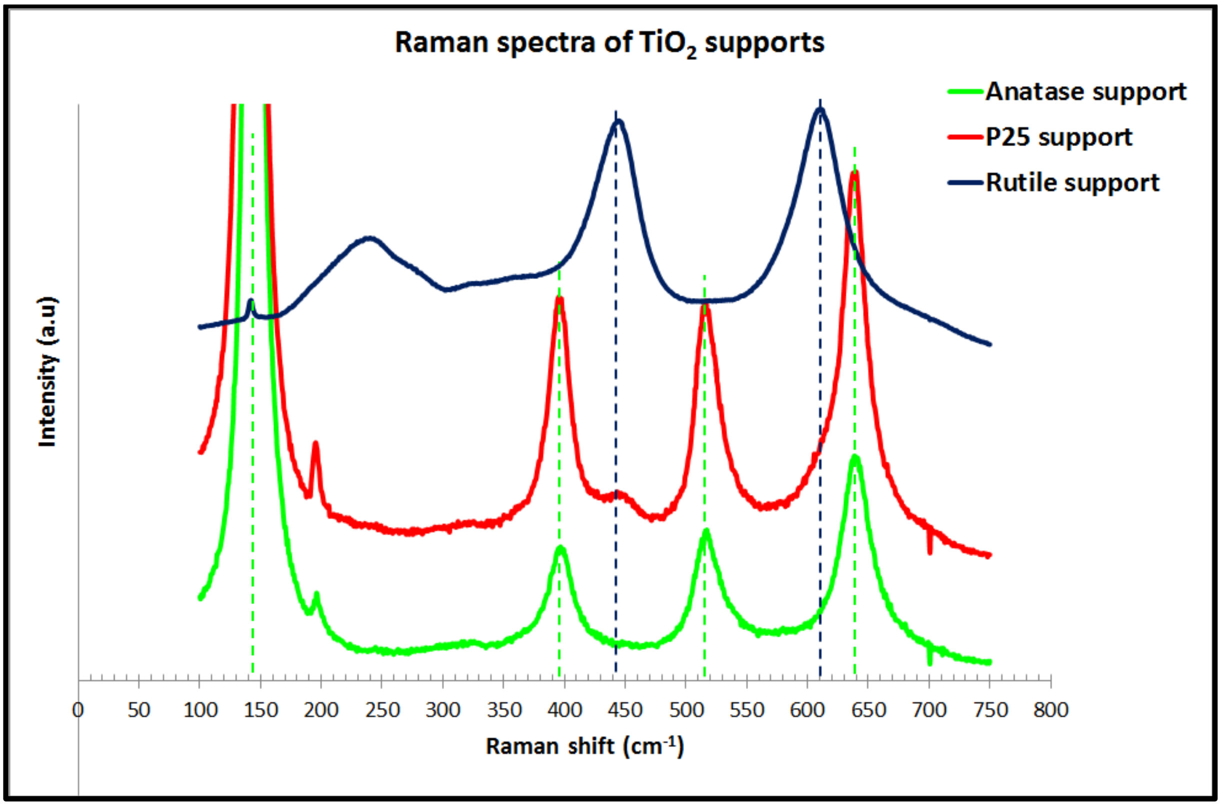

Figure 5.6: Raman spectra of titania supports showing characteristic bands.

The Raman spectrum of Anatase support shows characteristic bands at 141 cm^{-1}, 198 cm^{-1}, 398 cm^{-1}, 518 cm^{-1} and 639 cm^{-1}. These frequencies correspond to the $E_{g(1)}$, $E_{g(2)}$, $B_{1g(1)}$, A_{1g}, $B_{1g(2)}$ and $E_{g(3)}$ bands of anatase respectively. The position and intensity of the bands are in agreement with those reported in reference works such as Orendorz *et al,* (2007 p.4392). The Raman spectrum of P25-support clearly shows the presence of anatase bands. The bands can be seen at 141 cm^{-1}, 198 cm^{-1}, 399 cm^{-1} , 520 cm^{-1} and 640 cm^{-1}. At first glance, it appears as though rutile is not present. But when the spectrum is scaled up, the presence of rutile is apparent. This is seen as a hump at 444 cm^{-1}. The rutile bands are usually weak compared to the high intensity anatase bands. It is known that anatase TiO_2 has a larger Raman cross-section than rutile TiO_2. This is related to the strong polarizability of the Ti – O bond in anatase TiO_2 (Tosheva *et al*, 2010 p.1870)

The Raman spectrum of Rutile support shows bands characteristic of rutile phase. These bands could be seen at frequencies of 141 cm^{-1}, 240 cm^{-1}, 442 cm^{-1} and 610 cm^{-1}. These correspond to the B_{1g}, B_{2g}, E_g and A_{1g} bands respectively. The anatase $E_{g(1)}$ band, and rutile E_g and A_{1g} bands were monitored during catalyst calcination and reduction studies. The position and intensity of these bands give information on the interaction of the titania phases with cobalt species (Guadec & Colomban 2007 pp.32 – 34)

Stage 2 – Catalyst Characterization. (Calcination Study)

5.2. STAGE 2 – CATALYST CHARACTERIZATION (CALCINATION STUDY)

5.2.1 XRD

5.2.1.1. Qualitative and Quantitative Analysis

Qualitative PXRD results of the titania-supported catalysts revealed the presence of anatase, rutile, Co_3O_4 and CoO. The results of crystalline phase abundances of Anatase-supported catalysts showed anatase as the major phase, with traces of rutile also present. The concentration of Co_3O_4 was found to be 11.1%; 9.6%; 11.6%; and 11.3% for catalysts calcined at 200°C, 230°C, 300°C and 370°C respectively. No Co_3O_4 was observed in the catalyst calcined at 400°C. Instead, CoO and metallic cobalt were observed with an abundance of 2.3% and 2.6% respectively. The results are listed in Table 5. 3.

Table 5. 3: Quantitative PXRD results of Anatase-supported catalysts

Sample	Anatase % (3σ error)	Rutile % (3σ error)	Co_3O_4 % (3σ error)	CoO% (3σ error)
Anatase Support	100.0 (0.3)	-	-	-
Cat_Anat_200	87.9 (0.2)	0.95 (0.15)	11.1 (0.2)	0
Cat_Anat_230	90.1 (0.4)	0.32 (0.22)	9.6 (0.3)	0
Cat_Anat_300	87.4 (0.2)	0.97(0.15)	11.6 (0.2)	0
Cat_Anat_370	87.5 (0.2)	1.2 (0.14)	11.3 (0.2)	0
Cat_Anat_400**	95.1 (0.2)	0	0	2.3 (0.1)

**metallic hcp-Co also present at 2.6% (0.28)

Qualitative PXRD results of P25-supported catalyst the presence of anatase, rutile and Co_3O_4. No other phase was detected. Crystalline phase abundance analysis showed anatase as the major phase, followed by rutile and Co_3O_4. The cobalt oxide spinel concentration increased slightly from 11.7% for the catalyst calcined at 200°C up to 12.8% for the catalyst calcined at 300°C. The concentration then decreased to 10.7% for the highest calcination temperature.

The exothermicity of cobalt acetate decomposition may have come into play again in the high temperature calcination leading to a lower Co_3O_4 concentration. The catalysts calcined at 230°C and 370°C had Co_3O_4 concentrations of 12.5% and 11.9% respectively. It can be concluded, that overall, the P25-supported catalyst had similar Co_3O_4 concentration. Calcination temperature did not significantly alter the concentration of cobalt oxide spinel species.

Table 5. 4: Quantitative PXRD results of P25-supported catalysts

Sample	Anatase % (3σ error)	Rutile % (3σ error)	Co_3O_4 % (3σ error)	$CoTiO_3$% (3σ error)
P25 Support	83.5 (0.27)	16.5 (0.27)	-	-
Cat_P25_200	74.1 (0.18)	14.3 (0.14)	11.7 (0.13)	0
Cat_P25_230	73.6 (0.18)	13.9 (0.14)	12.5 (0.13)	0
Cat_P25_300	73.4 (0.17)	13.8 (0.13)	12.8 (0.13)	0
Cat_P25_370	74.4 (0.20)	13.8 (0.15)	11.9 (0.13)	1.8 (0.11)
Cat_P25_400	75.0 (0.17)	14.3 (0.13)	10.7 (0.12)	0

The PXRD results of Rutile-supported catalysts show an interesting phenomenon not seen in the Anatase- and P25-supported catalysts. Qualitative analysis revealed the presence of anatase, rutile, Co_3O_4 and $CoTiO_3$. Analysis of phase abundances showed that rutile was the major phase, followed by Co_3O_4 and $CoTiO_3$. The concentrations of Co_3O_4 spinel were 10.8%; 11.0%; 8.7%; 11.4% and 11.5% for catalysts calcined at 200°C, 230°C, 300°C, 370°C and 400°C respectively.

Table 5. 5: Quantitative PXRD results of Rutile-supported catalysts

Sample	**Anatase % (3σ error)**	**Rutile % (3σ error)**	**Co_3O_4 % (3σ error)**	**$CoTiO_3$ % (3σ error)**
Rutile Support	2.5 (0.27)	97.5 (0.27)	-	-
Cat_Rut_200	0.1 (0.44)	84.6 (0.45)	10.8 (0.15)	4.5 (0.20)
Cat_Rut_230	0.1 (0.48)	86.5 (0.32)	11.0 (0.16)	2.9 (0.40)
Cat_Rut_300	0.1 (0.35)	85.4 (0.36)	8.7 (0.15)	5.8 (0.14)
Cat_Rut_370	3.6 (2.37)	54.4 (0.40)	11.4 (0.79)	4.4 (0.41)
Cat_Rut_400	0.1 (0.19)	86.5 (0.30)	11.5 (0.32)	1.9 (0.28)

The phase abundance of $CoTiO_3$ ranges between ~2 – 6%. The concentrations were 4.5%; 2.9%; 5.8%; 4.4% and 1.9% for 200^{o}C; 230^{o}C; 300^{o}C; 370^{o}C and 400^{o}C calcinations respectively. It is clear from the PXRD results that the formation of $CoTiO_3$ was more favoured in Rutile-supported catalysts than Anatase- and P25-supported catalysts. The results show that the Co_3O_4 concentration of Rutile-supported catalysts is not significantly influenced by calcination temperature in the range between 200°C – 400°C.

5.2.1.1 Co_3O_4 crystallite size

The crystallite sizes of Co_3O_4 were determined from line broadening using volume-based column heights function L_{Vol}. The Co_3O_4 crystallite sizes for Anatase-supported catalysts increased gradually from 29 nm for the 200^{o}C calcination, up to 33 nm for the 300^{o}C calcination. The crystallite size decreased to 30 nm for the 370^{o}C calcination. The P25-supported catalysts showed a similar crystallite size of 29 nm for irrespective of the calcination temperature. The Rutile-supported catalysts also showed a constant Co_3O_4 crystallite size of 29 nm. Overall, the Co_3O_4 crystallite sizes were similar for all the TiO_2-supports and were within the size range reported in TEM results. The results are listed in Table 5.7.

Table 5. 6:Co_3O_4 crystallite size of titania supported catalysts at different calcination temperatures

Calcination Temp	Co_3O_4 crystallite size (nm)		
	(Anatase)	**(P25)**	**(Rutile)**
200	29	29	29
230	30	29	29
300	33	29	29
370	30	29	29
400	-*	29	29

* No Co_3O_4 detected

The results in Table 5.6 show that calcination temperature in the range between 200°C – 400°C does not influence the Co_3O_4 crystallite size. This observation is the same for all titania supports studied. It can also be seen that the titania phase does not influence the Co_3O_4 crystallite size This is evident when one looks at catalysts calcined at the same temperature as shown in Table 5.7. For catalysts calcined at 300°C, the crystallite sizes are similar across all the supports. This is in agreement with TEM measurements.

Table 5. 7: Co_3O_4 crystallite sizes across the different titania supports

Catalyst	Co_3O_4 crystallite size (nm)	Sigma (nm)
Cat_Anat_300	33	4.8
Cat_P25_300	29	2.2
Cat_Rut_300	29	3.2

Shimura *et al*, (2013 p.10) also observed no effect of the support crystalline phase, surface area and support pore size on the Co_3O_4 crystallite size. Sun *et al*, (2012 p.56) however observed an increase in the Co_3O_4 crystallite size in $ZrO_2/\gamma\text{-}Al_2O_3$ supported catalysts calcined at a temperature range from 250°C – 600°C. They reported a size increase from 16.4 nm up to 19.2 nm. They attributed the size increase to aggregation or sintering of Co_3O_4 crystallites.

Song *et al*, (2009 p.235) observed the effect of calcination temperature on Zr/SiO_2 supported cobalt catalysts. They reported Co_3O_4 crystallite size ranging from 30.8 nm – 35.5 nm. Their interesting observation was the actual crystallite size trend with calcination temperature. The crystallite size decreased to a minimum of 30.8 nm, starting from 35.5 nm. The size then increased to 34.5 nm, showing an inverse v-shape with increasing calcination temperature from 128^{o}C to 600^{o}C.

Looking at the studies of Shimura *et al*, (2013), Sun *et al*, (2012), Song *et al*, (2009) and our study, it is important to take note of the type of support and calcination temperature range for us to conclude on the effect of calcination temperature on Co_3O_4 crystallite size. The supports used in the above studies were TiO_2, ZrO_2/γ-Al_2O_3 and Zr/SiO_2 respectively. It is clear from the studies that the effect of calcination temperature was observed in Al_2O_3 and SiO_2 supported catalysts. No effect was observed in TiO_2-supported catalysts.

This phenomenon can be attributed to the interaction of Co_3O_4 species with the support. It is known that different supports interact differently with cobalt species (Storsæter *et al*, 2005 pp. 139 – 152; Bartholomew 1985 p. 56 – 61). Therefore, it can be inferred that the absence of the effect of calcination temperature in the range between 200^{o}C – 400^{o}C is due to the interaction of Co_3O_4 with TiO_2. In this case, the TiO_2 interacts strongly with Co_3O_4 crystallites thereby preventing aggregation or sintering of Co_3O_4 crystallites. In another scenario, the calcination temperature range used in our study may be too low to see any effect on Co_3O_4 crystallites. The oxide may just be too stable to be influenced into aggregation or sintering.

5.2.2. TEM

TEM analysis of the titania-supported catalysts calcined at 300^{o}C revealed the size of the cobalt oxide crystallites. The results also revealed the dispersion of the cobalt oxide species. Energy dispersive X-ray (EDX) mapping was used to distinguish between the cobalt oxide and titania species in the catalysts. The EDX maps were superimposed onto high angle annular dark field-scanning transmission electron microscopy (HAADF-STEM) images. The crystallite size of cobalt oxide species was determined by counting particles either from HAADF-STEM images and/or HAADF-STEM-EDX mapping images.

The results of Anatase-supported catalyst given in Figure 5.7 show particles with a size ranging from 5 – 40 nm with a mean particle size of 17.1. The goodness of fit test showed that the distribution follows a lognormal distribution. The particles appear to be well dispersed on the Anatase-support. However, some degree of agglomeration is evident from the images. The results of P25-supported given in Figure 5.8 show slightly larger particles of cobalt oxide than those seen in Anatase-supported catalysts. The particle size ranges from 5 – 70 nm with a mean of 32.7 nm. The particle size of these cobalt oxide species also follows a lognormal distribution. The dispersion was shown to be similar to that of Anatase-supported cobalt particles.

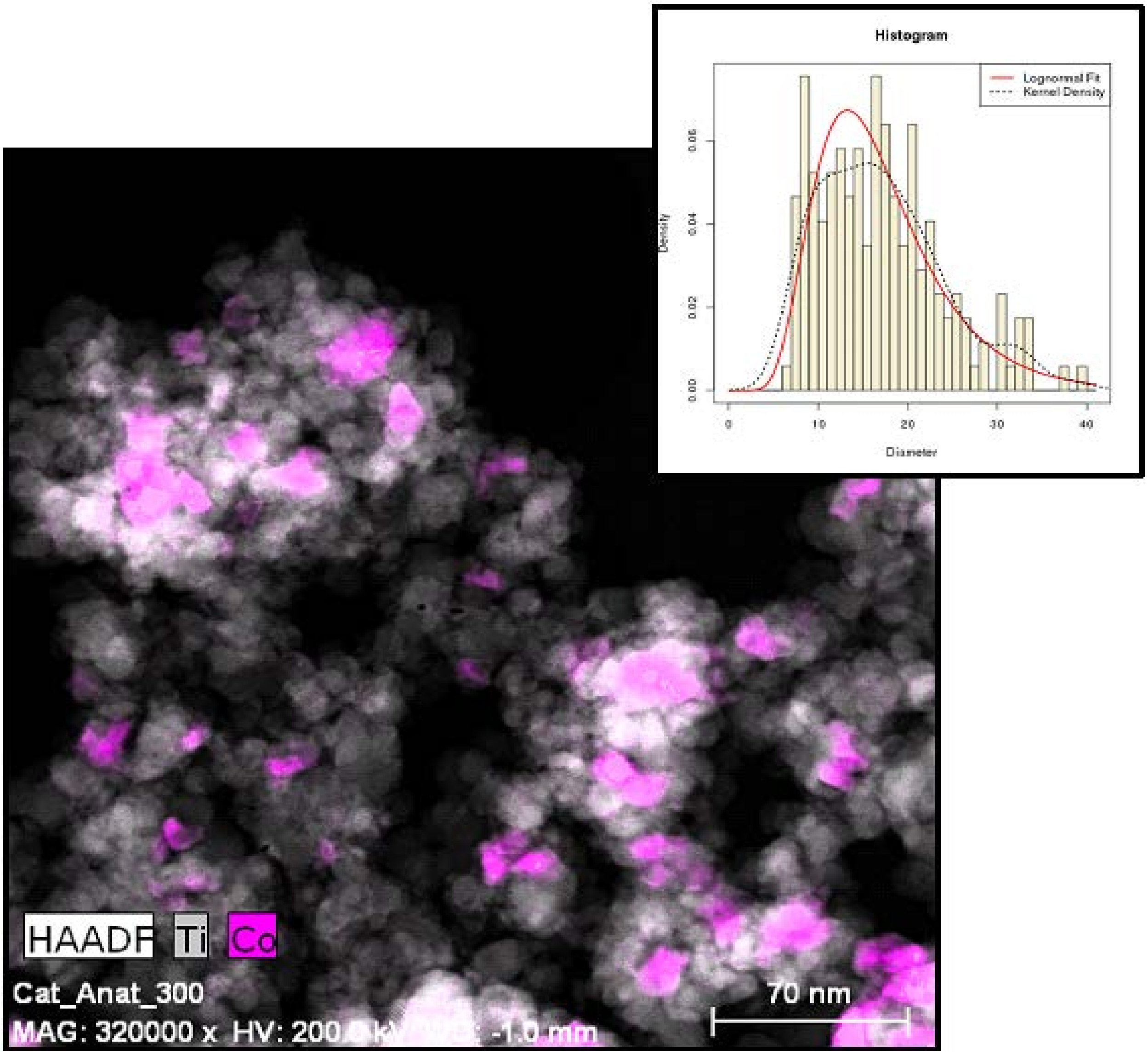

Figure 5. 7: EDX mapping super-imposed onto a HAADF-STEM image of Cat_Anat_300

The cobalt oxide particles supported in Rutile-support given in Figure 5.9 showed interesting characteristics. In the case of size, it was shown that the particle size ranged from 5 – 40 nm with a mean of 19.2 nm. The crystallites appear to have a hexagonal shape. Some particles appear to be hollow. It is not clear what could be causing the different morphology compared to the previous supports. The cobalt oxide particle size distribution showed a somewhat bimodal distribution. The goodness of fit test showed that the distribution did not follow a lognormal distribution.

The dispersion was shown to be similar to the previous catalyst samples. The Co_3O_4 particles are mostly located on the edge of large rutile particles. Similar observations were reported by Storsæter *et al*, (2005 p.146). The authors reported Co_3O_4 crystallite size ranging between 30 – 80 nm and were located on the edges of titania grains. Overall, the crystallite size results show the effect of the support. One property of the support that might influence the crystallite size is the porosity.

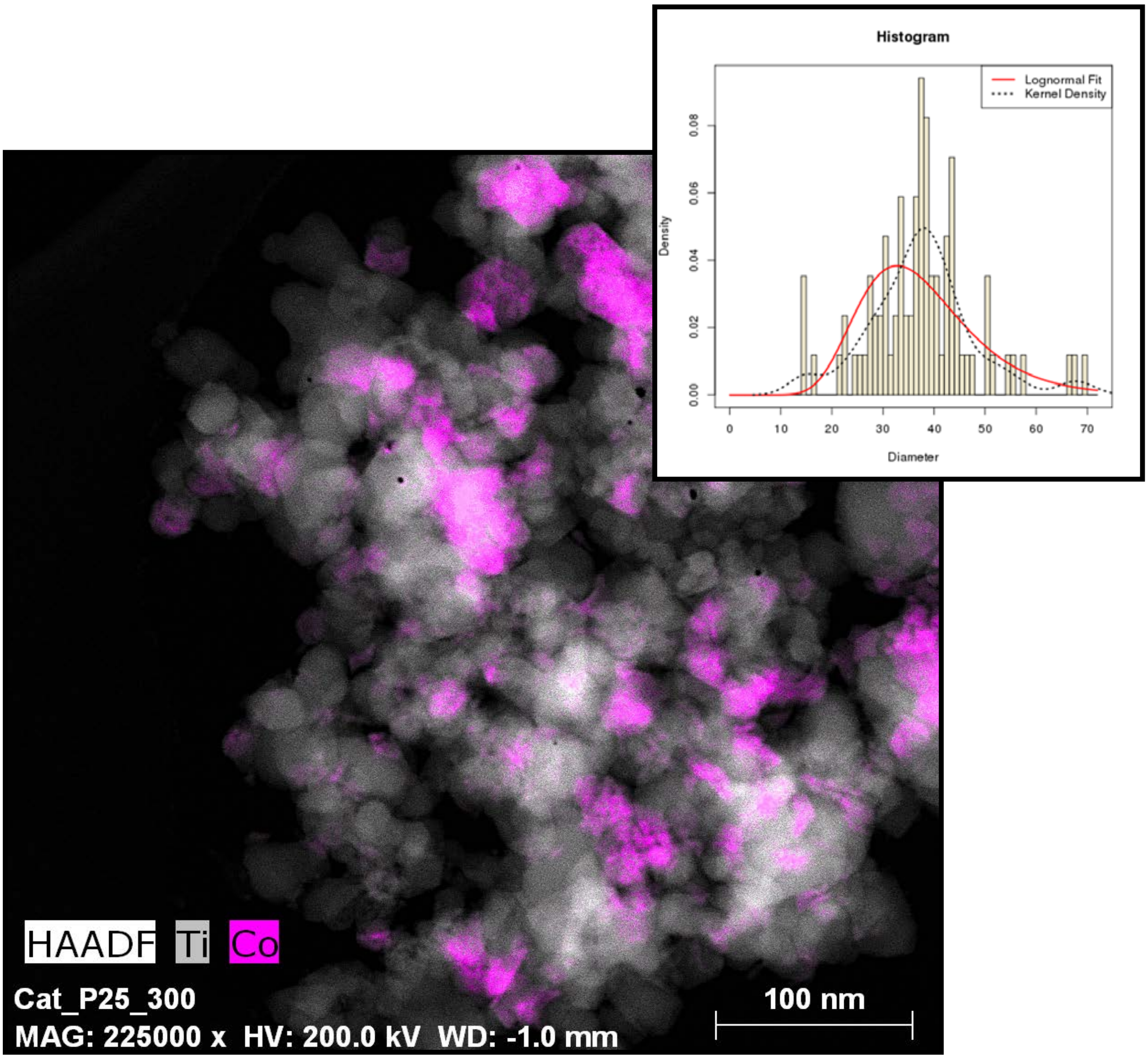

Figure 5. 8: EDX mapping super-imposed onto a HAADF-STEM image of Cat_P25_300

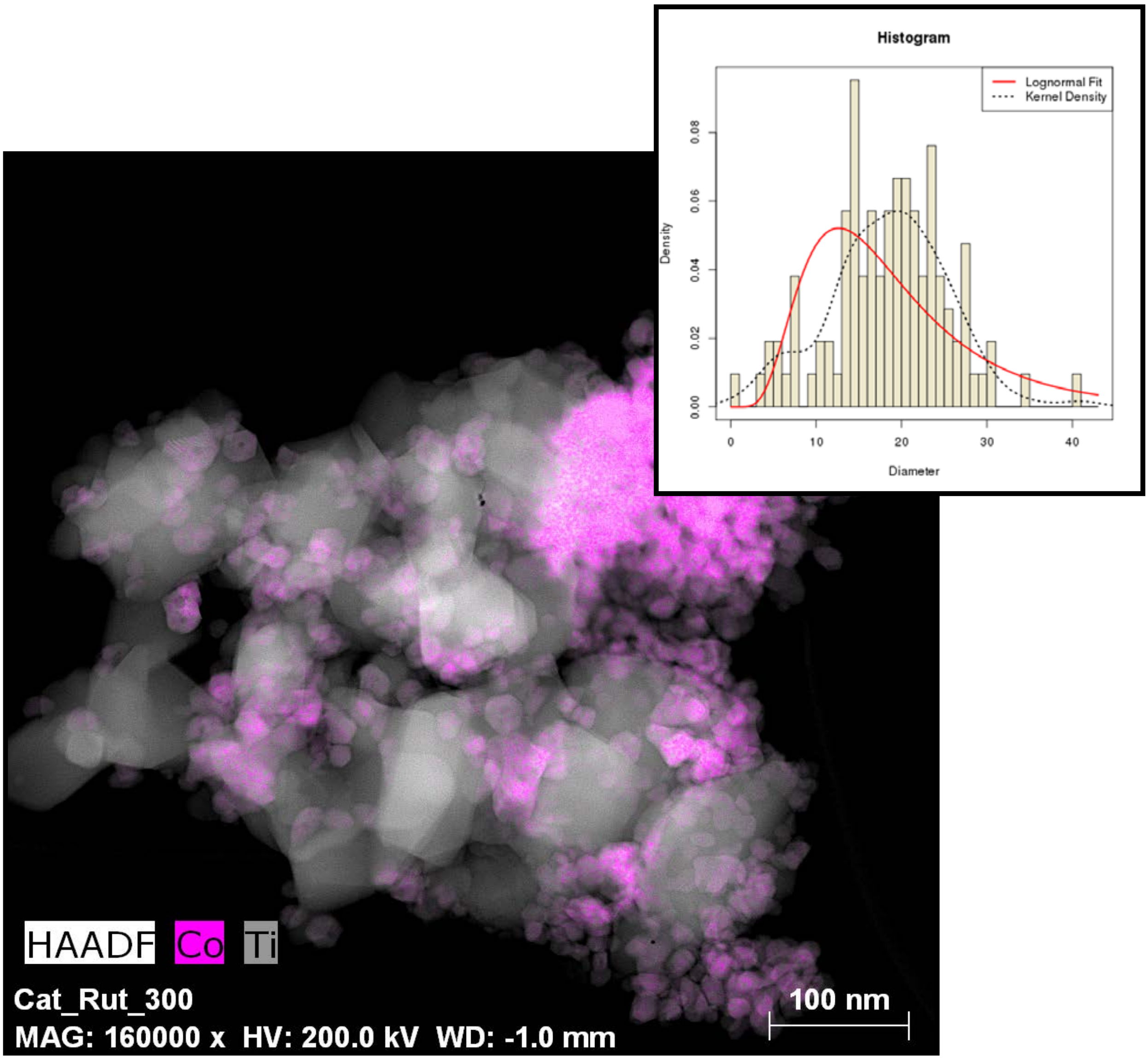

Figure 5. 9: EDX mapping super-imposed onto a HAADF-STEM image of Cat_Rut_300

5.2.3. BET Surface Area and Pore Size Distribution

The surface area and pore size distribution results of the titania supported catalysts after calcination at different temperatures are given in Figure 5.10 and Figure 5.11 respectively. The results of anatase-supported catalysts show an initial decrease in surface area for calcined catalysts when compared to the bare support. The surface area of anatase-supported catalysts decrease by up to 51% upon impregnation with cobalt acetate and calcination.

The observed surface area decline may be attributed to the blockage of pores as a result of the cobalt acetate solution entering the particle and filling pores. Upon calcination, the cobalt oxide species formed from cobalt acetate may block small pores and decrease the surface area of the catalysts (Zhao *et al*, 2003 p.733). The calcined anatase-supported catalysts show a surface area that is similar and is within the measurement uncertainty of the technique.

The surface area of P25-supported catalysts was not significantly influenced by the cobalt acetate impregnation and calcination step. The results are similar for all the calcination temperatures. The surface area of rutile-supported catalysts was not affected by the impregnation and calcination steps. The results are similar for the bare support and catalysts calcined at different temperatures. This might be due to the low loading of cobalt.

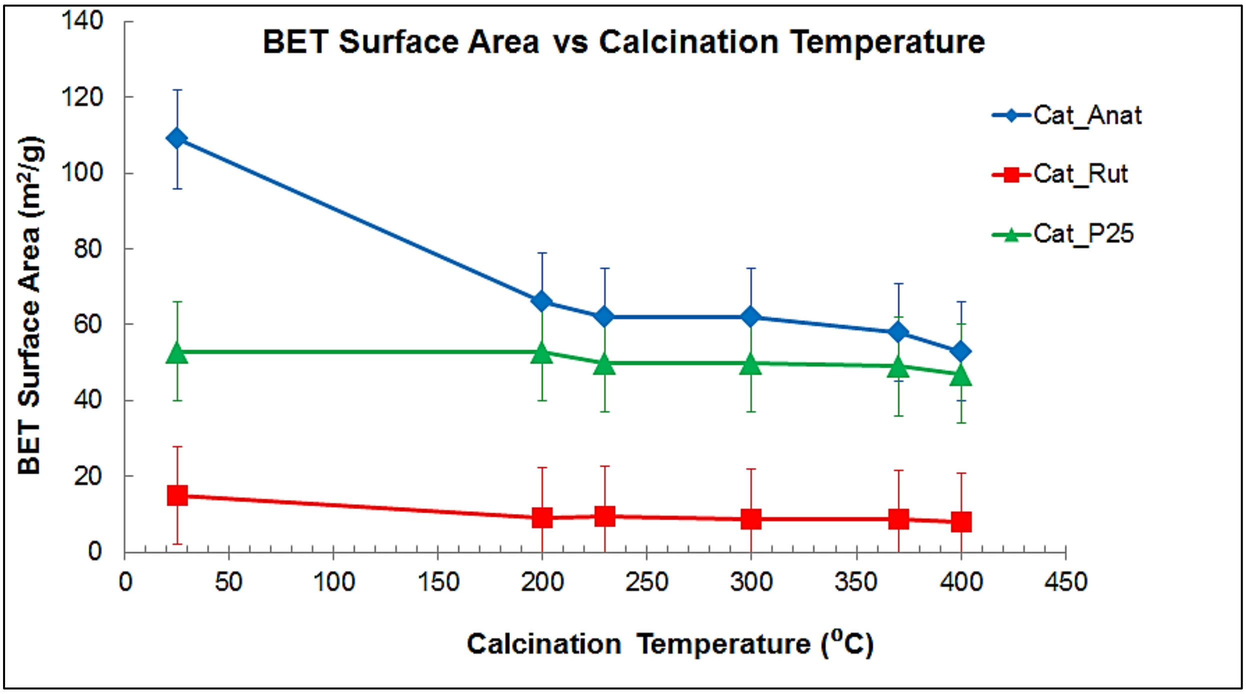

Figure 5. 10: Surface area results of titania supports and calcined catalysts plotted against calcination temperature.

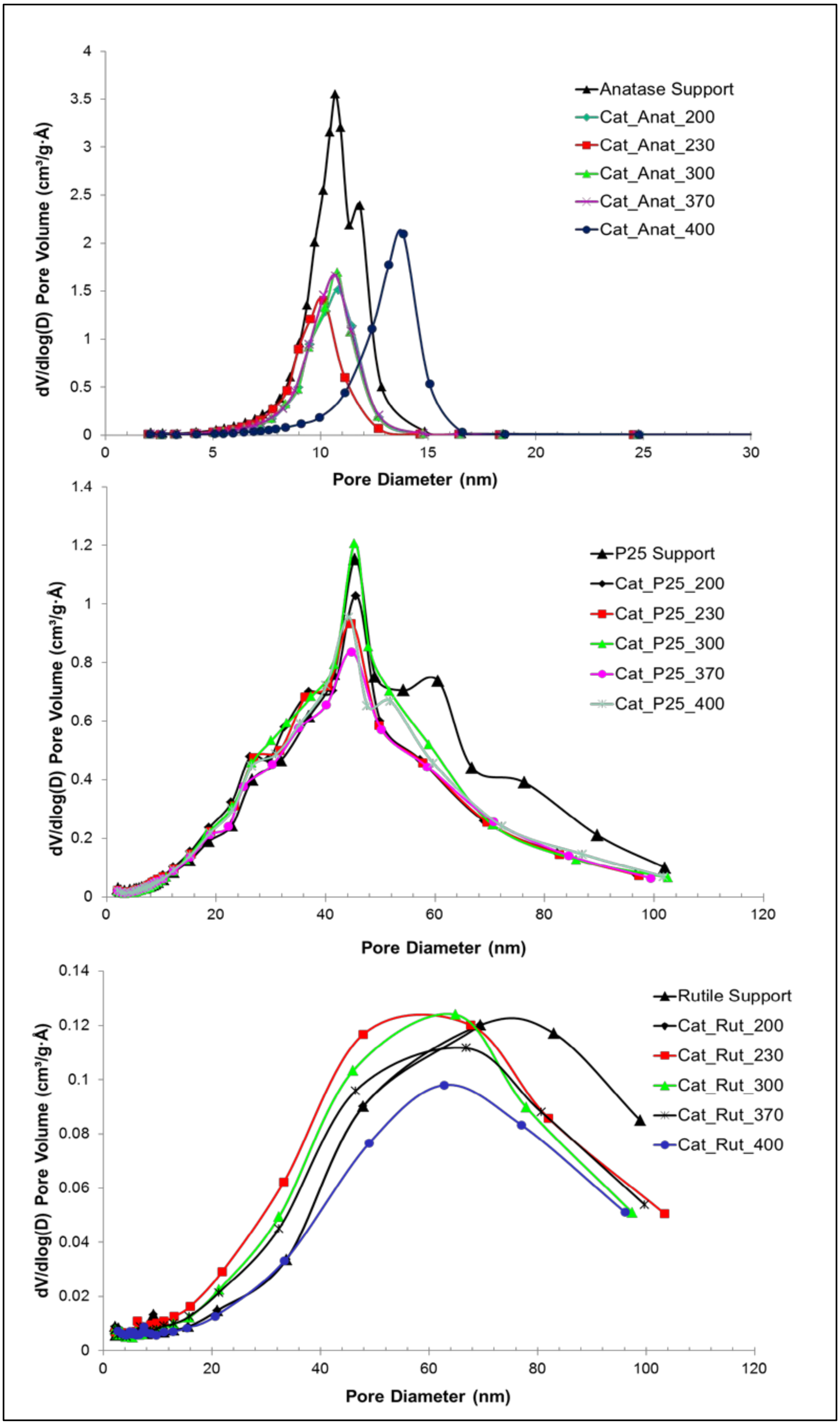

Figure 5. 11: Pore size distribution results of titania supports and calcined catalysts showing pore size characteristics.

The pore size distribution results of the titania-supported catalysts are given in Figure 5.11. The pore size distribution of Anatase-supported catalysts correlate with the surface area results, in that there is a gradual shift towards the larger pore sizes with increasing calcination temperature. The pore-size distribution of P25-supported catalysts did not change with impregnation and calcination. The results of Rutile-supported catalysts showed a slight shift towards larger pore sizes. Overall, the pore size distribution of the titania-supported catalysts did not change significantly with impregnation and calcination. Therefore it can be concluded that calcination in air at a temperature range between 200^{o}C – 400^{o}C does not significantly affect the pore structure of the present titania-supported catalysts.

5.2.4. Raman Spectroscopy

Anatase TiO_2 has six Raman active modes. These are A_{1g} + $2B_{1g}$ + $3E_g$ (Orendorz *et al,* 2007). The characteristic vibrations for Anatase occur at 141 cm-1 (E_g), 194 cm-1 (E_g), 396 cm-1 (B_{1g}), 513 cm-1 (A_{1g}), 519 cm^{-1} (B_{1g}) and 637 cm-1 (E_g).Rutile TiO_2 has four Raman active modes. These are A_{1g} + B_{1g} + B_{2g} + E_g (Yoshitake & Abe 2009 p.273). The bands for Rutile occur at 143 cm^{-1} (B_{1g}), 243 cm^{-1} (B_{2g}), 447 cm^{-1} (E_g) and 612 cm^{-1} (A_{1g}). Cobalt oxide spinel (Co_3O_4) has five Raman active modes which are A_{1g}, E_g and $3F_{2g}$. These bands occur at 192 cm^{-1} (F_{2g}), 482 cm^{-1} (E_g), 521 cm^{-1} (F_{2g}), 618 cm^{-1} (F_{2g}) and 691 cm^{-1} (A_{1g}) (Hadjiev *et al,*, 1988).

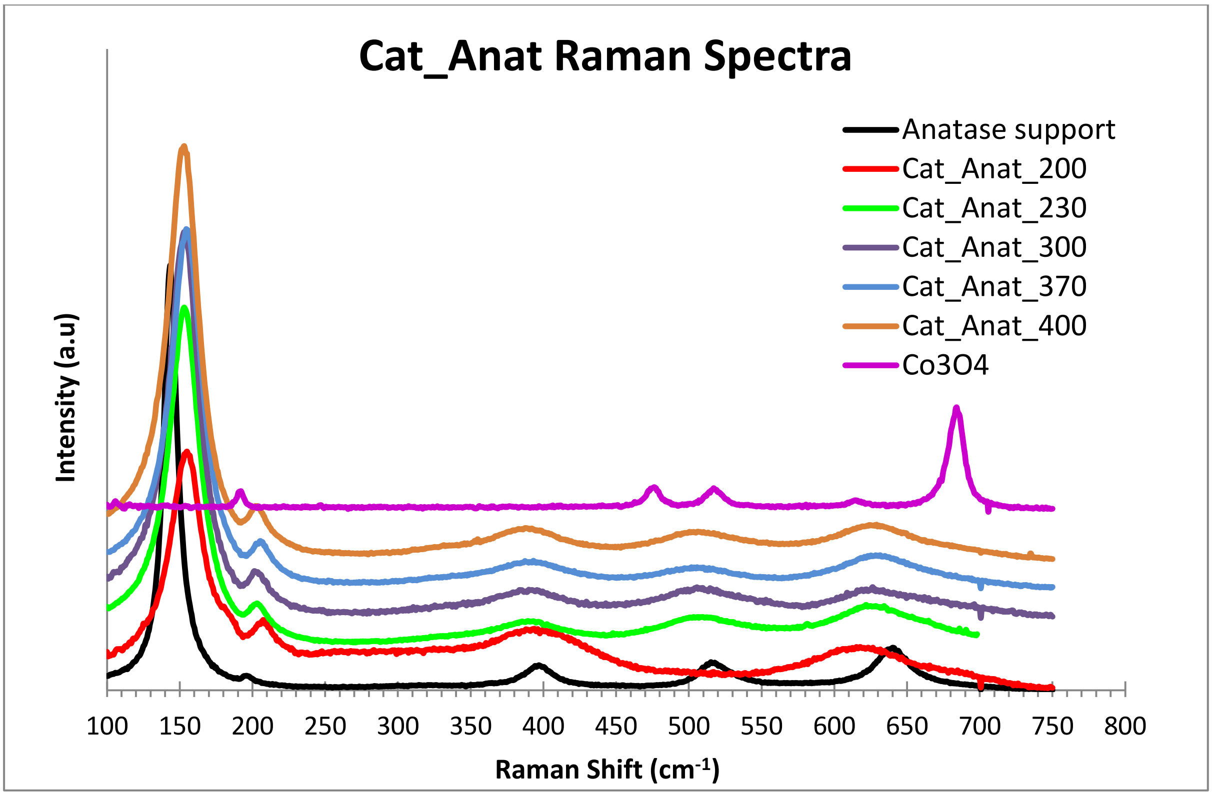

Figure 5. 12: Raman Spectra of Anatase-supported catalysts showing characteristic bands.

The Raman spectra of Anatase-supported catalysts are shown Figure 5.12. The spectra are compared with that of Anatase support and unsupported Co_3O_4. The spectrum of Anatase support shows characteristic anatase bands at 142 cm^{-1}, 192 cm^{-1}, 394 cm^{-1}, 514 cm^{-1} and 634 cm^{-1}. The catalysts also show the broadened anatase bands, albeit some are shifted. The high frequency E_g band of anatase shows a blue-shift and is observed at 152-154 cm^{-1} for all Anatase-supported catalysts. The peak shift is illustrated in Figure 5.13.The low frequency $2B_{1g}$ and E_g bands are red-shifted to lower wavenumbers of 382-388 cm^{-1}, 498-502 cm^{-1} and 614-624 cm^{-1} respectively. The strong Co_3O_4 band at 682 cm^{-1} was not observed in all Anatase-supported catalysts. The Raman bands of the Anatase-supported catalysts also show broadening when compared to the bare support. The broadening is also accompanied by loss of intensity. The broadening is particularly significant in the lower frequency bands of anatase.

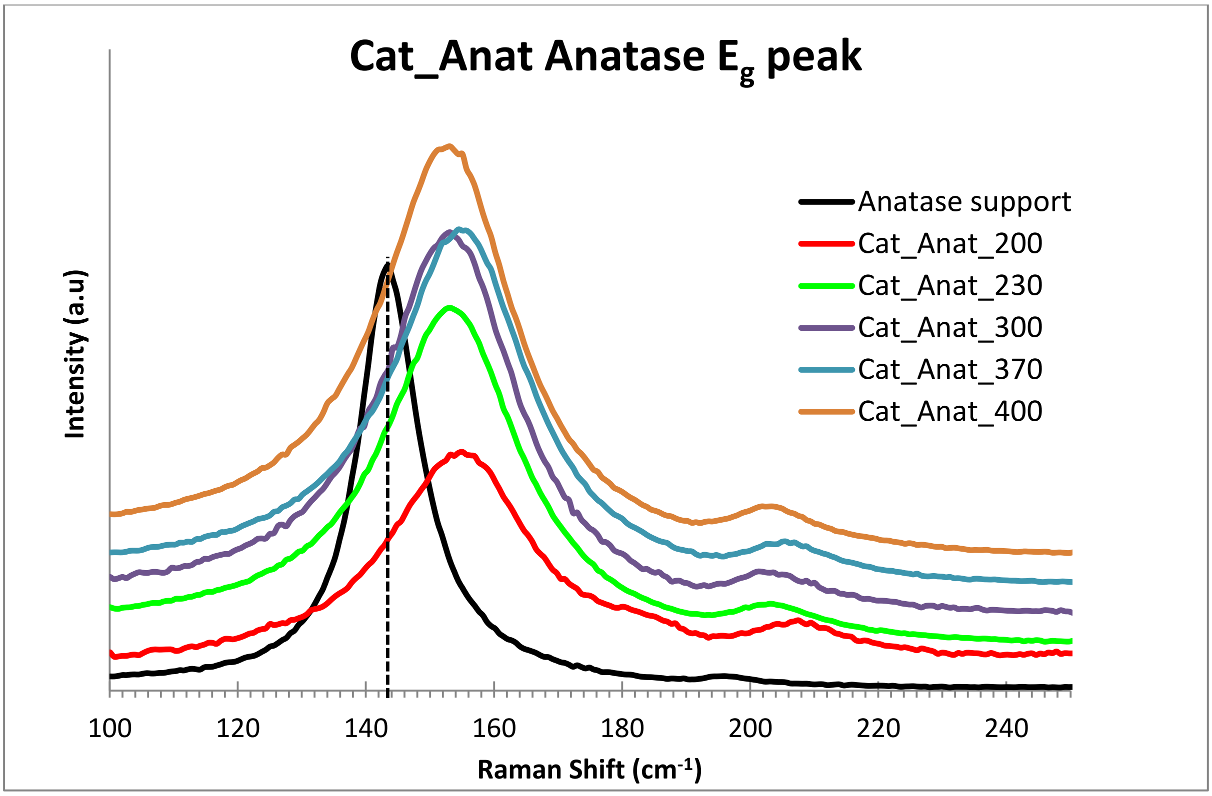

Figure 5. 13: Raman spectra of Anatase-supported catalysts showing the anatase E_g band

The Raman spectra of P25-supported catalysts showed the characteristic anatase bands similar to those seen in Anatase-supported catalysts. The anatase high frequency E_g band in P25-supported catalysts was also blue-shifted to higher wavenumbers. The band can be seen at 150-152 cm^{-1}. The lower frequency bands were also red-shifted towards lower frequencies. The Raman bands of the catalysts are significantly broadened compared to the bare P25-support. A broad band at higher frequencies of ~672 cm^{-1} is present in all the P25-supported catalysts. This broad band may be explained as a red-shifted Co_3O_4 A_{1g} mode. This band was not seen in Anatase-supported catalysts. The Raman spectra of P25-supported catalysts are shown Figure 5.14 and Figure 5.15.

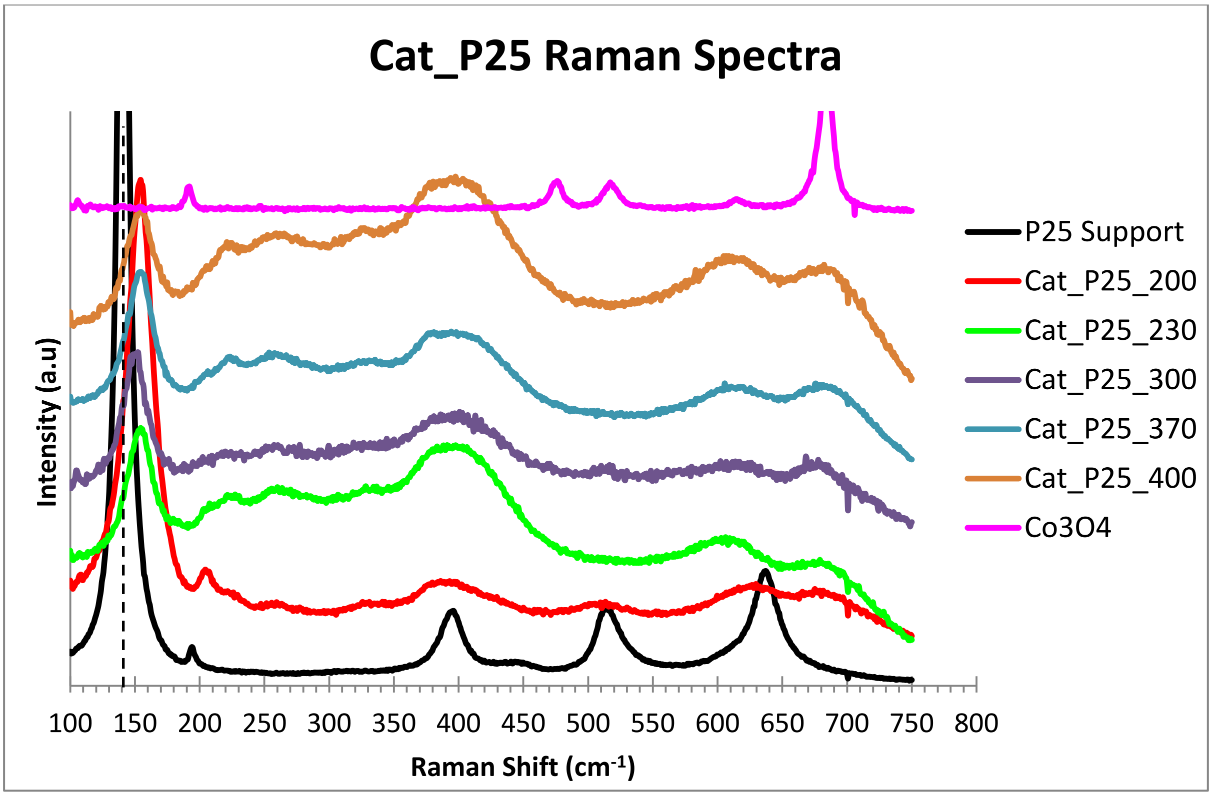

Figure 5. 14: Raman spectra of P25-supported catalysts

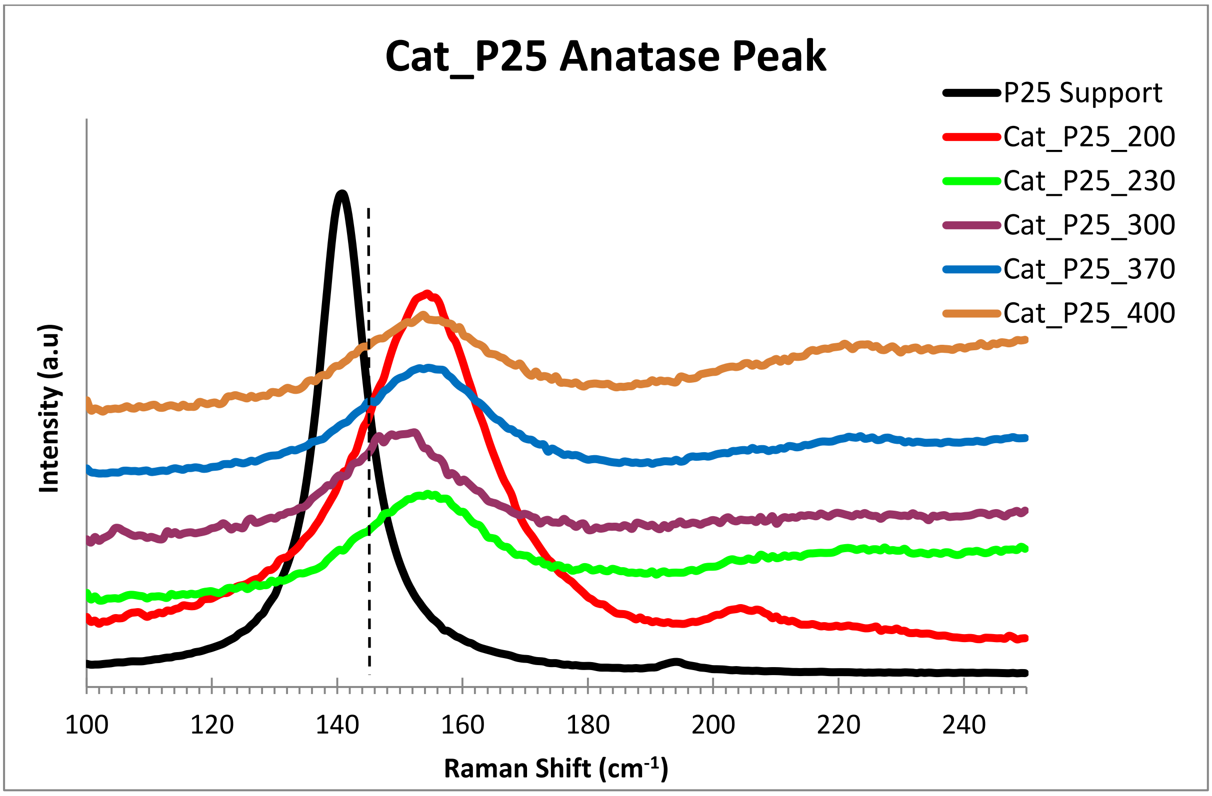

Figure 5. 15: Raman spectra of P25-supported catalysts showing the anatase E_g band

The Raman spectra of Rutile-supported catalysts are shown in Figure 5.16. The spectra show different characteristics to that of the bare support. The catalysts show bands at frequencies of 220 cm^{-1}, 251 cm^{-1}, 320 cm^{-1}, 365 cm^{-1}, 365 cm^{-1} and 695 cm^{-1}. These bands are similar in all catalysts calcined at different temperatures. It is important to note that the bands observed in the calcined Rutile-supported catalysts do not correspond to either rutile TiO_2 or Co_3O_4 bands. However, the broad band at 650 – 750 cm^{-1} may also include contributions from the A_{1g} band of Co_3O_4. This band usually occurs at a frequency of 691 cm^{-1}. There is no clear trend in terms the position and intensity of the bands. Therefore there is no clear influence of calcination temperature on the Raman spectra of Rutile-supported catalysts.

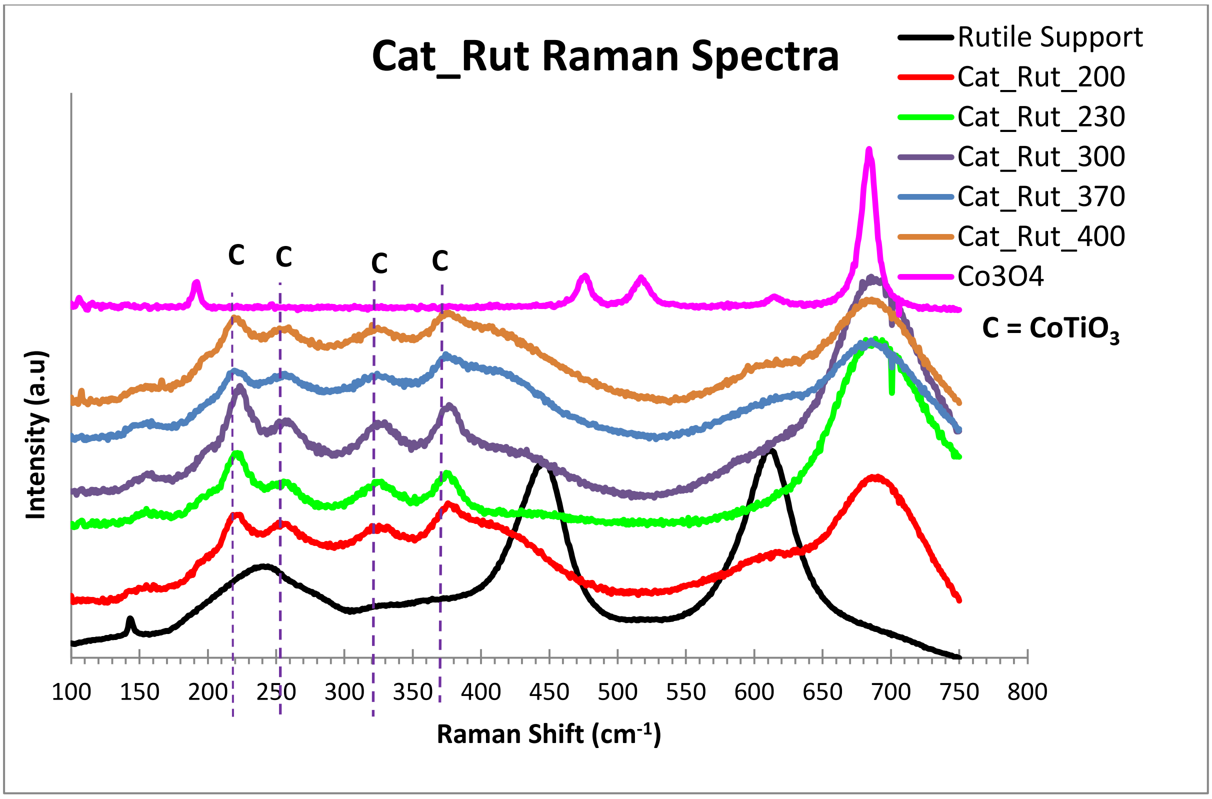

Figure 5. 16: Raman spectra of Rutile-supported catalysts showing characteristic bands.

The bands observed in Rutile-supported may be attributed to the presence of $CoTiO_3$ phase in these catalysts. It has been shown that $CoTiO_3$ has 10 characteristic Raman bands. These usually occur at frequencies of 208, 238, 267, 336, 383, 456, 478, 520, 604 and 696 cm^{-1} (Zhou *et al*, 2006 p.372; Sharma *et al*, 2009 pp.581 – 582) The Raman spectra are in agreement with XRD results which showed the presence of $CoTiO_3$ in Rutile-supported catalysts.

Raman spectra of Anatase-supported catalysts show peak shifts and broadening. The high frequency anatase E_g band was blue-shifted to higher wavenumbers of ~152 cm^{-1}, while the lower frequency bands were red-shifted to lower wavenumbers. The wavenumber shift has been linked to the nature of bond deformation (Gouadec & Colomban 2007:34). The interaction with cobalt ions may lead to defect formation and possible formation of oxygen vacancies as a result of substitution of Co^{2+} ions into the TiO_2 lattice. The blue-shift may point toward compressive strain experienced by the TiO_2 lattice due to interaction with cobalt ions. The red-shift may indicate tensile strain associated with the weakening of the Ti-O-Ti bonds (Santara*et al,*, 2011)

The disorder generated in the TiO_2-lattice of Anatase-supported catalysts is also evident in the peak broadening observed in Raman spectra. Kaushik*et al,,* (2013) have shown that the band broadening results from the loss of periodicity in the TiO_2 lattice as a result of cobalt substitution. Minh (2008) also observed an increase in the FWHM of Raman bands as a result of cobalt substitution and generation of oxygen vacancies.

Stage 3 – Catalyst Reduction

5.3. STAGE 3 - CATALYST REDUCTION

5.3.1. XRD

The crystallite sizes of metallic cobalt in the different titania-supported catalysts are listed in Table 5.8. It is known that there is volume decrease when going from Co_3O_4 to metallic cobalt. Ronning *et al*, (2010 p.292) have shown that there is a relationship between the Co_3O_4 crystallite size and Co^0 size. This relationship was derived from the cell volume and crystallite diameter, assuming spherical crystallite shape. Given the cell volume per cobalt atom as 11.12 Å^3/Co and 21.858 Å^3/Co for Co^0 and Co_3O_4 respectively, the relationship between their respective diameters is given by:

$$\boldsymbol{d_{(Co^0)} = 0.80 d_{(Co_3O_4)}}$$ **Equation 5. 1**

The crystallite size of cubic cobalt in anatase-supported catalyst obtained from the full pattern refinement using Rietveld refinement was found to be 36 nm. This shows a slight increase in size when compared to the Co_3O_4 crystallite size, which was shown to be 33 nm. The crystallite size of cubic cobalt in P25-support was found to be 28 nm. This value is equal to the Co_3O_4 crystallite size observed in the calcined catalyst. The larger-than-expected metallic crystallite size observed in anatase- and P25-supported catalysts may indicate early signs of sintering of cobalt during reduction.

Table 5. 8: XRD measured crystallite sizes of Co_3O_4 and Co^0 in the titania-supported catalysts

Catalyst	Crystallite Size			
	Co_3O_4 (nm)	Sigma (nm)	fcc Co^0 (nm)	Sigma (nm)
RP_Cat_Anat_300	33	4.8	36	6.2
RP_Cat_P25_300	29	2.2	28	1.1
RP_Cat_Rut_300	29	3.2	19	7.2

The crystallite size of cubic cobalt in Rutile-supported catalyst calculated was found to be 19 nm. The size is more-or-less equal to the theoretical value which is 20% smaller than the oxide size as described by Ronning *et al*. On comparing the metallic crystallite size across the titania supports, it can be seen that rutile-supported crystallites are the smallest followed by P25 and anatase crystallites. The order is as follows: anatase > P25 > rutile.

5.3.2. High Temperature XRD

The reduction of cobalt oxide in the titania-supported catalysts was also studied by in situ XRD. The diffractograms of Anatase- and Rutile-supported catalysts are displayed in Figure 5.17 and Figure 5.19 respectively. The diffractograms show that Co_3O_4 is reduced in two stages. These are $Co_3O_4 \rightarrow CoO \rightarrow Co^0$. The two-step reduction was similar in both supports, albeit with slight differences in reduction temperatures. Both fcc and hcp metallic cobalt were observed in the anatase- and rutile-supported catalysts (du Plessis *et al*, 2013 p.11642). An interesting observation was that there are different fcc/hcp ratios in the titania supports. A peculiar observation was that only fcc cobalt could be detected in P25-supported catalyst. This was shown in the XRD analysis of reduced and passivated catalysts. The absence of this cobalt phase is currently not understood and needs further investigation.

The reduction of Co_3O_4 to CoO in the Anatase – supported catalyst starts at 200°C and is confirmed by the disappearance of the diffraction line at 36,5°2θ. The evolution of CoO was confirmed by the appearance of the line at 49.8°θ. Co_3O_4 was completely reduced at 260°C, with the disappearance of the diffraction line at 36,5°2θ and 69°2θ. The gradual disappearance of the diffraction line at 49.8°2θ signalled the reduction of CoO to metallic cobalt. Metallic cobalt was detected at 300°C and was confirmed with the appearance of the diffraction line at 52°2θ. CoO was completely reduced to metallic cobalt at 340°C.

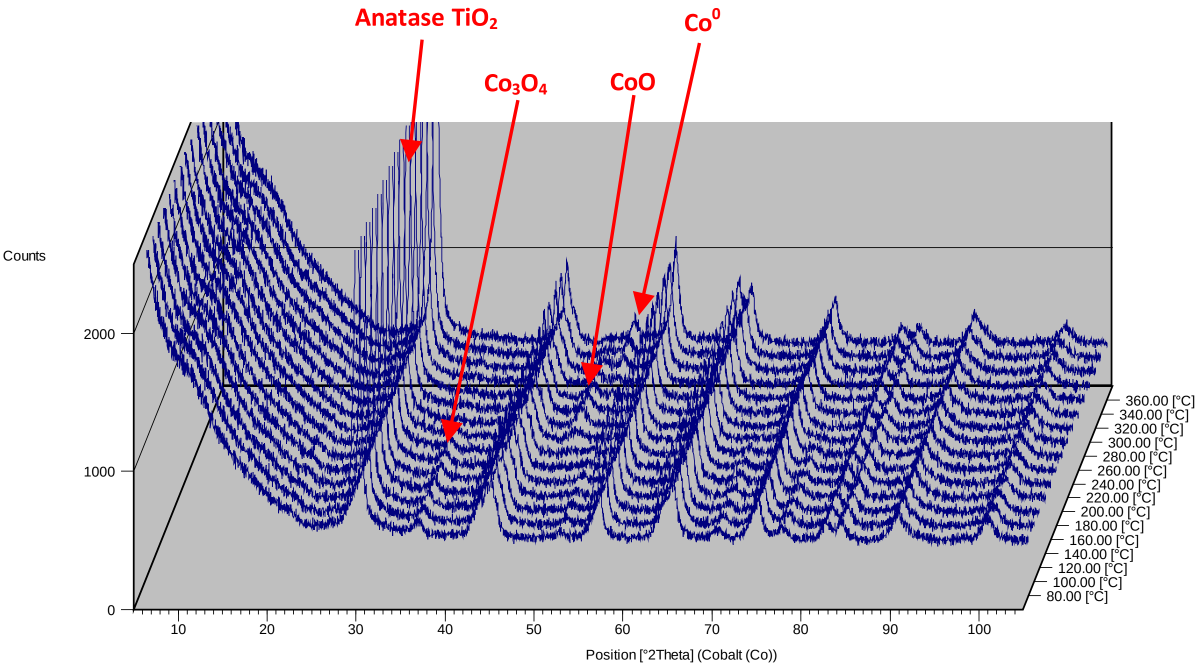

Figure 5. 17: High temperature XRD diffractograms of Anatase-supported catalysts

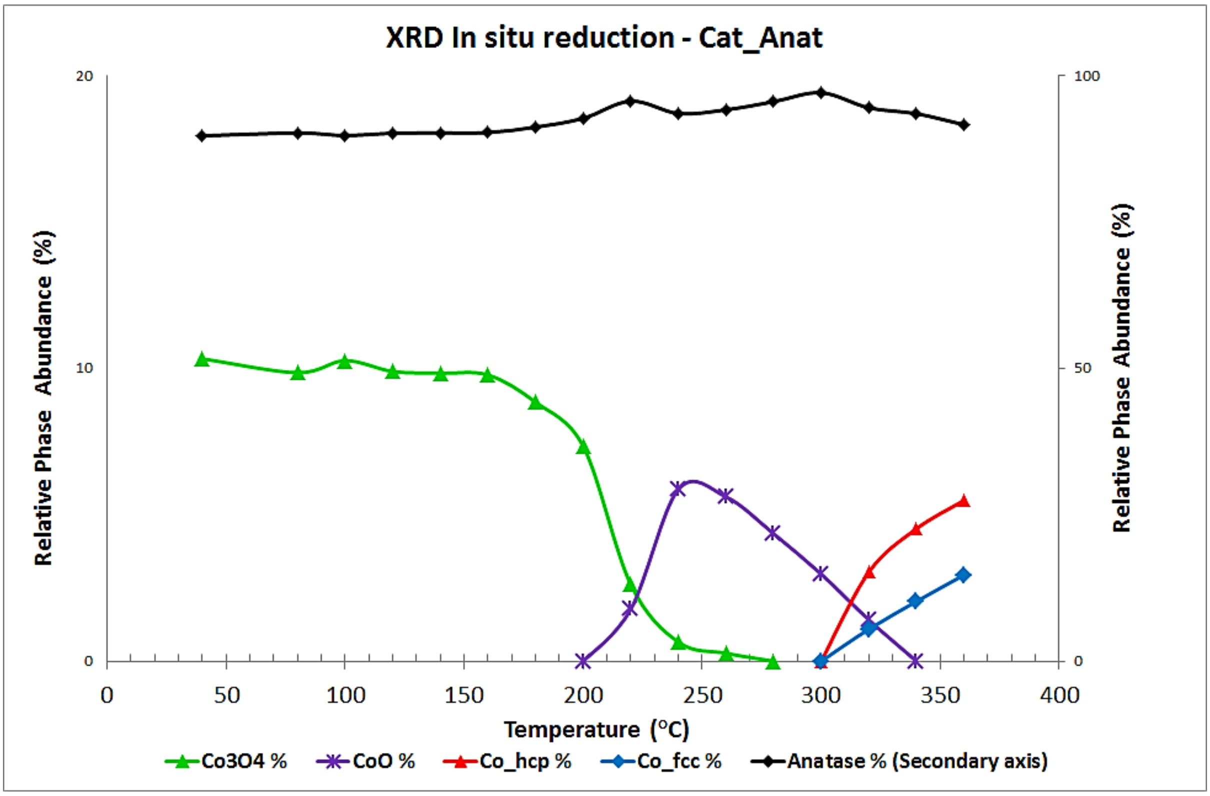

Figure 5. 18: High temperature XRD relative phase abundances of Anatase-supported catalysts

The starting crystallite size of Co_3O_4 was 8 nm. The crystallite size gradually decreased to 6 nm as the spinel phase was reduced to CoO. The crystallite size of CoO ranged between 8 – 9 nm. The starting sizes of fcc Co and hcp Co were 9 and 5 nm respectively. These increased to 17 and 7 nm respectively This size increase indicates early signs of sintering of metallic cobalt species in the titania-supported catalyst.

The reduction of Co_3O_4 to CoO in the Rutile – supported catalyst starts at 180°C confirmed by the disappearance of the diffraction line at 23°2θ, 37°2θ and 69°2θ. The evolution of CoO was confirmed by the appearance of the diffraction line at 52°2θ. Co_3O_4 was completely reduced at 220°C. The reduction of CoO to metallic cobalt started at 240°C with the appearance of the diffraction line at 78°2θ. CoO was completely reduced to metallic cobalt at 360°C. The relative abundance of $CoTiO_3$ decreased gradually throughout the reduction, decreasing by ~50% from the start of the experiment.

The starting average crystallite size of Co_3O_4 in Rutile – supported was found to be 10 nm. This size increased to 19 nm as the spinel phase got depleted. The starting crystallite size of CoO was 4 nm. The size increased to 7 nm as the rocksalt phase got depleted. The starting crystallite sizes of metallic cobalt fcc and hcp were 9 nm and 6 nm respectively. The crystallite sizes decreased to 6 nm and 4 nm respectively. The decrease in average crystallite size of metallic species may indicate something about the metal-support interaction. In this case, the strong metal-support interaction may stabilize the metallic species and prevent sintering.

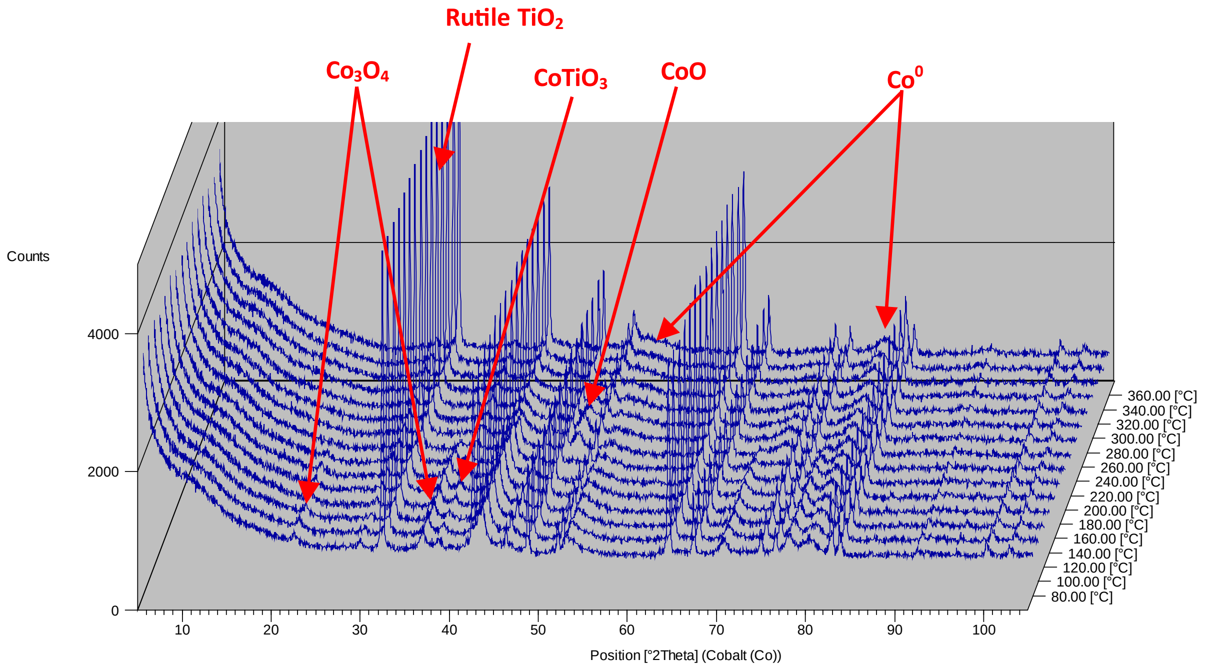

Figure 5. 19: High temperature XRD diffractograms of Rutile-supported catalysts

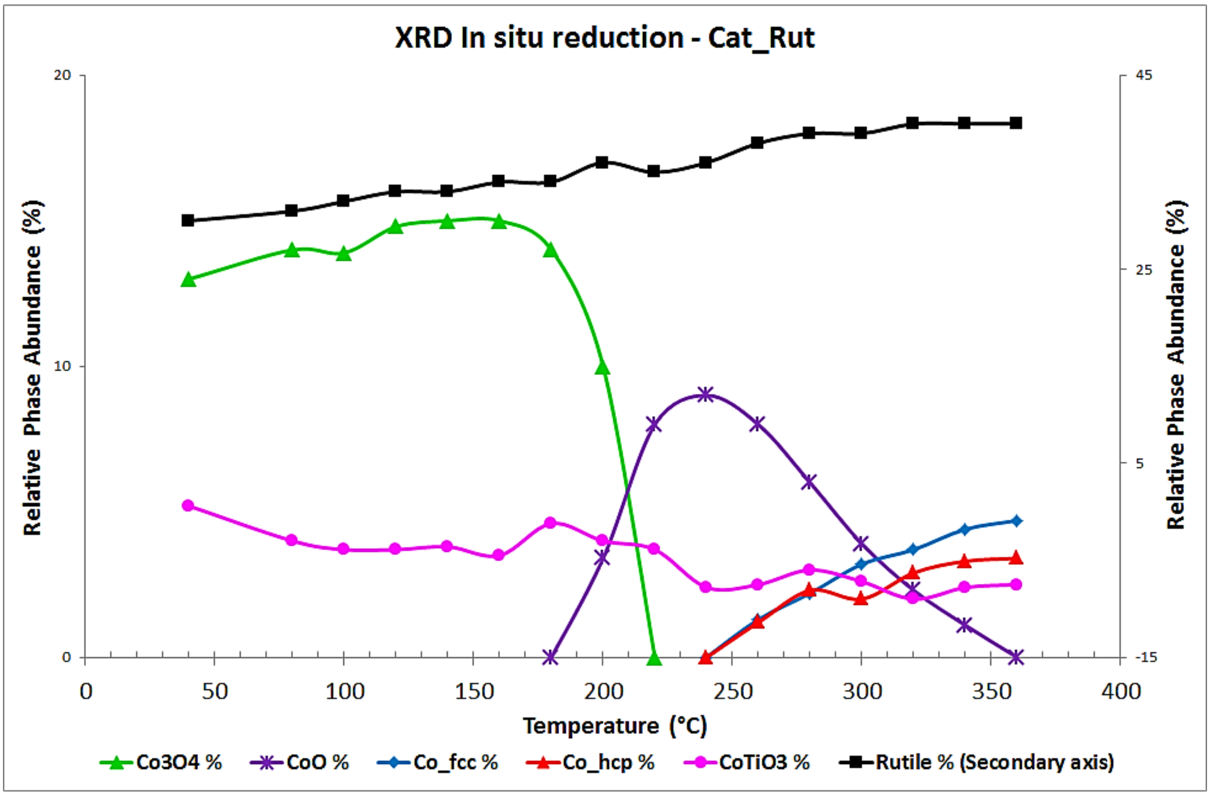

Figure 5. 20: High temperature XRD relative phase abundances of Rutile-supported catalysts

The quality of data fitting in Rietveld refinement is always of importance. For Anatase-supported catalyst, the average R_{wp} for 15 scans was 5.17% with a standard deviation of 0.1%. The average χ^2 was found to be 1.20 with a standard deviation of 0.02 was observed. For Rutile-supported catalyst, the average R_{wp} for 15 scans was found to be 4.5% with standard deviation of 0.29%. The average χ^2 was found to be 1.3 with a standard deviation of 0.28. These values indicate an adequate fit of the data. Du Plessis *et al*, (2013 p.11644) reported an R_{wp} value of 7.1 for their results. Karaca *et al*, (2010 p.789) reported an R_{wp} value less than 12 for their data fitting.

The XRD results of Anatase- and Rutile-supported catalysts show slightly different reduction behaviour of cobalt species. It was shown that Co_3O_4 reduction starts at a slightly lower temperature (180°C) in Rutile-supported catalyst when compared to the Anatase-supported catalyst (200°C). The reduction of CoO to metallic cobalt also occurs at lower temperature in Rutile-supported catalyst (240°C) than in Anatase-supported catalyst (300°C). This indicates different metal-support interaction in the different titania phases. Jongsomijit *et al,* (2005 p.576) have also reported a similar behaviour. In their study, they reported lower reduction temperatures for Rutile-supported catalyst (99% rutile) compared to an Anatase-supported catalyst (100% anatase).

5.3.3. TEM

HAADF-STEM analysis of reduced catalysts revealed the morphology and size of cobalt particles. The results of anatase-supported reduced catalyst show the presence of small and large particles concurrently situated inside the support pore structure. Cobalt dispersion is therefore generally poor in this catalyst. Some of the large particles appear to be composed of smaller particles which seem to have agglomerated during the reduction process. Other large particles appear solid and intact indicating crystallite growth. The particle size distribution was shown to fit a lognormal distribution with particles ranging from 5 to 40 with a mean particle size of 19.9 nm.

HAADF-STEM images of P25-supported reduced catalyst showed a uniform particle size. The particle size distribution analysis was showed to be a lognormal distribution with sizes ranging from 20 to 120 nm with a mean of 53 nm. No agglomeration was observed in this catalyst compared to the anatase-supported catalyst, however the particles appeared larger than those in anatase-supported catalyst. The crystallites particles appear solid with a somewhat spherical morphology. Shimura *et al,* (2013 pp.11 – 12) have observed a similar behaviour in terms of cobalt dispersion and the presence of rutile phase in a similar quantity as in P25-support. The authors reported a generally poor dispersion of cobalt in “pure anatase” supported catalyst, compared to a P25-equivalent support. In these catalysts, the presence of rutile in an optimum quantity was said to suppress agglomeration of cobalt crystallites. This effect was attributed to the extent of metal-support interaction. This phenomenon is discussed in detail in later sections of this work.

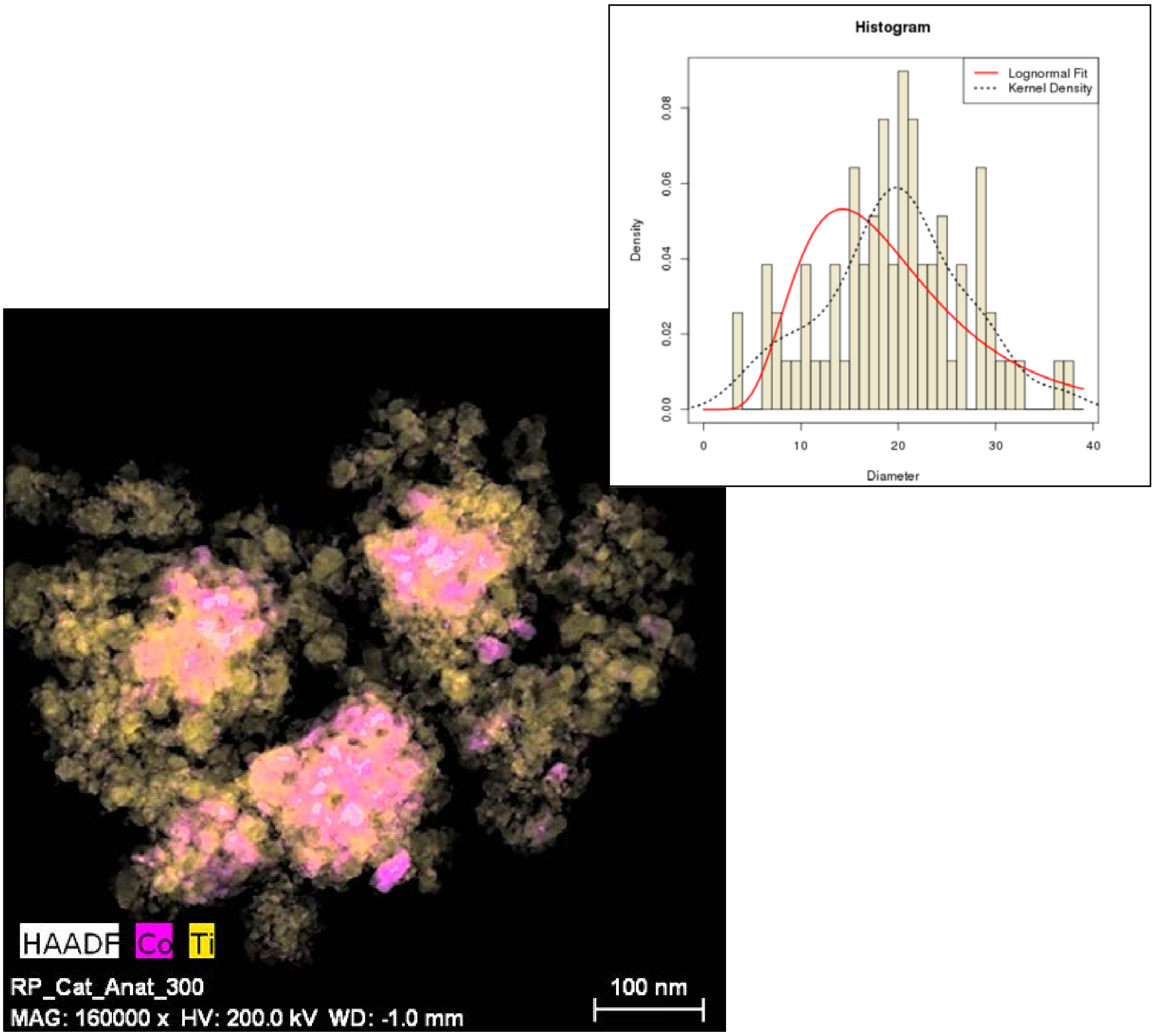

Figure 5. 21: HAADF-STEM EDX mapping of RP_Cat_Anat_300 showing agglomeration of small crystallites into clusters

The results of the Rutile-supported reduced catalyst on the other hand, showed a different behaviour. In this support, cobalt particles can be seen in close interaction with large rutile particles. These cobalt particles generally appear flat on the rutile surface, as opposed to the spherical solid-looking particles observed in anatase- and P25-supported reduced catalysts. The size of the cobalt particles ranged from 3 to 40 nm, with a mean diameter of 21 nm. This orientation might indicate something about the interaction of cobalt with Rutile-support.

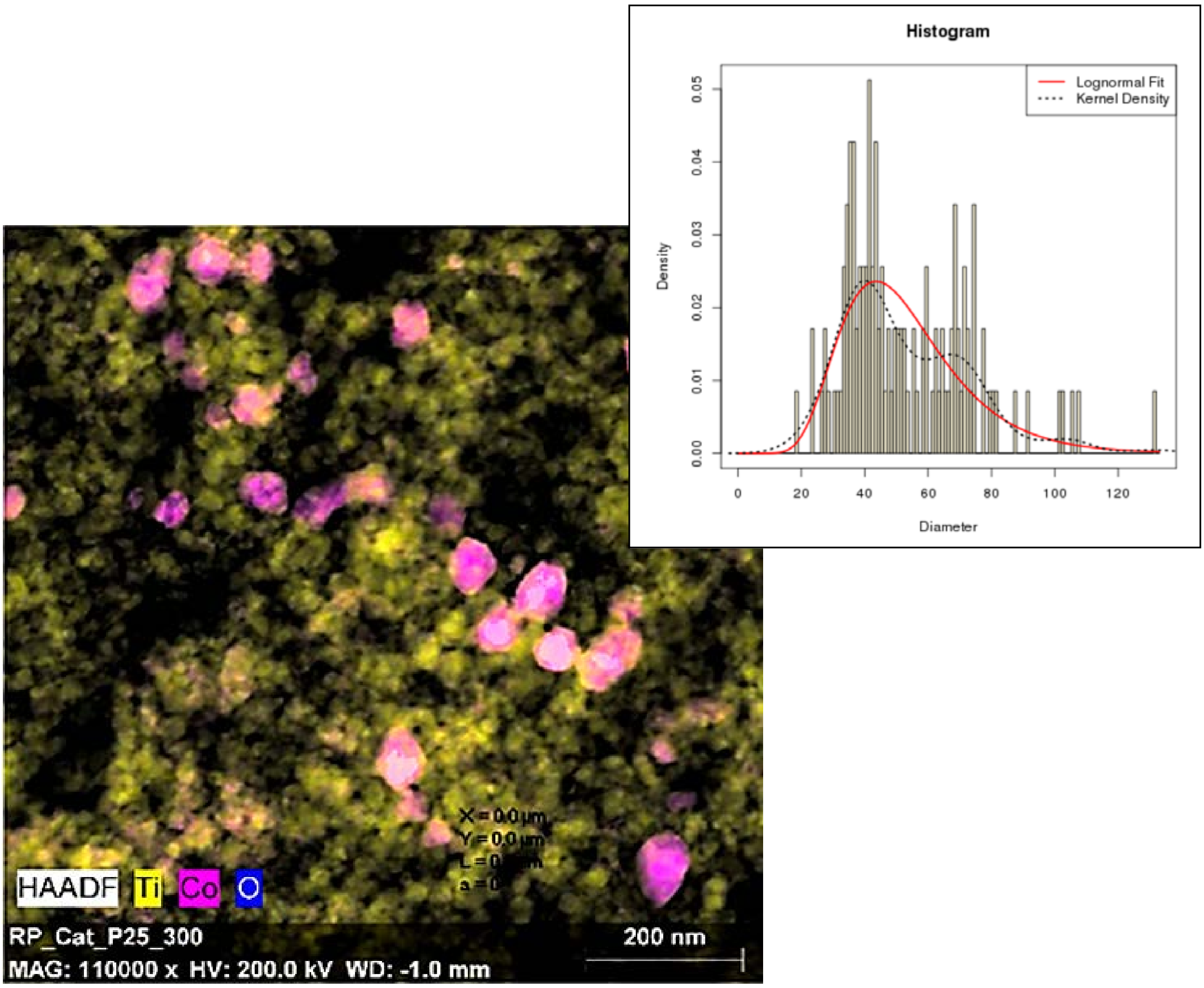

Figure 5. 22: HAADF-STEM EDX mapping of RP_Cat_P25_300

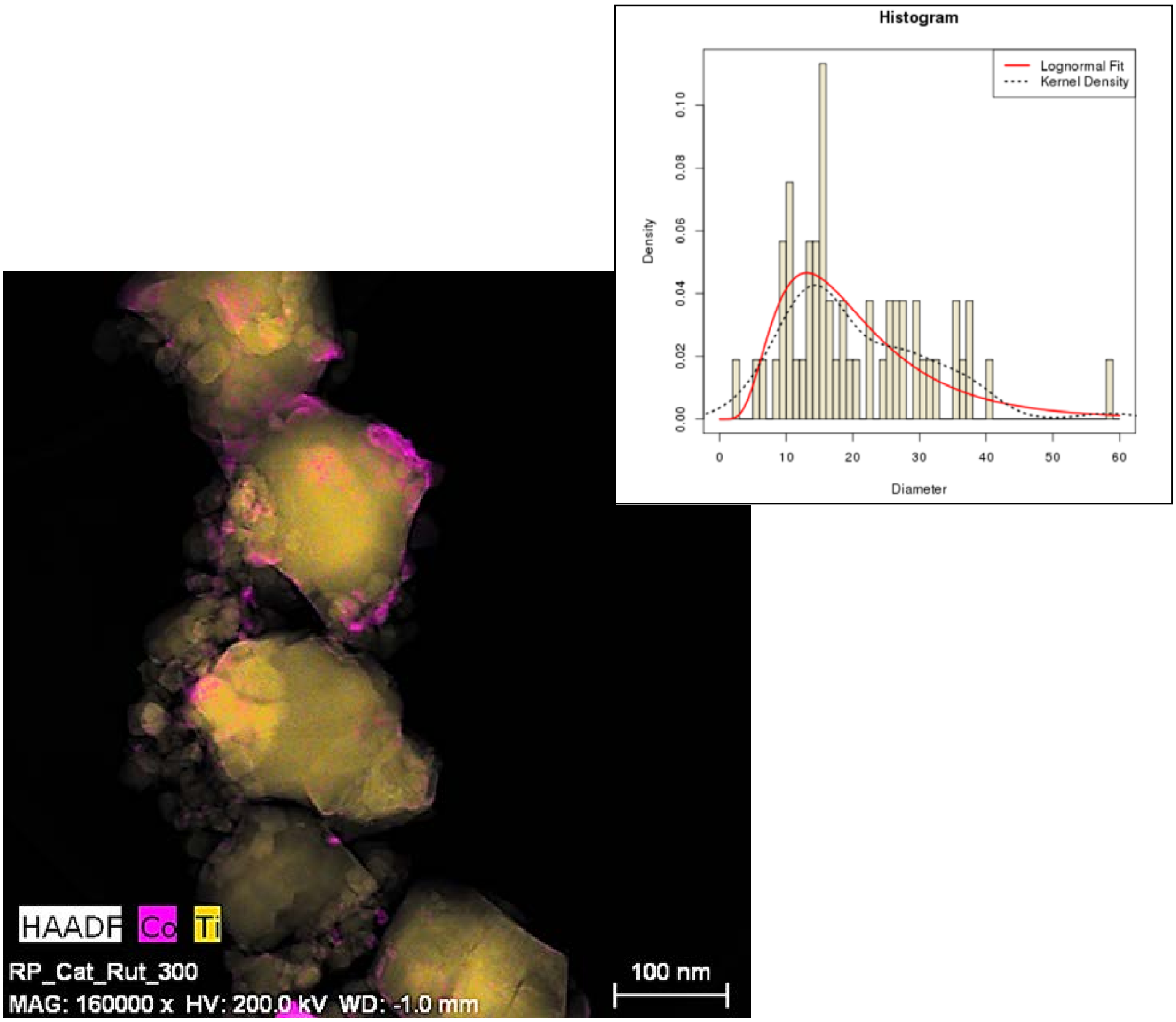

Figure 5. 23: HAADF-STEM EDX mapping of RP_Cat_Rut_300

The Kolmogorov-Smirnov test was used to elucidate whether the particle size distributions across the supports were statistically similar or different. The cumulative distribution functions of anatase- and P25-supported catalysts were compared as shown in Figure B.2. The null hypothesis is: there is no difference between the distributions. The Kolmogorov-Smirnov statistic D was calculated to be 0.4609. The statistic D_{crit} was found to be 0.1870. Since $D > D_{crit}$ we reject the null hypothesis, and conclude that the distributions of anatase- and P25-supported catalysts are statistically different.

Looking at the cumulative distribution functions of anatase- and rutile-supported catalysts, the same approach was taken. The statistic D was calculated to be 0.3262. The statistic D_{crit} was found to be 0.2415. Since $D > D_{crit}$ we reject the null hypothesis, and conclude that the distributions of anatase- and rutile-supported catalysts are statistically different. Comparing the cumulative distribution functions of P25- and rutile-supported catalysts, the statistic D was calculated to be 0.5060. The statistic D_{crit} was calculated to be 0.2155. Since $D > D_{crit}$ we reject the null hypothesis, and conclude that the distributions of P25- and rutile-supported catalysts are statistically different.

5.3.4. H_2-Chemisorption

Hydrogen chemisorption results of the titania-supported catalysts calcined at 300^{o}C are given in Table 5.9 below. Looking at the degree of reduction, Anatase-, and Rutile-supported catalysts showed a similar degree of reduction of 84% and 85% respectively. P25-supported catalyst showed a degree of reduction of 80%.

However, when looking at the active metal surface area, P25-supported catalyst was found to have a higher amount than Anatase- and Rutile-supported catalysts. In this case, P25-supported catalyst had an active metal surface area of 0.41 m^2/g_{cat}. Anatase- and Rutile-supported catalysts showed active metal surface area of 0.28 m^2/g_{cat} and 0.37 m^2/g_{cat}.

Cobalt dispersion also followed the same trend, with P25-supported catalyst showing the highest cobalt dispersion of 0.76%. Rutile- and Anatase-supported catalysts showed dispersion of 0.64% and 0.49% respectively. The current results are in agreement with that of Shimura *et al*, (2013 p.11). The authors also observed a higher active metal surface for a non-promoted supported on a P25 equivalent titania support consisting of 85% anatase and 15% rutile (Shimura *et al*, 2013 p.10). They also reported higher cobalt dispersion for this non-promoted catalyst compared to catalysts supported on 100% Anatase and another on 98% rutile supports.

Table 5. 9: H_2-Chemisorption results showing reduction properties of titania-supported cobalt species

Catalyst	Degree of Reduction (%)	Active Metal surface area (m^2/g_{cat})	Dispersion (%)
Cat_Anat_300	84	0.28	0.49
Cat_P25_300	80	0.41	0.76
Cat_Rut_300	85	0.37	0.64

The dispersion of cobalt on titania supports reported in our study and that of Shimura *et al*, concur with the dispersion model proposed by Jongsomjit *et al* (2005 p.575). In their model illustrated in Figure 5.24, it was shown that the presence of rutile phase in an optimum amount enhances the reduction of cobalt oxide with the result of highly dispersed metallic cobalt species. In our case, it can be inferred that P25-support contains rutile phase in an optimum amount, thus the observed high cobalt dispersion and large active metal surface area.

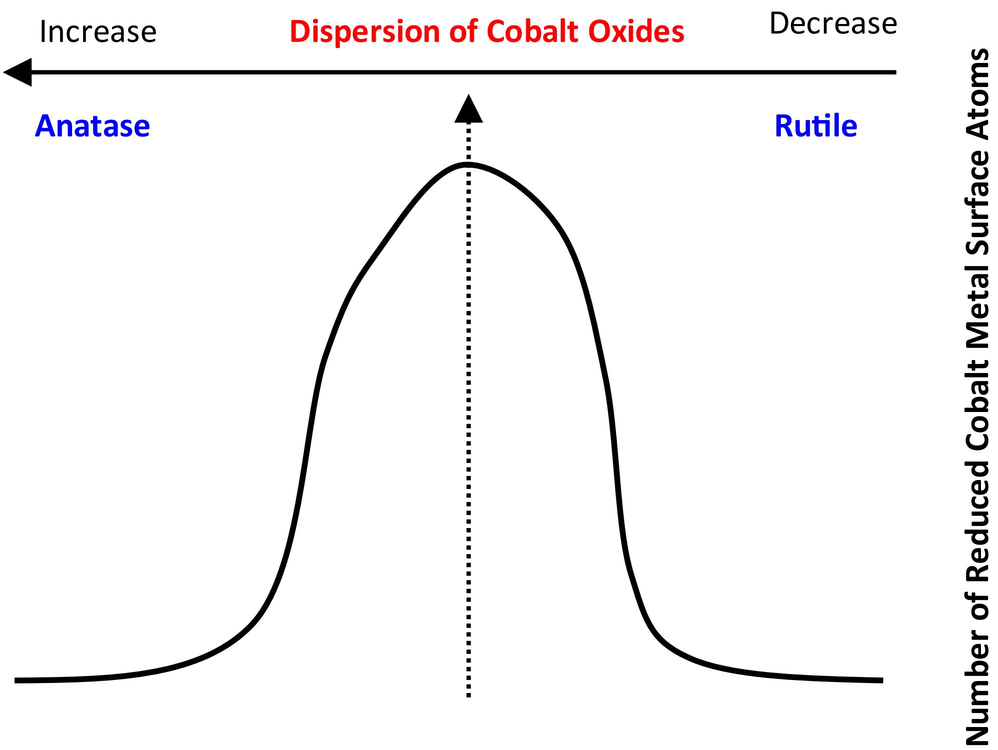

Figure 5.24: Conceptual Model of Cobalt dispersion on TiO_2 (Adapted from Jongsomjit *et al*, 2005 p.575)

5.3.5. Temperature Programmed Reduction (TPR)

The reduction behaviour of the titania-supported catalysts was further studied by TPR. The reduction of unsupported cobalt compounds and bare supports was also studied to aid in understanding the reduction of the titania-supported catalysts. The compounds studied were Co_3O_4, CoO and $CoTiO_3$. The TPR profiles of the unsupported cobalt compounds are given in Figure 5.25.

The TPR profile of Co_3O_4 shows one broad asymmetrical peak with a maximum at 380°C. This profile indicates that unsupported Co_3O_4 is reduced in one step directly to metallic cobalt. This is in agreement with the study of Bulavchenko *et al,* (2009 p.329), in which they state that unsupported Co_3O_4 is reduced in one step to yield metallic cobalt. Jongsomjit (2002 p.86) has also reported one-step reduction of unsupported Co_3O_4. This was evidenced in TPR results. Tang *et al,* (2008 p.71) have shown a two-step reduction with maxima at 300°C and 367°C for unsupported Co_3O_4. The different observations from the studies above may be attributed to factors such as particle size of the unsupported Co_3O_4 crystallites. It is know that the crystallite size can affect the reduction profile of metal oxides.

The reduction profile of unsupported CoO shows three peaks. The peak with the highest intensity has a maximum at 310°C. This main peak may be attributed to the reduction of CoO to metallic cobalt. The other peaks, one at 220°C and another at 520°C may indicate other species that are present in the bulk which are hard to reduce. Tang *et al,* (2008 p.71) reported a single peak with maximum at 482°C for the reduction of unsupported CoO to metallic cobalt.

The reduction profile of $CoTiO_3$ shows an interesting behaviour. The TPR profile shows three high intensity peaks with maxima at 320°C, 670°C and 790°C. The peak at 320°C can be attributed to the reduction of residual CoO. It is assumed that this phase might be coming from the starting material for $CoTiO_3$ preparation. This is observed by the similar reduction temperature (320°C) observed in the unsupported CoO sample. The peaks at 670°C and 790°C can be linked to the reduction of $CoTiO_3$ surface and bulk species respectively, to yield metallic cobalt and rutile TiO_2

(Yankin & Balakirev 2002 pp.11-12). No reduction of TiO_2 can be expected at the temperatures below 900°C. It has been shown that at temperatures below 862°C, $CoTiO_3$ is reduced to metallic cobalt and rutile TiO_2 as described by the reaction.

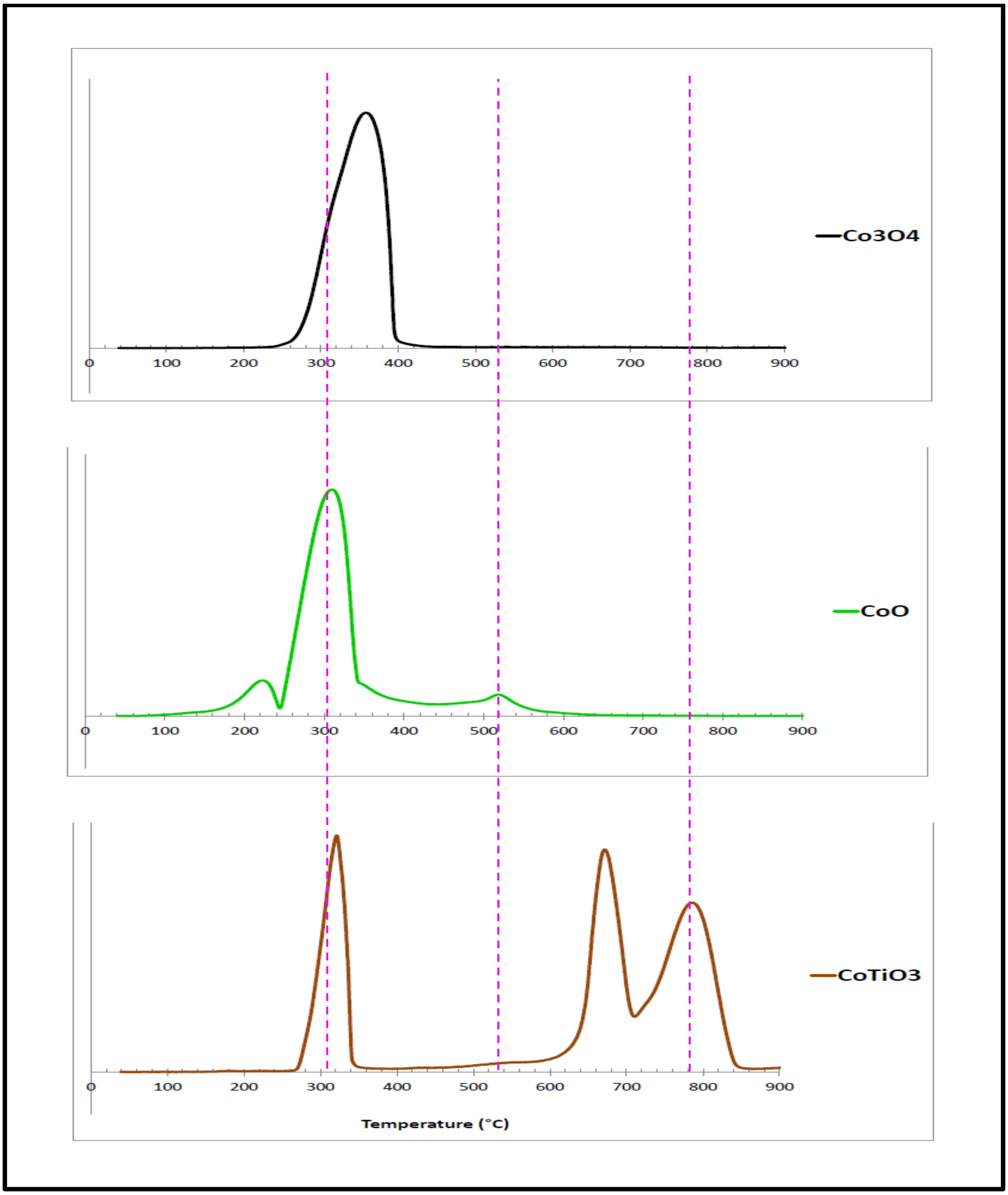

Figure 5.25: Temperature Programmed Reduction (TPR) results of cobalt compounds

The TPR profiles of the bare supports show an interesting phenomenon. The results show that all the supports interact with hydrogen. This behaviour implies that the supports are not as inert as initially expected. The phenomenon has been highlighted by Diebold (2003 p.68), and Pacchioni (2008 p.2). The observed reduction may have implications on the reduced catalyst properties. The reduction of TiO_2 is said to produce surface and bulk defects such as Ti^{3+} and oxygen vacancies (Strunk *et al,* 2010 p.16937). These defects can influence the anchoring of particles on the support surface (Chen & Goodman 2007 pp.42 – 43).

The reduction of the supports starts at ~300^{o}C and levels off at around ~750^{o}C. This is in agreement with the work of Xiong *et al*, (2012 p.2). These authors reported that TiO_2 interacted physically with hydrogen at a temperature below 300^{o}C. As the temperature increases to above 300^{o}C, electrons become transferred from the H atoms to O atoms in the lattice of TiO_2. As the O atom interacts with H atoms to form H_2O, oxygen vacancies are created. As the temperature increases up to 450^{o}C, the interaction of TiO_2 with hydrogen intensifies with the evolution of Ti^{3+}. These Ti^{3+} entities are formed due to the electron transfer from oxygen vacancies to Ti^{4+} ions. As the temperature increases to above 560^{o}C, more energy was supplied resulting in more electrons being transferred from the oxygen vacancies to the Ti^{4+}. The assumption of the formation of surface and bulk defects in our supports is confirmed by the absence of TiO or metallic Ti from XRD results. This indicates that the interaction of the TiO_2 supports with hydrogen does not lead to a full reduction of TiO_2 to TiO or Ti, but rather to TiO_{2-x} species (Pacchioni 2008 p.16).

The TPR profile of Anatase-supported catalyst shows main peaks at ~310^{o}C, ~480^{o}C and 600^{o}C. The peak at 310^{o}C is well defined while that at 480^{o}C is broad leading to a shoulder peak at ~600^{o}C. The first peak at 301^{o}C can be assigned to the first reduction step of Co_3O_4 to CoO. The second peak at 480^{o}C can be assigned to the second reduction step of CoO to metallic state. The broad shoulder peak at 600^{o}C may highlight the extent of metal-support interaction.

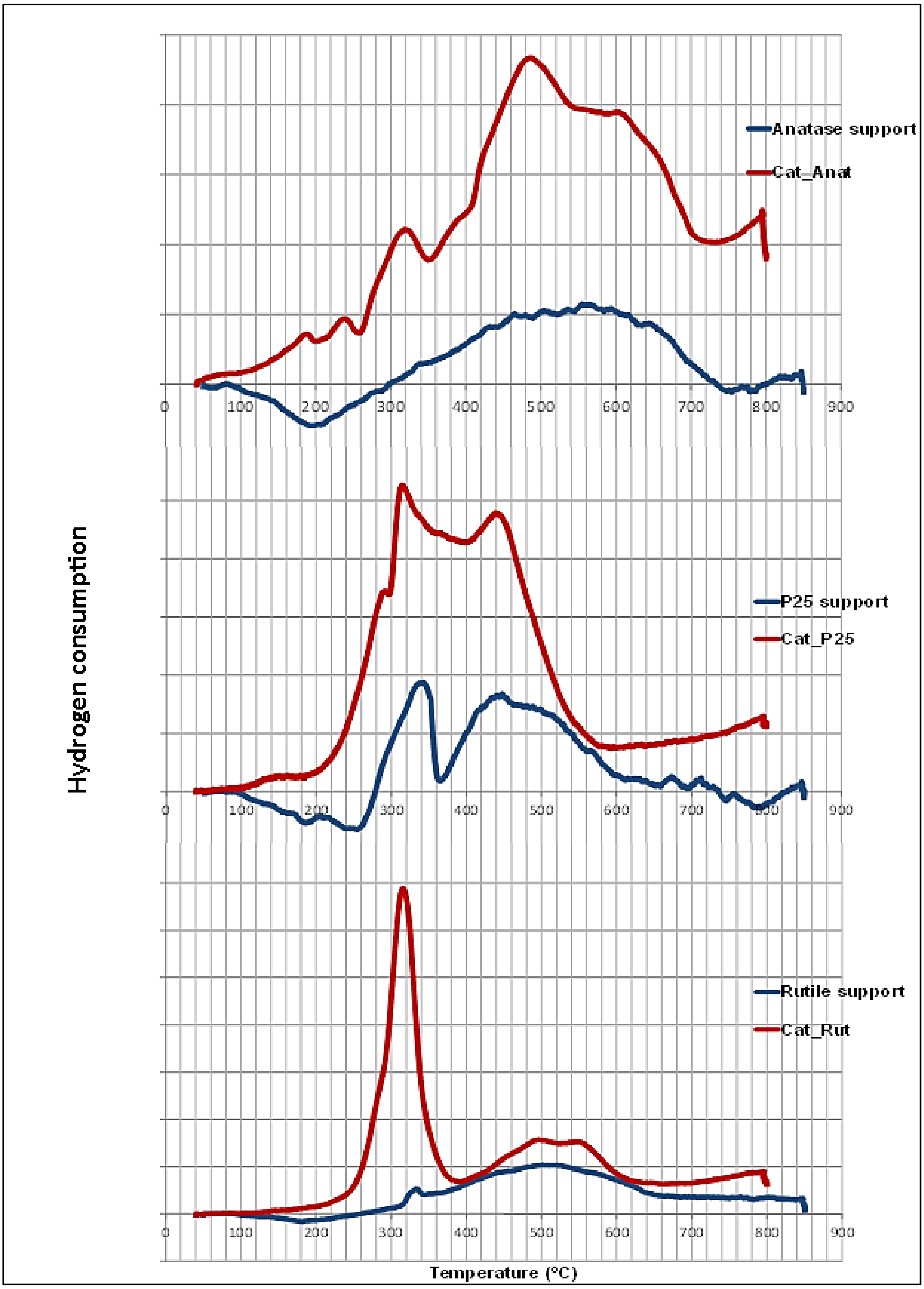

Figure 5.26: Temperature Programmed Reduction (TPR) results of titania-supported catalysts and supports showing the reduction profiles.

It is hypothesised that the high temperature peak results from reduction of cobalt species in strong interaction with the support. In this case, these cobalt species will be hard to reach by the hydrogen gas. And the water formed from the reduction reaction will not diffuse out easily due to the narrow pore structure of Anatase support. Another noteworthy observation is increase in H_2 consumption at temperatures >750^{o}C.

The reduction profile of P25-supported catalyst shows a different behaviour to that of Anatase-supported catalyst. The profile shows two main peaks at ~310^{o}C and ~440^{o}C. The peak at 310^{o}C can be assigned to the reduction of Co_3O_4 to CoO. The second peak at 440^{o}C can be assigned to the reduction of CoO to the metallic state. The profile shows that cobalt species supported in P25 are much more accessible for reduction than those in Anatase-support.

The reduction of Rutile-supported catalyst also shows an interesting behaviour. Overall, the profile is similar to that of the other titania supports in that there are two main peaks at ~310^{o}C, ~500^{o}C and 550^{o}C. The first peak which occurs at 310^{o}C can be assigned to the first reduction step. The peak at 500^{o}C can be assigned to the second reduction step. The last peak, which is actually a shoulder peak at ~540^{o}C can be attributed to the reduction of $CoTiO_3$ species, the presence of which was confirmed by XRD and Raman results.

The TPR results of the bare supports show that the supports are reduced by hydrogen. The TPR results in our study confirm the two step reduction process of cobalt oxide species. The results also show that there is different metal-support interaction in the different titania supports. It is interesting to note that the first reduction occurs at the same temperature (~310^{o}C) for all supports. This might indicate the same interaction of Co_3O_4 species with the titania supports. An interesting observation is the temperature of the second reduction step. In this case, slightly different temperatures were observed in the different supports. This might highlight different extent of interaction of CoO and metallic Co with the supports. In cases where the second reduction occurred at higher temperatures, a stronger metal-support interaction is inferred.

High temperature XRD reduction results were compared to TPR results. The first- and second-stage reduction reactions ($Co_3O_4 \rightarrow CoO$ and $CoO \rightarrow Co$ respectively) for Anatase-supported catalyst occur at 200°C and 300°C from XRD point of view. TPR meanwhile showed reduction temperatures of 310°C and 480°C for the first- and second-stage reduction reactions. In the case of Rutile-supported catalyst, XRD showed reduction temperatures of 180°C and 240°C for the first- and second-stage reductions respectively. TPR showed reduction temperatures of 310°C and 500°C for the first- and second-stage reductions respectively.

It can be seen that XRD generally showed lower reduction temperatures compared to TPR. This can be further explained by looking at the characterization techniques and the analysis conditions used in each technique. In XRD, pure H_2 gas was used while a 5% H_2/Ar mixture was used in TPR, at the same heating rate. Therefore the different reducing conditions could play a role in the reduction of cobalt species in the titania supports.

5.3.6. BET Surface Area and Pore Size Distribution

Surface area and average pore size results of reduced catalysts are given in Table 5.10. These results are compared those of calcined at 300^{o}C. The surface area of Anatase-supported reduced catalyst was found to be 59 m^2/g and the pore size was 9.9 nm. The results are clearly similar to that of calcined catalyst. The reduction process therefore did not influence the textural properties of the Anatase-supported catalyst.

The surface area of P25-supported reduced catalyst was shown to be 42 m^2/g and the pore size was 26.4 nm. The surface area is slighty lower than that of the calcined catalyst which was found to be 50 m^2/g. The pore size remained unchanged after reduction. The observed surface area is lower than that of the calcined catalyst given the error in the surface area measurement determined to be ± 6 m^2/g. The surface area of reduced Rutile-supported catalyst was found to be unchanged when compared to the calcined catalyst. The surface area was found to be 9 m^2/g and the pore size was 22.4 nm. These results show that reduction at 450^{o}C does not significantly influence the structural properties of titania-supported catalysts.

Table 5. 10: BET surface area and Pore size results of calcined and reduced catalysts

Catalyst	**Calcined**		**Reduced**	
	BET Surface area (m^2/g)	**Pore Size (nm)**	**BET Surface area (±6 m^2/g)**	**Pore Size (nm)**
Cat_Anat_300	62	9.8	59	9.9
Cat_P25_300	50	26.9	42	26.4
Cat_Rut_300	9	24.5	9	22.4

Stage 4 – Sintering Studies

5.4. STAGE 4 - SINTERING STUDIES

Sintering results of the titania-supported catalysts are given in this section. The sintering behaviour was studied by XRD and TEM. These techniques give volume-based and number-based crystallite sizes respectively. Therefore the XRD and TEM data were treated separately. The selected responses were *CS_fcc Co (XRD)*, *CS_hcp Co (XRD)* and *CS_Co (TEM)*. These responses represent the fcc cobalt crystallite size from XRD, hcp cobalt crystallite size from XRD and cobalt particle size from TEM respectively.

In the first section, the TEM derived particle sizes were expressed in terms of crystallite size distributions (PSD). The PSD curves are important in determining whether sintering has occurred. The mean and full width-at-half maximum (FWHM) of the PSD curve give information of the sintering behaviour, in that shifts towards larger particle sizes confirm sintering of cobalt crystallites. It is from these PSD curves that the mean particle size from a TEM point of view (*CS_Co (TEM)*) is obtained.

The XRD and TEM data was then modelled using statistical regression. The next step was empirical modelling using power law expression models developed to describe the sintering behaviour and to give kinetic terms such as the sintering rate constant k_s and sintering order n or m. The last section deals with phenomenological modelling of the sintering behaviour. In this section, the mechanistic models describing the evolution and growth of cobalt crystallites in the different catalyst systems are inferred from the sintering data and TEM results.

5.4.1. Particle Size Distributions (PSD) derived from TEM

It has been showed that particle size data derived from the TEM can be fitted to lognormal distribution function (LNDF). It should be acknowledged however, that some data may show deviation from this lognormal distribution. This was clear in the TEM results of calcined rutile-supported catalysts. To quantify the sintering behaviour of cobalt crystallites, the sintered catalysts particle sizes were fitted to the LNDF, resulting in PSD curves. In this case the position and width of the PSD curve are of importance. The PSD curves also serve to confirm the occurrence of sintering, albeit without inferring any mechanism. Datye *et al*, (2006 pp.59 – 67) have

cautioned against inferring sintering mechanism from the shape of the PSD curve. This is because both OR and PMC can have the same PSD shape.
The histograms of particle size measurements of the sintered anatase-, P25- and rutile-supported catalysts are given in Figure B.2, Figure B.3 and Figure B.4 in Appendix B.

Looking at the PSD curves of Anatase-supported sintered catalysts given in Figure 5.27, it can be seen that the PSD's shift towards larger particle sizes. The mean particle size increases from 30.2 nm at 4 hours up to 88 nm after 48 hours. The widths of the curves also become wider. This is evident in Table A. 4 where FWHM increases from 26.3 nm at 4 hours up to 76.0 nm after 48 hours. This might indicate that larger particles are being formed with time. The Kolmogorov-Smirnov was used to determine whether the particle size distributions of the sintered catalysts were statistically similar or different. This was to ascertain whether the broadening was significant. The data is summarized in Table A.3 in the Appendix A. It was shown that all the particle size distributions of sintered anatase-supported catalysts are statistically different as illustrated in Figure B. 6 . This confirms that the observed broadening and shift to larger particle sizes in anatase-supported catalysts is significant.

The PSD curves of P25-supported sintered catalysts are given in Figure 5.28. The PSD's shift slightly towards larger particle sizes. Table A. 5 shows that the mean increases from 50.7 nm at 4 hours up to 65.0 nm after 48 hours. From a glance the widths of the PSD curves do not appear to change considerably. However the FWHM still increases from 38.5 nm at 4 hours up to 51.4 nm. This might indicate that the sintering tendency of cobalt crystallites on P25 support is low compared to Anatase-supported catalysts. The Kolmogorov-Smirnov test showed that the sintered P25-supported catalysts at 4, 8 and 16 hours are statistically similar as illustrated in Figure B. 7. This strengthens the observation of low sintering tendency in P25 support. The catalysts at 32 and 48 hours were shown to be statistically different to that at 4 hours showing the occurrence of sintering with time.

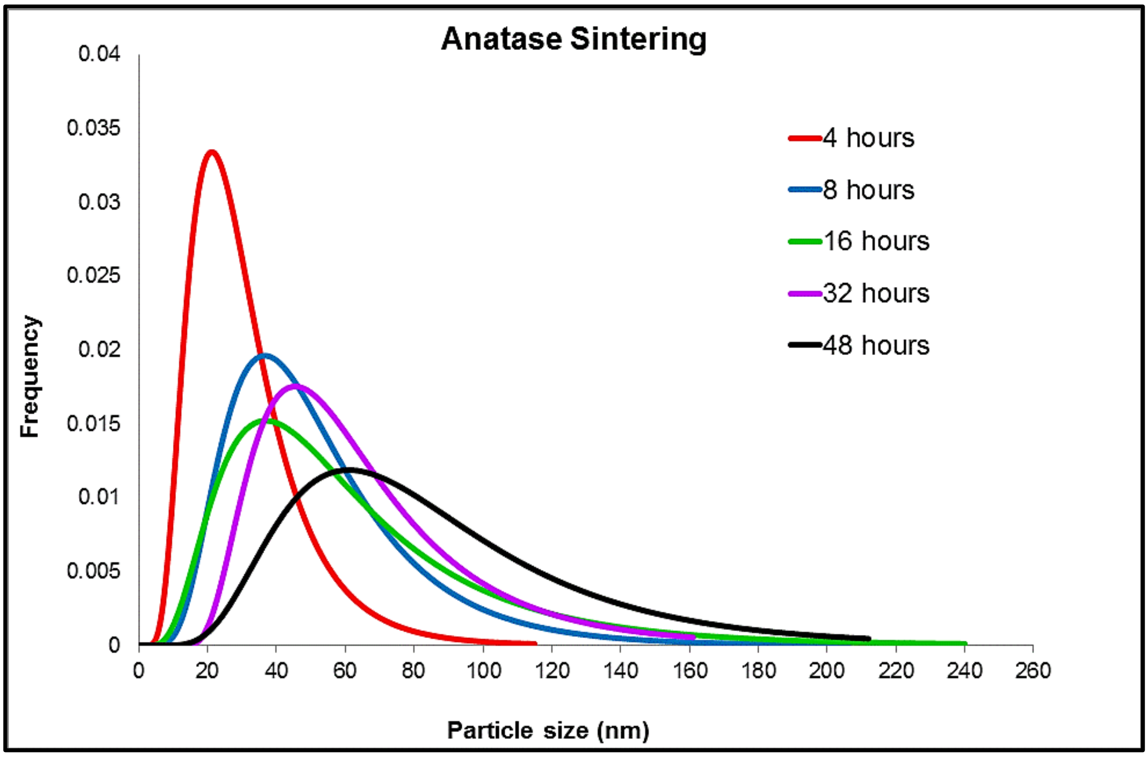

Figure 5. 27: Particle size distributions of Anatase-supported catalysts fitted onto lognormal distribution function, showing the effect of sintering time

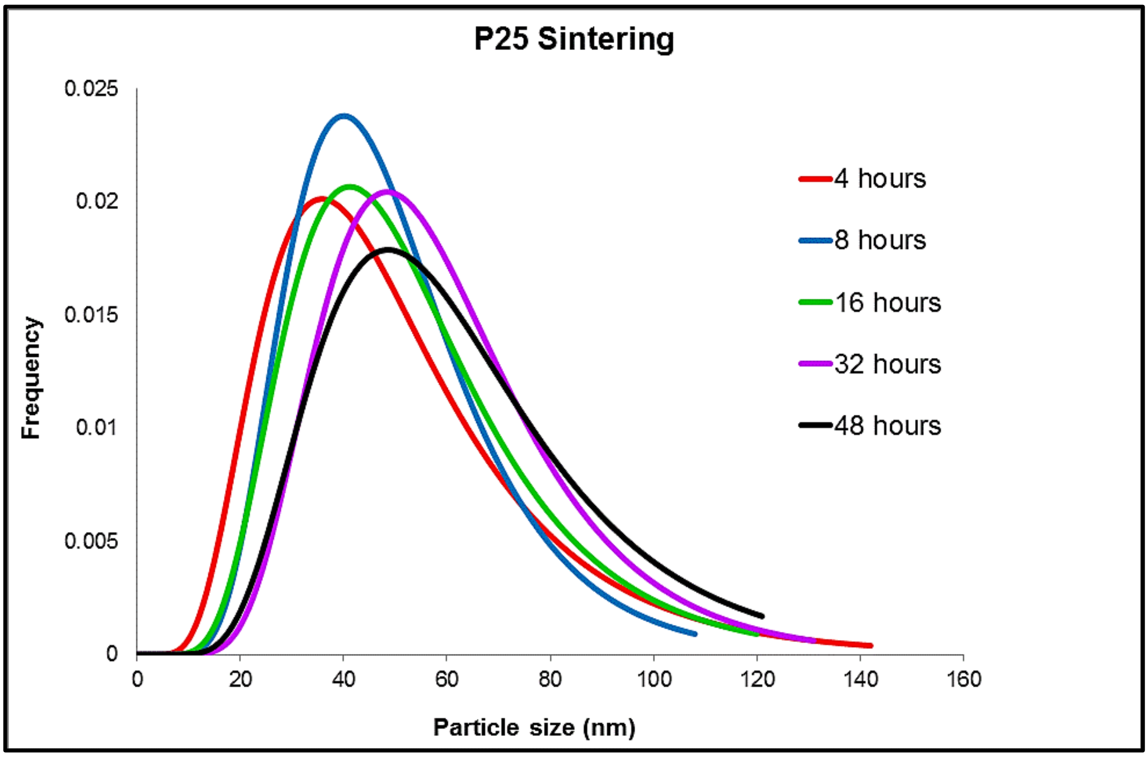

Figure 5. 28: Particle size distributions of P25-supported catalysts fitted onto lognormal distribution function, showing the effect of sintering time

The PSD curves of Rutile-supported sintered catalysts are given in Figure 5.29. The width and location of the PSD curves change with time. The mean changes from 16.9 nm at 4 hours up to 36.4 nm after 48 hours. The widths of the curves become narrower at the initial stages, and then broaden with time. This is shown in Table A. 6. This might imply changes in the sintering mechanism from OR to predominantly PMC. The assumption may highlight an effect of the support on the sintering behaviour of the cobalt crystallites. The Kolmogorov-Smirnov test showed that all the distributions of the rutile-supported catalysts are statistically different as illustrated in Figure B. 8. This indicates that the broadening and shift to larger particle sizes is significant.

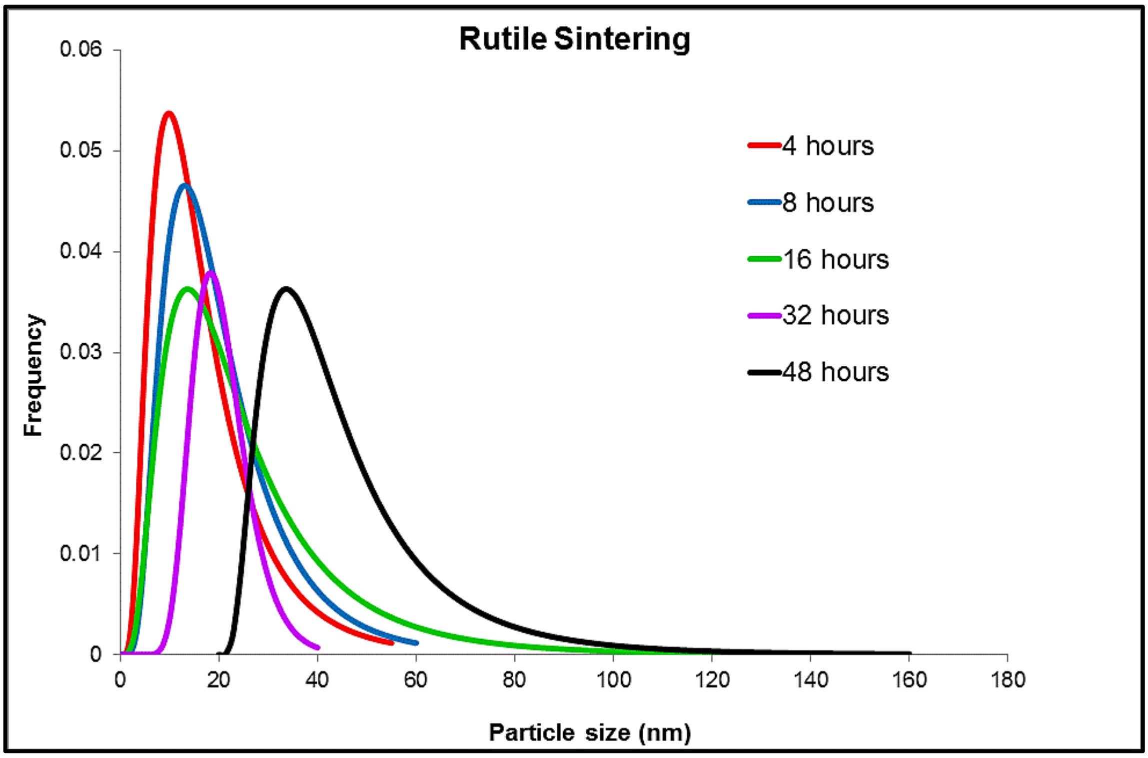

Figure 5. 29: Particle size distributions of Rutile-supported catalysts fitted onto lognormal distribution function, showing the effect of sintering time

Hansen *et al*, (2013 p.1725) have observed the effect of the long term annealing experiments on $MgAl_2O_4$-supported Ni catalysts. In this case, the PSD curves developed a tail towards the larger particles sizes. The width of the PSD curves also broadened. Datye *et al*, (2006 p.62) have observed gradual shifts in the PSD curves of alumina- and silica-supported Pd catalysts. The PSD's shifted towards larger crystallite sizes accompanied by broadening, with increasing annealing time.

The studies cited in literature validate the notion that PSD curves can be useful in confirming the occurrence of sintering in supported metal catalysts.

5.4.2. Statistical Modelling – Regression Analysis (XRD and TEM)

The data was analysed statistically. In this process, statistical parameters such as *R-squared*, *Adjusted R-squared*, *F-value*, *p-value*, *Standard Deviation* and *PRESS* were determined for the responses *CS_fcc Co (XRD)*, *CS_hcp Co (XRD)* and *CS_Co (TEM)*. These statistical terms were obtained from ANOVA calculations. The fit summary gave regression models that can best fit the data. Possible models explored were *linear*, *2 Factor Interaction (2FI)*, and *Quadratic*. Higher order models were not explored due to their increased complexity.

5.4.2.1.Response – fcc Cobalt Crystallite size (XRD)

The plots of fcc cobalt crystallites given in Figure 5.30 show a general increasing trend which levels off with time (Witten & Sander, 1981 p. 1400). The growth of anatase-supported fcc crystallites appears to start slow then increases after 8 hours, reaching the maximum after 48 hours. The growth of P25-supported fcc crystallites appears to go slow and only increases after 48 hours. However it is rutile-supported fcc crystallites that show the most resistance to sintering. The crystallite sizes remain within error of each other even after 48 hours. The results nonetheless suggest that if one extrapolates towards longer sintering times, a slight increase might be observed. However, this is speculative. The increasing trend of fcc crystallite size with time is in line with that reported by Karaca *et al,* (2010 p.790).

Since it easier to work with linear models, the plots of fcc cobalt crystallite size against time were transformed into log – log functions. This transformation made it easier to study the interaction of the variables involved. Of interest, was the interaction of the support type (i.e. anatase, P25, rutile) with sintering time. The linearized plots are given in Figure 5.31.

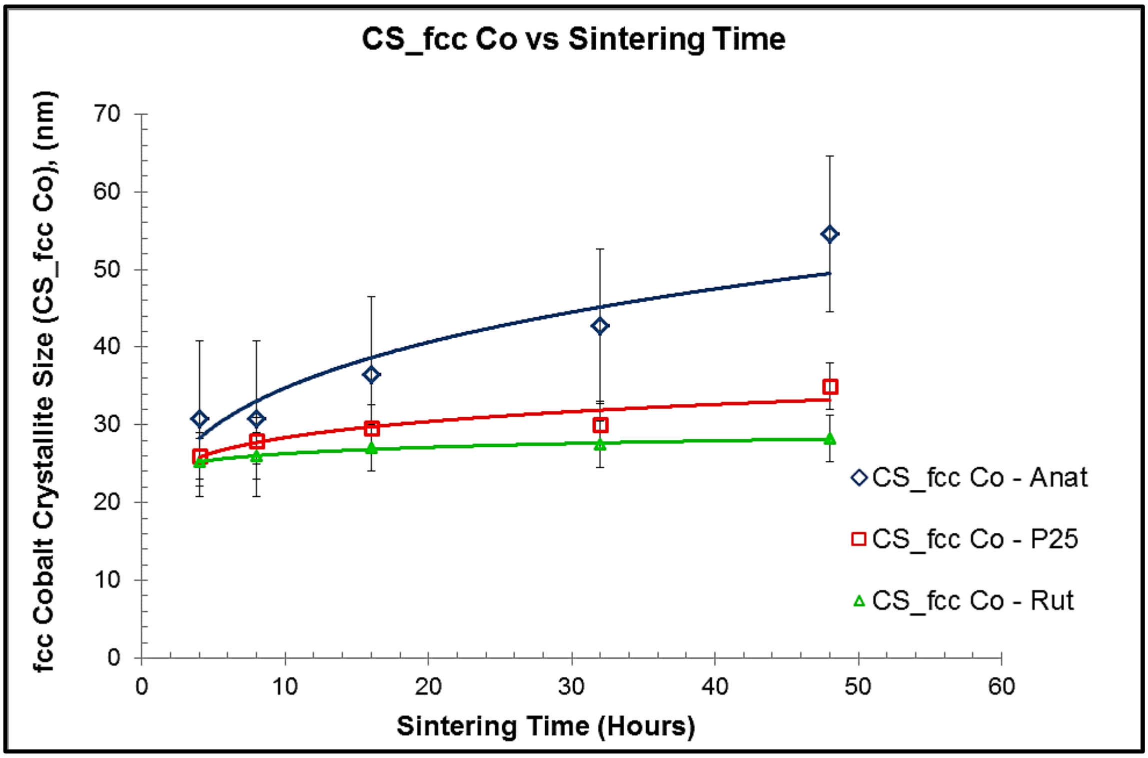

Figure 5. 30: Plots of fcc cobalt crystallite size against sintering time for the titania-supported catalysts (showing sigma error).

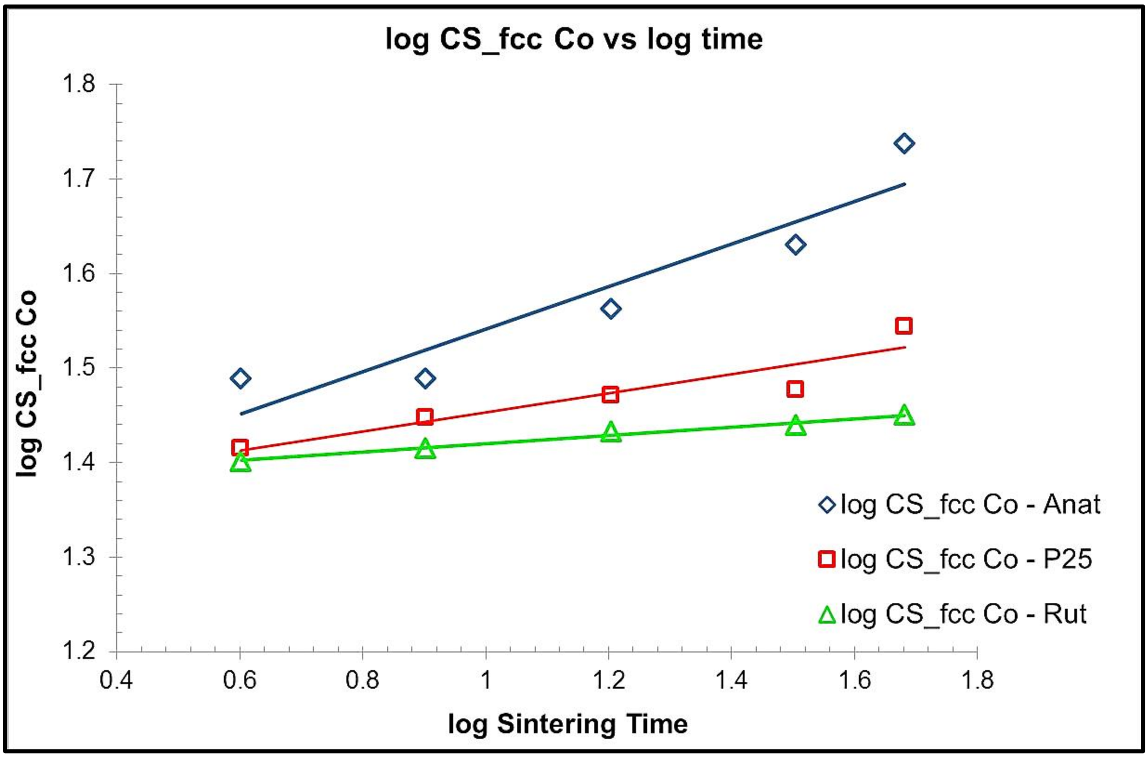

Figure 5. 31: Linearized log-log plots of fcc cobalt crystallite size against sintering time for the titania-supported catalysts.

Fit Summary

A high *Adjusted* R^2 and *Predicted* R^2 are desired for a model to be significant for fitting data. The results given in Table 5.11 showed that the *2FI* model had the highest *Adjusted* R^2 and *Predicted* R^2. Since the data was transformed into a linear model, it was worthwhile to compare the *Linear* model with the *2FI* model. The *Linear* model showed an *Adjusted* R^2 and a *Predicted* R^2 of 0.7432 and 0.5645 respectively. It should be noted that the *Quadratic* model showed even higher *Adjusted* R^2 and *Predicted* R^2 compared to the *Linear* and *2FI* models. This is to be expected since higher order models will always show better fit than lower order models (Motulsky & Christopoulos 2003 p.63). In this case, prior knowledge of the expected interaction tells us that the interaction cannot be described by the *Quadratic* model. Therefore, this model was not taken into consideration when analysing the regression results.

Table 5. 11: Fit summary for fcc cobalt crystallite size data

Model	Sequential p-value	Adjusted R-Squared	Predicted R-Squared
Linear	0.0001	0.7432	0.5645
2FI	<0.0001	0.9816	0.9629
Quadratic	0.4214	0.9810	0.9558

Model Summary

The model summary statistics given in Table 5. 12 list the most important terms required for a model to be significant. In addition to the *Adjusted* R^2 and *Predicted* R^2 already discussed, the *Standard Deviation* and *PRESS statistics* are also of importance. The *Std Dev* can be defined as the root mean squares error. A low *Std Dev* and low *PRESS* value are desired for a best fit model.

The *2FI* model showed a *Std Dev* of 0.013 and a *PRESS* value smaller than 0.05. The *Linear* model showed a *Std Dev* of 0.048 and a *PRESS* value of 0.054. The *2FI* model was therefore the best candidate for fitting the data.

Table 5. 12: Model summary statistics for fcc cobalt crystallite size

Model	Std Dev	R-Squared	Adjusted R-Squared	Predicted R-Squared	PRESS
Linear	0.048	0.8343	0.7432	0.5645	0.054
2FI	0.013	0.9882	0.9816	0.9629	4.64E-03
Quadratic	0.012	0.9891	0.9810	0.9558	5.52E-03

ANOVA Statistics

The ANOVA results of the *2FI* model given in Table 5. 13 showed a *p-value* of <0.0001. This indicates that the model is significant. In the case of model terms, a *p-value* less than 0.100 is desired for the model terms to be significant. The terms *A*, *B* and *AB* were shown to be significant. All these terms had *p-values* of <0.0001.

Table 5. 13: ANOVA Statistics for the 2FI model for fcc cobalt crystallite size

Source	Sum of Squares	df	Mean Square	F Value	p-value
Model	0.12	5	0.025	150.11	<0.0001
A - log Sintering Time	0.048	1	0.048	299.99	<0.0001
B - Support Type	0.050	2	0.025	153.17	<0.0001
AB	0.024	2	9.67E-03	72.11	<0.0001
Residual	1.48E-03	9	1.64E-03		

The ANOVA results of the *2FI* model were evaluated by diagnostic plots of residuals. The normal probability plot of residuals given in Figure 5.32 showed that the residuals are normally distributed (Ergen & Bayramoglu 2011 p.6635). The plot of externally studentized residuals given in Figure 5.33 showed randomly scattered residuals indicating a constant variance. The plot showed no outliers in the data (Wisniak & Polishuk 1999 pp. 64 – 66).

The *2FI* model was shown to be the best regression model to describe the sintering of fcc cobalt crystallites.

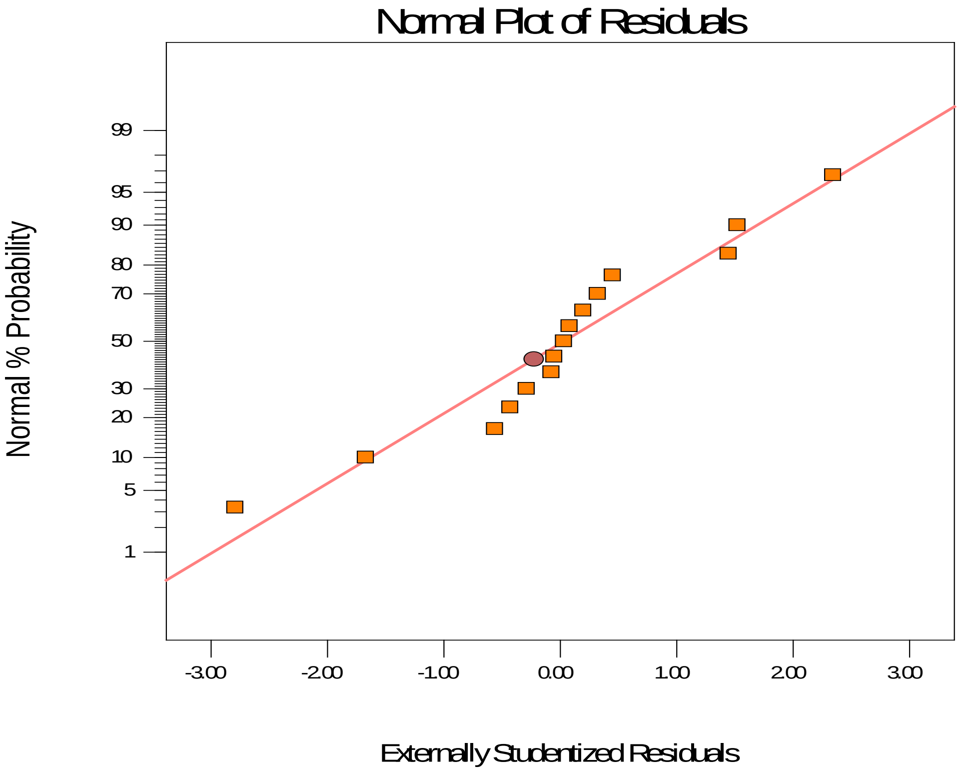

Figure 5. 32: Normal probability plot of residuals of the *2FI* model of fcc cobalt crystallites.

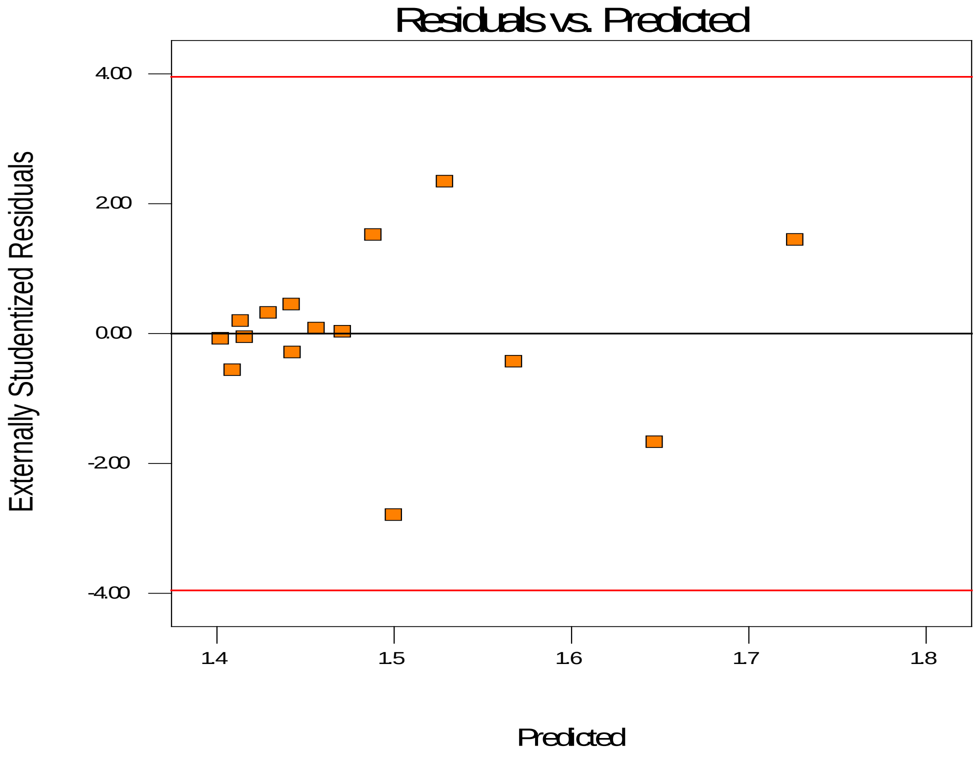

Figure 5. 33: A plot of externally studentized residuals of the *2FI* model of fcc cobalt crystallites.

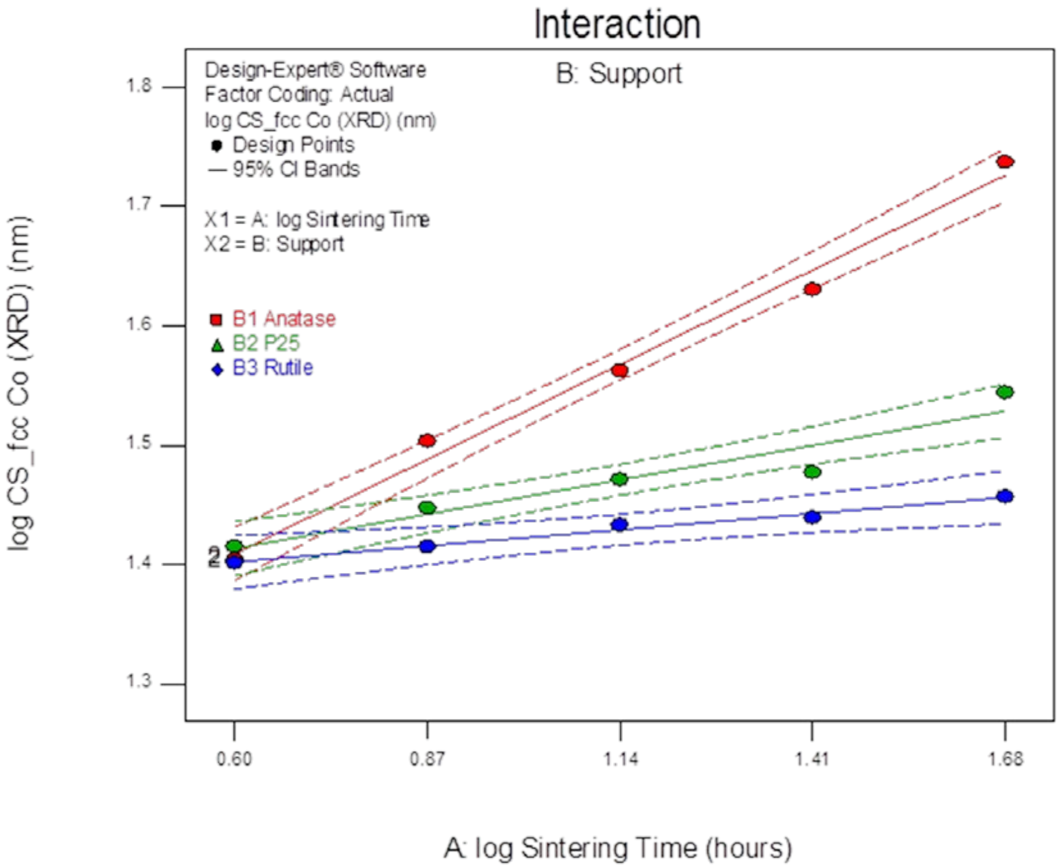

Figure 5. 34: An updated plot of log CS_fcc Co against log Sintering Time showing 95% CI bands and interaction between variables

The final plots of log CS_fcc Co against log Sintering Time showing 95% confidence interval bands and interaction of variables, are given in Figure 5.34. The linear nature of the log – log plots highlight our earlier assumption of a power law-type growth of fcc cobalt crystallites.

5.4.2.2.Response – hcp Cobalt Crystallite size (XRD)

The sintering of hcp cobalt crystallites showed a different behaviour to that of fcc cobalt crystallites. The crystallite size showed a stabilized behaviour with time showing an almost linear behaviour. It is accentuated that no hcp cobalt could be detected in P25-supported catalysts. The reason for absence of this phase is unclear. Looking at the results of anatase-supported catalyst, it can be seen that the hcp crystallite sizes remain constant and within error of the measurements as shown by the error bars. The same trend was seen in rutile-supported catalyst. The data was converted to a linear function by log – log transformation. The linearized plot is given in Figure 5.36.

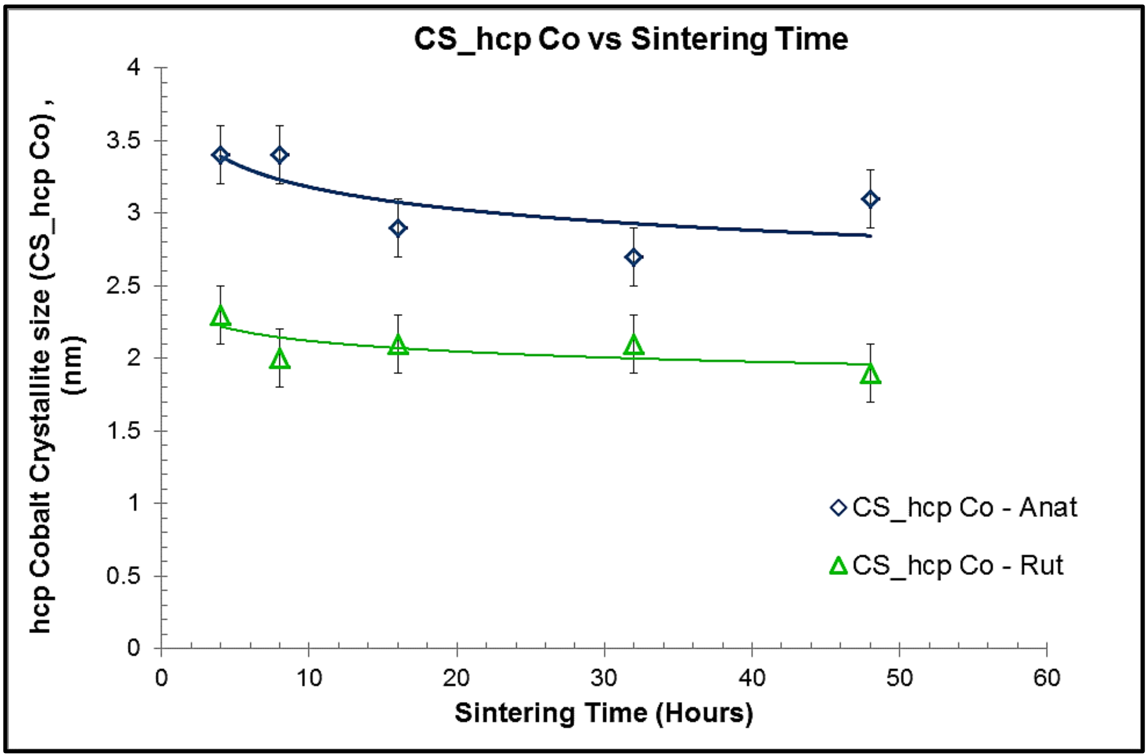

Figure 5. 35: Plots of hcp cobalt crystallite size against sintering time for the titania-supported catalysts. (showing sigma error).

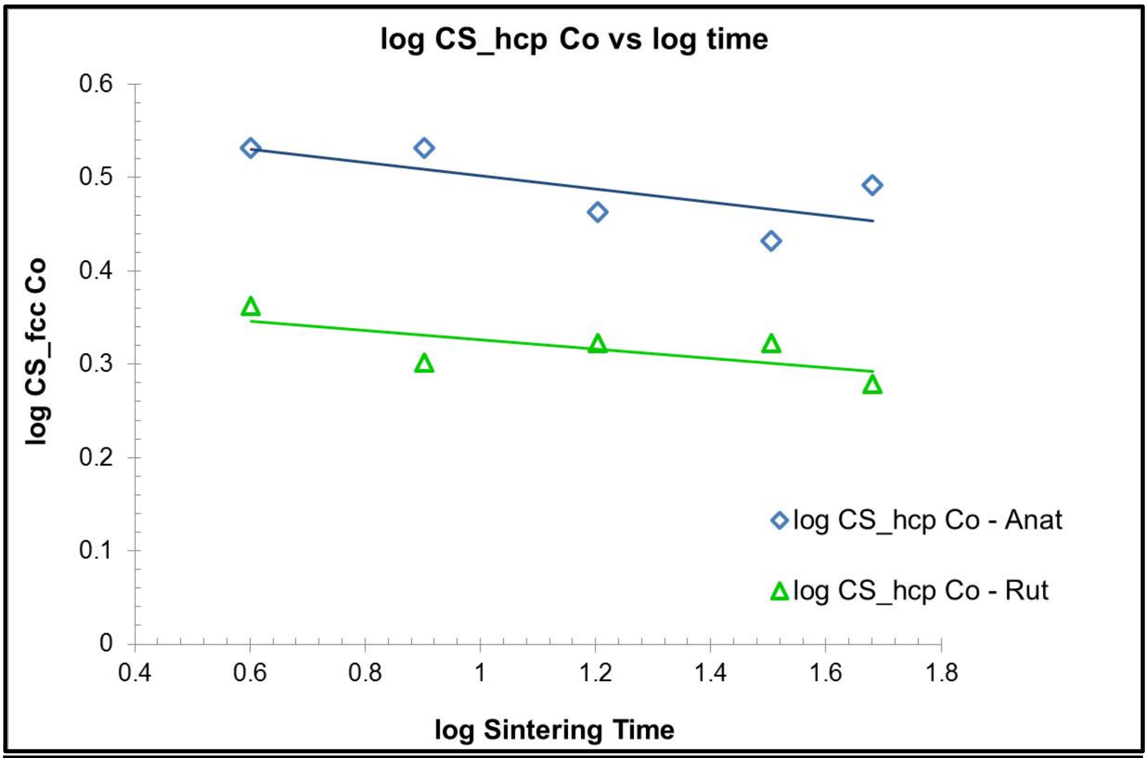

Figure 5. 36: Linearized plots of log hcp cobalt crystallite size against log sintering time for the titania-supported catalysts.

Fit Summary

The *2FI* model was compared to the *Linear* model since the hcp-cobalt crystallite size data was linearized. The results given in Table 5. 14 showed that the *Linear* model had the highest *Adjusted* R^2 and *Predicted* R^2. These were 0.9004 and 0.8427 respectively. The *2FI* model showed an *Adjusted* R^2 and *Predicted* R^2 of 0.8841 and 0.7461 respectively.

Table 5. 14: Fit summary for hcp cobalt crystallite size data

Model	Sequential p-value	Adjusted R-Squared	Predicted R-Squared
Linear	0.0001	0.9004	0.8427
2FI	0.9068	0.8841	0.7461

Model Summary

The results given in Table 5. 15 showed that the *Linear* model had the lowest *Std Dev* and. *PRESS* statistic value than the *2FI* model. This model was therefore analysed by ANOVA.

Table 5. 15: Model summary statistics for hcp cobalt crystallite size

Model	Std Dev	R-Squared	Adjusted R-Squared	Predicted R-Squared	PRESS
Linear	0.031	0.9225	0.9004	0.8427	0.014
2FI	0.034	0.9227	0.8841	0.7461	0.022

ANOVA Statistics

The statistics from ANOVA are given in Table 5.16. The *Linear* model was shown to be significant, with a *p-value* of 0.0001. Model terms *A* and *B* were also shown to be significant with *p-values* of 0.0624 and 0.0001 respectively.

Table 5. 16: ANOVA Statistics for the 2FI model for hcp cobalt crystallite size

Source	Sum of Squares	df	Mean Square	F Value	p-value
Model	0.081	2	0.0040	41.67	0.0001
A - log Sintering Time	4.73E-03	1	4.78E-03	4.90	0.0624
B - Support Type	0.076	1	0.076	78.44	0.0001
Residual	6.77E-03	7	9.66E-03		

The residuals plots were examined in order to assess the model. The normal probability plot of residuals showed residuals scattered in a straight line, indicating a normal distribution. The plot of externally studentized residuals also showed random scatter of the residuals. No outlier was observed in the data.

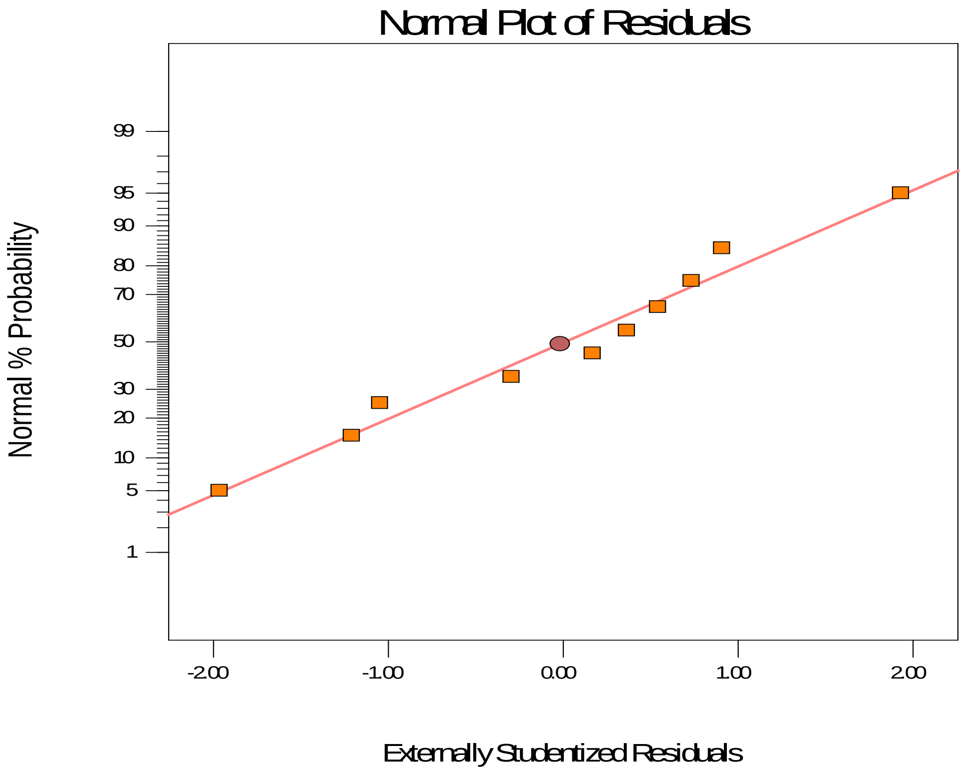

Figure 5. 37: A plot of Normal probability of residuals for response log CS_hcp Co

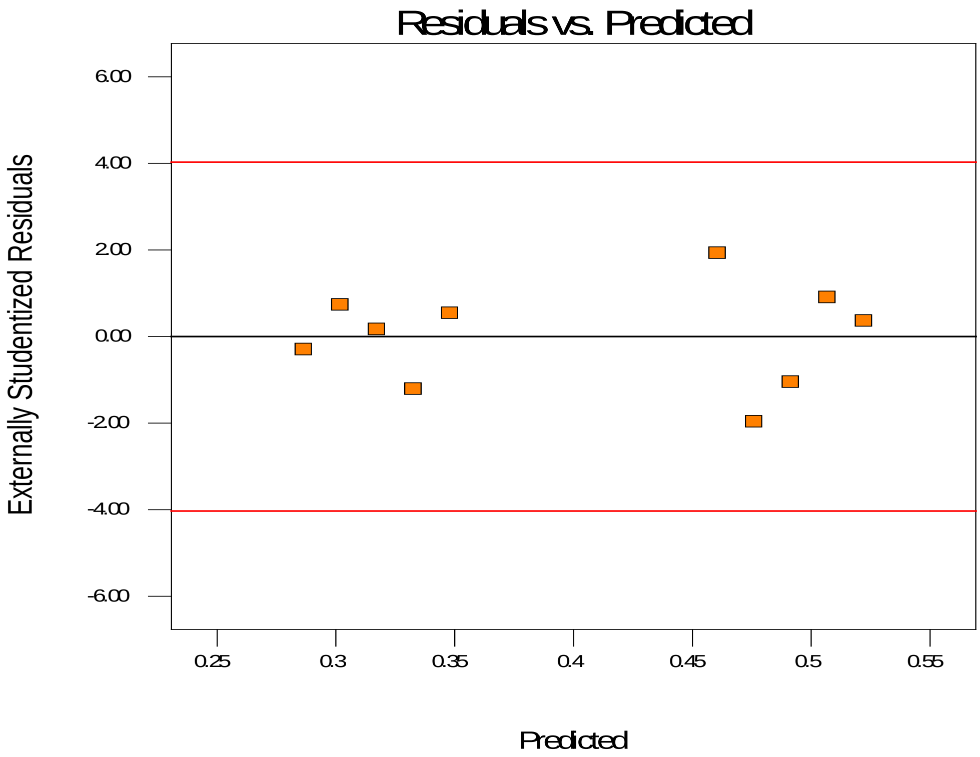

Figure 5. 38: A plot of externally studentized residuals for response log CS_hcp Co

The ANOVA results together with diagnostic plots confirm that the *Linear* model is adequate in describing the log-transformed sintering data of hcp-cobalt crystallites. The linear nature in turn indicates that the hcp crystallite size remains unchanged.. The final plots showing 95% confidence interval bands are given in Figure 5.39.

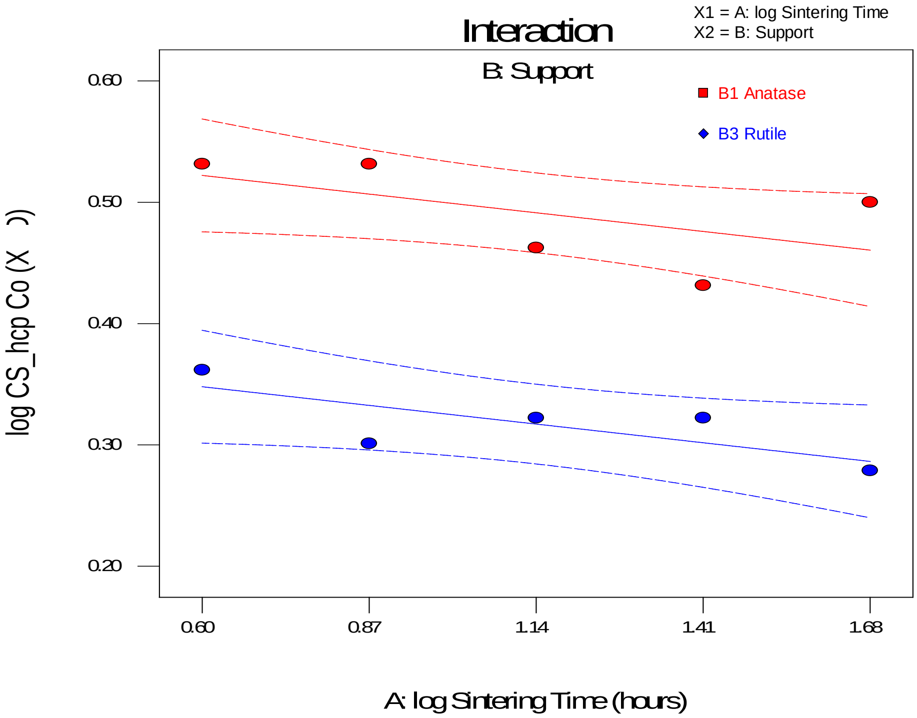

Figure 5. 39: Plots of response log CS_hcp Co against log Sintering Time (factor A) and Support (factor B) showing the 95% CI bands

5.4.2.3.Response – Cobalt Crystallite size (TEM)

The sintering of cobalt crystallites as studied by TEM was evaluated statistically by regression. The general plots of TEM derived cobalt crystallite size against sintering time are shown in Figure 5.40. The plots show that the crystallite size generally increases with increasing time showing a power law relationship. This response was transformed into a linear log – log relationship in order to accurately fit the data. The transformed log – log plot is given in Figure 5.41.

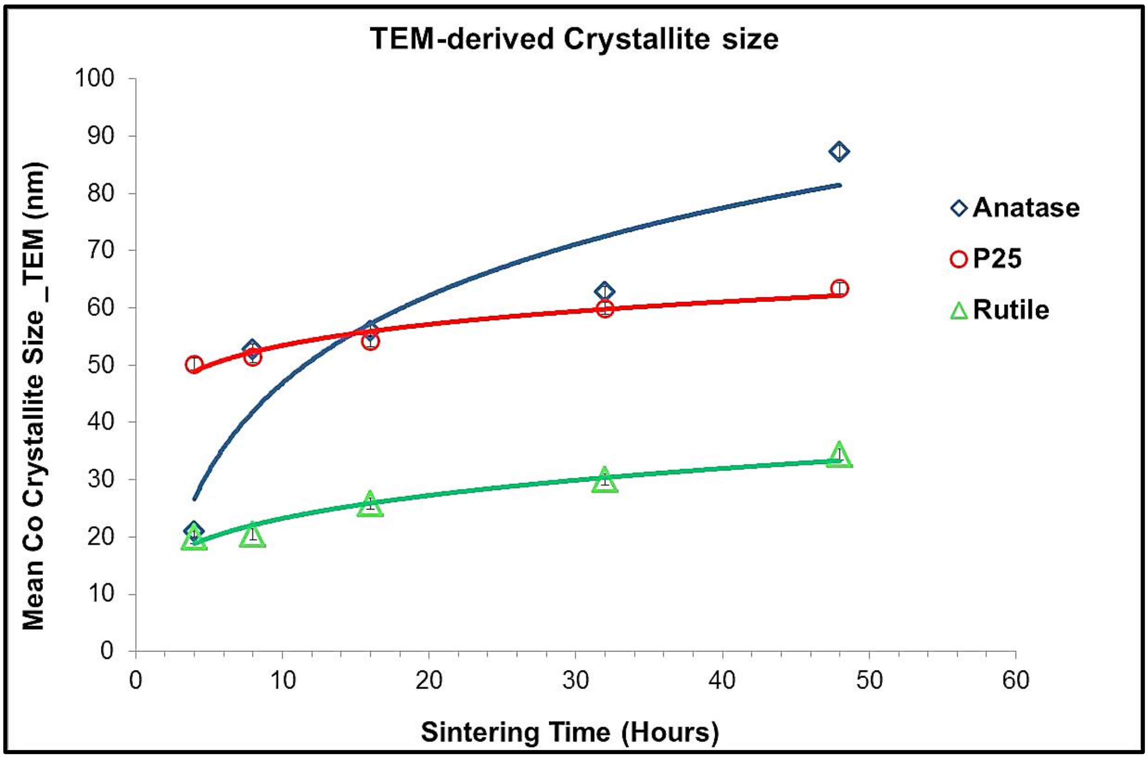

Figure 5. 40: Plots of TEM-based cobalt crystallite size against sintering time for Anatase, P25 and Rutile.

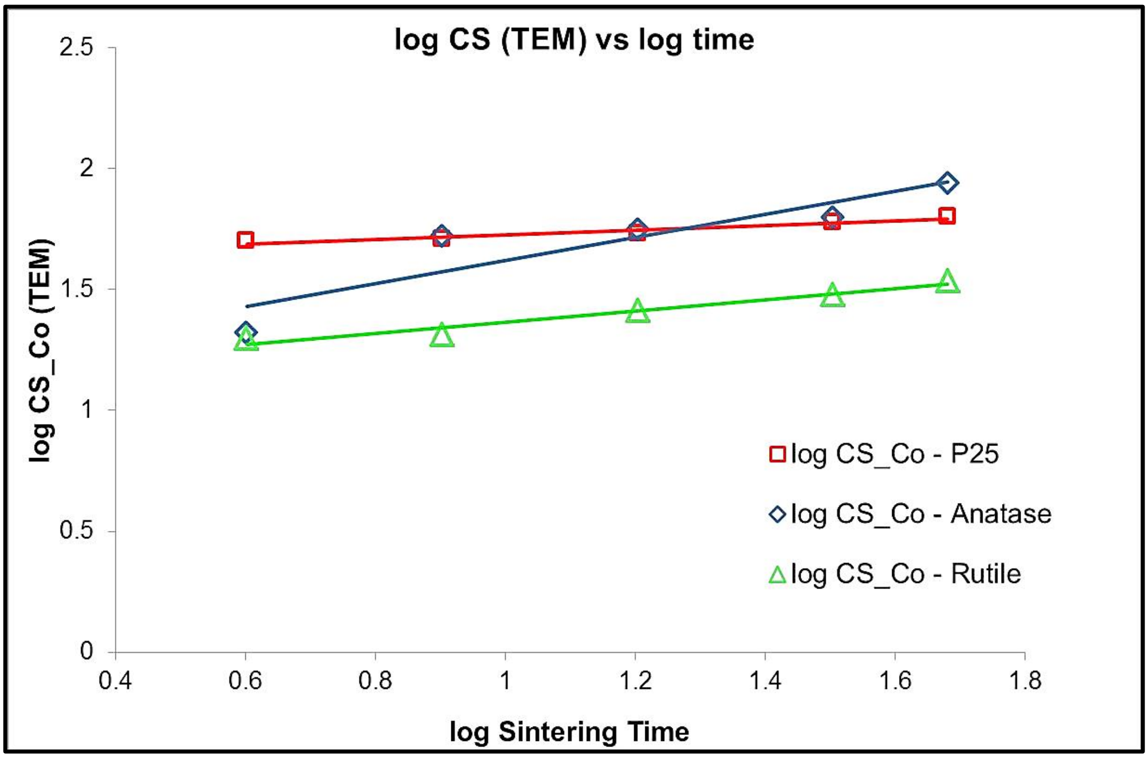

Figure 5. 41: Linearized plots of log cobalt crystallite size (TEM) against log sintering time for the titania-supported catalysts.

Fit Summary

The *2FI* model was compared to the *Linear* model. The fit summary given in Table 5.17 showed that the *2FI* model had the highest *Adjusted* R^2 and *Predicted* R^2. The *Linear* model showed the lowest *Adjusted* R^2 and *Predicted* R^2.

Table 5. 17: Fit summary for TEM derived cobalt crystallite size data

Model	Sequential p-value	Adjusted R-Squared	Predicted R-Squared
Linear	< 0.0001	0.9222	0.8692
2FI	< 0.0001	0.9932	0.9908
Quadratic	0.7398	0.9924	0.9879

Model Summary Statistics

Table 5.18 gives summary statistics for TEM derived crystallite sizes. The *2FI* model showed a *Std Dev* of 0.015 and *PRESS* value smaller than 0.005. The *Linear* model showed the highest *Std Dev* and *PRESS* value. It could be seen that the *2FI* model was more likely to fit the data than the *Linear* model. Therefore only the *2FI* model was analysed by ANOVA statistics.

Table 5. 18: Model summary statistics for TEM derived cobalt crystallite size

Model	Std Dev	R-Squared	Adjusted R-Squared	Predicted R-Squared	PRESS
Linear	0.056	0.9388	0.9222	0.8692	0.073
2FI	0.016	0.9956	0.9932	0.9908	5.11E-03
Quadratic	0.017	0.9957	0.9924	0.9879	6.72E-03

ANOVA Statistics

The statistics from ANOVA are given in Table 5.19. The *2FI* model was shown to be significant, with a *p-value* of <0.0001. The model terms *A*, *B*, and *AB* were shown to be significant. All the terms had *p-values* of <0.0001.

Table 5. 19: ANOVA Statistics for the 2FI model for TEM derived cobalt crystallite size

Source	Sum of Squares	df	Mean Square	F Value	p-value
Model	0.55	5	0.11	407.32	<0.0001
A - log Sintering Time	0.15	1	0.15	552.92	<0.0001
B - Support Type	0.37	2	0.19	683.79	<0.0001
AB	0.032	2	0.016	58.06	<0.0001
Residual	2.44E-03	9	2.72E-04		

The model was evaluated by looking at the residuals plots. The normal probability plot of residuals given in Figure 5.42 showed that the residuals were normally distributed. The externally studentized residuals plot given in Figure 5.43 showed randomly scattered residuals indicating a constant variance in the data. No outliers were identified from the plot. The *2FI* model has been shown to be adequate in fitting the data.

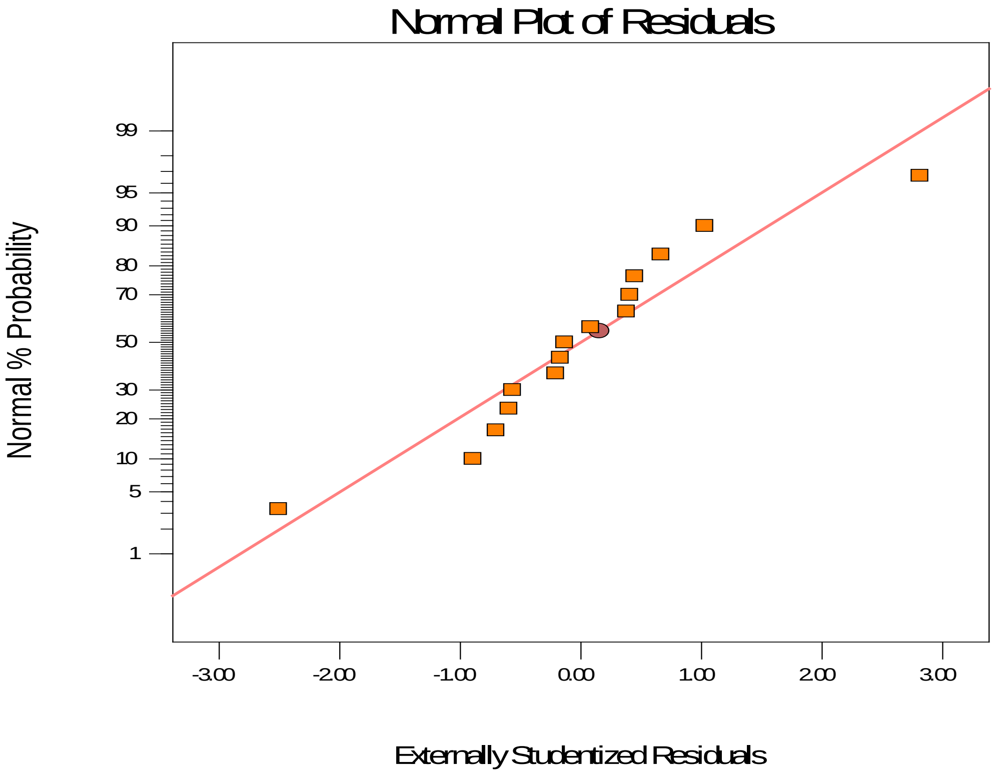

Figure 5. 42: A plot of Normal probability of residuals for response CS_Co (TEM)

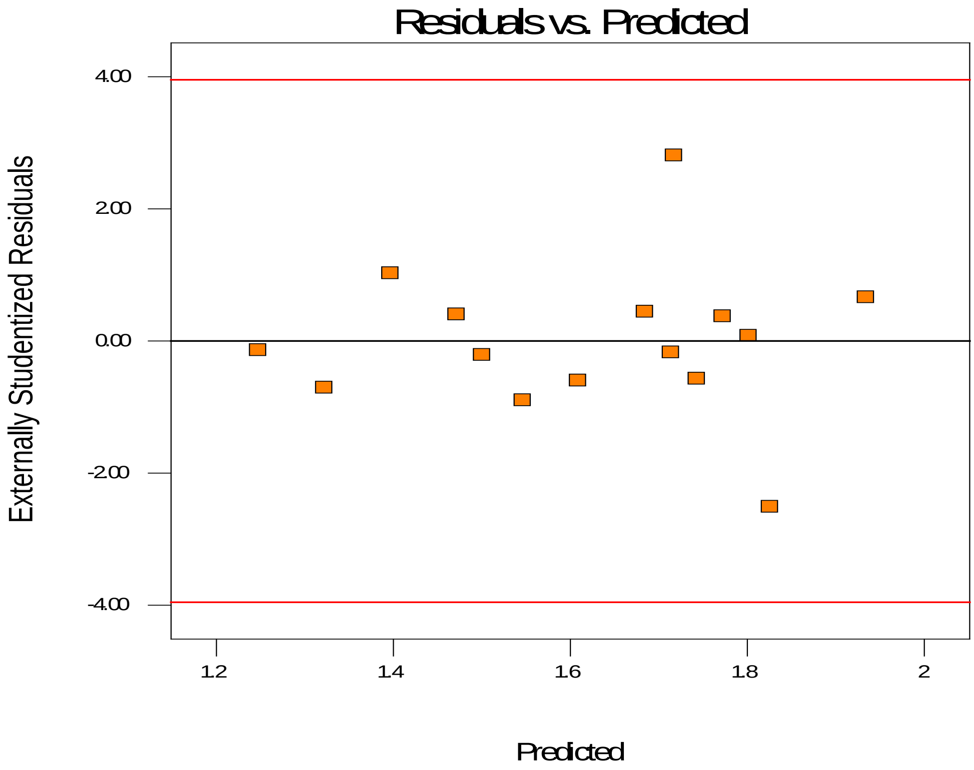

Figure 5. 43: A plot of externally studentized residuals for response CS_Co (TEM)

The sintering of fcc cobalt was shown to be different to that of hcp cobalt. The data showed that fcc cobalt crystallites grow with time exhibiting a power-law behaviour. Hcp cobalt crystallite size remained constant with time. The findings are in line with reported studies of supported cobalt catalysts.

Karaca *et al*, (2010 p.790) reported a similar behaviour in alumina-supported catalysts studied at realistic FTS conditions. The authors observed a 40% increase in fcc cobalt crystallite size after 6 hours. The hcp cobalt crystallites however, remained relatively constant throughout the run. Karaca *et al*, (2011 pp.14 – 26) later reported the same behaviour where the fcc cobalt crystallites sintered after 3 – 4h of reaction. The hcp crystallites remained constant.

Du Plessis *et al*, (2013 p.11644) reported a similar behaviour of fcc cobalt crystallites in alumina-supported catalysts. The authors observed a size increase for fcc cobalt crystallites while hcp cobalt crystallite size remained constant. Our results highlight that the sintering of cobalt crystallites on titania does not differ much from that of alumina-supported cobalt crystallites.

The 2*FI* model shows that the change in the response variable, say fcc cobalt crystallite size, cannot be predicted unless we know which titania phase is concerned. That is to say, the crystallite size can change differently depending on the specific titania phase used. A moderate or sharp power law increase may be observed depending on whether anatase or rutile support is used. This observation clearly shows that the titania phase affects the sintering behaviour of cobalt crystallites. The effect was further quantified by sintering kinetics studies discussed in the next section.

5.4.3. Evaluation and Comparison of Crystallite Size Data (XRD and TEM)

The preceding sections dealing with crystallite size measurements of sintered catalysts have highlighted differences between results measured by different techniques (XRD and TEM) and within each technique. It was observed that the XRD crystallite size measured for anatase-supported go from 30.8 nm up to 54.6 nm, while TEM crystallite sizes start from 30.2 nm up to 88.2 nm. XRD measured crystallite sizes of P25-supported went from 26.0 nm up to 35.0 nm indicating minor sintering. Meanwhile TEM measured crystallite sizes went from 50.7 nm up to 65.0 nm. In the case of rutile-supported catalysts, XRD measured crystallite sizes went from 25.2 nm up to 28.2 nm showing the lowest sintering. TEM measured crystallite sizes went from 16.9 nm up to 36.4 nm. These observations warrant a further discussion on the differences and the techniques.

In light of the discussion given in section 3.4.2, and looking at the crystallite size data of anatase-supported catalysts, it can be deduced that the larger sizes measured by TEM emanate from an aggregate of coherent scattering domains as measured by XRD. In this case, it can be expected that as sintering time increases, the aggregation of these scattering domains will increase forming a larger “crystallite” or “particle” as seen by TEM. It should also be kept in mind that the particles imaged by TEM may be in an oxide state or consist of a layer of oxide, leading to larger measured crystallite size. The same argument holds for P25-supported catalysts where the TEM measured crystallite size may consist of an aggregate of smaller domains measured in XRD. If it is assumed that the coherent scattering domain size does not change significantly with sintering time, it can be expected that XRD crystallite size will not increase significantly while TEM crystallite size increases as a result of the crystalline domain aggregation. This might explain the discrepancy between XRD and TEM results of anatase- and P25-supported catalysts.

5.4.4. Empirical Modelling of Sintering – SPLE and GPLE

The sintering order of the SPLE was of interest since it gives an idea of the sintering mechanism involved. The sintering order was obtained by linearizing the SPLE model by a log – log transformation. In this case, a plot of log (D/D_0) vs log time gives a slope of *n*.

The anatase-supported catalyst showed a sintering order *n* = 6 when fitted to the SPLE model. The sintering order highlights that both atomic and particle migration processes occur in the catalyst. The P25-supported catalyst showed a sintering order *n = 10* when fitted to the SPLE. In this catalyst, the sintering order did not change significantly with time. The rutile-supported catalyst showed a SPLE sintering order *n* = 4. The sintering order did not change with time.

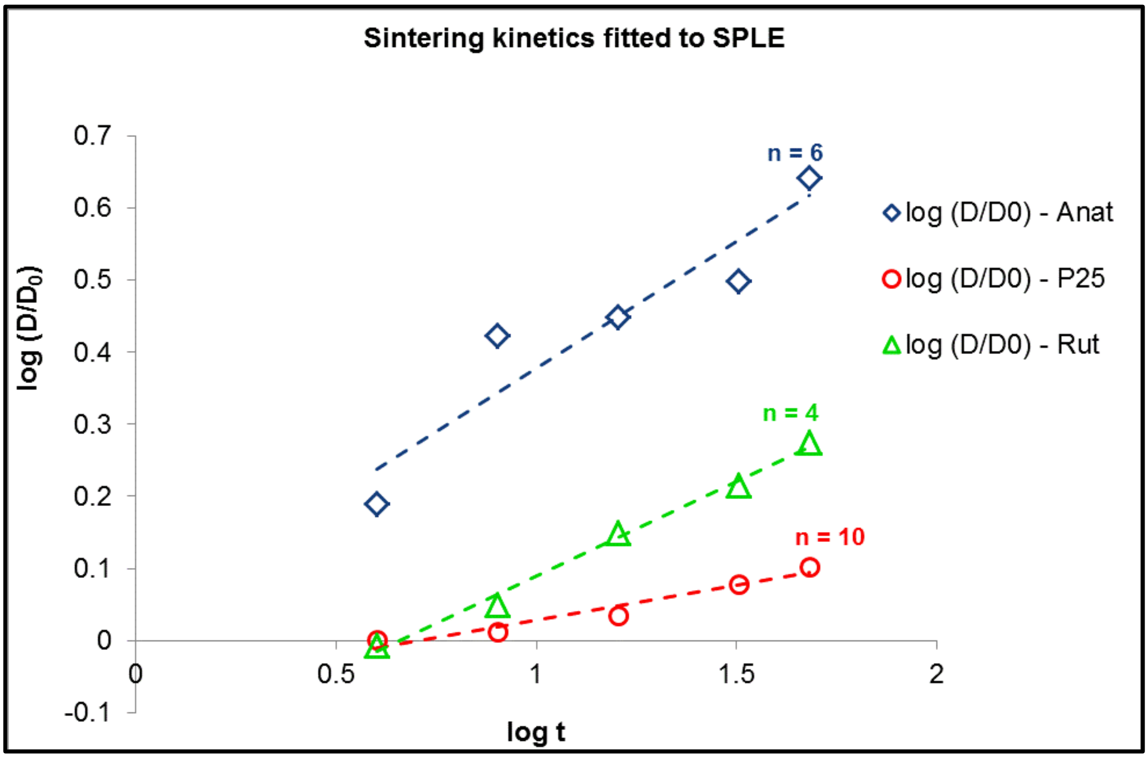

Figure 5. 44: Plots of log (D/D_0) against log time for anatase-, P25- and rutile-supported catalysts showing the sintering order as slope.

In the absence of sintering data for titania-supported cobalt catalysts, the sintering orders from our study were compared to those of other similar catalyst systems such as Ni/SiO_2 and Ni/Al_2O_3.It should be noted that these studies were conducted at slightly higher temperatures than our studies. Nonetheless, the studies serve as guidelines for typical sintering rate orders encountered for supported metal catalysts. A sintering order *n* = 3 – 13 was reported for a Ni/SiO_2 catalyst annealed at 500^{o}C in H_2. A sintering order *n* = 9.5 was reported for a Ni/Al_2O_3 catalyst annealed at 600^{o}C in H_2. A sintering order *n* = 4 – 11 was reported for a Ni/SiO_2 catalyst annealed at 700^{o}C in H_2 (Bartholomew 1993 p.7). It is clear from the studies that the SPLE sintering order generally varies from 3 – 13 for supported metal catalysts. It can be presumed that the sintering orders from our study are in line with those reported in literature.

Table 5. 20: Sintering results from the SPLE and GPLE kinetic models

Catalyst	D_{eq}	n (SPLE)	m* (GPLE)	k_s (h^{-1})
Anatase	4.72	6	1	0.25
P25	1.88	10	1	0.0065
Rutile	5.14	4	1	0.055

*Sintering order of best fit model.

D_{eq} was initially estimated for each catalyst system. This was followed by iteration to obtain the best fit in the models. In our study, both the first order (*m* = 1) and second order (*m* = 2) GPLE were fitted to the data. The plots are given in Figure 5.45 and Figure 5.46 respectively. The first order GPLE model gave a better fit to the data, and was consequently used to calculate the sintering rate constant k_s. Lif *et al*, (2002 p.149) also found that the first order GPLE gave a better fit to their data of alumina-supported nickel catalyst annealed at 210 – 250^{o}C in NH_2/H_2 atmosphere. The first-order sintering rate constant was found to be 0.25 h^{-1}, 0.0065 h^{-1} and 0.055 h^{-1} for anatase- , P25- and rutile-supported catalysts respectively. Since the GPLE allows one to compare different catalyst sintering behaviour, for the same sintering order, it is worthwhile to compare the sintering rate constants. It is clear that the Anatase-supported catalyst underwent more sintering than the P25- and Rutile-supported catalysts. This is evident from the sintering rate constants. It can be seen that the sintering rate constant of Anatase is almost ten times higher than that of Rutile-catalyst. In turn, the sintering rate constant of Rutile catalyst is almost ten times higher than that of P25 catalyst.

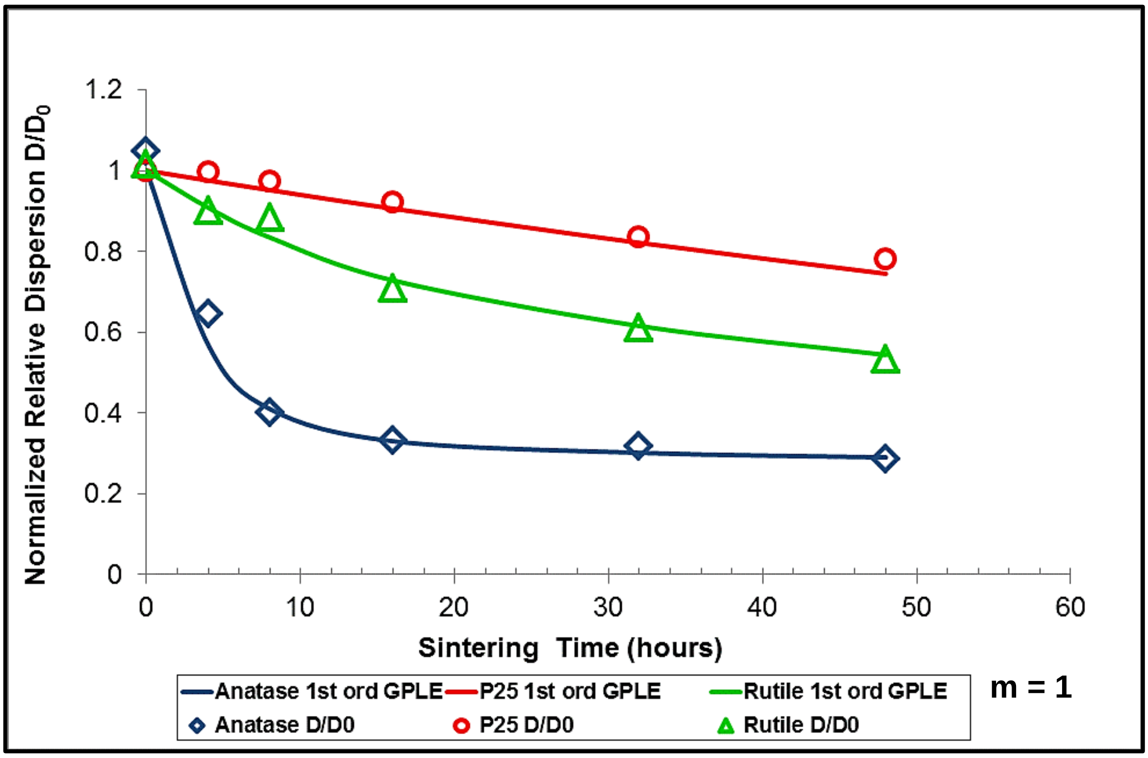

Figure 5. 45: Plots of normalized dispersion against time for anatase-, P25- and rutile-supported catalysts fitted to the GPLE (m=1)

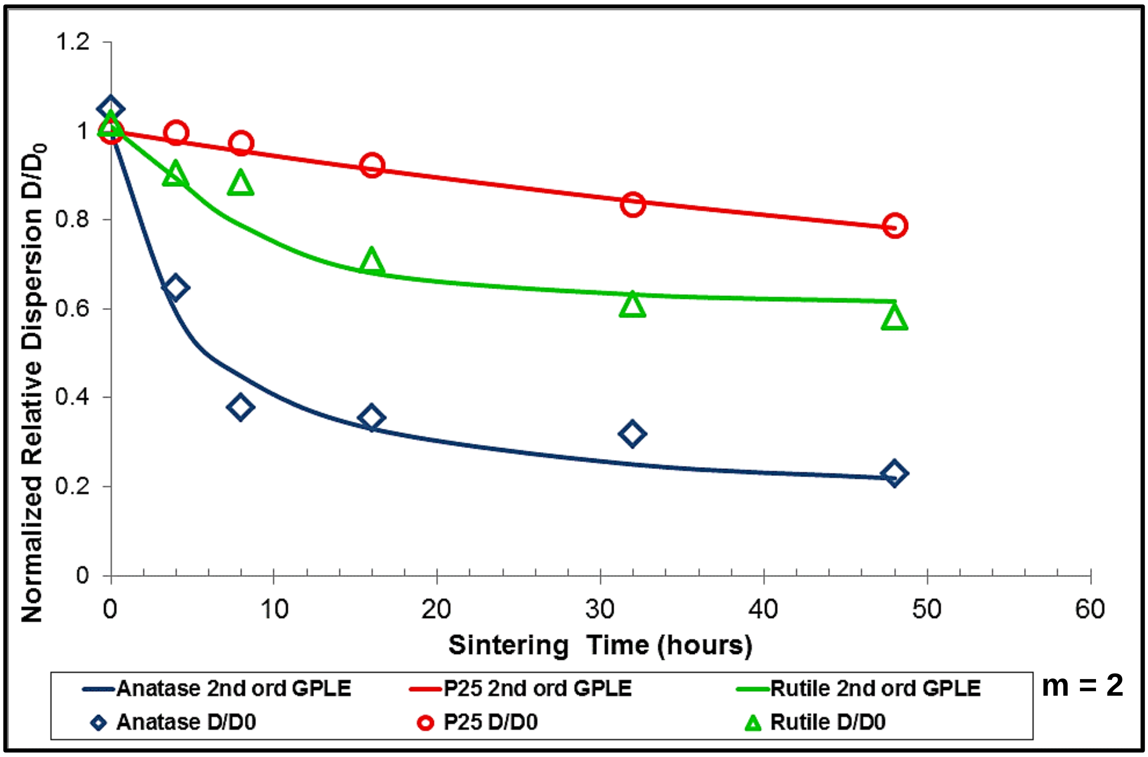

Figure 5. 46: Plots of normalized dispersion against time for anatase-, P25- and rutile-supported catalysts fitted to the GPLE (m=2)

In the absence of sintering data, the GPLE sintering rate constants were compared to similar studies reported by Bartholomew (1993 p.14) albeit at different temperature. In one study, a δ-Al_2O_3–supported nickel catalyst annealed at 600°C in H_2 showed a sintering rate constant of 0.037 h^{-1}. A similar nickel catalyst supported on γ-Al_2O_3 and annealed at the same temperature and atmosphere showed a sintering rate constant of 0.057 h^{-1}. The results clearly show the effect of the support on sintering of nickel crystallites.

The same argument may hold in our study. The different sintering rate constants observed in our study may indicate the effect of the titania phase on sintering behaviour of cobalt crystallites. There are few factors which are characteristic of each titania phase, that may explain the difference in sintering behaviour of cobalt crystallites. These factors include metal-support interaction, starting cobalt crystallite size, surface free energy and defects on the surface of the titania phase.

It has been shown that a strong interaction between the metal and support may lead to a better contact between the metal and support. This concept of wetting may be applied to our system of titania-supported cobalt catalyst. If we infer a strong interaction between cobalt crystallites and rutile support, as proposed by Shimura *et al*, (2013), we can expect better wetting of the rutile support by the cobalt species, compared to wetting of the anatase support. This observation was confirmed by TEM results which showed cobalt crystallites lying flat on rutile crystallites as pointed out by the arrows in the image. The wetting phenomenon is shown in Figure 5.47. It can be inferred further, that cobalt crystallites wetting the support, or interacting closely with the support, will sinter less than those in poor contact with the support. The strong interaction might inhibit growth of these crystallites, especially by coalescence mechanism. This might be the case for rutile-supported crystallites in our study.

Chen *et al*, (2006 pp. 666 – 667) observed a similar effect in titania-supported nickel catalysts. In their study, rutile-supported nickel crystallites were observed to be small and well dispersed than anatase-supported nickel crystallites. They concluded that the difference in crystallite size and dispersion was due to different metal-support interaction.

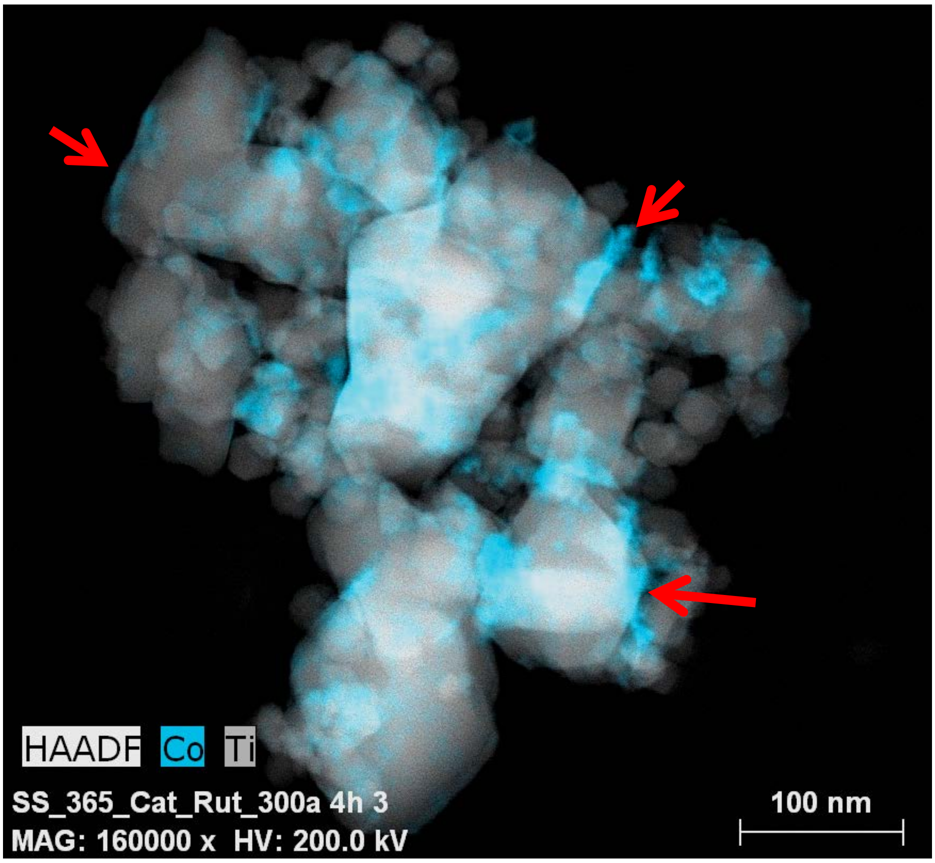

Figure 5. 47: A HAADF-STEM image superimposed with EDX mapping of Rutile-supported catalyst showing wetting of the support by cobalt species.

The starting cobalt crystallite size from a TEM point of view may also influence the sintering behaviour in these compared to anatase- and Rutile-supported catalysts. The trend in terms of starting cobalt crystallite size is as follows: P25 > rutile = anatase. This trend shows a reverse relationship with the sintering rate constants. In this case the trend is: anatase > rutile > P25. Therefore keeping all other factors constant, it can be seen that anatase-supported cobalt crystallites underwent more sintering (k_s = 0.25 h^{-1}) compared to rutile- (k_s = 0.055 h^{-1}) and P25-supported catalysts (k_s = 0.0065 h^{-1}). This is in line with thermodynamic principles, since smaller crystallites will coalesce straightaway to minimise the surface free energy. It should be kept in mind that the above sintering rate constants were derived from relative dispersion obtained from TEM measured crystallite sizes since the sintering kinetic models are fitted to dispersion data obtained from either TEM or H_2-chemisorption techniques (Bartholomew 1996 p.6).

The defect sites of the titania phase may also be of important in the interaction and sintering of cobalt crystallites. It is known that defects such as oxygen vacancies and Ti interstitials exist in the surface and bulk of titania phases (Selloni 2008 p.29). It has been shown that defects are likely to form on the surface of Rutile rather than in the bulk since this phase is more stable. In the case of anatase, the defects are likely to form in the bulk rather than on the surface since this phase has the lowest surface free energy.

It has been shown that metals preferentially form bonds on the defect sites on the surface of titania (Chen & Goodman 2007 pp.42 – 43). In this case, the defect site acts as an anchor for the metal onto the titania support. It is proposed that the observed difference in sintering behaviour of cobalt crystallites may be correlated to the effect of defect sites in the surface of Rutile support. Cobalt species supported on Rutile may be anchored by the surface defect sites, thereby inhibiting growth by coalescence or migration. In the case of anatase- and P25-supported catalysts, these defects are likely to be found in the bulk, therefore cobalt crystallites on the surface are not bound so strongly and subsequently agglomerate or coalesce.

The lower rate of sintering observed for P25-supported catalyst can be explained by looking at the starting cobalt crystallite size. This catalyst had the largest cobalt crystallite size amongst the three titania supported catalysts. Therefore the need for surface energy decrease is not as great as that of small crystallites in anatase- and rutile-supported catalysts. This low driving force therefore means that the tendency of particles to sinter will be lower than that of the other catalysts.

5.4.5.Phenomenological Modelling of sintering – Ostwald Ripening or Particle Migration

The two growth mechanisms involved in sintering of nanoparticles (Ostwald ripening and coalescence) were studied. It has been shown that these mechanisms may occur simultaneously in a catalyst (Hansen *et al*, 2013 p. 1720). In this case, one of the mechanisms will be the dominant mechanism at specific conditions. In our study, the SPLE sintering order was used to give an idea of the dominant mechanism during sintering of cobalt crystallites. It has been shown that sintering orders, $n = 2 – 4$ are indicative of atomic migration or interparticle migration via vapour phase. Sintering orders, $n = 5 – 15$ are said to be indicative of particle migration or coalescence (Harris 1995 p.103).

An SPLE sintering order $n = 6$ was reported for anatase-supported catalyst. This sintering order indicates that both Ostwald ripening and particle migration take place in the catalyst. This observation was confirmed by TEM results. HAADF-STEM images of the anatase catalyst annealed at 365°C for 4 hours showed the presence of large crystallites. The morphology of these large crystallites is the key aspect in deducing their growth mode. These crystallites have a “solid” appearance, as opposed to the “clustered” crystallites in the reduced & passivated catalyst. Therefore it can be inferred that these large “solid” crystallites grew by the Ostwald ripening mechanism. The HAADF-STEM images and conceptual illustration are given in Figure 5.46. The catalyst annealed for 48 hours showed evidence of particle migration in addition to atomic migration. In this case large crystallites can be seen coalescing in addition to the large “immobile” crystallites.

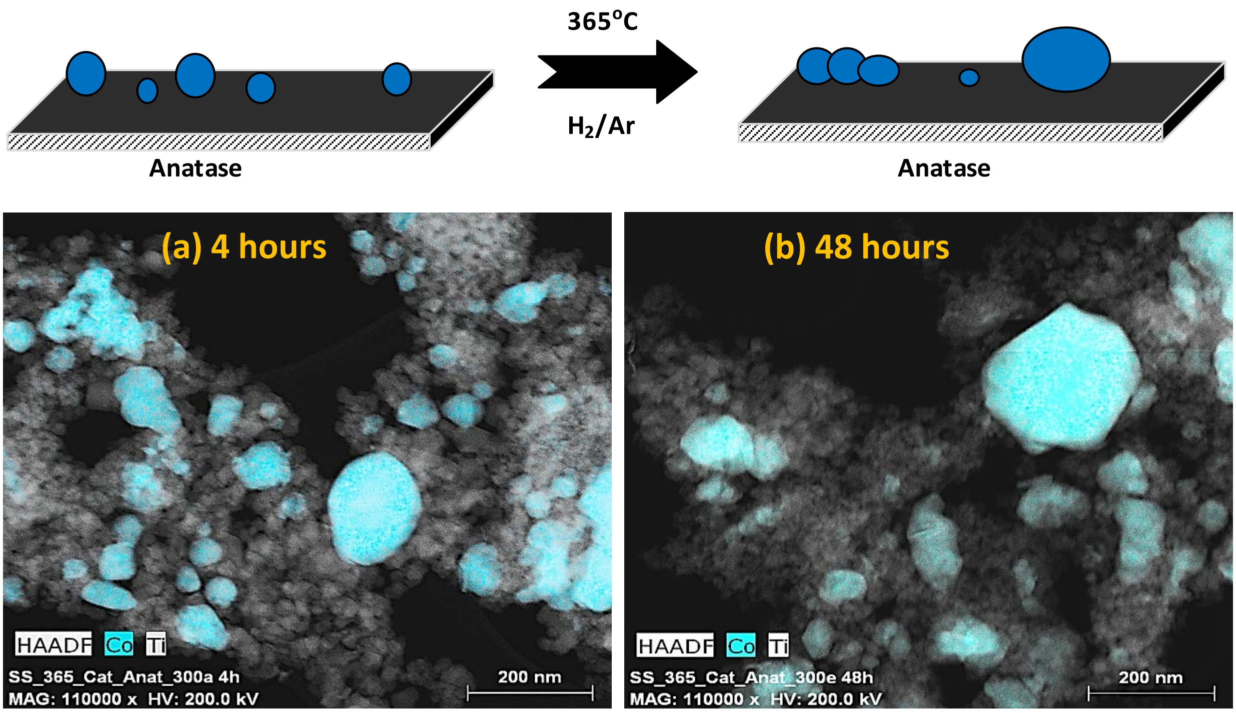

Figure 5. 48: HAADF-STEM – EDX map images of anatase – supported catalyst showing cobalt crystallites sintered for (a) 4 hours and (b) 48 hours.

The P25-supported catalyst showed an SPLE sintering order n = 10. This value indicates that particle migration was main mechanism in the P25-supported catalyst. TEM results also confirmed the observation. The P25-supported catalyst annealed for 4 hours showed the onset of coalescence. Some crystallites can be seen clearly touching or coalescing. It is interesting to note that the coalescing crystallites have a size similar to that of the reduced & passivated catalyst. Coalescence was also shown to be the dominant mechanism in the sample annealed for 48 hours. Crystallites can be seen coalescing into large “blobs”. The HAADF-STEM images and conceptual illustration are given in Figure 5.49.

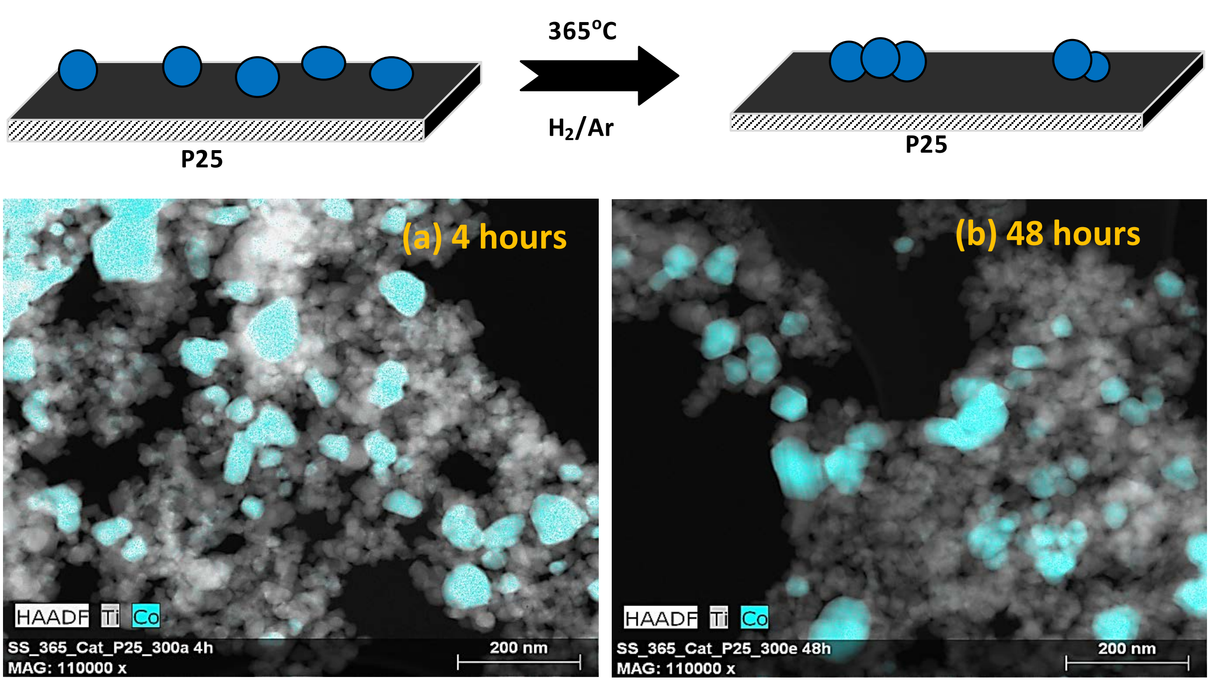

Figure 5. 49: HAADF-STEM – EDX map images of P25 – supported catalyst showing cobalt crystallites sintered for (a) 4 hours and (b) 48 hours.

The SPLE sintering order for Rutile catalyst was shown to be n = 4. This value indicates that Ostwald ripening was the dominant mechanism in the sintering of Rutile-supported cobalt crystallites. The sample annealed for 4 hours showed the presence of both large and small crystallites. The sample annealed for 48 hours showed the remnants of small crystallites in addition to large crystallites. The argument in the previous section is confirm by the SPLE sintering order and TEM results, in that a strong metal-support interaction might inhibit growth via coalescence. The only feasible path is therefore atomic migration or interparticle migration via vapour phase.

It should be kept in mind that the images shown in Figure 5.49, Figure 5.50 and Figure 5.51 only highlight the possible mechanism of sintering, and not necessarily the absolute particle size. The particle size was obtained from a series of HAADF-STEM images some of which consist of small particle; hence a size distribution is obtained for each supported catalyst.

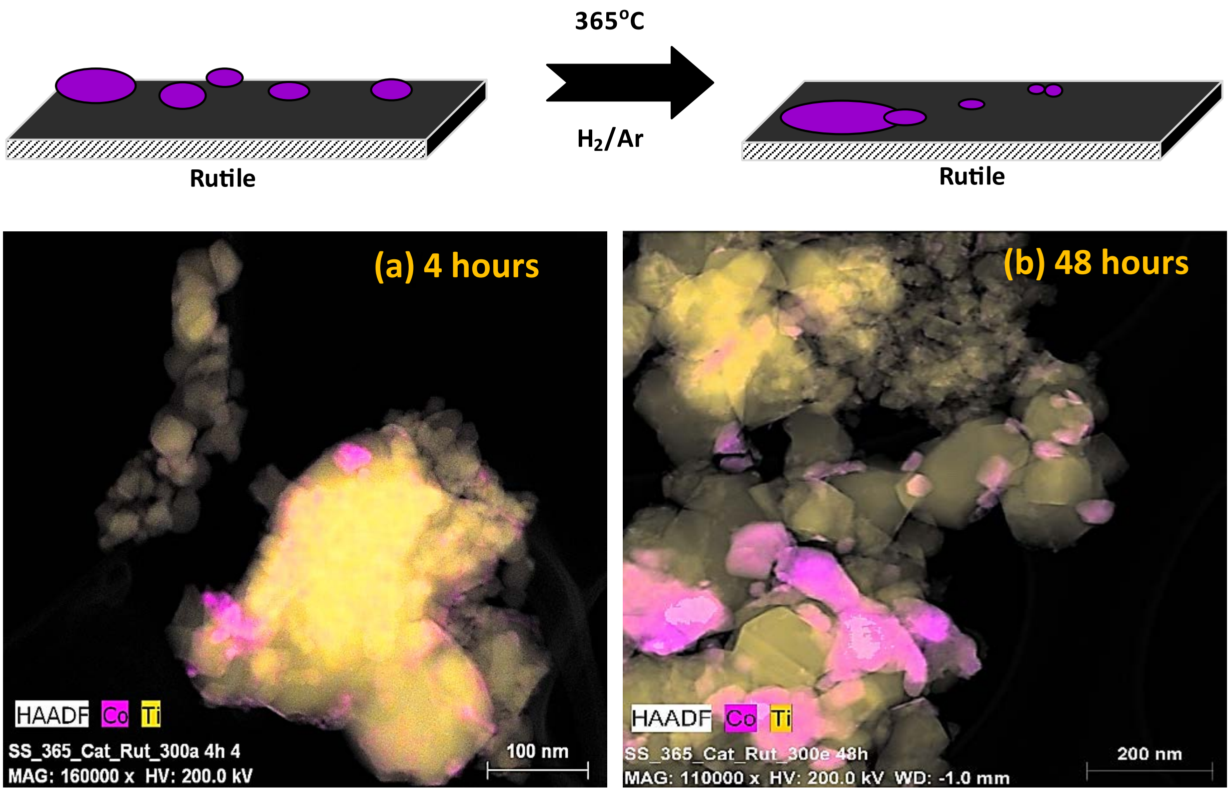

Figure 5. 50: HAADF-STEM – EDX map image of Rutile – supported catalyst showing cobalt crystallites sintered for (a) 4 hours and (b) 48 hours.

The results have shown that the type of type of titania support does influence the sintering behaviour of cobalt crystallites. In terms of sintering mechanism, the support may also influence the dominating sintering mechanism. In the case where the support interacts weakly with the cobalt crystallites, PMC will be the main mechanism since there will be no retardation effect from the support. In this case particles will migrate on the surface much more readily. This might be the case in anatase-supported catalysts

In the case where there is strong interaction between the metal and support, OR will be favoured. This because while the supports holds on to the metal crystallites tightly, it allows for the ejection of atomic species from the metal resulting in the decrease in the size of smaller particles and large particles grow larger at the expense of the smaller particles. This might be the case in Rutile-supported catalysts. The sintering behaviour of the cobalt crystallites is therefore highly influenced by the nature of metal-support interaction.

The support pore size is also postulated to play a role in the sintering of cobalt crystallites. Stassinos & Lee have stated that the effect of pore size can far outweigh the effect of metal-support interaction on the sintering kinetics. In our study it was shown that the P25 support had the largest pore size followed by rutile and anatase supports. Figure 5.52 shows that the GPLE first-order sintering rate constant of the catalysts decreases with increasing support pore size. Stassinos & Lee have showed through theoretical studies that the sintering rate constant decreases exponentially with increasing pore size. We can deduce that the pore size is one of the main factors which influence the sintering behaviour of titania-supported catalysts.

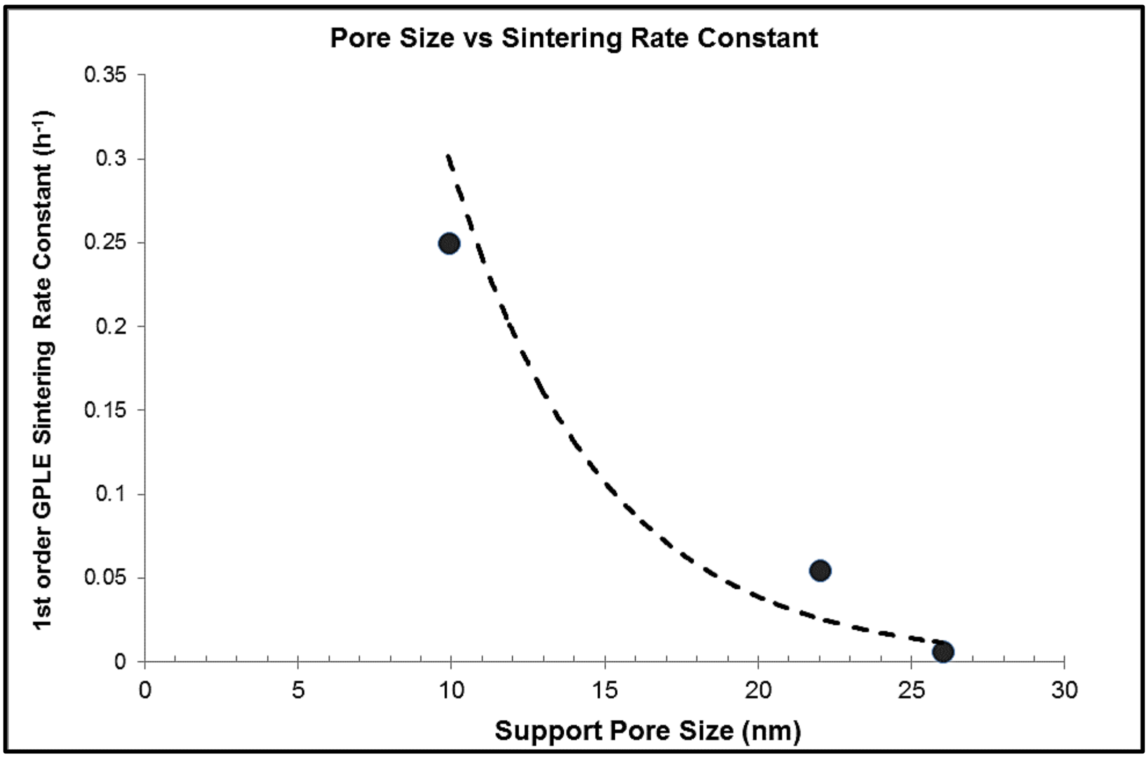

Figure 5. 51: Correlation of GPLE first-order sintering rate constant with support pore size.

Sintering was seen to be more prevalent in anatase-supported catalyst compared to P25- and rutile-supported catalysts. Since the goal of a catalyst manufacturer is to produce a stable, active and selective catalyst amongst other properties, from an industrial application point of view P25 is the most preferred support showing the least sintering probability which translates to a better stability of supported crystallites.

CHAPTER 6
SUMMARY AND CONCLUSIONS

6. CHAPTER 6 – SUMMARY AND CONCLUSIONS

6.1. SUMMARY

6.1.1. Stage 1 – Support Characterization

Three titania supports were obtained. The supports were identified as Anatase-, P25- and Rutile-support. These were characterized by XRD, TEM, BET and Raman spectroscopy. The findings are summarized here.

The Anatase-support was shown to consist of 100% anatase phase by XRD. The support consists of small particles with mean crystallite size of 11.7 nm and a FWHM of 8.1 nm as seen in TEM images. The support was shown to have the highest surface area and mesoporous pore structure. The P25-support was shown to consist of ~85% anatase and ~15% rutile phases. The support consists of two distinct classes of particles. There are small particles with an estimated size of ~30 nm, and large particles with an estimated size of ~50 nm and larger. The overall mean crystallite size from TEM was found to be 22.8 nm with a FWHM of 16.1 nm. The support was shown to have a surface area lower than that of the Anatase-support, but higher than that of the Rutile-support. P25-support also has a mesoporous pore structure. The Rutile-support was shown to consist of ~2% anatase and ~98% rutile phases. The support consists of large particles with a mean crystallite size of 79.7 nm and FWHM of 71.1 nm. This support had the lowest surface area, although still had a mesoporous pore structure.

Raman Spectroscopy showed characteristic differences between the support phases. Anatase was shown to consist of six characteristic bands while rutile showed four bands. The rutile bands are usually weak compared to anatase bands. Hence the identification of rutile phase in P25-support was almost overlooked.

6.1.2. Stage 2 – Catalyst Characterization (Calcination study)

The calcination temperature during catalyst preparation was varied between 200°C - 400°C. This was done in order to determine its effect on the physico-chemical characteristics of the cobalt catalysts.

It was found that calcination temperature did not affect the size of the Co_3O_4 crystallites. The support influenced the phase composition of the calcined catalysts. In this case, the titanate phase $CoTiO_3$ was preferentially formed in Rutile-supported catalysts and not in Anatase- and P25-supported catalysts. Calcination in air at a temperature range from 200°C – 400°C did not significantly affect the pore structure of the calcined catalysts. The mesoporous nature of the catalysts was retained after calcination.

6.1.3. Stage 3 – Catalyst Reduction

The calcined catalysts were reduced in H_2/Ar at 450°C to convert the cobalt oxide into metallic species. Different cobalt dispersion was observed in the titania supports from a H_2-chemisorption point of view. P25-support showed the highest cobalt dispersion among the supports, followed by Rutile-support and Anatase-support.

The starting metallic cobalt crystallite size was influenced by the type of titania support phase as evidenced by TEM analysis. Smaller particles were obtained in Anatase- and Rutile-supported catalysts. P25-support gave slightly larger cobalt crystallites. The smaller cobalt particles in Anatase-support were shown to undergo agglomeration in the reduction step. This was observed as clusters in TEM images.

TPR analysis of the bare supports showed that the supports were reduced by hydrogen. It is postulated that the interaction with hydrogen leads to the formation of surface and bulk defects such as oxygen vacancies and Ti^{3+} interstitials. These defects are thought to have an effect on the supported cobalt crystallites. The reduction behaviour of cobalt was shown to be influenced by the titania-support type. TPR showed different reduction profiles in the different supports, which might indicate different extents of metal-support interaction due to the postulated defects on the support surface. The titania support also influenced the presence of fcc and hcp cobalt. Both fcc and hcp cobalt were obtained in Anatase- and Rutile-supported catalysts. Only fcc cobalt was obtained in P25-supported catalysts.

6.1.4. Stage 4 – Sintering Studies

The sintering of cobalt crystallites supported on the different titania supports was studied. The particle size data from the TEM were fitted well to lognormal distribution function. The PSD fitted onto the lognormal function changed with sintering time, confirming the occurrence of sintering of the cobalt particles. The broadening and shift to larger sizes was shown to be significant using the Kolmogorov-Smirnov test. The crystallite size data from XRD and TEM showed a power-law type of growth when plotted against time. The crystallite size measurements highlighted important differences between the two techniques. These differences originate from their measurement principles.

The sintering kinetics was also studied. In this case, the data was fitted well to the simple power law expression (SPLE) and generalized power law expression (GPLE) models. These models describe sintering kinetics in terms of rate constant and rate order. The sintering data in all three supports were fitted well to the first order GPLE model. The sintering was shown to be different in the three supports as shown by different sintering rate constants.

Mechanisms of sintering were also studied by conjecture. It was concluded that both Ostwald ripening (OR) and particle migration and coalescence (PMC) might occur at different extents in the titania supports. It was inferred that Anatase-supported cobalt crystallites most likely underwent both OR and PMC. P25-supported cobalt crystallites most likely underwent PMC, while Rutile-supported cobalt catalyst most likely experienced both OR and PMC, OR being the dominant mechanism.

6.2. CONCLUSIONS

In light of the findings summarized in the previous section, it is appropriate to revisit the research questions and objectives of the study.

- The titania support phase influences the material science characteristics of model calcined, reduced and sintered crystallites. This effect may stem from the different metal-support interaction that occurs in the different titania phases. This leads to different interaction with metallic cobalt with subsequent different sintering behaviour. Sintering was seen to be more prevalent in anatase-supported catalyst compared to P25- and rutile-supported catalysts. From an industrial application point of view P25 is the most preferred support showing the least sintering probability.

- It can be inferred that a weak metal-support interaction exists between Anatase and cobalt crystallites. This leads to an increase in the prospect of sintering. Rutile, meanwhile shows a strong interaction with cobalt crystallites. This strong interaction suppresses the need for agglomeration or sintering of the crystallites. An interesting phenomenon is encountered in P25 support. In this support, it can be supposed that the presence of rutile phase at the optimum amount stabilizes the cobalt crystallites and prevents sintering hence the lowest sintering was observed.

- The nature of the cobalt-support interaction might be determined by the defect chemistry and surface energy of the titania support phase. It was shown that the support interacts with hydrogen during temperature programmed reduction. The postulation of this study is that surface defects are formed as result. It is known that oxygen vacancies are most likely to occur in the surface of rutile, while in anatase the vacancies prefer subsurface or bulk. It is said that the cobalt binds strongly on these oxygen vacancies resulting in strong metal support interaction. Thus lower sintering in Rutile support than Anatase support.

- Sintering is time-dependent. This was shown through sintering studies which showed larger crystallites with increasing sintering time. This effect was also evident in PSDs of cobalt crystallites which shifted to larger sizes with time. The effect of time was seen in all the titania supports studied and shown to be statistically significant.

6.3. FUTURE WORK

Due to the limited time available for the current research project, other aspects were not explored. Therefore these can be explored in future studies. The following recommendations are suggested.

- Catalytic measurements of fresh and sintered catalysts to determine the catalyst performance factors such as activity and selectivity to determine the effect of sintering and support. This may help reconcile differences observed in crystallite size measurements from XRD and TEM.

- The study of the effect of temperature on the sintering behaviour of model cobalt crystallites supported on the titania supports used in our study. In this respect, concepts such as the Tamman and Huttig temperatures can be studied. The Arrhenius plots can also be determined.

- The study of the effect of sintering atmosphere on the sintering behaviour of model cobalt crystallites supported on titania supports. In our study, the atmosphere was reducing, where H_2/Ar gas mixture was used. In future studies, a gaseous atmosphere similar to that encountered during Fischer-Tropsch synthesis can be explored. Different sintering behaviour has been reported for different atmospheres in literature, albeit for other catalyst systems. Therefore the effect of different atmosphere may be of interest for the current catalyst system.

7. REFERENCES

AGUIRRE, M.C., SANTORI, G., FERRETTI, O., FIERRO, J.L.G. & REYES, P., 2006. Morphological and structural features of Co/TiO2 catalysts prepared by different methods and their performance in the liquid phase hydrogenation of α, β unsaturated aldehydes. *Journal of the Chilean Chemical Society*, 51(1) 1-16.

AKBARI, B., PIRHADI TAVANDASHTI, M. & ZANDRAHIMI, M. 2011. Particle size characterization of nanoparticles: A practical approach. *Iranian Journal of Materials Science & Engineering*, 8 (2) 49-56.

ALLOYEAU, D., PRÉVOT, G., LE BOUAR, Y., OIKAWA, T.,LANGLOIS, C.,LOISEAU, A. & RICOLLEAU, C. 2010. Ostwald Ripening in nanoalloys: When thermodynamics drives a size-dependent particle composition. *Physical Review Letters*, 105, 255901-1-3.

ALLOYEAU, D., RICOLLEAU, C., OIKAWA, T., LANGLOIS, C., LE BOUAR, Y. & LOISEAU, A., 2008. STEM Nanodiffraction technique for the structural analysis of CoPt nanoparticles. *Ultramicroscopy*, 108, 656-662.

ALVAREZ, P. M., BELTRAN, F. J., POCOSTALES, J. P. & MASA, F. J. 2007. Preparation and structural characterization of Co/Al2O3 catalysts for the ozonation of pyruvic acid. *Applied Catalysis B: Environmental*, 72, 322-330.

ASLAN, N. 2008. Application of response surface methodology and central composite rotatable design for modelling and optimization of a multi-gravity separator for chromite concentration. *Powder Technology*, 185, 80-86.

ATASHI, H., SIAMI, F., MIRZAEI, A.A., & SARKARI, M., 2010. Kinetic study of Fischer-Tropsch process on titania-supported cobalt-manganese catalyst. *Journal of Industrial and Engineering Chemistry*,16, 952–961.

AZÁROFF, L.V. & BUERGER, M. J. 1958. The Powder Method in X-ray Crystallography. McGraw-Hill. New York.

AZIZI, D., SHAFAEI, S.Z., NOAPARAST, M. & ABDOLLAHI, H. 2012. Modelling and optimization of low grade Mn bearing ore leaching using response surface methodology and central composite design. *Transactions of Nonferrous Metals Society of China*, 22, 2295-2305.

BARKHUIZEN, D., MABASO, I., VILJOEN, E., WELKER, C., CLAEYS, M., VAN STEEN, E. & FLETCHER, J. C. Q. 2006. Experimental approaches to the preparation of supported metal nanoparticles. *Pure & Applied Chemistry*, 78 (9) 1759-1769.

BARTHOLOMEW, C. H. & R. J. FARRAUTO. 2006. Fundamentals of Industrial Catalytic Processes. 2nd Edition, Wiley-Interscience, New York

BARTHOLOMEW, C. H. & REUEL, R. C. 1985. Cobalt-support interaction: Their effects on adsorption and CO hydrogenation activity and selectivity properties*. Industrial & Engineering Chemistry, Product Research*, 24, 56-61.

BARTHOLOMEW, C. H. 1993. Sintering kinetics of supported metals: New perspectives from a unifying GPLE treatment. *Applied Catalysis A: General*, 107, 1 – 57

BARTHOLOMEW, C.H., 2001. Mechanisms of catalyst deactivation. *Applied Catalysis A: General*, 212, 17-60.

BERMANN, W. C., MAULDIN, C. H. & ARCURI, K. B. 1990. Cobalt-titania catalysts, process utilizing these catalysts for the preparation of hydrocarbons from synthesis gas and process for the preparation of the said catalysts. US Patent 4,962,078. Exxon Research and Engineering, Florhan Park, New Jersey.

BEZEMER, G.L., REMANS, T.J., VAN BAVEL, A.P. & DUGULAN, A.L., 2010. Direct evidence of water-assisted sintering of cobalt on carbon nanofiber catalysts during simulated Fischer-Tropsch conditions revealed with in-situ Mössbauer Spectroscopy. *Journal of American Chemical Society*, 132, 8540-8541.

BORG, Ø., ERI, S. BLEKKAN, E. A., STORSǢTER, S. WIGUM, H., RYTTER, E. & HOLMEN, A. 2007. Fischer-Tropsch synthesis over γ-Alumina-supported cobalt catalysts: Effect of support variables. *Journal of Catalysis*, 248, 89-100.

BORG, Ø., HAMMER, N., ERI, S., LINDVAG, O. A., MYRSTAD, R., BLEKKAN, E. A., RONNING, M., RYTTER, E. & HOLMEN, A. 2009. Fischer-Tropsch synthesis over un-promoted and Re-promoted γ-Al2O3 supported cobalt catalysts with different pore sizes. *Catalysis Today*, 142, 70-77.

BOTES, G.F., 2009. Influence of water and syngas partial pressure on the kinetics of a commercial alumina-supported cobalt Fischer-Tropsch catalyst. *Industrial Engineering and Chemical Research*, 48, 1859-1865.

BULAVCHENKO, O. A., CHEREPANOVA, S. V. & TSYBULYA, S. V. 2009. In situ XRD investigation of Co3O4 reduction. *Zeitschrift Fur Kristallographie*, 30, 329 – 334

CAMPBELL, C. T. & SELLERS, R. V. 2013. Anchored metal nanoparticles: Effects of support and size on their energy, sintering resistance and reactivity. *Faraday Discussion*, 162, 4-30.

CHEN, J., WU, X. & SELLONI, A. 2012. Electronic structure and bonding properties of cobalt oxide in the spinel structure. *Physical Review B*, 83, 085306 – 085315.

CHEN, M. S. & GOODMAN, D. W. 2007. Interaction of Au with titania: The role of reduced Ti. *Topics in Catalysis*, 44 (1-2) 41-47.

CHEN, R., DU, Y., XING, W. & XU, N. 2006. The effect of titania structure on Ni/TiO2 catalysts for p-nitrophenol hydrogenation. *Chinese Journal of Chemical Engineering*, 14 (5) 665-669.

CHU, W., CHERNAVSKII, P. A., GENGEMBRE, L., PANKINA, G. A., FONGARLAND, D. & KHODAKOV, A. Y. 2007. Cobalt species in promoted cobalt alumina-supported Fischer-Tropsch catalysts. *Journal of Catalysis*, 252, 215-230.

CLAEYS, M., DRY, M.E., VAN STEEN, E., VAN BERGE, P.J., BOOYENS, S., CROUS, R., VAN HELDEN, P., LABUSCHAGNE, J., MOODLEY, D.J. & SAIB, A.M. 2015. Impact of process conditions on the sintering behavior of an alumina-supported cobalt Fischer-Tropsch catalyst studied with an in situ magnetometer. *ACS Catalysis*, 5, 841 – 852.

CONDON, J. B. 2006. Surface area and porosity determinations by physisorption. Measurement and Theory. Elsevier, Amsterdam, Netherlands

DATYE, A.K., 2003. Electron microscopy of catalyst: recent achievements and future prospects. *Journal of Catalysis*, 216, 144-154.

DATYE, A.K., RIEGEL, G., BOLTON, J. R., HUANG, M. & PRAIRIE, M. R. 1995. Microstructural characterization of a fumed titanium dioxide photocatalyst. *Journal of Solid State Chemistry*, 115, 236-239.

DATYE, A.K., XU, Q., KHARAS, K.C. & McCARTY, J.M., 2006. Particle size distribution in heterogeneous catalysts: what do they tell us about the sintering mechanism? *Catalysis Today*, 111, 59-67.

DAVID, W. I. F. SHANKLAND, K., McCUSKER, L. B. & BAERLOCHER, C. 2002. Structure Determination from Powder Diffraction Data. IUCr Monographs on Crystallography, 13. Oxford University Press. Oxford.

DAVISSON, C.J. 1929. Electron Waves. *Journal of the Franklin Institute*, 208 (1247-42) 595-604.

DE BROGLIE, L. 1926. On the Parallelism between the Dynamics of a Material Particle and Geometrical Optics. Le Journal de Physique et le Radium, 7, 1, In de Broglie &Brillouin. 1929 Selected Papers on Wave Mechanics. Blackie & Son Ltd. London.

DIEBOLD, U. 2002. Structure and properties of TiO2 surfaces: a brief review. *Applied Physics A: Materials Science & Processing*, A76, 1-7.

DIEBOLD, U., 2003.The surface science of titanium dioxide. *Surface Science Reports*, 48, 53-229.

DU PLESSIS, H. E., FORBES, R. P., BARNARD, W., ERASMUS, W. J. & STEUWER, A. 2013. In situ reduction of cobalt model Fischer-Tropsch synthesis catalysts. *Physical Chemistry Chemical Physics*, 15, 11640 – 11645

ECKERT, M. 2012. Max von Laue and the Discovery of X-ray Diffraction in 1912. *Annalen de Physik (Berlin)*, 524 (5) A83-A85.

EDINGTON, J.W. 1975. Electron Diffraction in the Electron Microscope. In Monographs in Practical Electron Microscopy in Materials Science. Phillips Technical Library. MacMillan Press, London.

ERGAN, T., M. & BAYRAMOGLU, M. 2011. Kinetic approach for investigating the “microwave effect”: Decomposition of aqueous potassium persulfate. *Industrial & Engineering Chemistry Research*, 50, 6629 – 6637

EVANS, D.L., DREW, J.H. & LEEMIS, L.M. 2008. The distribution of the Kolmogorov-Smirnov, Cramer-von Mises, and Anderson-Darling test statistics for exponential populations with estimated parameters. *Communications in Statistics – Simulation and Computation*, 37, 1396 – 1421.

FADINI, A. & SCHNEPEL, F. M. 1989. Vibrational Spectroscopy. Methods and Applications. Ellis Horwood Ltd. Chichester.

FIEDOROW, R. M. J. WANKE, S. E. 1976. The sintering of supported metal catalysts I. Redispersion of supported platinum in oxygen. *Journal of Catalysis*, 43, 43 – 42

FLYNN, P. C. & WANKE, S. E. 1974. A model of supported metal catalyst sintering I. Development of model. *Journal of Catalysis*, 34, 390 – 399

FLYNN, P. C. & WANKE, S. E. 1975. Experimental studies of sintering of supported platinum catalysts. *Journal of Catalysis*, 37, 432 – 448

FREUNDLICH, M. M. 1963. Origin of the Electron Microscope. *Science, New Series*, 142 (3589) 185-188.

FUENTES, G. A. 1985. Catalyst deactivation and steady-state activity: A generalized power-law equation model. *Applied Catalysis*, 15, 33 – 40

GAI, P.L., 2001. Developments of electron microscopy methods in the study of catalysts. *Current Opinion in Solid State and Materials Science*, 5, 371-380.

GEERLINGS, J. J. C., HUISMAN, H. M. & MESTERS, M. A. M. 2000. Cobalt-based Fischer-Tropsch catalysts. US Patent 6,130,184. Shell Oil Company, Houston, Texas.

GENTRY, S. T., KENDRA, S. F. & BEZPALKO, M. W. 2011. Ostwald Ripening in Metallic Nanoparticles: Stochastic Kinetics. *The Journal of Physical Chemistry*, 115, 12736-12741.

GERLOCH, M. & CONSTABLE, E. C. 1994. Transition Metal Chemistry. VCH, Weinheim, Germany.

GNANAMANI, M. K., JACOBS, G., SHAFER, W. D., DAVIS, B. H. 2013. Fischer-Tropsch synthesis: Activity of metallic phases of cobalt supported on silica. *Catalysis Today*, 215, 13 – 17

GOEKE, G.S. & DATYE, A.K., 2007. Model oxide supports for studies of catalyst sintering at elevated temperatures. *Topics in Catalysis*, 46, 3-9.

GOUADEC, G. & COLOMBAN, P. 2007. Raman spectroscopy of nanomaterials: How spectra relate to disorder, particle size and mechanical properties. *Progress in Crystal Growth and Characterization of Materials*, 53, 1 – 56

GRANQVIST, C. G. & BURMAN, R. A. 1976. Size distributions for supported metal catalysts. Coalescence growth versus Ostwald Ripening. *Journal of Catalysis*, 42, 477-479.

GUINER, A. 1963. X-ray Diffraction in crystals, imperfect crystals and amorphous bodies. W. H. Freeman & Company. San Francisco.

GUO, B., SHEN, H., SHU, K., ZENG, Y. & NING, W. 2009. The study of the relationship between pore structure and photocatalysis of mesoporous TiO2. *Journal of Chemical Science*, 121 (3) 317-321.

HAASE, E.L. 1985. The determination of lattice parameters and strains in stressed thin films using X-ray diffraction with Seeman-Bohlin focusing. *Thin Solid Films*, 124, 283-291.

HADJIEV, V. G., ILIEV, M. N. & VERGILOV, I. V. 1988. The Raman spectra of Co3O4. Journal of Physics C: *Solid State Physics*, 21, L199 – L201 n

HANAOR, D. A. H. & SORRELL, C. C. 2011. Review of the anatase to rutile phase transformation. *Journal of Materials Science*, 46, 855-874.

HANSEN, T. W., DELARIVA, A. T., CHALLA, S. R. & DATYE, A. K. 2013. Sintering of catalytic nanoparticles: Particle Migration or Ostwald Ripening? *Accounts of Chemical Research*, 46 (8) 1720 – 1730

HARRIS, P. J. F. 1995. Growth and structure of support metal catalyst particles. *International Materials Review*, 40 (3) 97-115.

HELSEL, D. R. 1987. Advantages of nonparametric procedures for analysis of water quality data. *Hydrological Sciences Journal,* 32 (2) 179 -190.

HERNANDEZ-GARRIDO, J.C., YOSHIDA, K., GAI, P.L., BOYES, E.D., CHRISTENSEN, C.H. & MIDGLEY, P.A., 2011. The location of gold nanoparticles on titania: A study by high resolution aberration-corrected electron microscopy and 3d electron tomography. *Catalysis Today*, 160, 165-169.

HO, S. W., CRUZ, J. M., HOULALLA, M. & HERCULES, D. M. 1992. The structure and activity of titania supported cobalt catalysts. *Journal of Catalysis*, 135, 173-185.

HOUK, L. V., CHALLA, S. R., GRAYSON, B., FANSON, P. & DATYE, A. K. 2009. The Definition of “Critical Radius” for a collection of nanoparticles undergoing Ostwald Ripening. *Langmuir*, 25 (19) 11225-11227.

HU, M., NODA, S. & KOMIYAMA, S. 2002. A new insight into the growth mode of metals on TiO2 (110). *Surface Science*, 513, 530-538.

HUANG, W., ZUO, Z., HAN, P., LI, Z. & ZHAO, T., 2009. XPS and XRD investigation of Co/Pd/TiO2 catalysts by different preparation methods. *Journal of Electron Spectroscopy and Related Phenomena*, 173, 88-95.

HYDE, T. 2008. Crystallite size analysis of supported platinum catalysts by XRD. *Platinum Metals Reviews*, 52, 129 – 130.

JACOBS, G., DAS, T.K., ZHANG, Y., LI, J., RACOILLET, G. & DAVIS, B.H., 2002. Fischer-Tropsch synthesis: support, loading and promoter effects on the reducibility of cobalt catalysts. *Applied Catalysis A: General*, 233, 263-281.

JACOBS, G., JI, Y., DAVIS, B.H., CRONAUER, D., KROPF, A.J. & MARSHALL, C.L. 2007. Fischer-Tropsh synthesis: Temperature programmed EXAFS/XANES investigation of the influence of support type, cobalt loading, and noble metal promoter addition to the reduction behaviour of cobalt oxide particles*. Applied Catalysis A: General*, 333, 177-191.

JACOBS, G., SARKAR, A., LI, Y., LUO, M., DOZIER, A. & DAVIS, B.H., 2008. Fischer-Tropsch synthesis: Assessment of the ripening of cobalt clusters and mixing between Co and Ru promoter via oxidation-reduction-cycles over lower Co-loaded Ru-Co/Al2O3 catalysts. *Industrial Engineering and Chemical Research*, 47, 672-680.

JALAMA, K, KABUBA, J., XIONG, H. & JEWELL, L. L. 2012. Co/TiO2 Fischer-Tropsch catalyst activation by synthesis gas. *Catalysis Communications*, 17, 154-159.

JALAOLU, I.O. 2008. Catalyst optimization in gas-to-liquids technology: An operations view. MEng Dissertation, North-West University, South Africa.

JONGSOMJIT, B. 2002. Cobalt-support compound formation in alumina-supported cobalt catalysts. PhD Thesis, University of Pittsburg

JONGSOMJIT, B., SAKDAMNUSON, C. & PRASERTHDAM, P., 2005. Dependence of crystalline phases in titania on catalytic properties during CO hydrogenation of Co/TiO2 catalysts. *Materials Chemistry and Physics*, 89, 395-401.

JONGSOMJIT, B., WONGSALEE, T. & PRASERTHDAM, P., 2005. Study of cobalt dispersion on titania consisting various rutile: anatase ratios. *Materials Chemistry and Physics*, 92, 572-577.

KABABJI, H. A., JOSEPH, B. & WOLAN, J. T. 2009. Silica-supported cobalt catalysts for Fischer-Tropsch synthesis: Effects of calcination temperature and support surface area on cobalt silicate formation. *Catalysis Letters*, 130, 72-78.

KANEKO, K. 1994. Determination of pore size and pore size distribution 1. Adsorbents and catalysts. *Journal of Membrane Science*, 96, 59-89.

KARACA, H., HONG, J., FONGARLAND, P., ROUSSEL, P., GRIBOVAL-CONSTANT, A., LACROIX, M., HORTMANN, K., SAFONOVA, O. V. & KHODAKOV, A. Y. 2010. In situ XRD investigation of the evolution of alumina-supported cobalt catalysts under realistic conditions of Fischer-Tropsch synthesis. *Chemical Communication*, 46, 788 – 790

KARACA, H., SAFONOVA, O.V., CHAMBREY, S., FONGARLAND, P., ROUSSEL, P., GRIBOVAL-CONSTANT, A., LACROIX, M. & KHODAKOV, A.Y., 2011. Structure and catalytic performance of Pt-promoted alumina-supported cobalt catalysts under realistic conditions of Fischer-Tropsch synthesis. *Journal of Catalysis*, 277, 14-26.

KAUSHIK, A., DALELA, B., KUMAR, S., ALVI, P. A. & DALELA, S. 2013. Role of Co doping on structural, optical and magnetic properties of TiO2, *Journal of Alloys and Compounds*, 552, 274 – 278

KHODAKOV, A. Y. 2009. Enhancing cobalt dispersion in supported Fischer-Tropsch catalysts via controlled decomposition of cobalt precursors. *Brazilian Journal of Physics*, 39 (1A) 171-175.

KHODAKOV, A.Y., CHU, W. & FONGARLAND, P. 2007. Advances in the development of novel cobalt Fischer-Tropsch catalysts for synthesis of long-chain hydrocarbons and clean fuels. *Chemical Reviews*, 107 (5), 1692-1744.

KISS, G., KLIEWER, C.E., DEMARTIN, G.J., CULROSS, C.C. & BAUMGARTNER, J.E., 2003. Hydrothermal deactivation of silica-supported catalysts in Fischer-Tropsch synthesis. *Journal of Catalysis*, 217, 127-140.

KLOBES, P., MEYER, K. & MUNRO, R. G. 2006. Porosity and specific surface area measurements for solid materials. NIST RECOMMENDED PRACTICE GUIDE, Special Publication, 960-17, US Department of Commerce.

KOUACHI, K., LAFAYE, G., ESPECEL, C., CHERIFI, O. & MARECOT, P., 2008. Effects of support ad metal loading on the characteristics of Co based catalysts for selective hydrogenation of citral. *Journal of Molecular Catalysis A: Chemical*, 280, 52-60.

LAVADOS, A. K., KATSOULIDIS, A. P., LOSIFIDIS, A., TRIANTAFYLLIDIS, K. S., PINNAVAIA, P.J. & POMONIS, P. J. 2012. The BET equation, the inflection points of N2 adsorption isotherms and estimation of specific surface area of porous solids. *Microporous and Mesoporous Materials*, 151, 126 – 133

LECKEL, D. 2009. Diesel production from Fischer-Tropsh: The past, the present, and new concepts. *Energy & Fuels*, 23, 2342 – 2358.

LEOFANTI, G., PADOVAN, M., TOZZOLA, G. & VENTURELLI, B. 1998. Surface area and pore texture of catalysts. *Catalysis Today*. 41, 207 – 219

LEOFANTI, G., TOZZOLA, G., PADOVAN, M., PETRINI, G., BORDIGA, S., ZECCHINA, A. 1997. Catalyst characterization: characterization techniques. *Catalysis Today*, 34, 307 – 327

LEVI, A.F.J. 2006. Applied Quantum Mechanics. 2nd Ed. Cambridge University Press. Cambridge

LI, G., LI, L. & ZHENG, J. 2011. Understanding the defect chemistry of oxide nanoparticles for creating new functionalities: A critical review. *Science China Chemistry*, 54 (6) 876-886.

LI, H., YU, X., TU, S.T., YAN, J. & WANG, Z. 2010. Catalytic Performance and Characterization of Al2O3-supported Pt-Co catalyst coatings for preferential CO oxidation in a micro-reactor. *Applied Catalysis A: General*, 387, 215-223

LI, J. & COVILLE, N. J. 2003. Effect of pretreatment on reduction and activity of the boron-modified Co/TiO_2 Fischer-Tropsch catalyst. *Preparatory Paper of the American Chemical Society, Division of Fuels Chemistry*, 48 (2) 735-737.

LI, J., JACOBS, G., ZHANG, Y., DAS, T. & DAVIS, B.H., 2002. Fischer-Tropsch synthesis: effect of small amounts of boron, ruthenium and rhenium on Co/TiO_2 catalysts. *Applied Catalysis A: General*, 223, 195-203.

LI, J., JIANG, Z., QIAN, K. & HUANG, W. 2012 Effect of calcination temperature on surface oxygen vacancies and catalytic performance towards CO oxidation of Co_3O_4 nanoparticles supported on SiO_2. *Chinese Journal of Chemical Physics*, 25 (1) 103-109.

LI, Y., XU, B., FAN, Y., FENG, N., QIU, A., HE, J.M.J., YANG, H. & CHEN, Y., 2004. The effect of titania polymorph on the strong metal-support interaction of Pd/TiO2 catalysts and their application in the liquid phase selective hydrogenation of long chain alkadienes. *Journal of Molecular Catalysis A: Chemical*, 216, 107-114.

LIF, J., ODENBRAND, I. & SKOGLUNDH, M., 2007. Sintering of alumina-supported nickel particles under amination conditions; Support effects. *Applied Catalysis A: General*, 317, 62-69.

LIF, J., SKOGLUNDH, M. & LÖWENDAHL, L. 2002. Sintering of nickel particles supported on γ-alumina in ammonia. *Applied Catalysis A: General*, 228, 145 – 154

LINSINGER, T., ROEBBEN, G., GILLILAND, D., CALZOLAI, L., ROSSI, F., GIBSON, N. & KLEIN, C. 2012. Requirements on measurements for the implementation of the European Commission definition of the term “nanomaterial”. JRC Reference Report, *European Commision*, Report EUR 25404 EN.

LINSMEIER, C. & TAGLAUER, E., 2011. Strong metal-support interactions on rhodium model catalysts. *Applied Catalysis A: General*, 391, 175-186.

LIPSON, H. S. 1970. Crystals and X-rays. Wykeham Publishers Ltd. London.

LOK, C.M. 2011. Cobalt catalysts, United States Patent, US 2011/0054048.

LOK, C.M. 2011. Cobalt Catalysts. US Patent 2011/0054048A1.

LONG, D. A. 1977. Raman Spectroscopy. McGraw-Hill Inc. London.

LUCREDIO, A. F., BELLIDO, J. D. A., ZAWADZKI, A. & ASSAF, E. M. 2011. Co catalysts supported on SiO2 and γ-Al2O3 applied to ethanol steam reforming: Effect of the solvent used in the catalyst preparation method. *Fuel*, 90, 1424-1430.

LUIS, A. M., NEVES, M. C., MENDONCA, M. H., & MONTEIRO, O. C. 2011. Influence of calcination parameters on the TiO2 photocatalytic properties. *Materials Chemistry and Physics*, 125, 20-25.

MAKOKHA, A.B., MOYS, M.H., MUUMBO, A.M. & KIPRONO, R.J. 2012. Optimization of in-mill ball loading and slurry solids concentration in grinding of UG-2 ores: A statistical experimental design approach. *Minerals Engineering*, 39, 149-155.

MASSEY, F.J. 1951. The Kolmogorov-Smirnov Test for Goodness of fit. *Journal of the American Statistical Association,* 46, 68 – 78.

MATHPAL, M. C., TRIPATHI, A. K., SINGH, M. K., GAIROLA, S. P., PANDEY, S. N. & AGRAWAL, A. 2013. Effect of of annealing temperature on Raman spectra of TiO_2 nanoparticles. *Chemical Physics Letters*, 555, 182-186.

MAULDIN, C.H. & RILEY, K.L. 1991. Titania-supported catalysts and their preparation for use in Fischer-Tropsch synthesis. United States Patent, 4,992,406.

McCREERY, R. L. 2000. Raman Spectroscopy for Chemical Analysis. Wiley-Interscience. New York.

McMURRY, S.M. 1994. Quantum Mechanics. Addison-Wesley Publishing, Wokingham.

MERKUS, G. 2009. Particle Size measurements: Fundamentals, Practice, Quality. Springer

MINGARD, K., MORRELL, R., JACKSON, P., LAWSON, S., PATEL, S. & BUXTON, R. 2009. Good practice guide for improving the consistency of particle size measurement. Measurement Good Practice Guide No.11, *National Physical Laboratory.*

MINH, N. V. 2008. Nano-particles of Co doped TiO2 Anatase: Raman Spectroscopy and structural studies. *Journal of the Korean Physical Society*, 52 (5) 1629 – 1632

MIRZAEI, A. A., SHAHRIARI, S. & ARSALANFAR, M. 2011. Effect of preparation conditions on the catalytic performance of Co/Ni catalysts for CO hydrogenation. *Journal of Natural Gas Science and Engineering*, 3, 537-546.

MITCHELL, D.R.G., WANG, X. & CARUSO, R.A., 2008. Plasmon imaging: An efficient TEM-based method for locating noble metal particles dispersed on oxide catalysts at very low densities. *Micron*, 39, 344-347.

MNQANQENI-MADIKIZELA, N.N. & COVILLE, N.J. 2004. Surface and reactor study of the effect of zinc on titania-supported Fischer-Tropsch cobalt catalysts. *Applied Catalysis*, 272, 339-346.

MOTULSKY, H.J. & CHRISTOPOULOS, A. 2003. Fitting models to biological data using linear and nonlinear regression. A practical guide to curve fitting. GraphPad Software Inc., San Diego CA, www.graphpad.com

MOODLEY, D.J., VAN DER LOOSDRECHT, J., SAIB, A.M., OVERETT, M.J., DATYE, A.K. & NIEMANTSVERDRIET, J.W., 2009. Carbon deposition as a deactivation mechanism of cobalt-based Fischer-Tropsch synthesis catalysts under realistic conditions. *Applied Catalysis A: General*, 354, 102-110.

MORGAN, B. J. & WATSON, G. W. 2010. Intrinsic n-type defect formation in TiO_2: A comparison of rutile and anatase from GGA+U calculations. *Journal of Physical Chemistry C*, 114, 2321-2328.

MOULIJN, J.A., VAN DIEPEN, A.E. & KAPTEIJN, F., 2001. Catalyst deactivation: is it predictable? What to do? *Applied Catalysis A: General*, 212, 3-16.

NAGAOKA, K., TAKANABE, K. & AIKA, K. 2003. Influence of the reduction temperature on catalytic activity of Co/TiO_2 (anatase-type) for high pressure dry reforming of methane. *Applied Catalysis A: General*, 255, 13-21.

OH, J. W., BAE, J. W., PARK, S. J. KHANNA, P. K. & JUN, K. W. 2009. Slurry-phase Fischer-Tropsch synthesis using Co/γ-Al_2O_3, Co/SiO_2 and Co/TiO_2: Effect of support on catalyst aggregation. *Catalysis Letters*, 130, 403-409.

OHNO, T., SALUKAWA, K., TOKIEDA, K. & MATSUMURA, M. 2001. Morphology of a TiO_2 photocatalyst (Degussa P25) consisting of anatase and rutile crystalline phase. *Journal of Catalysis*, 203, 82-86.

OHTANI, B., PRIETO-MAHANEY, O. O., LI, D. & ABE, R. 2010. What is Degussa (Evonik) P25? Crystalline composition analysis, reconstruction from isolated pure particles and photocatalytic activity test. *Journal of Photochemistry & Photobiology A: Chemistry*, 216 (2-3) 179-182.

OKAMOTO, H. 2008. Co-O (Cobalt-Oxygen). *Journal of Phase Equilibria and Diffusion*, 29 (6) 548 – 549

OKUDA, H., NAKAJIMA, K., FUJIWARA, K., MORISHITA, K. & OCHIAI, S. 2008. Point-focusing monochromator crystal realized by hot plastic deformation of a Ge wafer. *Journal of Applied Crystallography*, 41, 798-799.

OMNÈS, R. 1999. Understanding Quantum Mechanics. Princeton University Press. New Jersey.

ORAON, B., MAJUMDAR, G. & GHOSH, B. 2006. Application of response surface method for predicting electroless nickel plating. *Materials and Design*, 27, 1035-1045.

ORENDORZ, A., BRODYANSKI, A., LÖSCH, J., BAI, Z. H., CHEN, Z. H., LE, Y. K., ZIEGLER, C. & GNASER, H. 2007. Phase transformation and particle growth in nanocrystalline anatase TiO2 films analysed by X-ray diffraction and Raman spectroscopy. *Surface Science*, 601 (18) 4390-4394.

OVERETT, M. J., BREEDT, B., DU PLESSIS, E., ERASMUS, W. & VAN DER LOOSDRECHT, J. 2008. Sintering as a deactivation mechanism for cobalt supported on alumina Fischer-Tropsch catalyst. *American Chemical Society, Division of Petroleum Chemistry*, Inc, Preprints, 53, 126-130.

OZKAYA, D. 2008. Particle size analysis of supported platinum catalysts by TEM. *Platinum Metals Reviews*, 52, 61 – 62.

PACCHIONI, G. 2008. Reduced and doped TiO_2: What is the nature of the defect states?. Workshop on Nanoscience for Solar Energy Conversion. The Abdus Salam International Centre for theoretical Physics.

PARK, J-.Y., LEE, Y-.J., KARANDIKAR, P.R., JUN, K-.W., HA, K-.S. & PARK, H-.G., 2012. Fischer-Tropsch catalysts deposited with size-controlled Co_3O_4 nanocrystal: Effect of Co particle size on catalytic activity and stability. *Applied Catalysis A: General*, 411-412, 15-23.

PÄRNA, R. JOOST, U., NÕMMISTE, E. KÄÄMBRE, T., KIKAS, A., KUUSIK, I., HIRSIMÄKI, M., KINK, I. & KISAND, V. 2011. Effect of cobalt doping and annealing on properties of titania thin films prepared by sol-gel process. *Applied Surface Science*, 257, 6897-6907.

PASZKOWICZ, W. 2006. Ninety Years of Powder Diffraction: From Birth to Maturity. *Synchrotron Radiation in Nature Science*, 5 (1-2) 115-126.

PETITO, S. H., MARSH, E. M., CARSON, G. A. & LANGELL, M. A. 2008. Cobalt oxide surface chemistry: The interaction of CoO(100), Co_3O_4(110) and Co_3O_4(111) with water. *Journal of Molecular Catalysis A: Chemical*, 281, 49 – 58

PORTER, J. F., LI, Y. G., & CHEN, C. K. 1999. The effect of calcination on the microstructural characteristics and photoreactivity of Degussa P25 TiO_2. *Journal of Materials Science*, 34, 1523-1531.

RAJ, K. J. A. & VISWANATHAN, B., 2009. Effect of surface area, pore volume and particle size of P25 titania on the phase transformation of anatase to rutile. *Indian Journal of Chemistry*, 48A, 1378-1382.

REIMER, L. 1997. Transmission Electron Microscopy. Physics of Image Formation and Microanalysis. Springer-Verlag. New Yor.k

RIVA, R., MIESSNER, H., VITALI, R. & DEL PIERO, G., 2000. Metal-support interaction in Co/SiO2 and Co/TiO2. *Applied Catalysis A: General*, 196, 111-123.

RONNING, M., TSAKOUMIS, N. E., VORONOV, A., JOHNSEN, R. E., NORBY, P., VAN BEEK, W., BORG, Ø., RYTTER, E. & HOLMEN, A. 2010. Combined XRD and XANES studies of a Re-promoted Co/γ-Al_2O_3 catalysts at Fischer-Tropsch synthesis conditions. *Catalysis Today*, 155, 289-295.

ROUSSEAU, J. –J. 1998. Basic Crystallography. John Wiley & Sons Ltd. Chichester

RUCKENSTEIN, E. & PULVERMACHER, B. 1973. Growth kinetics and size distributions of supported metal crystallites. *Journal of Catalysis*, 29, 224 – 245

RUSKA, E.1986. The Development of the Electron Microscope and of Electron Microscopy. Nobel Lecture Available at www.nobelprize.org/nobel-prizes/physics/.../1986/ruska/lecture.pdf accessed 01/06/2012

RYTTER, E., SKAGSETH, T.H., ERI, S. & SJÅSTAD, A.O., 2010. Cobalt Fischer-Tropsch catalysts using nickel promoter as a rhenium substitute to suppress deactivation. *Industrial Engineering and Chemical Research*, 49 (9), 4140-4148.

RUSSO, O. 2012. A Combination of adsorption techniques for the study of catalyst properties. Scuola di Catilisi, Bari, Giugno.

SADEQZADEH, M., CHAMBREY, S., HONG, J., FONGARLAND, P., LUCK, F., CURULLA-FERRE, D., SCHWEICH, D., BOUSQUET, J. & KHODAKOV, A.Y. 2014. Effect of different reaction conditions on the deactivation of alumina-supported cobalt Fischer-Tropsch catalysts in a milli-fixed-bed reactor: Experiments and modelling. *Industrial & Engineering Chemistry Research*, 53, 6913 – 6922.

SADEQZADEH, M., HONG, J., FONGARLAND, P., LUCK, F., CURULLA-FERRE, D., SCHWEICH, D., BOUSQUET, J. & KHODAKOV, A.Y. 2012. Mechanistic modelling of cobalt-based catalyt sintering in a fixed bed reactor under different conditions of Fischer-Tropsch synthesis. *Industrial & Engineering Chemistry Research*, 51, 11955 – 11964.

SAIB, A.M., BORGNA, A., VAN DER LOOSDRECHT, J., VAN BERGE, P.J. & NIEMANTSVERDRIET, J.W., 2006. Preparation and characterization of spherical Co/SiO_2 model catalysts with well-defined nano-sized cobalt crystallites and comparison of their stability against oxidation with water. *Journal of Catalysis*, 239, 326-339.

SAIB, A.M., MOODLEY, D.J., CIOBÎCĂ, I.M., HAUMAN, M.M., SIGWEBELA, B.H.,WESTRATE, C.J., NIEMANTSVERDRIET, J.W. & VAN DER LOOSDRECHT, J., 2010. Fundamental understanding of deactivation and regeneration of cobalt Fischer-Tropsch synthesis catalysts. *Catalysis Today*, 154, 271–282.

SAMUEL, P. 2003. GTL Technology – challenges and opportunities in catalysis. *Bulletin of the Catalysis Society of India*, 2, 82-99.

SANTARA, B. PAL, B. & GIRI, P.K. 2011. Signature of strong ferromagnetism and optical properties of Co doped TiO_2 nanoparticles. *Journal of Applied Physics*, 110, 114322

Sasol LTD website, 2014. http://www.sasol.co.za/innovation/gas-liquids/technology accessed 20/12/2014

SAVIO, A. K. P. D., STARIKOV, D., BENSAOULA, A., PILLAI, R., DE LA TORRE GARCIA, L. L. & ROBLES HERNANDEZ, F. C. 2012. Tunable TiO_2 (anatase and rutile) materials manufactured by mechanical means. *Ceramics International*, 38, 3529-3535.

SECORDEL, X., BERRIER, E., CAPRON, M., CRISTOL, S., PAUL, J. F., FOURNER, M. & PAYEN, E. 2010. TiO_2-supported rhenium oxide catalysts for the methanol oxidation: Effect of support texture on the structure and reactivity evidenced by an operando Raman study. *Catalysis Today*, 155, 177-183.

SEHESTED, J., GELTEN, J.A.P. & HELVEG, S., 2006. Sintering of nickel catalysts: Effect of time, atmosphere, temperature, nickel-carrier interaction and dopants. *Applied Catalysis A: General*, 309, 237-246.

SELLONI, A. 2008. Materials-related aspects of TiO_2-based photocatalysis. Workshop on Nanoscience for Solar Energy Conversion. The Abdus Salam International Centre for theoretical Physics.

SEWELL, G. S., VAN STEEN, S. & O'CONNOR, C. T. 1996. Use of TPR/TPO for the characterization of supported cobalt catalysts. *Catalysis Letters*, 37, 255-260.

SHAO, J., ZHANG, P., TANG, X., ZHANG, B., SONG, W., XU, Y. & SHEN, W. 2007. Effect of preparation method and calcination temperature on low-temperature CO oxidation of Co_3O_4/CeO_2 catalysts. *Chinese Journal of Catalysis*, 28 (2) 163-169.

SHARMA, Y. K., KHARKWAL, M., UMA, S. & NAGARAJAN, R. 2009. Synthesis and characterization of titanates of the formula $MTiO_3$ (M = Mn, Fe, Co, Ni and Cd) by co-precipitation of mixed metal oxalates. *Polyhedron*, 28, 579-585.

SHELL, 2014. Shell MDS. Available at http://www.shell.com.my/products-services/solutions-for-businesses/smds.html accessed on 20/06/2014

SHIMURA, K., MIYAZAWA, T., HANAOKA, T. & HIRATA, S. 2013. Fischer-Tropsch synthesis over TiO2-supported cobalt catalysts: Effect of TiO_2 crystal phase and metal ion loading. *Applied Catalysis A: General*, 460-461, 8-14.

SHIRAISHI, Y. HIRAKAWA, H., TOGAWA, Y., SUGANO, Y., ICHIKAWA, S. AND HIRAI, T. 2013. Rutile crystallites isolated from Degussa (Evonik) P25 TiO_2: Highly efficient photocatalyst for chemoselective hydrogenation of nitroaromatics. *ACS Catalysis*, 3, 2318-2326.

SILLS, R. 2013. ABCs of GTL. 4th World Shale Oil & Gas Summit. Houston

SIMONSEN, S.B., CHORKENDORFF, I. DAHL, S., SKOGLUDH, M., SEHESTED, J. & HELVEG, S. 2011. Oswald ripening in a Pt/SiO_2 model catalyst studied by in-situ TEM. *Journal of Catalysis*, 281,147-155.

SING, K. S. W. 1998. Adsorption methods for the characterization of porous materials. *Advances in Colloid and Interface Science*, 76 – 77

SING, S. K. W., EVERETT, D. H., HAUL, R. A. W., MOSCOU, L., PIEROTTI, R. A., ROUQUEROL, J. & SIEMIENIEWSKA, T. 1985. Reporting physisorption data for gas/solid systems with special reference to the determination of surface area and porosity. *Pure & Applied Chemistry*, 57 (4) 603-619.

SMITH, D.J. 2008. Progress and perspectives for atomic-resolution electron microscopy. *Ultramicroscopy*, 108, 159-166.

SONG, S. H., LEE, S. B., BAE, J. W., PRASAD, P. S. S., JUN, K. W. & SHUL, Y. G. 2009. Effect of calcination temperature on the activity and cobalt crystallite size of Fischer-Tropsch Co-Ru-Zr/SiO_2 catalyst. *Catalysis Letters*, 129, 233-239.

STENCEL, J. M. 1990. Raman Spectroscopy for Catalysis. Van Nostrand Reinhold Catalysis Series. Van Nostrand Reinhold. New York.

STORSÆTER, n.d, S., TØTDAL, B., WALMSLEY, J.C., TANEM, B.S. & HOLMEN, A., 2005. Characterization of alumina-, silica-, and titania-supported cobalt Fischer-Tropsch catalysts. *Journal of Catalysis*, 236, 139-152.

STRUNK, J., VINING, W. C. & BELL, A. T. 2010. A Study of oxygen vacancy formation and annihilation in submonolayer coverages of TiO_2 dispersed on MCM-48. *Journal of Physical Chemistry*, 114, 16937-16945.

SUBRANANIAN, S.1992. Temperature-programmed reduction of platinum group metals catalysts. *Platinum Metals Review*, 36 (2) 98-103.

SUN, Y., SUN, Q., JIANG, F. LIU, J. & ZHANG, Z. 2012. Effects of calcination and reduction temperatures on the performance of Co-Pt-ZrO_2/γ-Al_2O_3 catalysts for Fischer-Tropsch synthesis. *Journal of Fuel Chemistry and Technology*, 40 (1) 54-58.

TABUCHI, M., TAMEOKA, H., KAWASE, T. & TAKEDA, Y. 2009. Development of new X-ray CTR scattering measurement system using Johansson monochromator. *Transactions of the Materials Research Society of Japan*, 34 (4) 589-591.

TAKANABE, K., NAGAOKA, K., NARIAI, K. & AIKA, K. –I. 2005. Influence of reduction temperature on the catalytic behaviour of Co/TiO_2 catalysts for CH_4/CO_2 reforming and its relation with titania bulk crystal structure. *Journal of Catalysis*, 230, 75 – 85

TANG, C. W., WANG, C. B. & CHIEN, S. H. 2008. Characterization of cobalt oxides studied by FTIR, Raman, TPR and TG-MS. *Thermochimica Acta*, 473, 68-73.

TAYLOR, M. N. ZHOU, W., GARCIA, T., SOLSONA, B., CARLEY, A. F., KIELY, C.J. & TAYLOR, S.H. 2012. Synergy between tungsten and palladium supported on titania for the catalytic total oxidation of propane. *Journal of Catalysis*, 285, 103-114.

TEOH, L. G., LEE, Y. C., CHANG, Y. S., FANG, T. H. & CHEN, H. M. 2010. Preparation and characterization of nanocrystalline titanium dioxide with surfactant-mediated method. *Current Nanoscience*, 6 (1) 1-5.

THIEL, P. A., SHEN, M., LIU, D. J. & EVANS, J. W. 2009. Coarsening of two-dimensional nanoclusters on metal surfaces. *Journal of Physical Chemistry*, 13 (113) 5047-5067.

THOMAS, J. M. & GAI, P. L. 2004. Electron microscopy and the materials chemistry of solid catalysts. *Advances in Catalysis*, 48, 171-227.

THOMAS, T.M. & MIDGLEY, P.A., 2011. The modern electron microscope: A cornucopia of chemico-physical insights. *Chemical Physics*, 385, 1-10.

THÜNE, P.C., WESTSTRATE, C.J., MOODLEY, P., SAIB, A.M., VAN DER LOOSDRECHT, J., MILLER, J.T. & NIEMANTSVERDRIET, J.W., 2011. Studying Fischer-Tropsh catalysts using transmission electron microscopy and model systems of nanoparticles on planar supports. *Catalysis Science & Technology*, 1, 689-697.

TSAKOUMIS, N.E., RØNNING, M., BORG, Ø., RYTTER, E. & HOLMEN, A., 2010. Deactivation of cobalt based Fischer-Tropsch catalysts: A review. *Catalysis Today*, 154, 162-182.

VAN BERGE, P. J., VAN DER LOOSDRECHT, J. & VISAGIE, J. L. 2008. Cobalt catalyst. US Patent 7375055

VAN BERGE, P.J., VAN DER LOOSDRECHT, J. & VISAGIE, J.L., 2004. Cobalt Catalysts. US Patent 6,806,226B2

VAN DER LOOSDRECHT, J., BALZHINIMAEV, B., DALMON, J.A., NIEMANTSVERDRIET, J.W., TSYBULYA, S.V., SAIB, A.M., VAN BERGE, P.J. & VISAGIE, J.L., 2007. Cobalt Fischer-Tropsch synthesis: Deactivation by oxidation? *Catalysis Today*, 123, 293-302.

VAN DER LOOSDRECHT, J., BARRADAS, S., CARICATO, E. A., NGWENYA, N. G., NKWANYANA, P. S., RAWAT, M. A. S., SIGWEBELA, B. H., VAN BERGE, P. J. & VISAGIE, J. L. 2003. Calcination of Co-based Fischer-Tropsch synthesis catalysts. *Topics in Catalysis,* 26 (1-4) 121-127.

VAN DER LOOSDRECHT, J., VAN DER KRAAN, A.M., VAN DILLEN, J. & GEUS, J.W., 1997. Metal-support Interaction: Titania-supported and silica-supported nickel catalysts. *Journal of Catalysis*, 170, 217-226.

VINCENT, M., SANCHEZ, E., SANTACRUZ, I. & MORENO, R. 2011. Dispersion of TiO2 nanopowders to obtain homogeneous nanostructured granules by spray-drying. *Journal of the European Ceramic Society*, 31, 1413-1419.

VOUTOU, B. & STEFANAKI, E. C. 2008. Electron Microscopy: The Basics. Physics of Advanced Materials Winter School, Aristotle University of Thessaloniki.

WANG, X., TIAN, W., ZHAI, T., ZHI, C., BANDO, Y & GLOBERG, D. 2012. Cobalt(II,III) oxide hollow structures: fabrication, properties and applications. *Journal of Materials Chemistry*, 22, 23310 – 23326

WANG, Z.L. & COWLEY, J.M., 1987. Surface plasmon excitation for supported metal particles. *Ultramicroscopy*, 21, 77-94.

WANG, Z.L. 1995. Elastic and Inelastic Scattering in Electron Diffraction and Imaging. Plenum Press, New York.

WEBB, P. A. & ORR, C. 1997. Analytical methods in fine particle technology. Micromeritics Instrument Corporation, Norcross, GA, USA.

WEBB, P. A. 2003. Introduction to chemical adsorption analytical techniques and their applications in catalysis. *Micromeritics Instrument Corporation Publications*, January 2003.

WEIBEL, A., BOUCHET, R., BOULC'H, F. & KNAUTH, P. 2005. The big problem of small particles: A comparison of methods for determination of particle size in nanocrystalline anatase powders. *Chemistry of Materials*, 17, 2378-2385.

WILLARD, H. H., MERRITT, L. L., DEAN, J. A, & SETTLE, F. A. 1988. Instrumental Methods of Analysis. 7th Ed. Wadsworth Publishing. California.

WILLIAMS, D. B. & CARTER, C. B. 2009. Transmission Electron Microscopy, A textbook for Materials Science. 2nd Edition, Springer-New York.

WISNIAK, J. & POLSHUK, A.1999. Analysis of residuals – A useful tool for phase equilibrium data analysis. *Fluid Phase Equilibria*, 164, 61 – 82

WITTEN, T. A. & SANDER, L. M. 1981. Diffusion-limited aggregation, a kinetic critical phenomenon. *Physical Review Letters*, 47 (19), 1400 – 1403

WYNBLATT, P. & GJOSTEIN, N. A. 1975. Supported metal crystallites. *Progress in Solid State Chemistry*, 9, 21 – 58

XIONG, L. B., LI, J. L., YANG, B. & YU, Y. 2012. Ti3+ in the surface of titanium dioxide: Generation, properties and photocatalytic application. *Journal of Nanomaterials*, 1 – 13

YAN, J., WU, G., GUAN, N., LI, L., LI, Z. & CAO, X. 2013. Understanding the affect of surface/bulk defects on the photocatalytic activity of TiO2: anatase versus rutile. *Physical Chemistry Chemical Physics*, 15, 10978-10988.

YANKIN, A. M. & BALAKIREV, V. F. 2002. Phase equilibria in the Co-Mn-Ti-O system over wide ranges of temperatures and oxygen pressures. *Inorganic Materials*, 38 (4) 309 – 319

YOSHITAKE, H. & ABE, D. 2009. Raman spectroscopic study of the framework structure of amorphous mesoporous titania. *Microporous and Mesoporous Materials*, 119, 267-267

YOUNG, I. T. 1977. Proof without prejudice: Use of the Kolmogorov-Smirnov test for the analysis of histograms from flow systems and other sources. *The Journal of Histochemistry and Cytochemistry*, 25 (7) 935 – 941.

ZHANG, H. & BANFIELD, J. F. 1998. Thermodynamic analysis of phase stability of nanocrystalline titania. *Journal of Materials Chemistry*, 8, (9) 2073-2076.

ZHANG, Y., WEIDENKAFF, A. & RELLER, A. 2002. Mesoporous structure and phase transition of nanocrystalline TiO_2. *Materials Letters*, 54, 375-381.

ZHAO, H., CHEN, J. & SUN, Y. 2003. Effect of calcination temperature on the performance of Co/ZrO2 catalysts for Fischer-Tropsch synthesis. *Preparatory Paper of the American Chemical Society, Division of Fuels Chemistry*, 48 (2) 733-734.

ZHDANOV, V. P., LARSSON, E. M. & LANGHAMMER, C. 2012. Novel Aspects of Ostwald Ripening of supported metal nanoparticles. *Chemical Physics Letters*, http:dx.doi.org/10.1016/j.cplett.2012.03.010.

ZHENG, J., CHU, W., ZHANG, H., JIANG, G. & DAI, X. 2010. CO oxidation over Co3O4/SiO2 catalysts: Effects of porous structure of silica and catalyst calcination temperature. *Journal of Natural Chemistry*, 19, 583-588.

ZHOU, G. W., LEE, D. K., KIM, Y. H., KIM, C. W. & KANG, Y. S. 2006. Preparation and spectroscopic characterization of illmenite-type $CoTiO_3$ nanoparticles. *Bulletin of the Korean Chemical Society*, 27 (3) 36

ZUO, Z.; HUANG, W.; HAN, P. & LI, Z., 2009. Theoretical and experimental investigation of the influence of Co and Pd on the titanium dioxide phase transition by different calcined temperature. *Journal of Molecular Structure*, 936, 118-124.

APPENDIX A

Table A. 1: XRD-derived crystallite size data used in model determination

Anatase

Time	CS_fcc Co (nm)	Sigma (nm)	CS_hcp Co	Sigma (nm)	log time	log CS_fcc	log CS_hcp
4	31	3.7	3	0.2	0.6	1.49	0.53
8	31	2.3	3	0.2	0.9	1.49	0.53
16	37	4.8	3	0.1	1.2	1.56	0.46
32	43	6.6	3	0.1	1.51	1.63	0.43
48	55	9.6	3	0.2	1.68	1.74	0.49

P25

Time	CS_fcc Co (nm)	Sigma (nm)	CS_hcp Co	Sigma (nm)	log time	log CS_fcc Co	log CS_hcp Co
4	26	1.4	-	-	0.6	1.41	-
8	28	1.5	-	-	0.9	1.45	-
16	30	2.5	-	-	1.2	1.47	-
32	30	2.8	-	-	1.51	1.48	-
48	35	3.0	-	-	1.68	1.54	-

Rutile

Time	CS_fcc Co (nm)	Sigma (nm)	CS_hcp Co	Sigma (nm)	log time	log CS_fcc Co	log CS_hcp Co
4	25	2.3	2	0.2	0.6	1.4	0.36
8	26	2.0	2	0.1	0.9	1.41	0.3
16	27	2.0	2	0.1	1.2	1.43	0.32
32	28	2.1	2	0.1	1.51	1.44	0.32
48	28	2.2	2	0.1	1.68	1.45	0.28

Table A. 2: TEM-derived particle size data used in model determination

Anatase

Time	CS_Co (nm)	Sigma (nm)	log Time	log CS_Co
4	30.2	17.1	0.60	1.48
8	52.3	24.3	0.90	1.72
16	58.1	28.8	1.20	1.76
32	65.3	38.3	1.51	1.81
48	88.2	40.8	1.68	1.95

P25

Time	CS_Co (nm)	Sigma (nm)	log Time	log CS_Co
4	50.7	18.7	0.60	1.70
8	52.4	21.3	0.90	1.71
16	54.6	23.5	1.20	1.73
32	61.7	21.0	1.51	1.78
48	65.0	24.0	1.68	1.80

Rutile

Time	CS_Co (nm)	Sigma (nm)	log Time	log CS_Co
4	16.9	10.3	0.60	1.22
8	20.2	5.8	0.90	1.31
16	23.0	14.5	1.20	1.36
32	24.6	11.0	1.51	1.39
48	36.4	20.8	1.68	1.56

Table A. 3: Data derived from Kolmogorov-Smirnov test comparing the particle size distribution functions of the sintered catalysts with that at 4 hours for each support.

Sample	s(n)	α	D	D_{crit}	Result*
Anat-8h	0.1432	1.36	0.4427	0.1947	Reject H0
Anat-16h	0.1429	1.36	0.4511	0.1935	Reject H0
Anat-32h	0.1341	1.36	0.4530	0.1824	Reject H0
Anat-48h	0.1412	1.36	0.7188	0.1920	Reject H0
P25-8h	0.1342	1.36	0.1047	0.1825	Accept H0
P25-16h	0.1490	1.36	0.1335	0.2027	Accept H0
P25-32h	0.1344	1.36	0.2358	0.1828	Reject H0
P25-48h	0.1575	1.36	0.3117	0.2142	Reject H0
Rut-8h	0.1466	1.36	0.4225	0.1994	Reject H0
Rut-16h	0.1401	1.36	0.1973	0.1905	Reject H0
Rut-32h	0.1264	1.36	0.2572	0.1720	Reject H0
Rut-48h	0.1539	1.36	0.4416	0.2094	Reject H0

*Hypothesis:

H0: There is no statistical difference between the distributions.

H1: There is a statistical difference between the distributions.

Table A. 4: Statistical data obtained from fitting lognormal distribution functions onto anatase-supported particle size data

Catalyst	Mode	95% CI (Mode)	Median	95% CI (Median)	Mean	95% CI (Mean)	FWHM	95% CI (FWHM)	RMSE
Cat_Anat-4h	20.0	19.7 – 20.3	26.3	26.1 – 26.5	30.2	29.9 – 30.5	26.3	25.9 – 26.7	0.000376
Cat_Anat-8h	37.1	36.7 – 37.5	46.6	46.2 – 47.0	52.3	52.0 – 52.6	44.1	43.1 – 44.5	0.000356
Cat_Anat-16h	34.3	33.7 – 34.9	48.7	48.4 – 49.0	58.1	58.4 – 58.8	51.9	51.4 – 52.4	0.000510
Cat_Anat-32h	35.2	34.5 – 35.9	53.2	52.8 – 53.4	65.3	64.4 – 66.2	58.4	57.5 – 58.4	0.000713
Cat_Anat-48h	59.9	59.1 – 60.7	77.5	77.0 – 78.0	88.2	87.4 – 89.0	76.0	75.8 – 76.2	0.000484

Table A. 5: Statistical data obtained from fitting lognormal distribution functions onto P25-supported particle size data

Catalyst	Mode	95% CI (Mode)	Median	95% CI (Median)	Mean	95% CI (Mean)	FWHM	95% CI (FWHM)	RMSE
Cat_P25-4h	40.2	39.9 – 40.5	46.9	46.7 – 47.1	50.7	50.4 – 51.0	38.5	37.8 – 38.5	0.00036
Cat_P25-8h	41.7	41.5 – 41.9	48.5	48.0 – 49.0	52.4	51.9 – 52.9	39.7	37.9 - 41.5	0.00192
Cat_P25-16h	39.5	39.0 - 40.0	49.1	48.8 – 48.4	54.6	54.0 – 55.2	45.5	44.7 – 46.3	0.00048
Cat_P25-32h	48.6	48.0 – 49.2	57.0	56.7 - 57.3	61.7	61.2 – 62.2	47.3	46.1 – 48.5	0.00100
Cat_P25-48h	49.9	48.9 – 50.9	59.5	59.0 – 60.0	65.0	64.3 – 65.7	51.4	49.8 – 53.0	0.00100

Table A. 6: Statistical data obtained from fitting lognormal distribution functions onto rutile-supported particle size data

Catalyst	Mode	95% CI (Mode)	Median	95% CI (Median)	Mean	95% CI (Mean)	FWHM	95% CI (FWHM)	RMSE
Cat_Rut-4h	10.7	10.5 - 10.9	14.5	14.4 – 14.6	16.9	16.8 – 17.0	14.9	14.8 – 15.0	0.00039
Cat_Rut-8h	18.3	18.2 – 18.4	19.5	19.4 – 19.6	20.2	20.1 – 20.3	11.2	11.0 – 11.4	0.00038
Cat_Rut-16h	9.8	9.4 – 10.2	17.4	17.2 – 17.6	23.0	22.5 – 23.5	19.8	19.5 – 20.1	0.00100
Cat_Rut-32h	15.7	15.6 – 15.8	21.2	21.1 – 21.3	24.6	24.3 – 24.9	21.7	21.8 – 21.9	0.00031
Cat_Rut-48h	16.2	15.2 – 17.2	27.8	27.4 – 28.2	36.4	35.4 – 37.4	31.6	31.1 – 32.1	0.00117

APPENDIX B

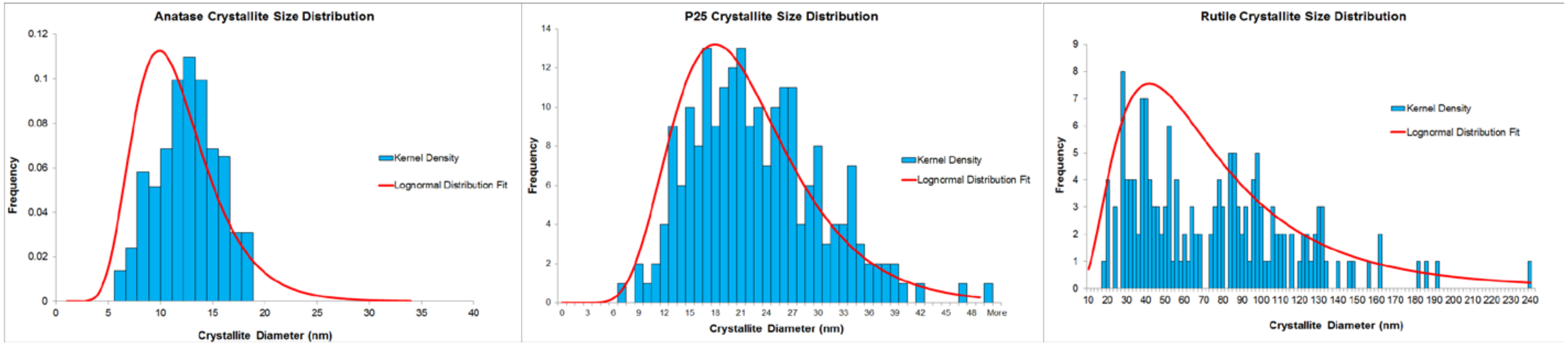

Figure B. 1: Histograms of particle size distribution for titania supports (Anatase, P25 and Rutile)

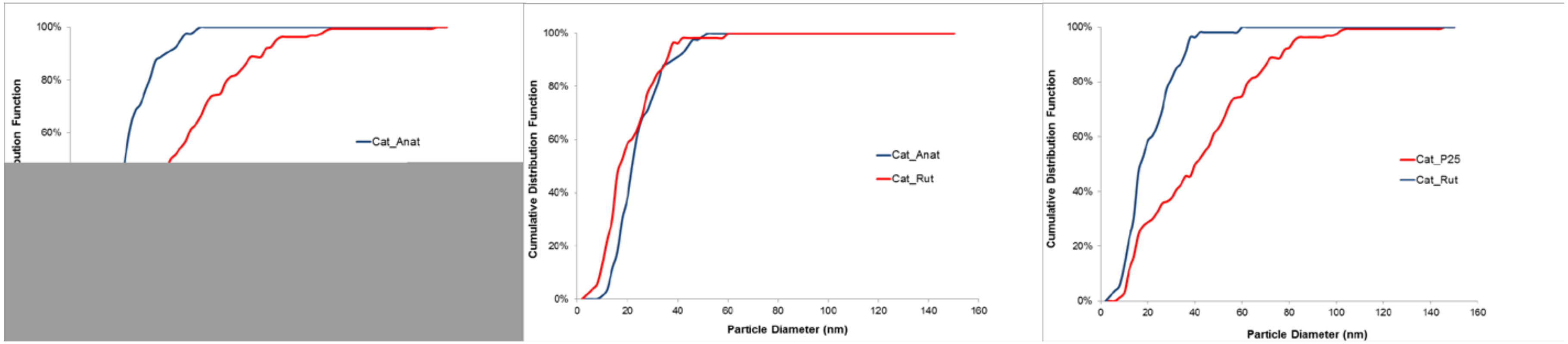

Figure B. 2: Cumulative Distribution Functions of anatase-, P25- and rutile-supported catalysts showing the cobalt particle size distribution.

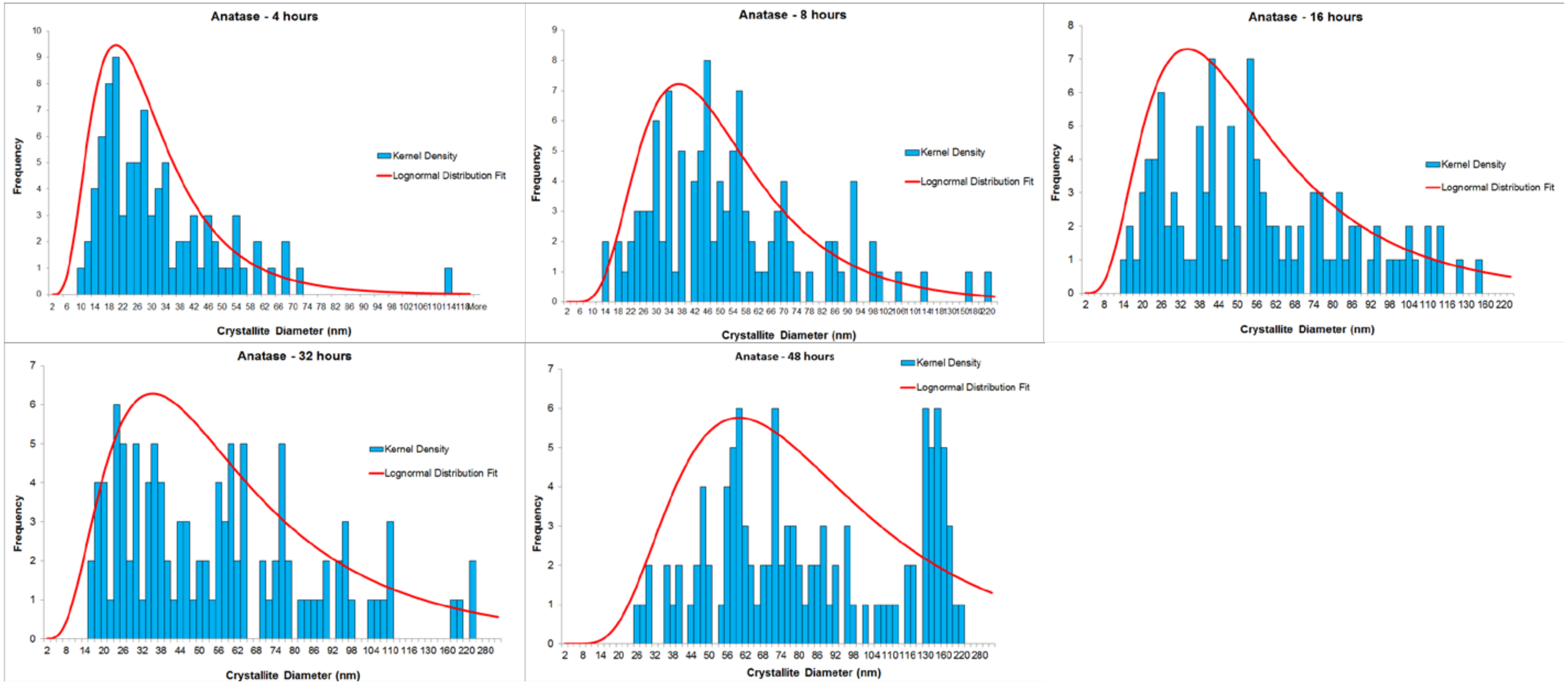

Figure B. 3: Histograms of particle size distribution for sintered anatase-supported catalysts.

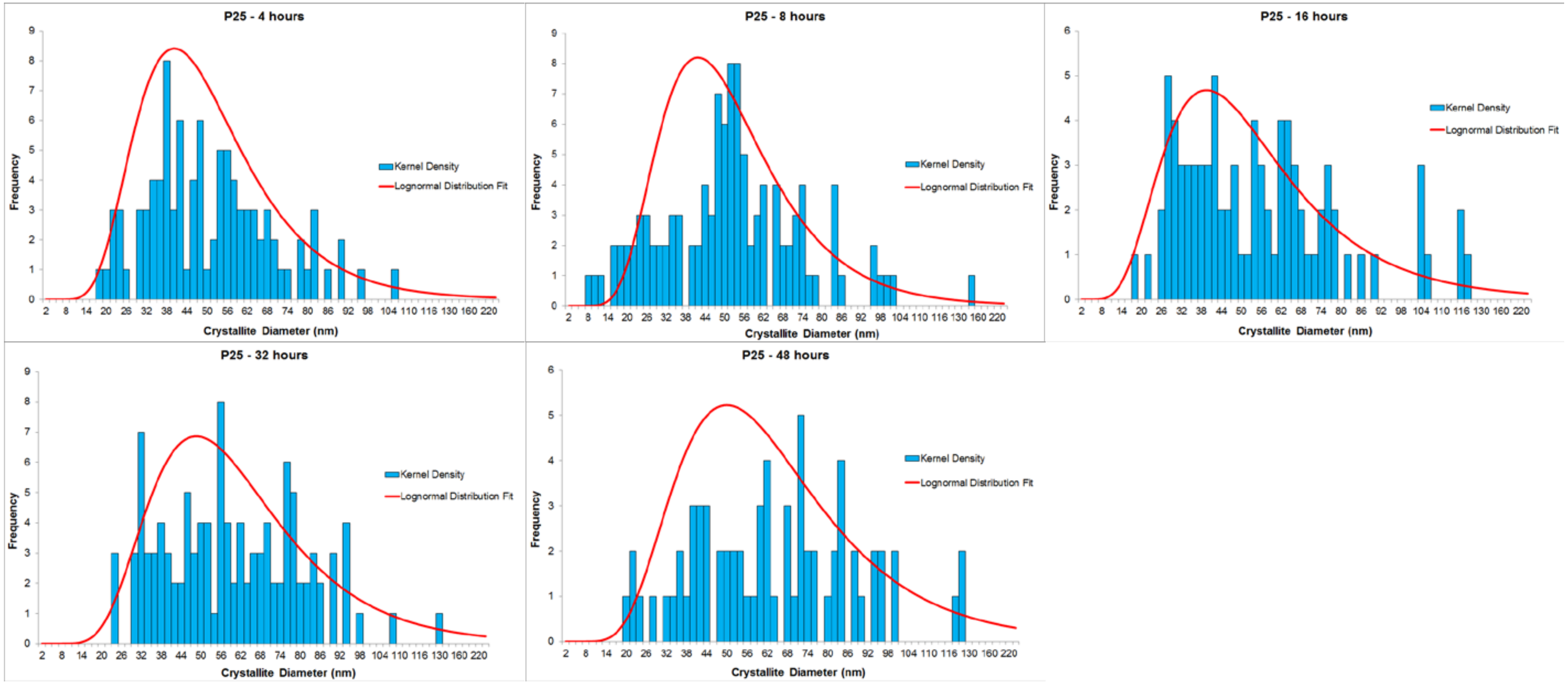

Figure B. 4: Histograms of particle size distribution for sintered P25-supported catalysts.

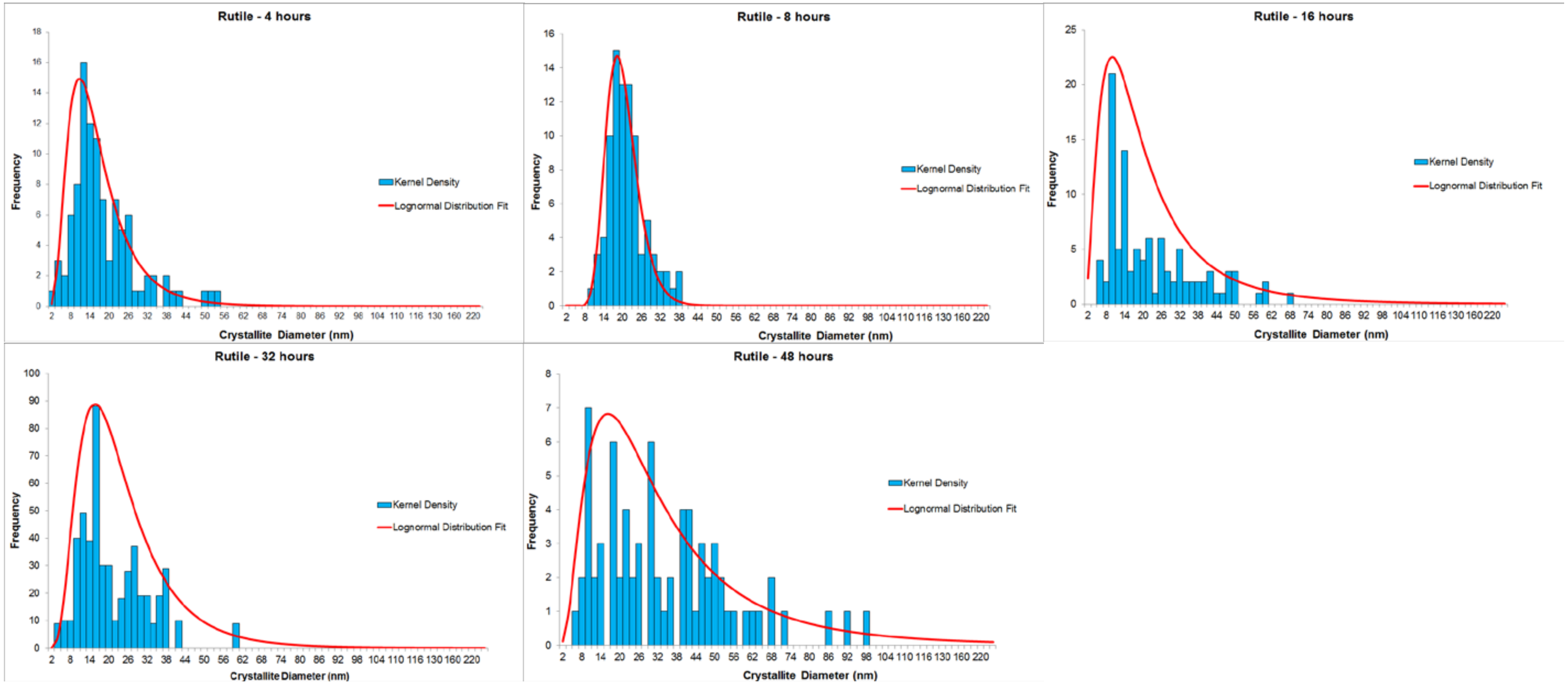

Figure B. 5: Histograms of particle size distribution for sintered rutile-supported catalysts.

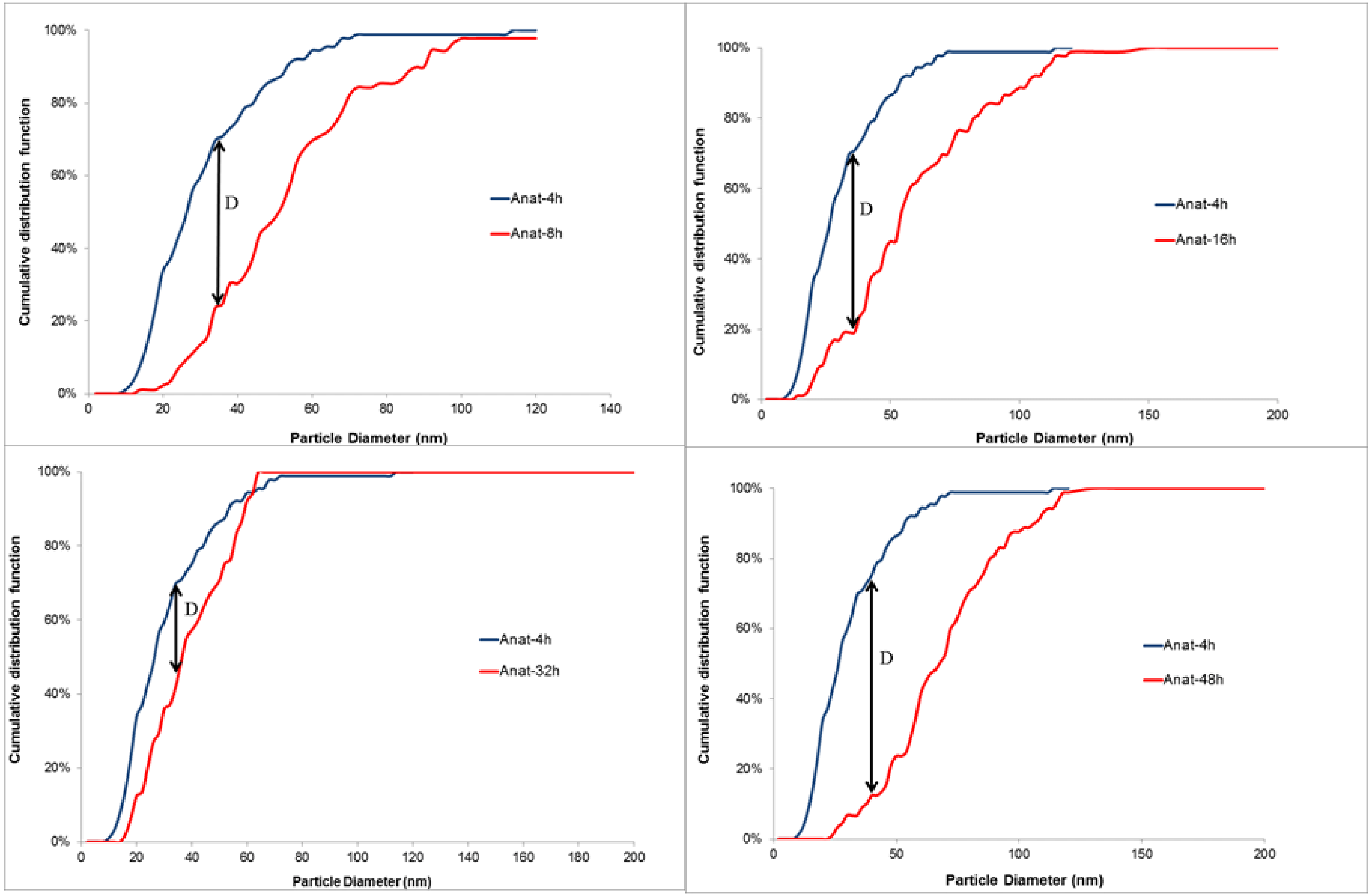

Figure B. 6: Cumulative distribution functions for sintered anatase-supported catalysts showing differences according to the Kolmogorov-Smirnov test.

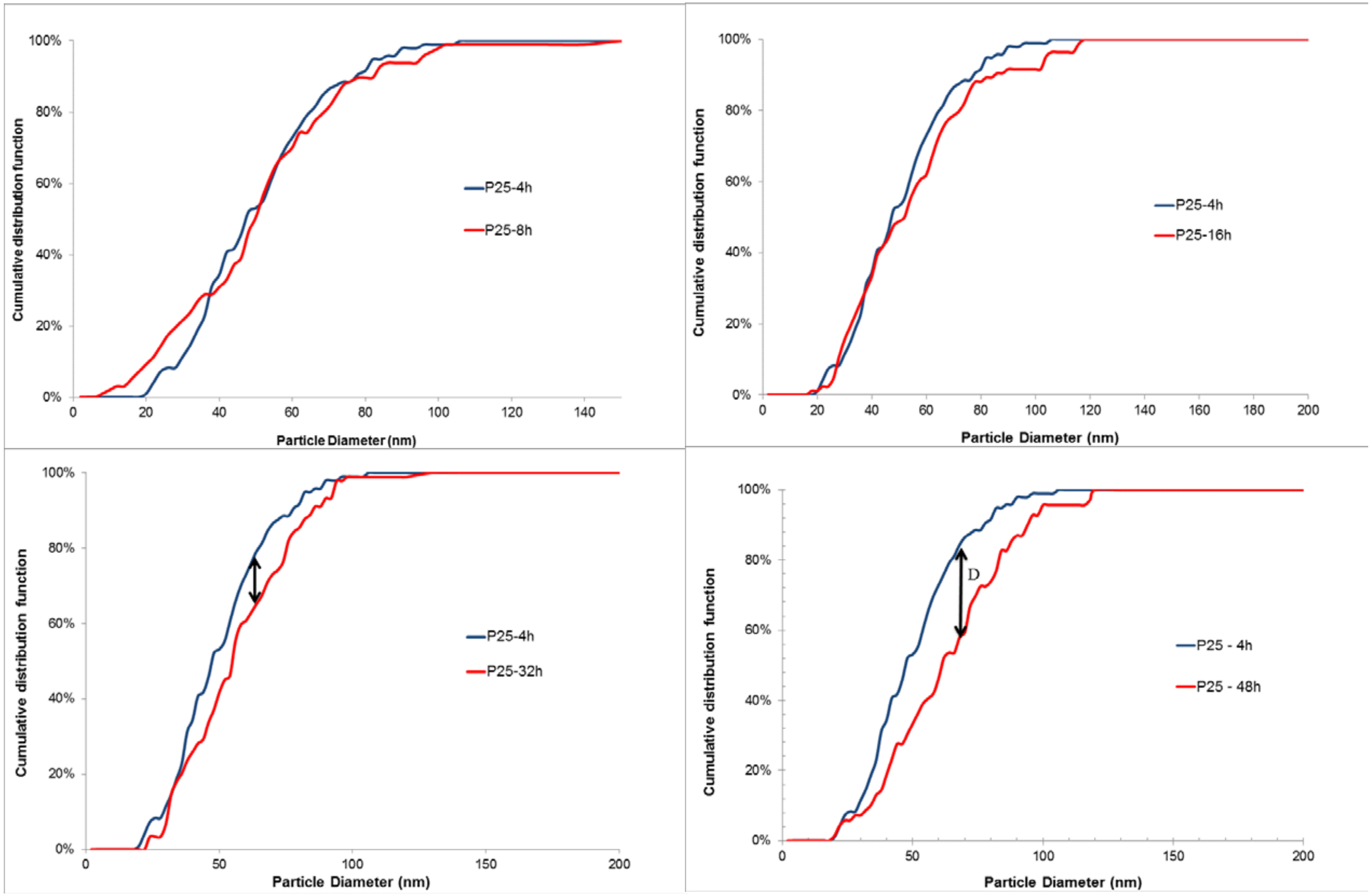

Figure B. 7: Cumulative distribution functions for sintered P25-supported catalysts showing differences according to the Kolmogorov-Smirnov test.

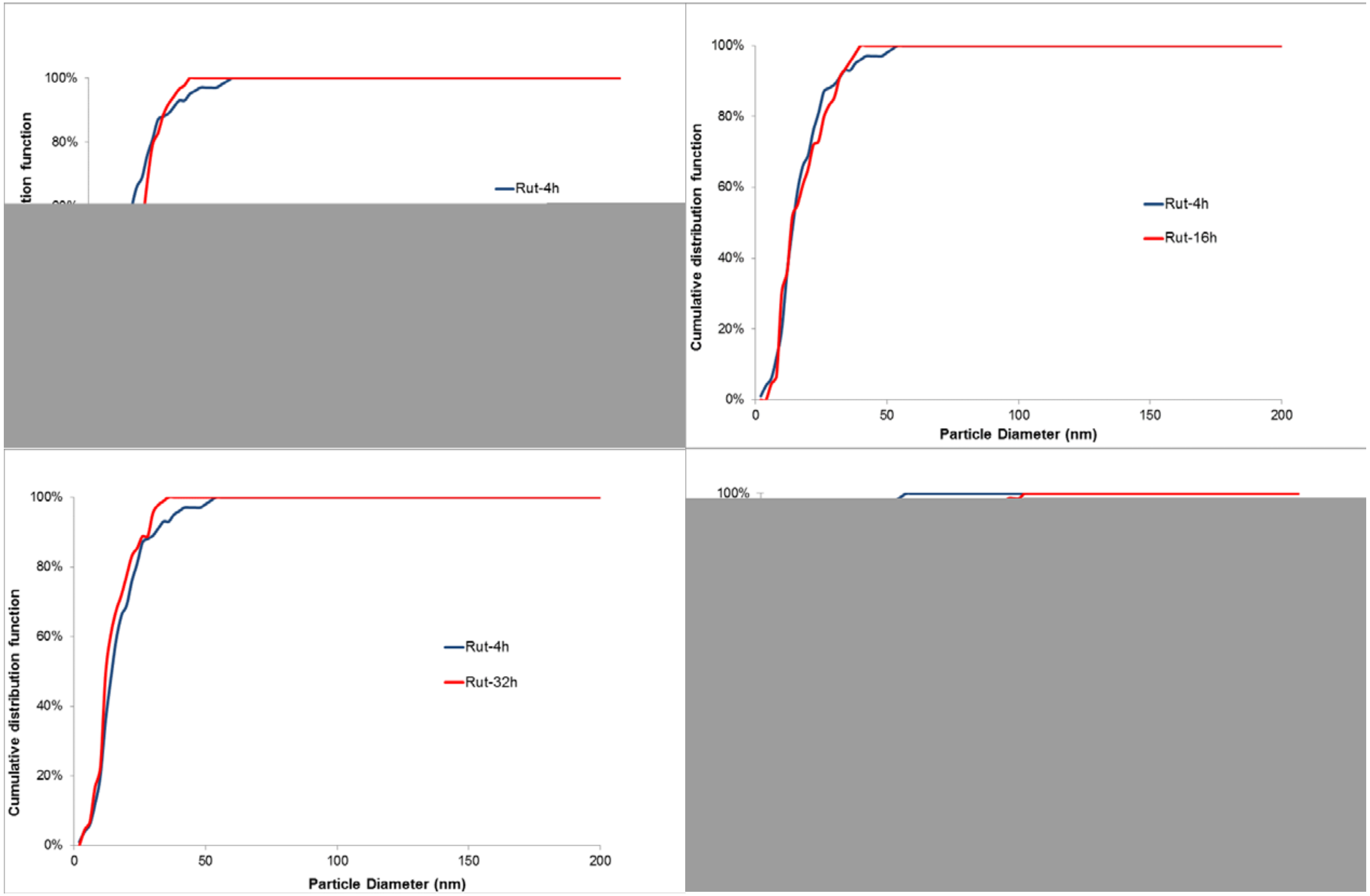

Figure B. 8: Cumulative distribution functions for sintered rutile-supported catalysts showing differences according to the Kolmogorov-Smirnov test